On the ambient medium and a stellar association around the supermassive black hole Sagittarius A*

Observations in the near- and mid-infrared with VLT and JWST

INAUGURAL-DISSERTATION

zur
Erlangung des Doktorgrades
der Mathematisch-Naturwissenschaftlichen Fakultät
der Universität zu Köln

vorgelegt von

Seyedeh Elaheh Hosseini
aus Mashhad, Iran

Köln, 2023

Berichterstatter:	Prof. Dr. Andreas Eckart
	Prof. Dr. J. Anton Zensus
Vorsitzender:	Prof. Dr. Dennis Mücher
Tag der mündlichen Prüfung:	20. July 2023

Abstract

The Galactic Center has been an intriguing topic for several decades. The center of the Milky Way is located at a distance of 8 kiloparsec from us and harbors a supermassive black hole (SMBH), known as Sagittarius A* (Sgr A*). The center of the Milky Way is the nearest galactic nucleus to us. Therefore, it provides a great opportunity to study galactic nuclei in general. Furthermore, high-resolution telescopes enable us to observe the stars in the close vicinity of the SMBH. Despite the proximity to the center of our Galaxy, it is obscured by dust lanes and gas clouds, making it invisible in the optical regime. Therefore, in order to study the heart of our Galaxy, we must conduct infrared, radio, and X-ray observations.

In this thesis, I study the Galactic Center in the near and mid-infrared regime. I first focus on the ambient medium of the SMBH, Sgr A*. I analyze L'-band observations to investigate the probable bow shock features of the S2 star around the time of its periapse along its orbit around Sgr A* in May 2018. I place an upper limit of 10^9 cm^{-3} on the density of the ambient medium of Sgr A*. However, the bow-shock synchrotron model provides a tighter upper limit of about 10^5 cm^{-3} at 1500 Schwarzschild radii. This upper limit allows for a wide variety of ambient media properties at the S2 star's pricenter distance, but excludes the standard thin cold disk model. The improvements in the photometric sensitivity of the Extremely Large Telescope can provide tighter constraints on the ambient medium density around Sgr A*.

Investigating the ambient medium around Sgr A* by studying one of the most important stars of the S-cluster provides a suitable foundation for concentrating my studies in the next step on the stars in the vicinity of the supermassive black hole. The closest stellar population to Sgr A* is the S-cluster, which played an important role in establishing the existence of the supermassive black hole at the center of our Galaxy and in determining its mass of 4.6×10^6 $M_\odot$. However, the S-cluster is not the only stellar population in the region. At a projected distance of ~0.15 pc to the south-west of Sgr A*, there is the stellar association of IRS 13E. In my work, I discovered another apparent concentration of stars at a distance of about 0.25 pc to the north-east of Sg A*. I investigated this sample of 42 stars which are located close to the bow shock source IRS 1W within a radius of $1.35''$ corresponding to 0.05 pc. I analyze the proper motions of these sources with K_s-band observations, determine their brightness in the H- and L'-band and investigate their colors. The velocity dispersion of this subsample motivates me to consider them as an association of stars. I name them N-sources due to their northward moving direction. This association of stars can be a bound system due to a putative intermediate-mass black hole (IMBH) with a mass of about 10^{3-4} $M_\odot$. Another plausible scenario could be a projection of a disk-like distribution of young He-stars and/or dust-enshrouded stars. The non-detection of any bright source in X-ray at the position of N-sources weakens the IMBH scenario, whereas

the location of IRS 13E and N-sources on the west and east side of Sgr A*, respectively, strengthens the disk-like distribution scenario.

The most important component of the Galactic Center research is the SMBH, Sgr A*, which is a variable radio, near-infrared, and X-ray source. For this reason, in the last part of my thesis, I conducted a research on the SMBH in near- and mid-infrared. In near-infrared, I investigate the simultaneous K_s- and L'-band observations in 2018. These observations were conducted in collaboration with the Event Horizon Telescope campaign to study the flare activities of Sgr A*. I detected a flare activity in K_s-band in the observations. However, after switching the filter to observe in L'-band, there the flare is not detectable anymore. This could be due to the time gap between switching the filters or it could be one of the K_s-band flares of Sgr A* which does not have a L'-band counterpart. The origins of these flares are believed to lie in the accretion flow onto Sgr A*. Most models include some form of synchrotron emission to explain the occurring flares from the radio to the NIR regime. However, the correlation pattern between the wavelengths is not yet completely understood.

Related to this, in mid-infrared, I analyze observations of the Galactic Center in the N-band with the Very Large Telescope/VISIR. The previous attempts to detect the counterpart of Sgr A* in N-band led to placing an upper limit on the flux density of Sgr A*. I was able to obtain a matching upper limit of 10 mJy on the brightness of the mid-infrared counterpart of Sgr A*. This result is in agreement with the theoretically expected spectral energy density of the mean emission from Sgr A*.

Finally, the launch of the most powerful infrared space telescope, the James Webb Space Telescope (JWST), opened a new era in astrophysics. It will improve our understanding of the universe, star formation, and galaxy formation from about two hundred million years after the Big Bang to the current activities of the SMBH residing in the center of our Galaxy. Due to the delay in its launch, I hereby present preliminary results of the first JWST observations of the Galactic Center with NIRSpec. I compile a high-resolution, low-noise spectrum towards the Galactic Center, which demonstrates the great potential of JWST. Several lines can be identified in the spectrum, e.g. the [FeIII] line which might originate from the mini-spiral lying in the field of view. In general, the spectrum is in good agreement with the previous ground-based spectral studies of the Galactic Center. Furthermore, I present MIRI observations of three quasars, with redshifts of 0.4, 1.5, and 2.9, to establish the foundations for the upcoming MIRI Galactic Center observations. The quasars are observed in all four channels of MIRI. Heavy elements such as Cr, Fe, Mg, K, Si, Ar, and others are detected in their spectra once again demonstrating the great capabilities of JWST.

Contents

CHAPTER 1

Introduction

1.1 Motivation

Humans have always been curious about the universe in which we live. We were mesmerised by the night sky. Some people found the celestial bodies so intriguing that they believed they were gods and worshiped them. Observing the night sky immediately brings us to the orbits of stars and planets on the plane of sky. The efforts of scientists to understand these orbits started very early in 380 B.C., when the geocentric model was designed by Eudoxus. In 10th century, Persian polymaths such as Abu-Sa'id al-Sijzi (945-1020) and Abu Rayhan al-Biruni (973-1050) introduced the heliocentric universe and only in the late 16th century, in the west world the geocentric model was substituted with the heliocentric model by Copernicus (1473-1543), Galileo (1564-1642) and Kepler (1571-1630). Nowadays, we know that, beside the solar system, the entire Milky Way galaxy is revolving around the center of our Galaxy, which harbours, at its heart, a radio source known as the supermassive black hole (SMBH), Sagittarius A* (Sgr A*).

During the last decades, technological developments brought up unprecedented opportunities to investigate the center of our Galaxy. The center of our Galaxy is obscured in the visible regime. Therefore, we need observe it in other wavelengths than optical. The Galactic Center research over the last decade has been stunning due to outstanding ground-based telescopes such as the Very Large Telescope (VLT), the Very Large Telescope Interferometer (VLTI)/GRAVITY and the Event Horizon Telescope (EHT) and – last but not least – the largest and most powerful space telescope ever built, the James Webb Space Telescope (JWST). The VLTI/GRAVITY observations could measure the precession of the S2 star's orbit around Sgr A*, which is a stunning evidence to prove the general relativity (Parsa et al. 2017; Gravity Collaboration et al. 2018). Furthermore, the EHT could produce an amazing image of the "shadow" of the black hole M87* and Sgr A* (Event Horizon Telescope Collaboration et al. 2019, 2022), which added overwhelming evidence for the existence of black holes. Moreover, the upcoming years are going to be revolutionary with respect to solving our questions about the cosmos, but also bringing up many more questions due to the breathtaking observations of JWST and – in a few years time – by the help of Extremely Large Telescope. All in all, a new era of discoveries in the Galactic Center is awaiting us.

1.2 Objectives of this thesis

Our Galactic Center (GC) is a unique laboratory to study different astrophysical processes and phenomena such as star formation, stellar dynamics, the physics of the interstellar medium and the emission associated with the accretion onto the closest SMBH, Sgr A*. The existence of a SMBH at the GC, located at about 8 kpc away from us, plays an important role in understanding the physical processes and the interaction between SMBHs and their host galaxies. As one example, the expected bow-shock formation of stars passing through the immediate ambient medium around a SMBH results in flux density enhancements, predominantly observable in the mid-infrared wavelength domain. The high flux density sensitivity of the MIRI camera on-board of JWST combined with the pointing stability of the telescope, will allow us to compare measurements of stars in this region at different epochs. Hence, in the future we will be able to measure or put limits on the density of the interstellar medium in this region. As I will show, this thesis has laid the ground work for this program.

Similarly, the GC region is predestined to be a promising location for the detection of intermediate mass black holes (IMBHs) with masses around 10^4 $M_\odot$. The best candidate so far is putatively located at the center of the IRS13E stellar association in the overall GC stellar cluster. The discovery of an additional, apparent dense stellar association adjacent to IRS1W, N-sources, reported in this work, which lies opposite of IRS13E eastward of SgrA*, thus lays the groundwork for more sensitive observations with MIRI on-board JWST. MIRI will allow us to carry out this investigation with the inclusion of spectroscopy such that the entire 3-dimensional velocity field can be probed for dynamical evidence of the stellar response to a putative IMBH.

Taken together, in this thesis I will address the following important scientific questions, always under the aspect of the relevance for the JWST-MIRI program:

- What is the ambient medium density of the SMBH, Sgr A*? This is a crucial question as measuring it more precisely will help us to understand the accretion flow towards Sgr A*.

- Are there other stellar populations in the vicinity of the SMBH, Sgr A*? If so, what are their properties? This is essential, as the stellar populations around the SMBH reveal some information about itself, e.g. the S-star proper motions had an important role in proving the existence of a black hole at the center of our Galaxy in the first place.

- However, the existence of such young stars in the close vicinity of a SMBH is also a big paradox, referred as "Paradox of Youth".

- What is the flare activity correlation of Sgr A* in K_s- and L'-band?

- What is the upper limit on the mid-infrared flux density of Sgr A*?

- What science output can we expect from JWST for the GC?

The aforementioned questions will be covered in this thesis, which has the following structure: Before addressing the individual questions, I will first provide the essential astrophysical background to understand the objectives by giving a general overview of the structure of our Galaxy and the GC environment (Chapter 2). This is followed by a brief description of the importance and challenges of infrared ground-based astronomy, the related observational techniques and the data reduction procedure (Chapter 3). In Chapter 4, I briefly discuss the space-based observatories. I introduce the largest and most powerful space telescope ever built, the James Webb Space Telescope, and shortly discuss its instruments.

In the scientific work part, I first focus on the S2 star in Chapter 5. I show that using L'-band observations to study the bow shock features of such a star transiting in the immediate vicinity of the SMBH Sgr A* can be used to put an upper limit on the gas density of the ambient medium in the vicinity of the SMBH. In this region the ISM is dominated by the accretion flow onto SgrA* and the winds emerging from it. Next, in Chapter 6 I report the discovery of a dense association of stars located at ~6 arcseconds distance from Sgr A* and discuss the features that make them candidates to be a dense association of stars. In Chapter 7, will conduct additional observations towards the position of Sgr A* to study its activity and to investigate the potential of JWST for GC research by analysing first GC data released by it. In addition, I study three quasars in the redshift range between 0.4 and 2.9 observed by MIRI in order to present the its capabilities, which will be used in future observations to investigate the inner half a parsec of the GC. I note that due to the delay in JWST, no MIRI data on the GC had been taken yet. However, already now, the preparatory work on JWST data presented here has lead to the acceptance of the GC as a MIRI team guaranteed time target, that will be observed later in 2023. The investigation presented here will also be relevant for the preparation of additional scientific observing programs conducted by JWST and the MIRI spectrometer system. Finally, I summarise the dissertation's highlights, and provide the foundation for further research in Chapter 8.

CHAPTER 2

Astrophysical Background

This chapter provides the necessary background knowledge to understand the results of this dissertation. This thesis is about the phenomenon occurring at the center of our Galaxy in the close vicinity of the supermassive black hole Sagittarius A*. Therefore, I provide some briefing on the components of our galaxy, from a few hundred parsec scale to the very center of our Galaxy.

2.1 The Milky Way

The Milky Way galaxy is part of the Local Group and is located on the outskirt of the Laniakea supercluster (Tully et al. 2014). Additionally, the fact that we are located on the Milky Way's periphery makes it considerably harder to investigate the Galactic Center. As every nation had its own fantasy and stories about the night sky, Persians were not so different. In Persian, galaxy is called "**Kahkeshan**". This name refers to the idea that a bunch of hay, which was pulled over the night sky, where hay straws were pulled out from that bunch and were left on the night sky. These straws appear as the bright band in the night sky known as the Milky Way. The "Miky Way" is also alluded to as "**Raah e Shiri**" in Persian which literally means Milky Way. The Milky Way is a barred spiral galaxy consisting of more than 400 billion stars, gas clouds, dust and dark clouds and a dark matter halo and was formed 12 billion years ago. Fig. 2.1 is an artistic illustration of the Milky Way which shows its components and surroundings. In the following, I briefly introduce each of our Galaxy components.

The **dark matter halo** surrounds our galaxy. This spherical-shape halo has a mass of 1 trillion $M_{\odot}$ and extends hundreds of kpc. It gravitationally influences the rotation of the Galaxy and contains dark matter sub-halos. At least 14 **dwarf galaxies** orbit the Milky Way which have been formed in the dark matter halo. There exist **streamers** of stars tracing the orbits of dwarf galaxies. These streams were disrupted by the Milky Way and became a part of it. Furthermore, there exist **Fermi bubbles** composed of plasma starting from the galactic disk at the Galactic Center and continuing perpendicular to it above and below it for about 9 kpc with the maximum diameter of about 6 kpc. Fermi bubbles are visible

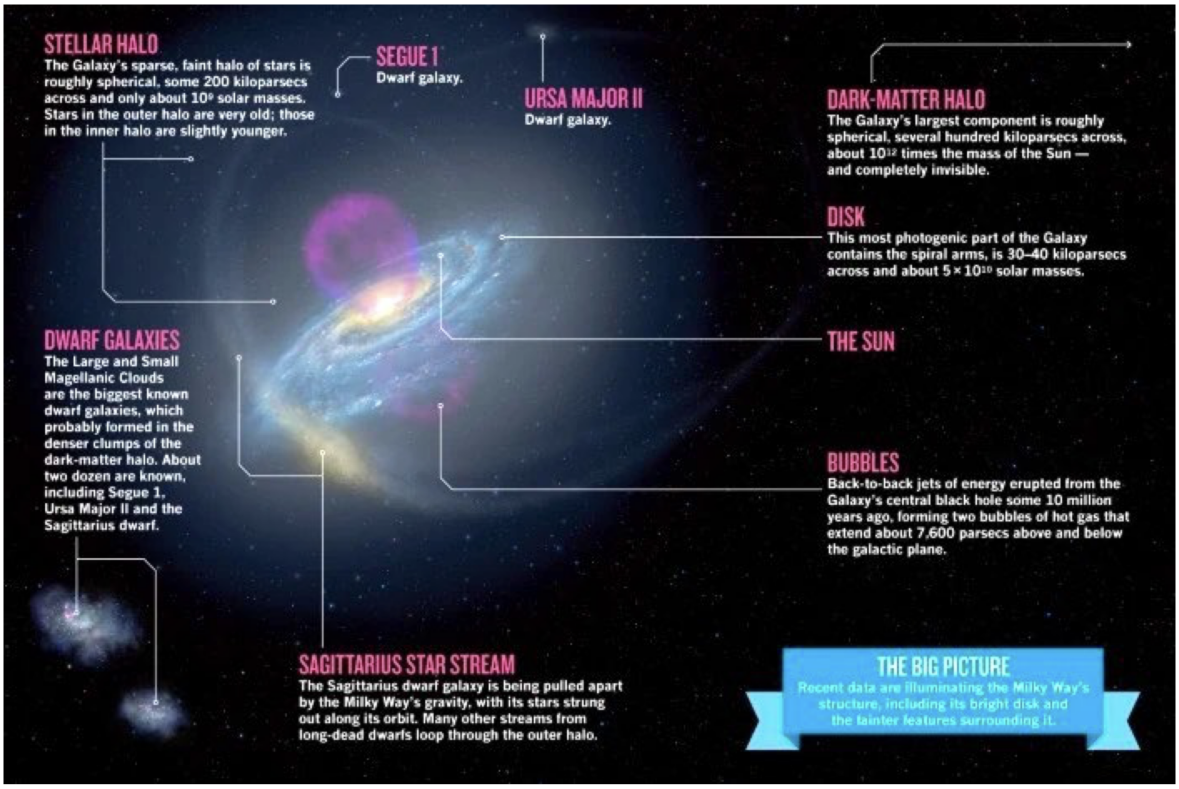

Figure 2.1: An artistic view of the Milky Way galaxy and its surroundings. Image credit: Finkbeiner (2012)

in maps observed at photon energies of more than 1 GeV. The emission might be caused by the inverse Compton scattering of cosmic-ray electrons on the cosmic microwave background and other radiation fields. **eROSITA bubbles** start from the galactic plane and extend for 14 kpc perpendicular to the galactic disk above and below the Galactic Center with a maximum width of 14 kpc (Predehl et al. 2020). The **halo** contains the oldest stars in the Galaxy, globular clusters and very hot diffused highly ionised gas, which produces a gamma-ray halo. The rotation curves of other spiral galaxies and other evidence show that the halo is dominated by cold dark matter (Babcock 1939; Kahn & Woltjer 1959; Roberts & Rots 1973; Einasto et al. 1974; Ostriker et al. 1974; Rubin et al. 1985; Carignan et al. 2006; White & Rees 1978; Navarro et al. 1997). The halo is approximately spherical with no sharp borders (Springel et al. 2005). The border of the halo is considered to be at the position, where the gravity of the neighbouring galaxy is stronger than the gravity of the host galaxy. For the Milky Way this happens at about half the distance to Andromeda (M31) at 780 kpc (McConnachie et al. 2005). The **stellar halo** is a spherical halo of stars and globular clusters, with a radius of 65 000 lyr (Eggen et al. 1962; Hesser 1992; Helmi 2008). The **galactic disk** is made of young massive blue stars.The disk of our Galaxy is a flattened, rotating system which contains the Sun (at about 2/3 of the way from the center to the edge of the disk) and other intermediate-to-young stars. The **bulge** is the central part of the Milky Way (Baade 1946; Arp 1965; Oort 1977), which is thicker and brighter than the disk and, in the case of the Milky Way, is a bar (Blitz & Spergel 1991; Dwek et al. 1995; Stanek et al. 1996). The bulge is visible in the optical wavelengths located outside of the dust lanes. The high extinction in the Galactic disk prevents us to determine the structure of the bulge. At the very heart of the stellar content of the bulge lies a supermassive black hole known as Sagittarius A* (Sgr A*) with a mass of approximately 4 million solar masses (Balick & Brown 1974; Goss & McGee 1996a; Eckart & Genzel 1996; Ghez et al. 1998; Eckart et al. 2017; GRAVITY Collaboration et al. 2019; Event Horizon Telescope Collaboration et al. 2022, and references therein). In about six billion years it is possible that the Milky Way and Andromeda will collide with the speed of $\sim$100 km s^{-1} and merge over one billion years and form one huge elliptical galaxy (Sohn et al. 2012; van der Marel et al. 2012; van der Marel et al. 2012).

2.2 The Galactic Center

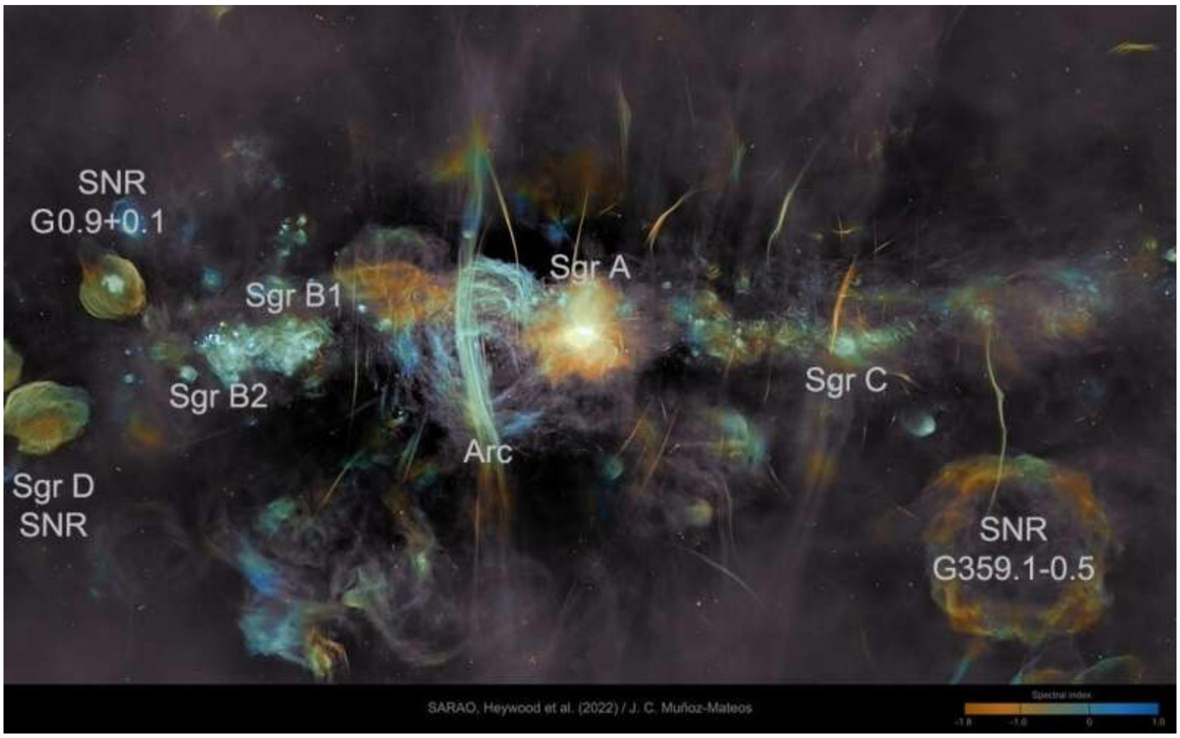

Figure 2.2: The Milky Way's center over a few square degree, observed by MeerKAT, an array of 62 radio dishes in South Africa. Sgr A at the center of the image hosts the supermassive black hole, Sgr A*. Image credit: Photo, Ian Heywood (Oxford U.), SARAO; Colour Processing, Juan Carlos Munoz-Mateos(ESO).

The center of our Galaxy contains stars, stellar remnants, dust and molecular and ionised gas. The center of the Milky Way galaxy is located at a distance of 8178 pc from us (Reid 1993; Eisenhauer et al. 2005; Ghez et al. 2008; Gravity Collaboration et al. 2019) which makes it the closest nucleus to us to observe. Moreover, the Galactic Center harbours a supermassive black hole, Sgr A*, at its heart, making it a unique laboratory to investigate galactic nuclei, star formation, dynamics and evolution of gas and stars in galactic nuclei, accretion emission and effects of general relativity.

The Sagittarius A (Sgr A) radio complex was discovered in the Sgr constellation at the center of the Milky Way galaxy by Karl Jansky in 1932 (Goss & McGee 1996b). It is believed to trace matter orbiting Sgr A*. Fig. 2.2 shows a stunning image observed by the South Africa MeerKAT radio telescope which covers about 6.5 square degrees. It indicates

Sgr A along with several giant molecular clouds, such as Sgr B1 and B2 as well as several synchrotron emitting filaments (Heywood et al. 2022). By zooming onto the position of Sgr A in Fig. 2.2 and moving from the radio regime to a shorter regime, such as the X-ray domain, we can identify main components of the Sgr A complex. It consists of the supernova remnant Sagittarius A East, the spiral structure of Sagittarius A West, and the compact radio source at the center of the spiral structure, SMBH, Sgr A* (see Fig. 2.3). In the following, I briefly describe the building components of Sgr A complex. **Sgr A East** is a non-thermal X-ray/radio source appearing as a shell-like structure which is considered as a supernova remnant (Ekers et al. 1975, 1983), with a size of about 10.5 times 8 pc (e.g. Yusef-Zadeh & Morris 1987). **Sgr A West** is a three-armed structure, the so-called mini-spiral,

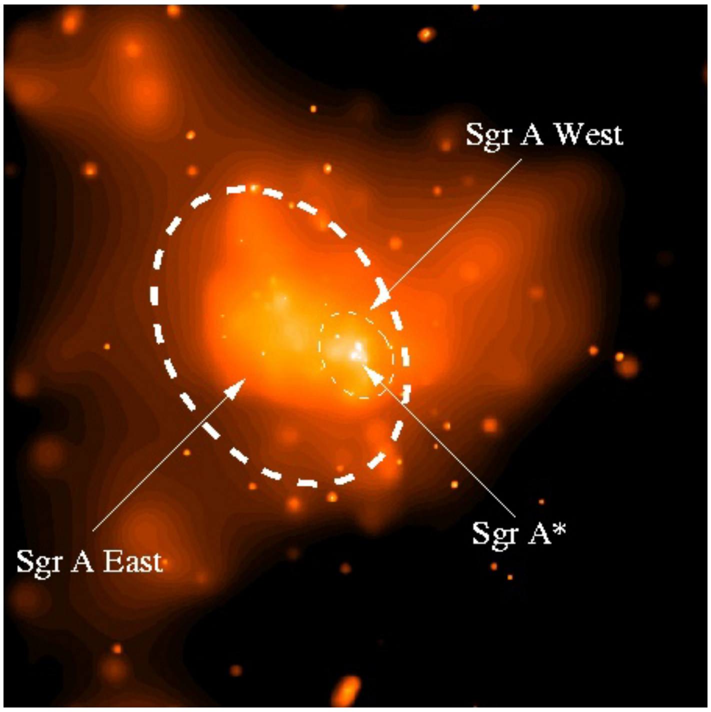

Figure 2.3: The figure is a zoom-in at the position of Sgr A in Fig. 2.2 observed in the X-ray domain over an extent of a few ~10 pc. The Chandra image illustrates the Sgr A complex in the X-ray domain. The white thick dashed ellipse in image denotes the non-thermal emission from the supernova remnant, Sgr A East. The thin dashed ellipse shows Sgr A West and the position of Sgr A* is depicted. Image credit: NASA/Penn State/G.Garmire et al.

which is surrounded by Sgr A East (see Fig. 2.4) (Ekers et al. 1983; Lo & Claussen 1983). Fig. 2.4 shows vividly the three-armed structure of the mini-spiral. It consists of ionised and atomic gas and dust stretched over 3 pc with a temperature of about 10 000 K (Yusef-Zadeh et al. 1998; Kunneriath et al. 2012). The structures are streamers of ionised matter infalling from the inner edge of the circumnuclear disk (CND) from east to west in projection with a speed of approximately 100 km s^{-1} (Yusef-Zadeh et al. 1998). These orbiting streamers are named as the Northern arm, the Eastern Arm/Bar and the Western Arc. The enclosed mass corresponding to an assumed Keplerian rotation of these streamers around the center is about 3.5 million $M_\odot$, which was the first indication of a supermassive black hole at the center of our Galaxy. The **CND** is a clumpy molecular ring with a radius of 1.5 to 7 pc

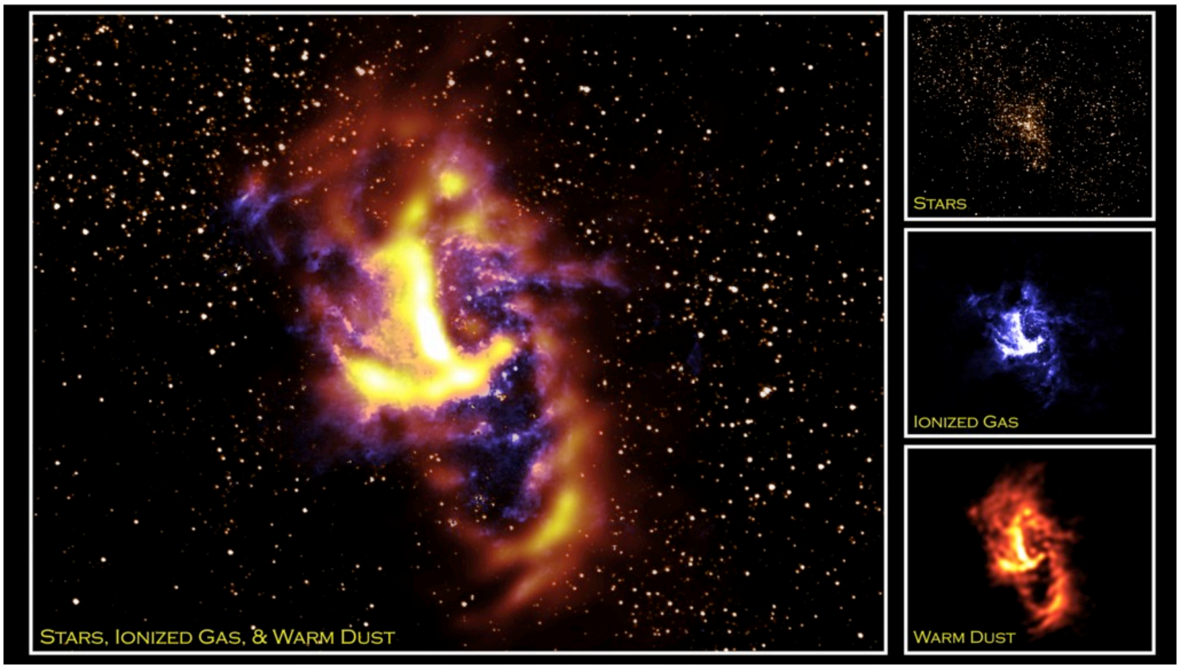

Figure 2.4: The figure is a zoom in-at the position of Sgr A in Fig. 2.3 showing a multi-wavelength image of the central 10 light-years of the Galactic Center. The upper right image shows a cluster of massive, young stars. The middle image illustrates the ionised gas by stars. The bottom image shows the heated up dust by stars. Image credit: Stars and Ionised Gas: NASA/HST/NICMOS; Warm Dust: NASA/DLR/USRA/DSI/FORCAST Team/Lau et al. 2013

and a mass of about a few 10^4 $M_\odot$ (Genzel et al. 1985; Mezger et al. 1989; Requena-Torres et al. 2012). It is believed that the CND orbits Sgr A* and is fed by gas infall from dense molecular clouds. It contains dense molecular clouds with densities up to about 10^4 to 10^7 cm^{-3} and warm dust with a temperature of up to a few hundred Kelvin (Guesten et al. 1987; Zylka et al. 1995; Wright et al. 2001; Herrnstein & Ho 2002; Christopher et al. 2005). The **nuclear stellar cluster** (NSC) is the accumulation of stars at the center of our Galaxy. The infrared observations revealed the existence of this high density population of stars in the innermost parsec of the Galactic Center whereas this region is not visible in the optical images due to high extinction. Nowadays, by the aid of Adaptive Optics we reach a resolution of 1 mpc for the Galactic Center in the near-infrared. Moreover, interferometry techniques elevate the reached astrometric resolution in the Galactic Center up to micro parsec, enough to resolve the cluster. The NSC stars are relatively old with the age of more than 5 Gyrs (Blum et al. 2003; Pfuhl et al. 2011). The cluster is dominated by old, late-type giants, super-giants and asymptotic giant branch stars. Moreover, it contains young stars with masses of 30 - 100 $M_\odot$, hot early-types, blue super-giants and Wolf-Rayet stars (Krabbe et al. 1995; Genzel et al. 1996; Paumard et al. 2006; Tanner et al. 2006). In the following, I discuss about the components within a few tenth of a parsec distance from the supermassive black hole, Sgr A*.

2.3 The Supermassive Black Hole in the Galactic Center

Looking at the Milky Way on the night sky, one notices the dark lanes of dust. A strong dense component towards the Galactic Center causes an optical extinction of $A_V = 30$ mag. Therefore, Galactic Center observations are carried out in other wavelengths to lower the extinction. Fig. 2.5 shows the central half a parsec of our Galaxy in L′ band. The

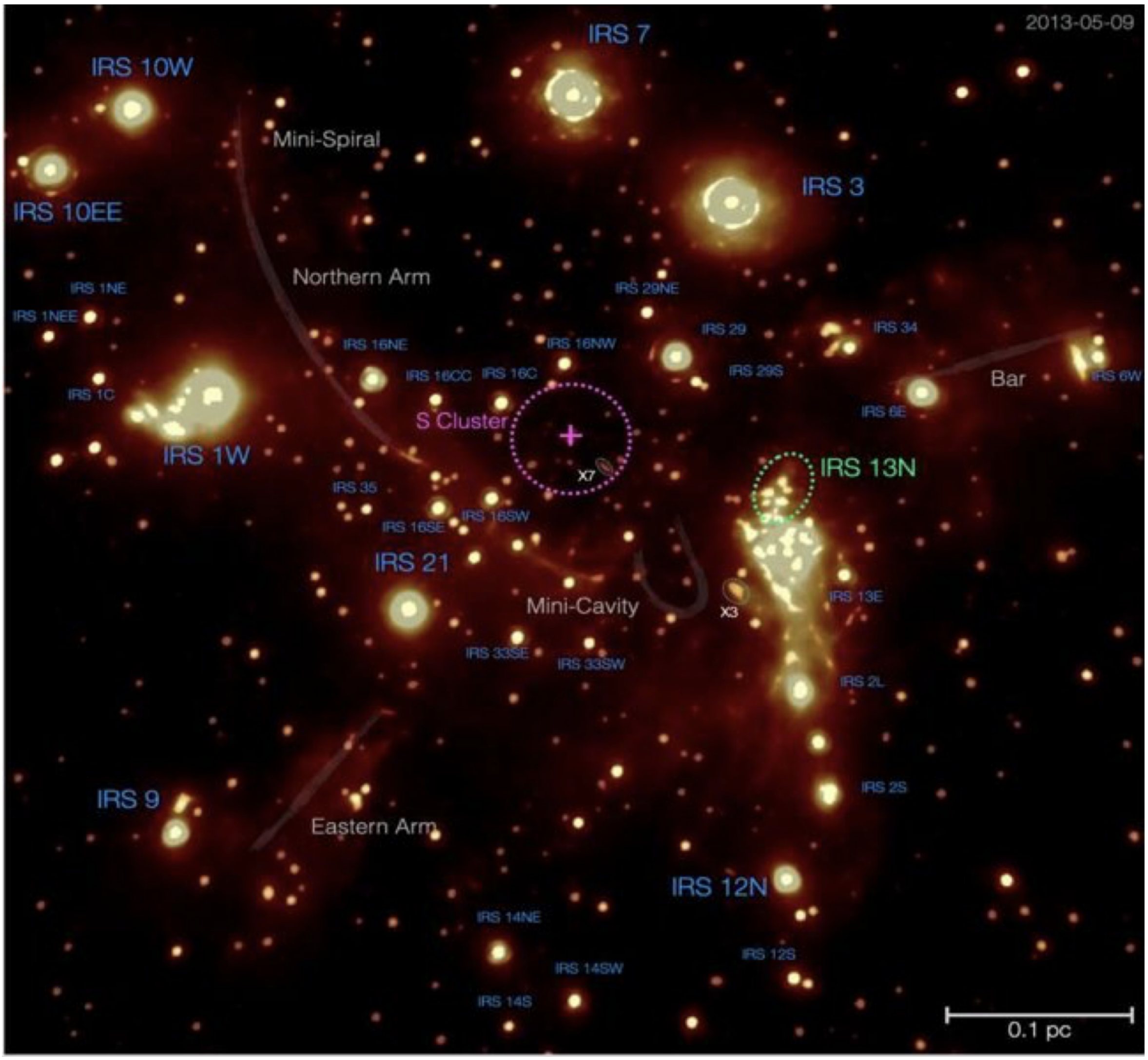

Figure 2.5: The L′ band image of the Galactic Center. The position of Sgr A* is denoted by a magenta cross. The dashed circle around the position of Sgr A* shows the region of S-star cluster. The IRS 13N and IRS 13E are on the south-west side of Sgr A*. The IRS 1S is located on the north-east side of Sgr A*. Image credit: L. Thomkin

non-thermal radio point source Sgr A* (Brown 1982) residing at the center of our own Galaxy was discovered at the center of the NSC by using the Green Bank 35 km radio link interferometer at Huntresville (Balick & Brown 1974). It is a very compact bright source and always visible in radio but variable in infrared (Witzel et al. 2021a) and has a dim accretion flow. The mass of the SMBH associated with Sgr A* is obtained by various means such as analyzing the Keplerian orbits of S-stars (e.g. Eckart & Genzel 1997; Ghez et al. 2000; Eckart et al. 2002; Eisenhauer et al. 2003; Ghez et al. 2008; Gillessen et al. 2009a,

2017) , the relativistic approach using the stars S2, S38, and S55 (Parsa et al. 2017) and using the stellar orbit of the S2 star (GRAVITY Collaboration et al. 2019). It is located at a distance of 8 kpc from us (Shapley 1928; Reid 1993; Reid et al. 2007; Eisenhauer et al. 2003; Gillessen et al. 2017; Parsa et al. 2017; GRAVITY Collaboration et al. 2019), which makes it the closest SMBH to us and the best laboratory to investigate black holes and galactic nuclei. Stellar proper motion measurements around Sgr A* are done in NIR via speckle imaging and later on adaptive optics (Eckart & Genzel 1997; Schödel et al. 2002; Ghez et al. 2000; Eckart et al. 2002; Eisenhauer et al. 2003). After the outstanding success of the shadow of M87 (Event Horizon Telescope Collaboration et al. 2019), it was the time to release a time-averaged image of the shadow of Sgr A* (Event Horizon Telescope Collaboration et al. 2022). The temperature of the peak brightness is about 1.2×10^9 K. The diameter of the ring is 51.8 ± 2.3 μarcsec , or 0.42 AU, which is consistent with the prediction of the general relativistic models of the accretion flow onto a Kerr black hole with the mass of Sgr A*. The EHT collaboration results show that Sgr A* has a non-zero and prograde spin with a spin axis inclination of less than 50 degrees to the line of sight. This is only a start of outstanding findings of EHT. Due to the upcoming increase in the number of EHT stations, there are more refinements of the properties of Sgr A* expected to come with future observations.

2.4 The closest stellar cluster to Sgr A*: the S-star Cluster

The "S-star Cluster " or "S-cluster" (Fig. 2.7) is a distinct population of faint young stars within a ~ 0.04 pc distance from the SMBH, Sgr A* (see the multi-wavelength image of the central parsec in Fig. 2.6). The S-cluster is observed optimally in K_s-band (2.2 μm) due to low extinction (less than 3 mag). These stars are mostly young, massive, B main-sequence stars with very high velocities of a few thousand km s^{-1} in addition to some late-type stars (Eckart et al. 1999; Ghez et al. 2003; Eisenhauer et al. 2005; Genzel et al. 2010). Stars around Sgr A* move on Keplerian orbits and up to now the orbits of 39 S-stars are known (Gillessen et al. 2017; GRAVITY Collaboration et al. 2019; Peißker et al. 2020b). Until recently, it was believed that the stars in the orbits of the S-stars had a random distribution, supporting the Hill mechanism as a possible migration theory. However, according to Peißker et al. (2020b), the stars' orbits appear to be in an intercrossing two-disk distribution. S2 star is the only star which has been observed throughout its ~ 15.9-year orbit and its orbital studies have been used to determine the enclosed dark mass at the center of our galaxy (~ 4×10^6 $M_\odot$) . It is an O8-B0 young dwarf, with a mass of 15 $M_\odot$ and an age of less than 10^6 yr determined by Ghez et al. (2003) and later by Eisenhauer et al. (2005). It had its closest aproach towards Sgr A* in 2018. Therefore, it was a suitable candidate to observe any bow shock features in order to identify the properties of the medium in the vicinity of SMBH, Sgr A* (see also Chapter 5).

2.4.1 Paradox of Youth

In the Galactic Center, there are several factors to prevent star formation such as elevated UV radiation, stellar winds and tidal forces from the SMBH (Morris 1993). Star formation should only be possible within a 25 parsec distance from the SMBH in the center of our Galaxy. However, we observe young stars with the age of less than 5 Myr. Therefore, the

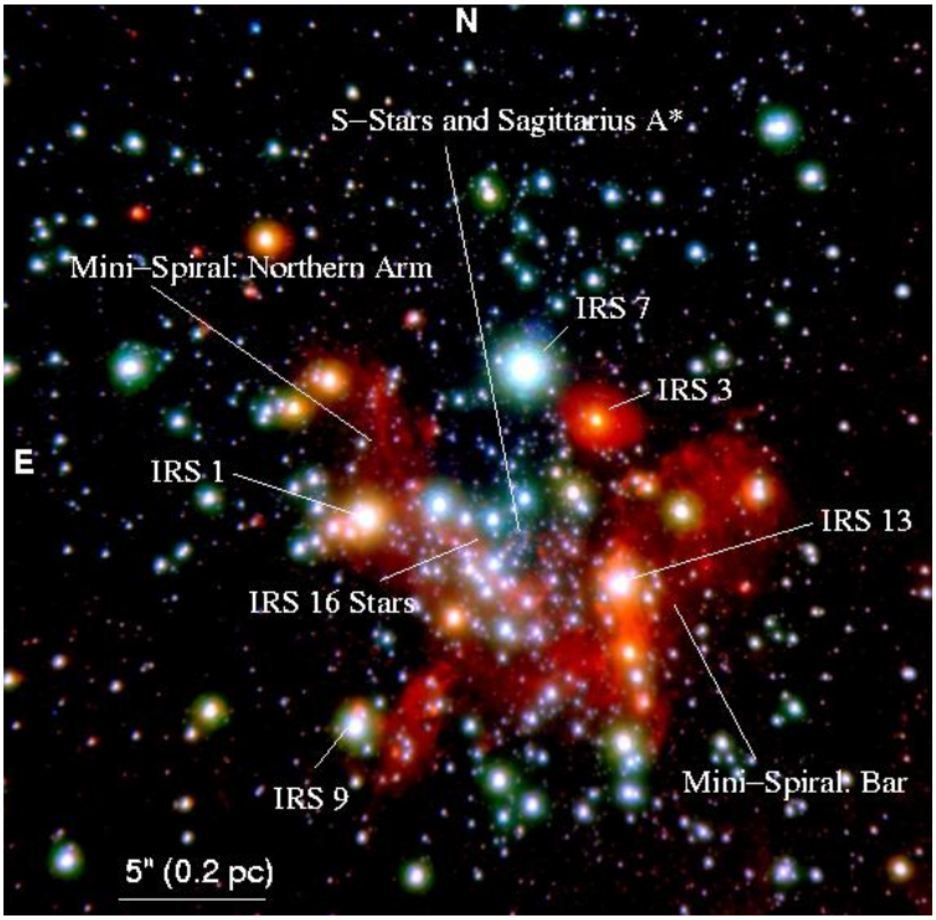

Figure 2.6: The superposition of the H, K and L′ band images observed by the Very Large Telescope (ESO). Image credit: University of Cologne

presence of such young stars within the central parsec of our Galaxy is not well understood and is referred to as the "Paradox of youth" (Ghez et al. 2003).

2.4.2 Star formation models

The investigations to solve this paradox led to three scenarios which I briefly describe in the following. These scenarios are referred to as the rejuvenation, the in-spiral and the in-situ scenario. The **rejuvenation** approach, which is the least favoured one, suggests that late-type stars collide with other stars. Therefore, they loose their cold outer layer and make them appear younger (Morris 1992, 1993; Genzel et al. 2003; Zajaček et al. 2020a,b). The **in-spiral** scenario is based on assuming that stars form outside the central parsec and the presence of an intermediate mass black hole to shorten the dynamical friction timescale (Gerhard 2001; McMillan & Portegies Zwart 2003; Portegies Zwart et al. 2006; Berukoff & Hansen 2006; Rizzuto et al. 2020; Peißker et al. 2021b). The last and most favoured scenario is the **in-situ** approach. It suggests that the stars actually form in a gravitationally unstable accretion disk or within an infalling molecular cloud (e.g. Morris 1993; Levin & Beloborodov 2003; Hobbs & Nayakshin 2009; Paumard et al. 2006; Jalali et al. 2014).

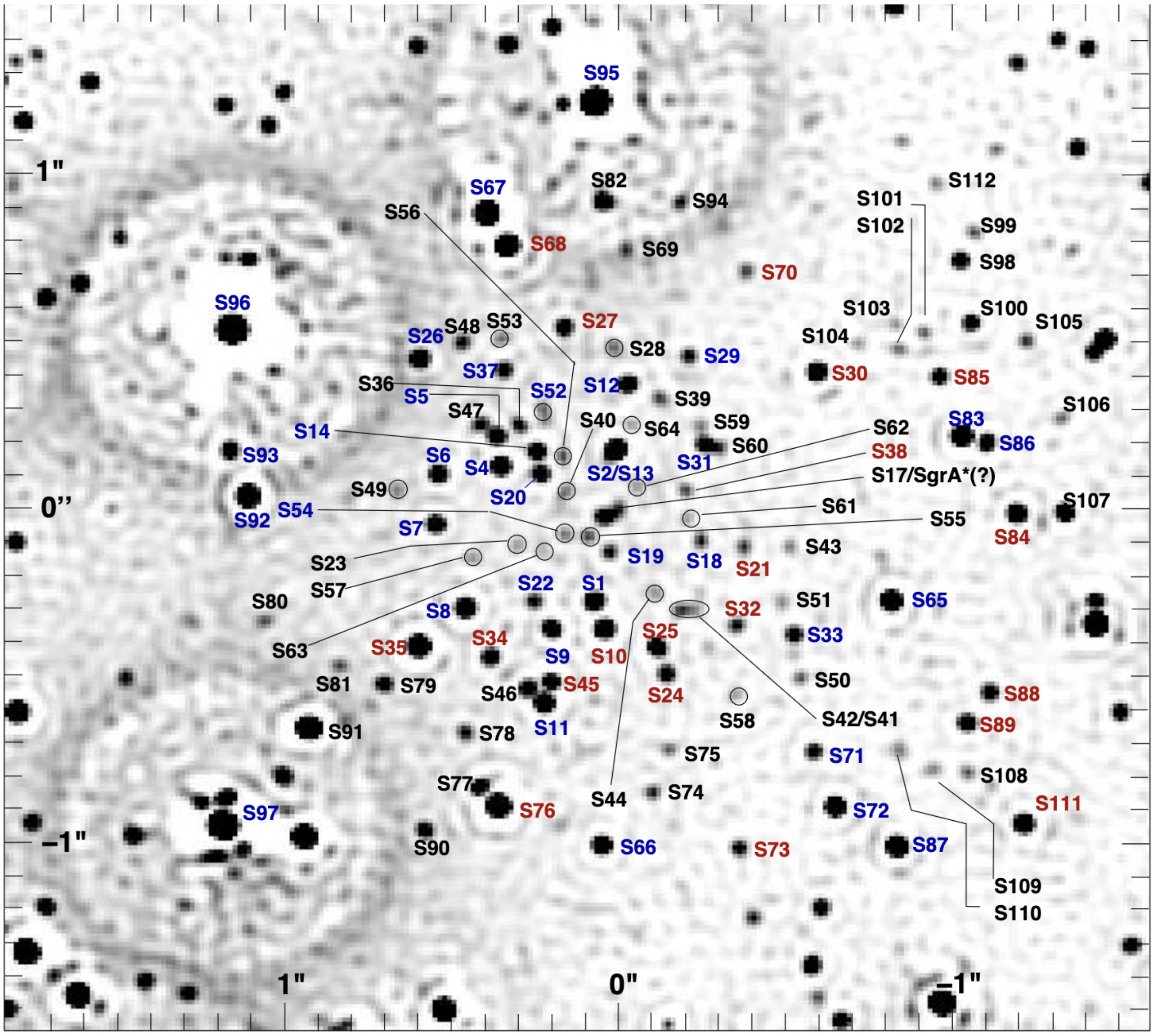

Figure 2.7: The S-cluster in an image obtained by NACO/VLT in 2007. North is up and east is to the left. The SMBH, Sgr A*, is located close to S2. Image credit: Gillessen et al. (2009a)

2.5 A stellar cluster in the vicinity of Sgr A*: IRS 13

The S-star cluster which is located within half a parsec around Sgr A* is not the only accumulation of stars around the SMBH. IRS13, dense association of stars ,which is located at the projected distance of $\sim 0.12 - 0.16$ pc on the south-west of Sgr A*, is a suitable candidate to study the aforementioned star formation scenarios in the Galactic Center. IRS 13 comprises a northern part, IRS13N, and an eastern part, IRS13E. The northern part contains young, infrared-excess sources (Maillard et al. 2004; Eckart et al. 2004; Paumard et al. 2006; Mužić et al. 2008; Eckart et al. 2013). The eastern part contains mostly massive Wolf-Rayet stars and the violet supergiant E1(OBI) and some late-type stars, probably background stars (Maillard et al. 2004; Moultaka et al. 2005; Paumard et al. 2006; Fritz et al. 2011). The velocity dispersion of IRS13E sources and the existence of an X-ray spectrum in the region strengthen the scenario of in-spiral star formation. Therefore, the mass of the putative IMBH residing within the IRS13E would be about $\sim 10^4$ $M_\odot$ (Maillard et al. 2004; Schödel et al. 2005; Spitzer 1969; Portegies Zwart & McMillan 2002; Rose et al. 2021)

2.6 IRS1W star and its surrounding

IRS 1W is a star with a bow-shock source and is located within the northern arm of the mini-spiral at a distance of about ~ $6.05''$ north-east of the SMBH, Sgr A*. It could have been formed in the northern arm of the mini-spiral or from the accreted gas and dust in the infalling material of the northern arm. IRS 1W has been identified as a bow-shock source with a central Wolf-Rayet star (Ott et al. 1999; Tanner et al. 2005) with a temperature of ~ 300 K (Tanner et al. 2002; Tanner et al. 2003; Tanner et al. 2005). The stellar-wind properties and kinematics of IRS 1W are similar to the properties of the clockwise orbiting He emission-line stars. Therefore, it seems that IRS 13 is not the only dense association of stars in the close vicinity of Sgr A* and a number of sources around the IRS 1W source also form an association of stars (see Chapter 6).

CHAPTER 3

Infrared Ground-Based Observations

3.1 Infrared astronomy

The Earth's atmosphere protects us from a wide range of radiation and blocks out high energy radiation such as X-rays, gamma rays and most of the ultraviolet radiation as well as most of the infrared radiation and very low energy radio waves (see Fig. 3.1). The thermal radiation beyond the red part of the visible light was discovered by William Herschel in 1800 and is called infrared (IR) radiation. He demonstrated experimentally that the Sun emits electromagnetic radiation outside the visible spectrum by dispersing sunlight with a prism and placing thermometers at the exit points of the different colors, showing that the temperature would increase even when the thermometer was placed above the visibly red part of the diffracted light. The wavelength range of the IR radiation is between 1 to 1000 μm. The IR observational range is divided into three bands of near-infrared (NIR), mid-infrared (MIR) and far-infrared (FIR) wavelengths and the first NIR observations started in the 1960s. The NIR band ranges from 0.7 to 5 μm, MIR observations from 5 to 30 μm and FIR ranges from 30 to 1000 μm.

Infrared astronomy is essential to investigate star forming regions, cool stars, bow shocks, exoplanets, cool clouds and cosmic dust to achieve a comprehensive view on the structure, composition and behavior of the celestial objects. Transitions in the infrared regime are vital for understanding the physical processes in the distant galaxies and interstellar clouds. Almost all objects embedded in dust are visible in the infrared. The research on the early universe happens at IR wavelengths, as the visible and ultraviolet light emitted in the early universe is now only observable in infrared as it appears to us at infrared wavelengths due to the effects of the cosmological redshift. However, while the atmospheric opacity at these energies is essential to provide stable living conditions on earth, it makes astronomical observations in the infrared more challenging. On earth most of the incident infrared light is absorbed by water vapor and carbon dioxide in the atmosphere and only a few narrow wavelength ranges in infrared allow the light to reach the ground-based infrared telescopes. These ranges are referred to as atmospheric windows. The best solution to minimize the effect of atmospheric emission and absorption in the ground-based

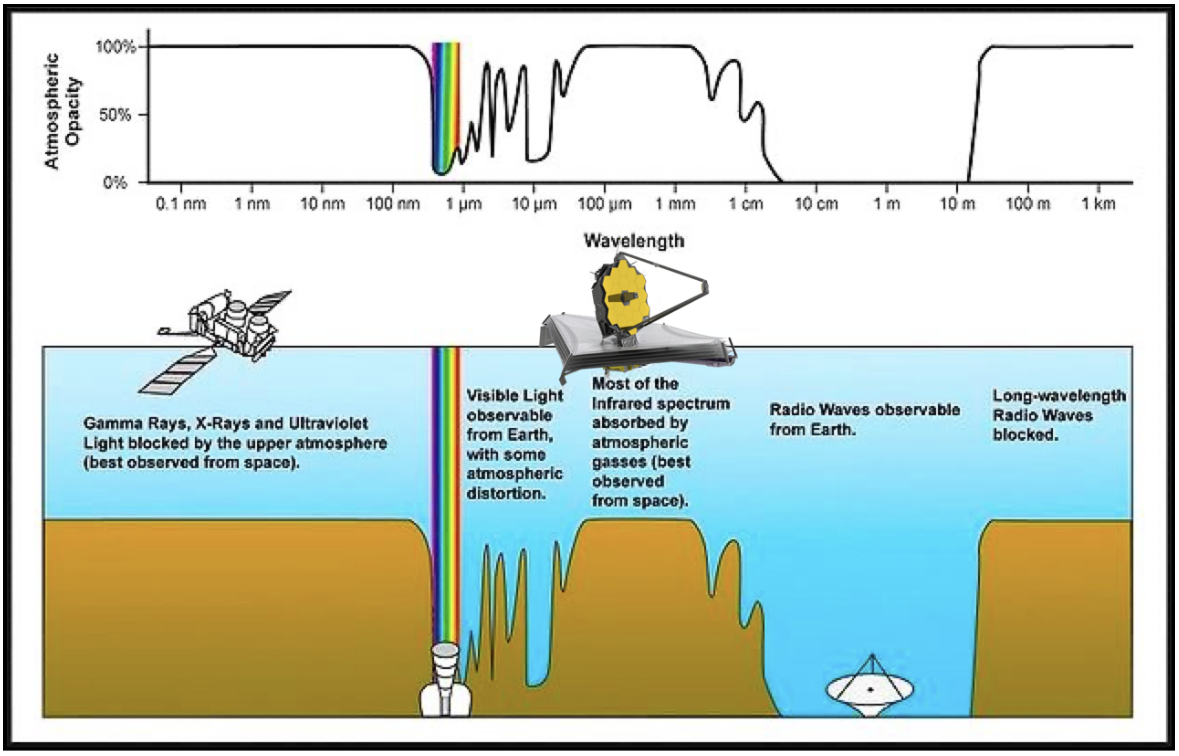

Figure 3.1: In this edited diagram, the brown curve shows how transparent the atmosphere is at the given wavelength to radiation from space. The major windows are at visible wavelengths (marked by the rainbow) and at radio wavelengths from about 1 mm to 10 m. The radio telescope ALMA operates in a borderline region, where the opacity depends strongly on how high and dry the site is. In space, observations can be done outside the atmospheric windows as illustrated by XMM-Newton, Hubble and the Spitzer Space Telescope and the James Webb Space Telescope. Image credit: ESA/JPL-Caltech, edited.

infrared observations is to place the telescopes on high, dry mountains where minimal abundances of water vapor reduce the amount of absorption affecting incident rays from astronomical objects. This is exemplified by the locations chosen for many of the world's most prominent telescopes such as the Very Large Telescope in the Atacama Desert, W. M. Keck and Subaru observatory on the mount Mauna Kea in Hawaii, and in near future the Extremely Large Telescope in the Atacama Desert. Infrared astronomy faces the challenge of atmospheric emission, which reaches its peak at 10 μm. To overcome this challenge, astronomers employ the "Chopping and Nodding" observation technique (section 3.3). However, for observing at certain wavelengths in the mid-infrared to far-infrared range, where there are no atmospheric windows, the only viable options are to utilize rockets, balloons, aircrafts, or space telescopes.

The ground-based observations which I investigated in this dissertation are obtained by the Very Large Telescope (VLT) operated by the European Southern Observatory (ESO). Figure 3.2 illustrates the VLT which consists of four Unit Telescopes (UT1 to 4) and four movable Auxiliary Telescopes (AT). The UTs can be used individually, furthermore they can be combined and make a baseline of 130 m and the ATs can provide a baseline of 200 m (Glindemann et al. 2003) and operate as the Very Large Telescope Interferometer.

Figure 3.2: The platform of VLT ESO harbors the four UTs and four movable ATs on Cerro Paranal, Chile. The panorama pictures the Milky Way galaxy and the satellite galaxies around the Milky Way such as the Small and Large Magellanic clouds. Image credit: ESO

In the Mapuche language, the UTs are named Antu (Sun), Kueyen (Moon), Melipal (Southern Cross), and Yepun (Evening Star)[1]. The primary mirror of the UTs has a diameter of 8.2 m, while the ATs have a diameter of 1.8m[2]. The UTs became operational in May 1998 followed by ATs between 2004 to 2007. The VLT is located in one of the driest areas on Earth, in the Atacama desert of Chile, on top of Cerro Paranal at an altitude of 2635m which provides optimal observational conditions such as the least water vapor in the atmosphere and the least atmospheric turbulence for the infrared observations. These highly favorable environmental factors and the telescope's position in the southern hemisphere make it uniquely suited to ground-based observations of the Galactic Center.

This work presents ground-based observations in the near-infrared (NIR) and mid-infrared (MIR) wavelengths. The NIR observations were conducted using the Nasmmyth Adaptive Optic System (NAOS) and the Coudé Near-Infrared Camera (CONICA), collectively referred to as the NACO instrument[3]. NACO is capable of imaging and spectroscopy within the 1- 5 μm range. The MIR observations are conducted using the VLT spectrometer and imager (VISIR) on the UT3.

In sections 3.2 and 3.3, I briefly introduce the principles of adaptive optics and the chopping/nodding technique, respectively. These techniques are used to observe in the NIR and MIR with ground-based telescopes such as the VLT. Adaptive optics enhances the NIR observations, and chopping/nodding method corrects for the background in MIR observations. These two techniques are widely used to observe in the IR regime. In this work the adaptive optics assisted observations are carried out by NACO, and the chopping/nodding technique is employed at VISIR.

[1]These beautifully meaningful Mapuche names are taken from the essay of Albanez Castilla, a 17-year-old pupil from Calama.

[2]https://www.eso.org/public/teles-instr/paranal-observatory/vlt/

[3]NACO observes between 1 and 5 μm. It was installed on the platform of UT4 from 2001 to 2013, in 2014 it was moved to UT1 and later at 2018 it was decommissioned after Period 103.

3.2 Adaptive Optics Technique in the Near-Infrared

The angular resolution of telescopes in ideal conditions is given by the diffraction-limited resolution of

$$\theta = 1.22\frac{\lambda}{D}\,, \tag{3.1}$$

which is determined by the observing wavelength (λ) and the primary mirror diameter of the telescope (D). Instrumental effects of the telescopes and atmospheric turbulence reduce the image quality of the infrared telescopes and makes it impossible for the ground-based telescopes to reach this diffraction-limited resolution. Due to the atmospheric turbulence, the Fried parameter r_0 and the correlation time of the turbulence τ_0 become influential factors (Fried 1996). The Fried parameter depends on the strength of the turbulence, and the wavelength λ raised to the power of as 6/5 and the correlation time of the turbulence (τ_0) is related to r_0 and the wind speed. For instance, at 2.2 μm the diffraction-limited resolution of the VLT is ~ 0.057"; however, the atmospheric turbulence alters the VLT resolution to $\lambda/r_0 \sim 0.7''$. Moreover, at the aforementioned wavelength for average observing conditions at Paranal on VLT, the value of r_0 is approximately 60 cm. If the wind speed is 10 m/s, then τ_0 is of the order of 60 ms[4]. Adaptive Optics (AO) is a powerful method to account for the atmospheric turbulence and small degradation of the image caused by the telescope structure deviation in real-time to enhance the telescope resolution to approximate the diffraction limit and to allow for exposure beyond the correlation time τ_0. The more stable atmospheric conditions result in larger r_0 and τ_0 and better performance of AO. Fig. 3.3 illustrates a schematic view of an AO loop. The tip-tilt method is considered to be the simplest Adaptive Optics set up.

The incident plane wavefront (WF) is distorted as it passes through the atmosphere. The corrugated wavefront of the guide star (GS) is split by a dichroic mirror at the beam-splitter and a part of the beam reaches the wavefront sensor (WFS). The WFS measures the residual WF errors and they get processed and analyzed by a Real Time Computer (RTC) which controls a deformable mirror (DM). The DM is a thin mirror mounted on a set of piezoelectric actuators. 1170 actuators are used in NACO, which enable deformation in the mirror to correct for the deformations in the WF. The AO loop repeats every few milliseconds to compensate the real-time atmospheric turbulence and conduct near-diffraction-limited observations. In order to observe our targets with the aid of AO, the WFS needs a bright star as a GS in the isoplanatic patch. The GS can be a natural GS (NGS) on the observed patch or an artificial star created by the laster beams called the laser guide star (LGS). In the case of GC observations, the supergiant IRS 7, with a K_s-band magnitude of 7 and located at a distance of about 5.6$''$ to the north of Sgr A*, is used as the NGS (Becklin & Neugebauer 1975; Lebofsky et al. 1982; Yusef-Zadeh & Morris 1991). The LGSs in UT4 at the VLT are produced by the Sodium-laser (589.5 nm) at 90 km in the mesosphere of visual magnitude of 11. The AO performance depends on the accuracy of the WFS measurements, the number of actuators, the seeing (r_0 and τ_0), the brightness of the GS, and the closeness of the GS to the observed region. The AO system employed on the UT1 in a good seeing condition can reach a Strehl ratio of about a few percent, 50% and 70% in J, K_s and L' band images, respectively.

[4]NACO manual: https://www.eso.org/sci/facilities/paranal/decommissioned/naco/doc.html

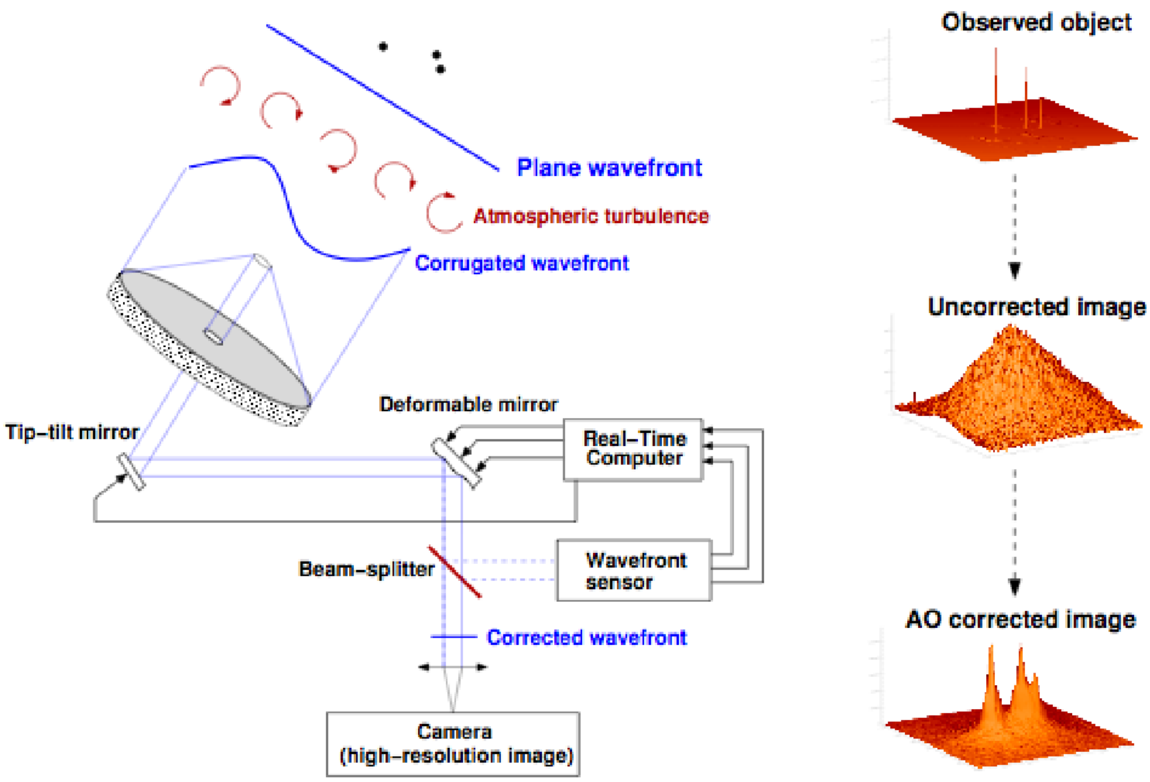

Figure 3.3: Principle of the Adaptive Optics which is widely used for infrared observations. It consists of a wavefront sensor, a tip-tilt mirror, a deformable mirror, a real-time computer and a beam-splitter. Image credit: ESO NACO user manual.

3.3 Chopping/Nodding in the Mid-Infrared

The VLT spectrometer and imager for the MIR, VISIR, is located at UT3 and has been in operation since 2005. It was upgraded in 2011. It provides diffraction-limited images from 5 to 20 μm in three atmospheric windows, M, N and Q-band at 5, 8-13 and 17-20 μm, respectively (see Fig. 3.4). Furthermore, it offers long-slit spectroscopy with a spectral resolution between 150 to 30 000 km s^{-1}. Mid-infrared observations provide unique information about warm dust and gas such as silicates, silicon, carbon, aluminum oxides or polycyclic aromatic hydrocarbon (PAH) molecules. However, the majority of the MIR emission is absorbed by H_2O, CH_4, CO_2, CO, O_2 and O_3 in the Earth's atmosphere (see Fig. 3.4). In low humidity environments, the sky becomes near-transparent at N band wavelengths between 10.5 and 12.0 μm. However, in Q band the transmissivity decreases quickly with the wavelength. The influence of precipitable water vapor (PWV) is a crucial factor in achieving high quality MIR ground-based observations. Therefore, Paranal is equipped with a real-time PWV monitoring program. The N band observations can be carried out with a precipitable water vapor (PWV) column of even higher than 3 mm, whereas the Q band observations must be obtained with a PWV of below 3mm. Almost only 10% of a year in Paranal the PWV content is below 1 mm.

The spatial resolution is limited either by the telescope diffraction (solid line in Fig. 3.5) or by the seeing based on the Foddier formula (seeing~ $\lambda^{-0.2}$, the dot-dashed lines in Fig. 3.5). Figure 3.5 shows that for the optical seeing below 0.6″, the VISIR data are diffraction

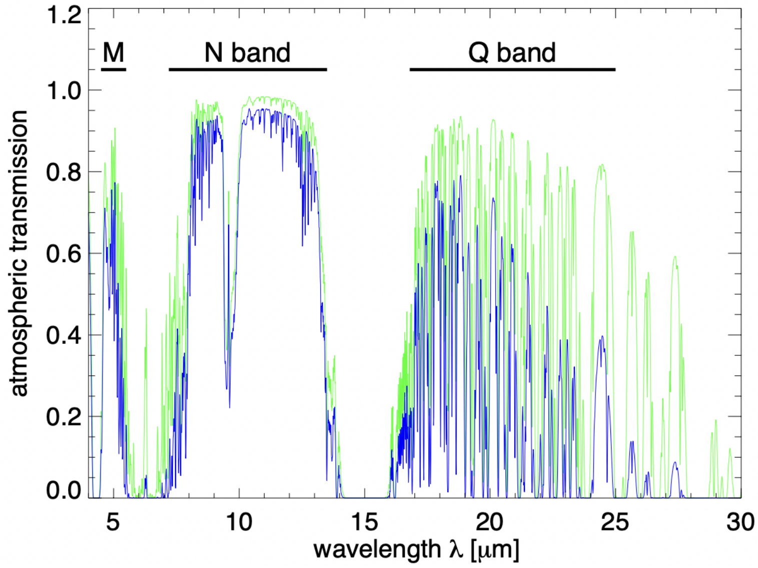

Figure 3.4: Green shows the MIR atmospheric transmission for an altitude of 2600 m at zenith for 1 mm of PWV, whereas the blue line shows the transmissivity for 3 mm of PWV and airmass of 1.5 (Lord 1992) Image credit: ESO VISIR user manual

limited. However, MIR background emission is a big issue. The MIR background is caused by either the sky or the telescope. Based on Kirchhoff's law, the black-body radiation of the Earth's atmosphere with a temperature of 253 K and the VLT telescope with a temperature of 283 K peak in their emission in the MIR. Therefore, the detectors of the telescope are cooled to 9 K to avoid internal background contamination. As the number of the photons received by the detector is of the order of 10^8 photon/s, the Detector Integration time (DIT) is of the order of a few tens of milli-seconds. One efficient technique to correct for the variable background of the MIR imaging observations caused by the sky or the telescope is chopping and nodding. In the chopping technique, at the position of nod A, we observe two images - one on-source image, which captures the source and the background together, and the other off-source image, which captures only the background. This technique is applied via the movement of the secondary mirror of the telescope between two positions on the sky at a faster rate than the background fluctuations which is usually of the order of a few seconds. The VISIR chopping frequency in N band is 0.25 Hz and in the Q band is 0.5 Hz. Subtracting the off-source images from the on-source images in the chopping technique corrects the sky and telescope emission. On the other hand, moving the secondary mirror for chopping results in two different optical light paths between the two chopper positions, produces a residual background. Such residual background is mainly suppressed by the nodding. In nodding, the telescope is moved off-source to nod position B and the same chopping method is repeated. Depending on the chopping/nodding setting of the telescope, after subtracting the two nodding position images from each other, we end up with 3 to 4 images. Figure 3.6 shows an illustration of the chopping/nodding technique. The high background emission from the atmosphere and telescope drastically decreases the sensitivity of the ground-based MIR telescopes in comparison with the space-borne ones, whereas the ground-based ones provide higher spatial resolution. The VISIR images offer the spatial resolution of about 0.3″ which is an

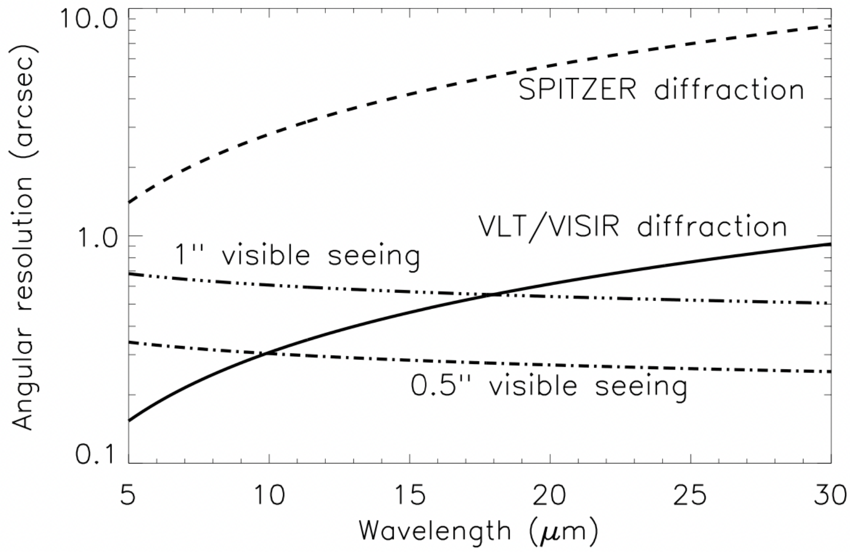

Figure 3.5: VLT/VISIR diffraction limit versus seeing is in solid line. For 0.5″ and 1″ visible seeing the Roddier dependence is in dashed-dot lines and the Spitzer Space Telescope diffraction limit is in dashed line. The spatial resolution in the space-borne telescopes is limited by the size of the telescope. Image credit: ESO VISIR user manual

order of magnitude higher than the resolution of the Spitzer Space Telescope (SST) (see Fig. 3.5). However, the broad band imaging of the mid-infrared instrument (MIRI) of JWST offers imaging with the spatial resolution of 0.11″ due to the large primary mirror. In the case of the GC, it is difficult to utilize the imaging capabilities of the MIRI JWST due to the interference of intense radiation emitted by very bright sources.

3.4 Standard Data Reduction Process

The observational data from the ground-based telescopes presented in this thesis are observed by two instruments at VLT, NACO and VISIR. The detector, thermal emission from the telescope and the sky emission leave fingerprints on the images. In order to address such issues, we need to correct the data. The process of correcting data is known as data reduction. The main data reduction procedure applied to the data obtained by NACO and VISIR are very similar. The regular data reduction processes applied to the data from NACO consist of sky subtraction, flat-fielding, bad/dead-pixel correcting, jittering, and mosaicing. I shortly describe the data reduction steps.

Sky subtraction: This is a method used to mitigate the impact of atmospheric thermal radiation. It involves capturing sky frames from a nearby field that do not contain any discernible sources of interest. The sky frames are subtracted from the object frames. In the GC, the sky frames are taken from the region located at 713″ west and 400″ north of IRS 7. In L′ band, due to the strong atmospheric emission after each object frame, one sky exposure is taken. However, for shorter wavelengths such as in the K_s band, the sky exposures are captured every 2 hours.

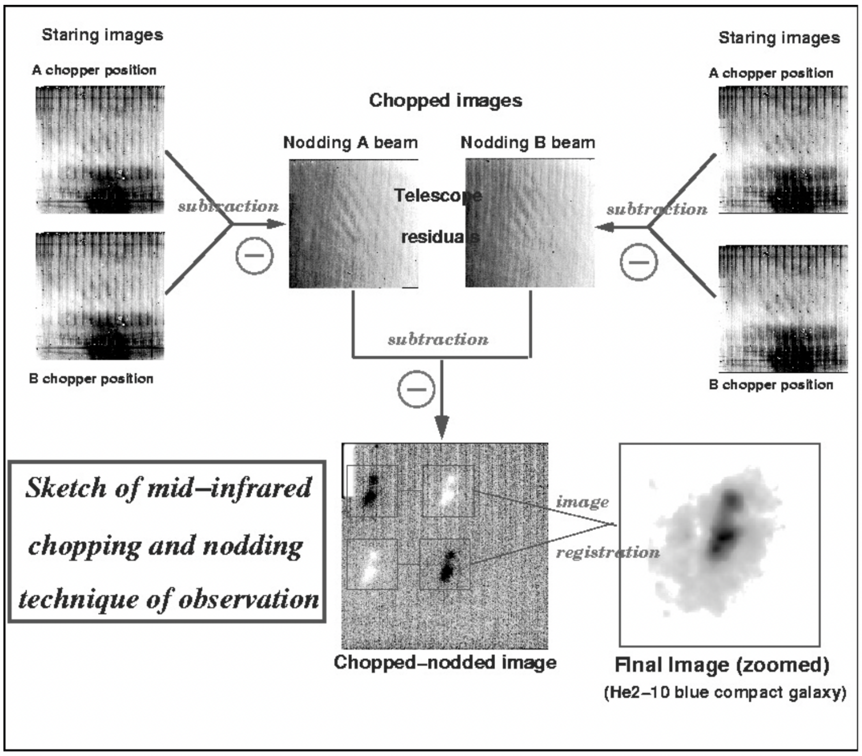

Figure 3.6: Illustration of the chopping and nodding technique in MIR observations on the blue compact galaxy He2-10 which only appears after the chopping/nodding technique. Image credit: VISIR commissioning team, June 2004, ESO VISIR user manual

Flat fielding: The detector's response function can be recorded using either a sky flat-field technique or a lamp flat-field technique. The sky flat-field technique involves capturing images while the detector is illuminated by the twilight sky of the observation night, while the lamp flat-field technique involves capturing images with a lamp switched on and off. These flat-fields are maps presenting the pixel response of the detector array. The object frames are divided by these maps to obtain the same detector response for the entire image. However, in the MIR data obtained by VISIR, besides the chopping/nodding corrections, there is no need for flat fielding due to the large fluctuations at the MIR wavelengths.

Bad/dead-pixel correcting: These pixels are those with either very high values compared to their neighboring pixels or a response function of zero.These pixels are detected and substituted with the interpolation value from their neighboring pixels.

Jittering: The object frames are recorded by small offsets from each other. This method enables us to prevent one source lying on the same position on the detector. In case of imperfections in the detector the source gets observed within the offset frames and minimizes the detector's effect on the observation.

Mosaicing: Shifting and stacking the reduced images produces a mosaic image of the observed region or object, increasing the signal-to-noise ratio.

After the successful application of the standard data reduction procedures at longer wavelengths such as the L', M and N band, the data are ready for scientific analysis. However, at shorter wavelengths such as the K_s band, which is essential to study point sources, the data still suffers from the degradation due to the variations of the point spread function. In order to reach the diffraction limited images, I apply deconvolution to the data. In section 3.5, I discuss some of the degradation factors and describe the deconvolution method utilized in this work

3.5 Lucy Richardson Deconvolution

In an ideal case, if we could have an aberration-free telescope and no atmospheric effects, the image of a point source, as represented by the point spread function (PSF), would exhibit an Airy pattern. The pattern is described by the Airy function, due to the diffraction of light by the telescope aperture. The following equation presents the Airy function.

$$I(\theta) = I_0 \left(\frac{2J_1(\pi D/\lambda \sin\theta)}{\pi D/\lambda \sin\theta}\right)^2 ,$$

where I_0 is the maximum intensity of the diffraction pattern and J_1 is the first order Bessel function of the first kind. The PSF varies over the observation time and the field of view (FOV) due to the atmospheric turbulence and the time variations of the instrument. In order to produce images which are close to the diffraction limit, I apply deconvolution algorithms to the observed images. The convolution of the real object $O(x,y)$ with a $PSF(x,y)$, and the $c(x,y)$-function, which describes the detector read-out noise, anisoplanasy and other non-linear terms, all together describe the observed image $I(x,y)$:

$$I(x,y) = PSF(x,y) \odot O(x,y) + c(x,y) ,$$

where $\odot$ is the multiplication in Fourier space and thus describes the convolution operator. In the absence of any noise, the Fourier transform of the real object is described by a division in the Fourier space,

$$\hat{O}(u,v) = \frac{\hat{I}(u,v)}{\widehat{PSF}(u,v)} ,$$

where $\hat{O}(u,v)$, $\hat{I}(u,v)$ and $\widehat{PSF}(u,v)$ represent the Fourier transforms of $O(x,y)$, $I(x,y)$, and $PSF(x,y)$, respectively. Here, u and v refer to the spatial frequencies which correspond to the x and y coordinates. By employing the observed images and the derived PSF, I can determine the original object via deconvolution. However, the noise term and the uncertainties in determining the PSF are the limitations of deconvolution. For the Galactic Center images we use deconvolution algorithms such as LUCY (Lucy 1974), CLEAN (Högbom 1974) and Wiener filtering, which work effectively and reproduce the detection-limited flux densities (Ott et al. 1999).

The Lucy-Richardson algorithm (Lucy 1974; Richardson 1972) is an iterative procedure based on Bayes' theorem on conditional probabilities. The deconvolution of the initial image with the PSF results in the production of the point like source. The first step to apply deconvolution is to pick or create an appropriate PSF which is a suitable representation of a point like sources in the image. There are several methods to generate the PSF for the Galactic Center images. A single isolated star or several point sources from the image may be used to estimate the PSF. The software package StarFinder (Diolaiti et al. 2000) is utilized to extract the sources. StarFinder is an IDL-based package which can estimate the PSF from the median of several isolated point sources in the image selected by the user.

The Lucy-Richardson algorithm – through an iterative process – enables us to separate the flux density contributions of close sources in the crowded stellar fields such as the Galactic Center. The Lucy-Richardson algorithm uses $PSF(x,y)$ to convolve the estimate of the object distribution $O_n(x,y)$,

$$I_n(x,y) = O_n(x,y) \odot PSF(x,y) \ ,$$

where $I_n(x,y)$ is the obtained image and it is compared with the observed image $I(x,y)$,

$$Q(x,y) = \frac{I(x,y)}{I_n(x,y)} \odot PSF(x,y) \ .$$

The high spatial frequencies are affected by noise. The convolution with $PSF(x,y)$ suppresses their effects and consequently reduces the noise level. Finally, multiplying the original object distribution with $Q(x,y)$ results in a new object distribution estimation,

$$O_{n+1}(x,y) = O_n(x,y) \odot Q(x,y) \ .$$

The user determines the number of iterations in the deconvolution algorithm, which requires some fine-tuning. The number of iterations are important because of two aspects. Firstly, the higher number of iterations can lead to a long running time on the computer. Secondly it can produce artifacts in the deconvolved images and resolve the diffused background into point sources.

Finally, I note that the entire photometry analysis applied on the data presented in this work is done via aperture photometry by utilizing the Photutils package[5], which is a phyton-based package and is developed to be used for the analysis of JWST data.

In summary, in this chapter I briefly introduced the challenges and limitations of the ground-based observations for infrared astronomy. I discussed two observational techniques, AO and chopping/nodding, employed in infrared ground-based observations. The VLT/NACO observation presented in this thesis are AO assisted and the VLT/VISIR observations utilized the chopping/nodding technique. In the next Chapter 4, I describe the infrared space-based telescope, JWST.

[5]https://photutils.readthedocs.io/en/stable/

CHAPTER 4

Infrared Sapce-Based Observations

In the previous chapter, I described the importance of infrared observations to investigate star-forming regions and obscured regions in the optical domain, such as the Galactic Center. There I discussed how ground-based infrared observations are limited to the atmospheric windows; additionally, the resolution of the images is affected by atmospheric turbulence. As was established before, the only way to completely circumvent the problem of atmospheric absorption and to observe at those wavelengths to which the atmosphere is opaque is to place an observatory outside its reach. With this in mind, this chapter will deliver an introduction to and an overview of the James Webb Space Telescope - the largest and most powerful space telescope ever built.

4.1 James Webb Space Telescope Contributors

The first space-based infrared telescope was the *InfraRed Astronomical Satellite (IRAS)*, launched in 1983. IRAS performed a survey of the entire night sky and succeeded in detecting 350,000 infrared sources at wavelengths of 12, 25, 60, and 100 μm . The launch of IRAS marked the beginning of an era of the space-borne infrared observatories including the *Infrared Space Observatory*, the *Near-Infrared Camera and Multi-Object Spectrometer (NICMOS)* mounted on the Hubble Space Telescope with the mirror size of 2.4 m, the *Spitzer Space Telescope* with the mirror diameter of 0.85 m, the *Herschel observatory*, and the largest and most powerful ever launched into space telescope, the *James Webb Space Telescope*, often known as JWST or the Webb Telescope, with a mirror size of 6.6 m (see Fig. 4.1 for size comparisons).

The outstanding James Webb Space Telescope mission became possible with the international partnership involving the European Space Agency (ESA), 12 European nations, the National Aeronautics and Space Administration (NASA), and the Canadian Space Agency (CSA)[1]. NASA's Goddard Space Flight Center took the lead in project management and coordination of the development of the JWST, while Northrop Grumman was the main

[1] https://sci.esa.int/web/jwst/-/45728-europe-s-role

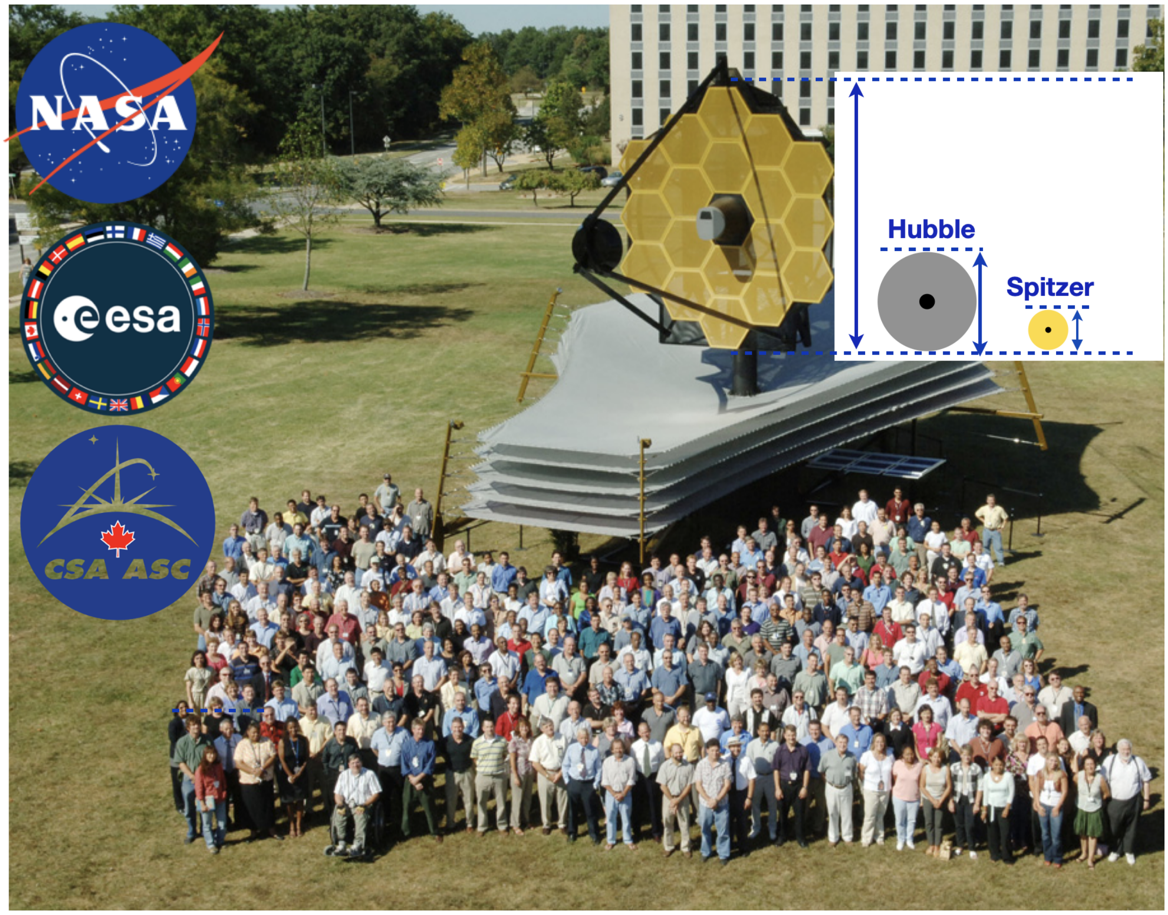

Figure 4.1: The full-scale replica of James Webb Space Telescope at the Goddard Space Flight Center in Greenbelt, where the mirrors and instruments were assembled and tested, and some of the telescope team members in front of the telescope. Over 1200 scientists, engineers and technicians form 14 countries around the world contributed to the largest and most potent space telescope ever developed and deployed. Together, NASA, ESA, and CSA were able to make this mission possible. A size comparison of the primary mirrors of the James Webb Space Telescope, Hubble, and Spitzer is shown in the upper right corner of the image. Image credit: Webb/NASA, edited

industrial partner. The near-infrared camera was provided by the University of Arizona[2], the fine guidance sensor/ near-infrared imager and slitless spectrograph is built by the Canadian Space Agency (CSA), the near-infrared spectrograph was built by Airbus in Ottobrunn and Friedrichshafen[3] and 50% of the mid-infrared instrument (MIRI) , the optical and mechanical component, was developed by the European consortium including the University of Cologne[4] (Fischer et al. 2006, 2008) and the Max Planck Institute for Astronomy in Heidelberg. The detectors and the cooling systems of MIRI were provided by the Jet Propulsion Laboratory and NASA's Goddard Space Flight Center. The MIRI consortium is led by the UK Astronomy Technology Center in Edinburgh. Germany has the largest contribution to the Webb's mission among the European contributors. The German Space

[2]https://www.nasa.gov/mission_pages/webb/observatory/index.html
[3]https://www.dlr.html
[4]https://astro.uni-koeln.de

Agency at the German Aerospace Center (DLR)[5] is coordinating the national contributions to the European Space Agency. Europe provided the Ariane 5 launcher and the entire launch services, and a team of scientists and engineers to support the science operations (see Fig. 4.2). The technical and scientific operations of the JWST are coordinated by 15 astronomers from ESA at the Science Operation Center (SOC). It is located at the Space Telescope Science Institute (STScI) in Baltimore, USA. The European contributions to the JWST mission guarantee full access to the observatory for ESA member states astronomers.

This remarkable telescope is specifically designed to look at faint distant objects in order to provide previously elusive answers to some of our questions about the universe concerning topics like reionisation, early universe galaxy formation at high redshifts above 7 and their evolution, the assembly of galaxies, the planet formation and habitable zones, the star formation and porto-planetary systems, and the planet formation. There is great optimism that JWST's scientific discoveries will lead to breakthroughs in all fields of astronomy.

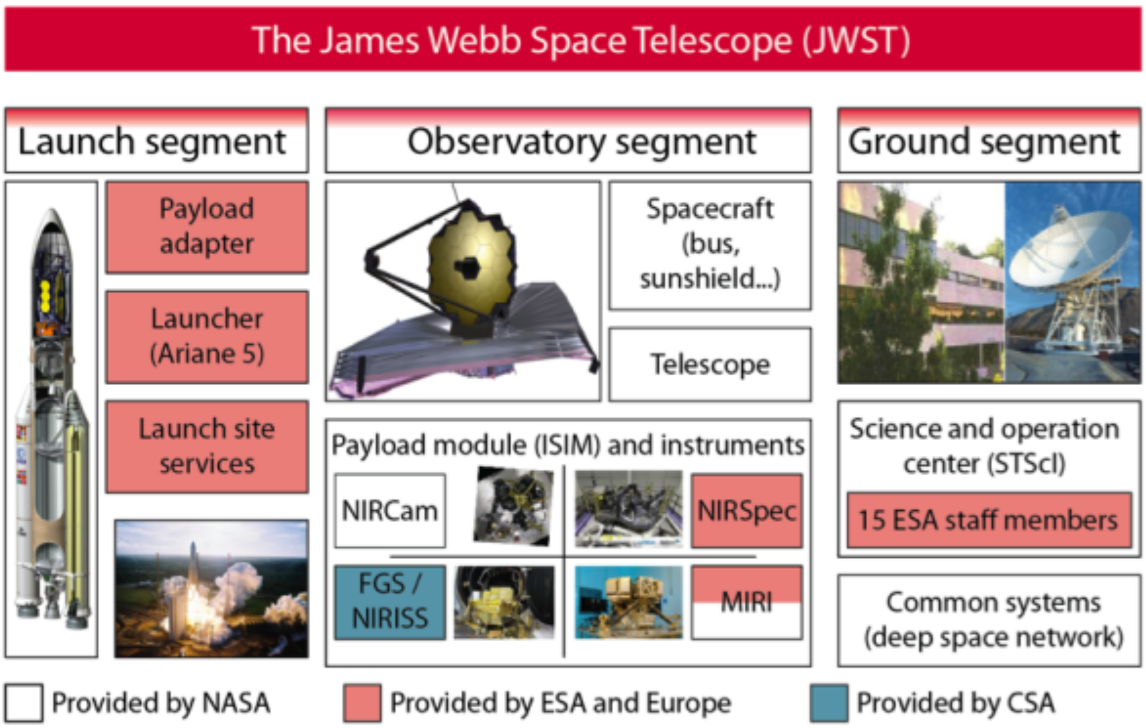

Figure 4.2: The four science instruments installed on the JWST, the mission requirements including the contributing institute. The ESA and Europe contributions are highlighted in red, the NASA contributions in white, and the CSA contributions in blue. ESA provided the entire launch segment, NIRSpec instrument, 50% of the MIRI instrument, and a team of staff members for the ground segment. Image credit: ESA

I briefly describe the structure of the James Webb Space Telescope and specifically discuss two instruments of the JWST, MIRI, and present a showcase of simulations of observations with JWST MIRI, which will be used to conduct the Galactic Center observations and deepen our understanding about the supermassive black hole, Sgr A*, as well as its ambient medium.

[5]DLR stands for Deutsches Zentrum für Luft- und Raumfahrt

4.2 James Webb Space Telescope mission and technology

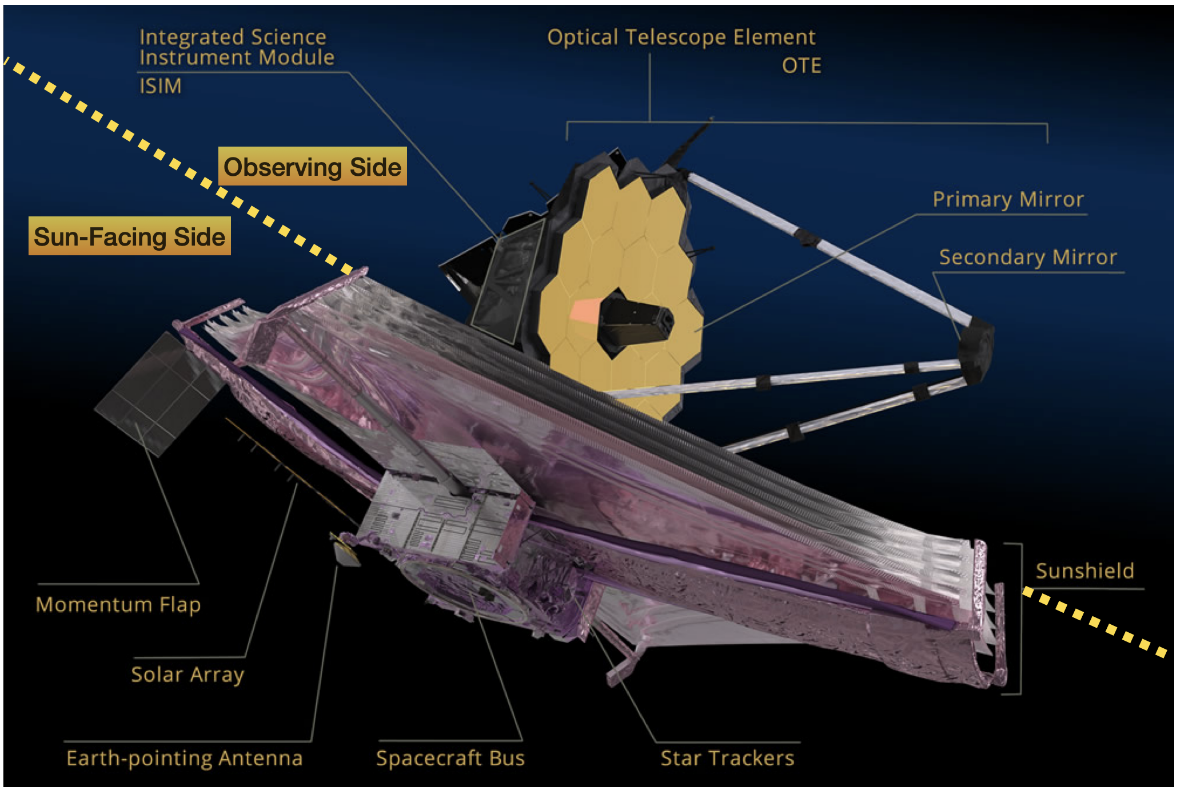

Figure 4.3: The James Webb Space Observatory is comprised of the OTE, the ISIM, the sunshield, and the spacecraft bus. The Optical Telescope Element (OTE) consists of the primary and secondary mirrors of the telescope. The Integrated Science Instrument Module (ISIM) hosts the telescope's science instruments and cameras. The multilayer sunshield protects the observatory from the light and heat emitted by the sun and earth, as well as the spacecraft bus. The trim flap stabilises the satellite. The solar power array is on the sun-facing side of the telescope and converts the sunlight into electricity. The Earth-pointing antenna sends the data to the Earth and receives the commands from NASA's Deep Space Network. The star tracker contains small telescopes for the observatory. Image credit: Webb/NASA/Observatory, edited

The launch of IRAS in 1983 started the era of infrared space-borne observatories. After the successful IRAS project, the Infrared Space Observatory was launched to observe at wavelengths between 2.5 and 240 from 1995 to 1998. The next infrared observatory, NICMOS, ran from 1997 to 1999 and from 2002 to 2008, operating at wavelengths between 0.8 and 2.4 μm. Spitzer observed between 2003 and 2020 at 3.6–160 μm, whereas Herschel Space Observatory operated between 2009 and 2013 at 55–672 μm. The James Webb Space Telescope (Fig. 4.3) was launched as the successor to the Hubble Space Telescope.

The James Webb Space Telescope, with a primary mirror measuring 6.6 m across and a collecting area of $\sim 25m^2$ is observing in the infrared regime, orbiting a halo around the second Lagrange point of the Sun-Earth system (Gardner et al. 2006). It is a three-mirror anastigmat telescope with a concave primary mirror and a convex secondary mirror that works slightly off-axis. The tertiary mirror eliminates the astigmatism. The JWST was originally scheduled to launch in October 2018, but due to a number of technical difficulties, the launch date was postponed to 2021. On December 25, 2021, at 13:20 CET, the JWST was eventually launched by an Ariane 5 launcher to L2 from Europe's Spaceport in Kourou, French Guiana. The JWST orbits around the sun at a distance of about 1.5 million km from the Earth (Fig. 4.4).

The importance of the L2 point is that at this spot, the telescope's shield protects the telescope from the radiation of the sun, earth, and moon, which helps to keep the telescope cold enough not to interfere with the observation of faint and distant objects in the infrared. Moreover, observing the events that happened only 50 million years after the Big Bang and revolutionizing our understanding of the universe.

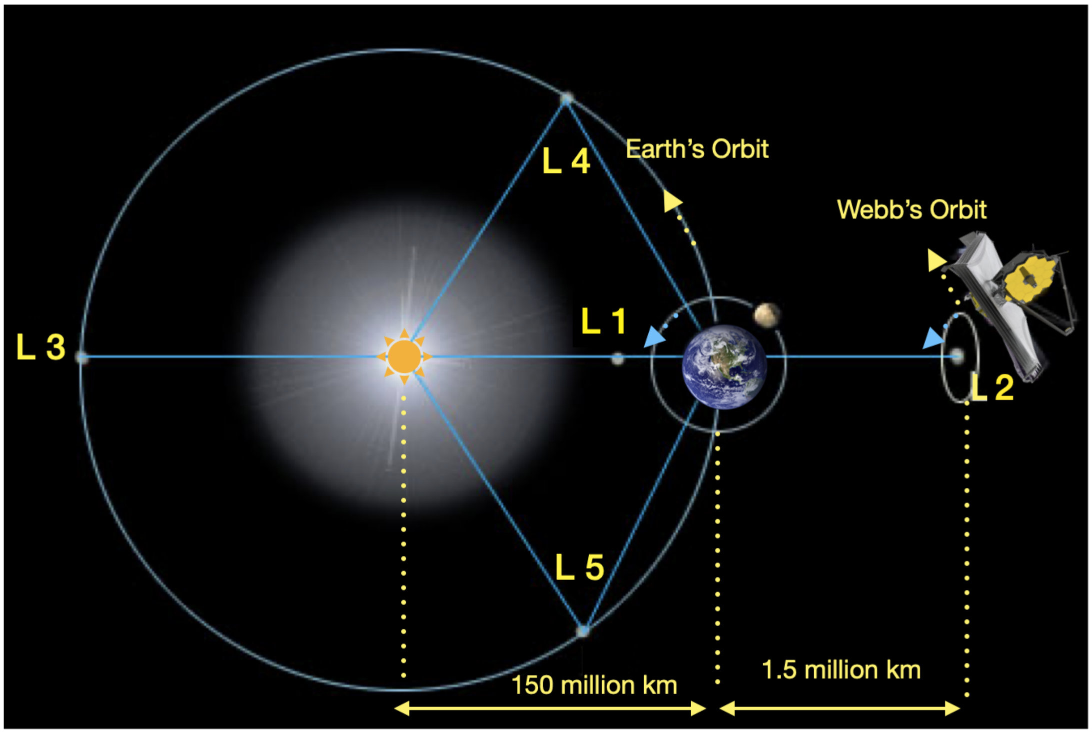

Figure 4.4: Five Lagrange points (L1, L2, L3, L4, and L5) are shown in their respective locations. The three-body system, which in this example revolves around the sun, moves along with any small object located at any of the Lagrange points. The Earth, Sun, and Moon are all located on one side of the Webb telescope, which gives it the ability to block their radiation from the observing-side of telescope with the aid of the sunshield of the telescope. The Webb telescope also orbits around the L2 point. The graphic shows the telescope's orbit around the L2 point, which has an orbital period of around six months. The Webb telescope took 30 days to reach the L2 point. The orbital trajectories of the Moon around the Earth and the Webb telescope around the L2 point are indicated by the blue arrows on their respective orbits. The Earth's orbit and Webb's orbit around the sun both are shown with yellow arrows. Image credit: STScI, edited and annotated

The space-based part of the James Webb Space Telescope is the observatory part of it, which includes the Optical Telescope Element (OTE), the Integrated Science Instrument Module (ISIM), the sunshield, and the spacecraft bus (see Fig. 4.3). I give a brief overview of each of the Webb observatory's components in the sections that follow.

1. The **OTE** is comprised of the mirrors and the backplane. The **primary mirror** of the JWST is a round mirror with a diameter of 6.5 m. Such a large mirror has never been built before for a space telescope (see Fig. 4.1). The primary mirror is made of 18 hexagonal-shaped beryllium segments (weighing SI 20 kg each), and it is manufactured in segments to fit into the rocket. The mirrors are gold-coated via vacuum vapor deposition in order to enhance the infrared light reflection. The gold coat thickness is 1000 Å and is covered by a thin layer of SiO_2, glass, to protect it from any scratches. The other component of OTE is the **backplane**. It is the telescope's spine on which carries the primary mirror, other optics, and the science module. The backplane has to carry 2400 kg.

2. The **sunshield** is a five-layer, 21.197 m × 14.162 m, Kapton shield coated with aluminium and doped silicon. In order to look at the early universe galaxies, which are very faint and distant galaxies, in infrared, we need to lower the thermal glow of the telescope mirror and keep the telescope in cryogenic temperature. In order to keep the telescope cold, it is sent to the L2 point of the Earth-Sun system and equipped with the sunshield, where the sunshield can acts as a parasol to protect the telescope from the sunlight, the Earth, and the Moon radiation and heat as well as the warm spacecraft bus (see Fig. 4.3) and permit the telescope to cool down to 50 K [6]. It took a few months to cool down the telescope to 50 K because for months after the sunshield was deployed, the heaters kept the instruments warm due to preventing any icing on the electronics or mirrors. The sun-facing side of the telescope reaches the maximum temperature of 383 K, and the observing-side has a minimum temperature of 36 K.

3. The **spacecraft Bus** hosts the computer, the reaction wheels, and most of the control system.

4. The **momentum flap** is responsible for balancing the solar pressure on the sunshield.

5. The **Earth-pointing antenna** is the communicator part of the observatory with the Earth. It receives commands from the control center and sends back data to Earth.

6. The **solar array** is located on the sun-facing side of the telescope. This module receives the sunlight and uses it to generate electricity for the Webb observatory.

7. The **star trackers** are used to point the observatory at the targets.

8. The **integrated science instrument module (ISIM)** comprises the four science instruments of the Webb telescope. ISIM consists of three near-infrared instruments and one mid-infrared instrument. The near-infrared instruments are the Fine Guidance Sensor/Near InfraRed Imager and Slitless Spectrograph (NGS-NIRISS), the Near-Infrared Camera (NIRCam), the Near-Infrared Spectrograph (NIRSpec), and the Mid-Infrared Instrument (MIRI). Figure 4.5 shows the wavelength range across which each of the Webb telescope's scientific instruments works. The telescope can undertake observations with all four of its science instruments simultaneously since each of the instruments occupies a different part of the total field of view (FOV). Figure 4.6 displays the FOV and the data type obtained by each instrument.

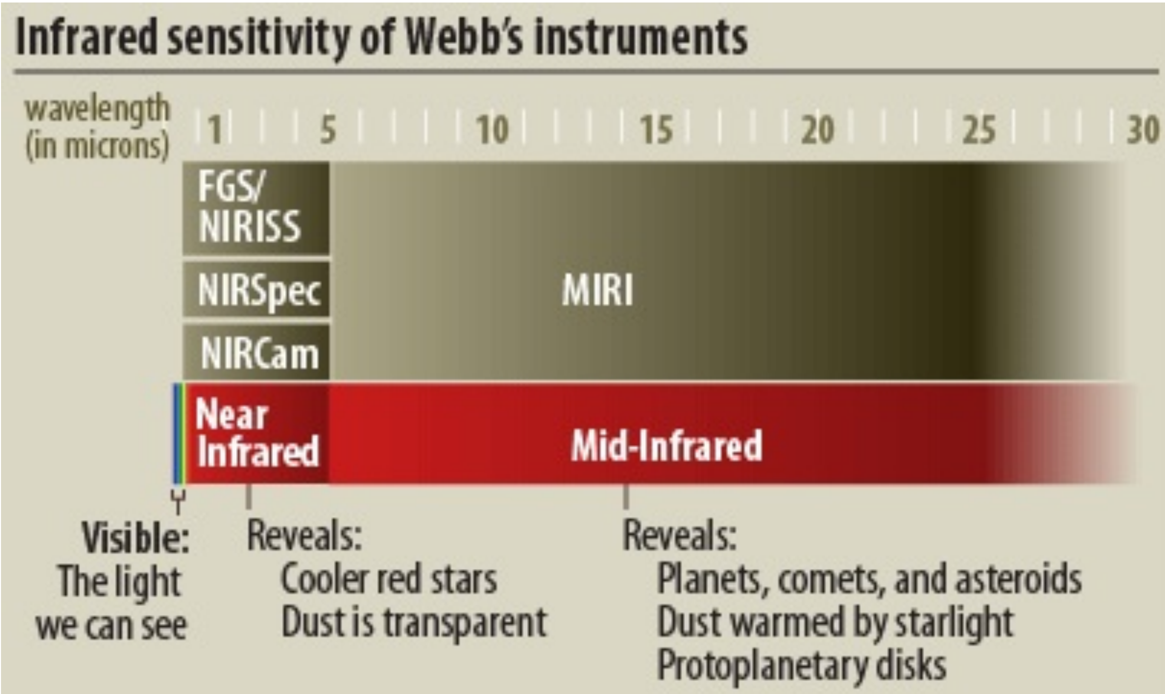

Figure 4.5: While MIRI works between 5 and 28 *mum*, FGS/NIRISS, NIRSpec, and NIRCam observe between 0.6 and 5 *mum*. Image credit: Webb/NASA/Observatory

- **NIRSpec** is a multi-object spectrometer in the near-infrared regime. It is a wide-field ($3.4' \times 3.6'$) multi-object near-infrared spectrometer observing between 0.6 and 5.0 μm with spectral resolutions of $R \sim 100$, $R \sim 1000$ and $R \sim 2700$. NIRSpec is able to perform large spectroscopic surveys due to the powerful Multi-Object Spectroscopy (MOS) mode. The MOS is equipped with micro-shutter technology, allowing it to obtain the spectra of around 200 objects simultaneously. This equipment is intended to find galaxies in the early cosmos, 200 million years after the Big Bang. In addition, it is a good option for studying the spectra of distant galaxies. NIRSpec is provided by ESA, with some elements provided by NASA's Goddard Space Flight Center.

- **MIRI** is the mid-infrared instrument of the Webb telescope, which provides imaging, coronagraphy, and integral field spectroscopy with a combined mid-infrared camera ($1.3' \times 1.7'$) and spectrograph ($R \sim 100$ and $R \sim 3000$) between 5 and 28 μm (Wright et al. 2008, 2010; Rieke et al. 2015). This instrument supports all science goals of the mission and has to be kept cool to $-266°C$. MIRI utilises a cryocooler, an active cooling system with helium, to bring its temperature to only 7 degrees above absolute zero. This instrument allows us to observe the mid infrared with an unparalleled sensitivity, enabling us to detect signals which in older telescope generations would have been indistinguishable from the background noise. MIRI is provided by the partnership of the European Space Agency (ESA), a consortium of nationally funded European institutes, the NASA Jet Propulsion Laboratory (JPL), and NASA's Goddard Space Flight Center.

[6] The sunshield acts as a sunscreen with the Sun protection factor of 1.2 million.

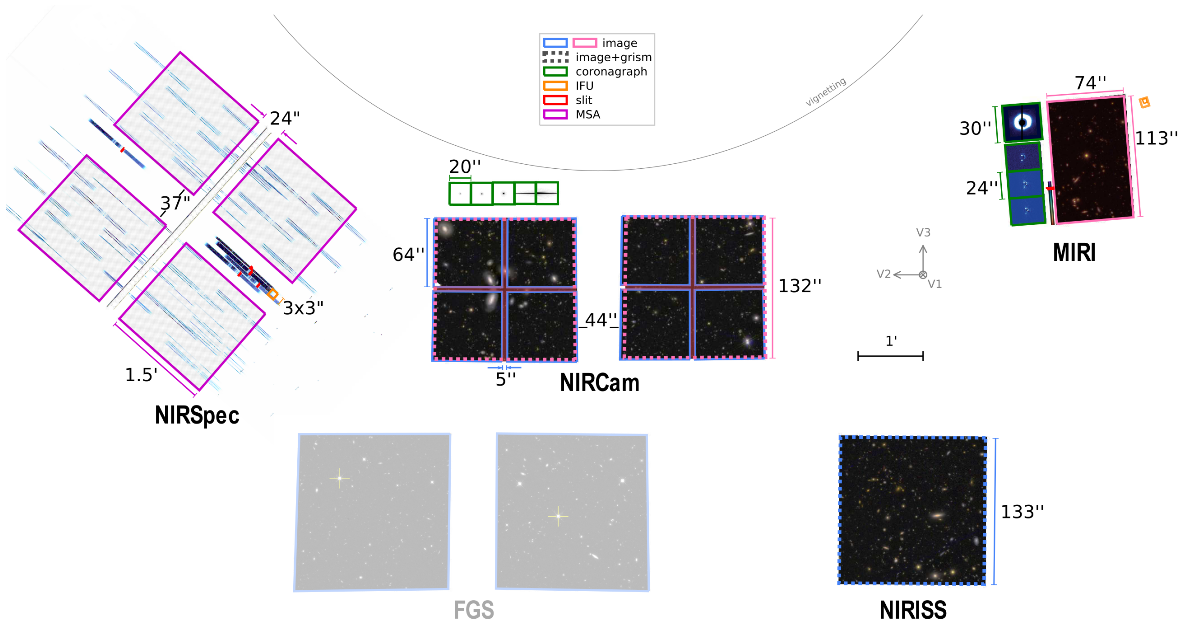

Figure 4.6: The area on the sky and the FOV of each of the four instruments of the JWST are described, including illustrations of the types of data that can be obtained by some of them. Colors around the FOV of each instrument indicate the observing modes. Image credit: STScI

- **NIRCam** is a two-channel wide field ($2.2' \times 4.4'$) near-infrared camera that provides imaging in the wavelength range between 0.6 and 5.0 μm with narrow, medium, and broad band filters (Fig. 4.6) and produces the highest resolution images of the Webb telescope (Beichman et al. 2012; Rieke et al. 2005). It offers coronagraphic and spectroscopic capabilities to characterize exoplanets and planetary systems. It was used to align the primary mirror segments.

- **FGS/ NIRISS** is provided by the Canadian Space Agency (CSA) and observes in the wavelength range of 0.8 to 5.0 μm (see Fig. 4.6). FGS provides the accurate pointing system of the Webb telescope. The instrument does imaging and slitless spectroscopy in three modes with a wide-field camera of $2.2' \times 2.2'$ (Doyon et al. 2012). The importance of this telescope component is to address the science objectives such as first light detection, high-redshift galaxies, star birth, exoplanet detection and characterization, and exoplanet transit spectroscopy.

In this thesis, I explore three quasars observed with Medium Resolution Spectroscopy (MRS) of MIRI instrument. Therefore, I shortly explain the MRS.

4.2.1 Medium Resolution Spectroscopy with MIRI

MIRI MRS uses 4 integral field units, which simultaneously observe from 4.9 to 27.9 μm over a field of view up to $6.6'' \times 7.7''$ in size (see Fig. 4.7). These four concentric IFUs starting from the center are called channel 1 to 4. The size of the channels and the observed wavelengths from the center outward increases. Spectra are projected into two detectors, the SHORT Detector and LONG Detector. Channel 1 and 2 are on the SHORT detector and

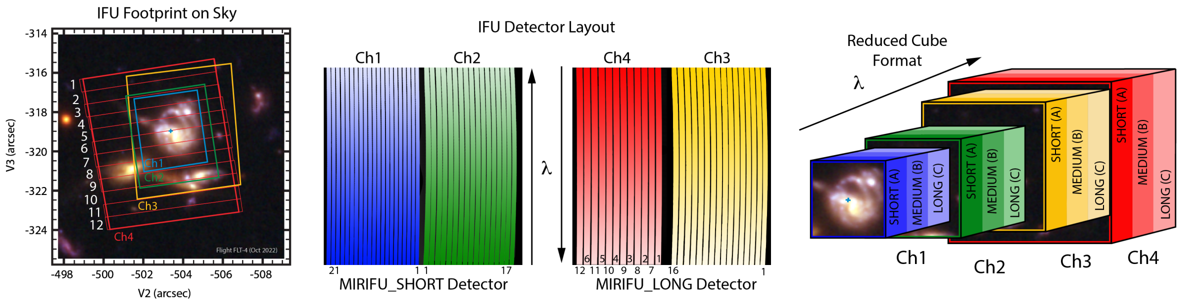

Figure 4.7: The image on the left shows the footprint of IFU on the sky. The four MRS channels are projected on the sky. The middle image illustrated the two detectors. The right image denotes that the observers receive the MRS data as a 3-D cube. Each channel contains three grating settings. Image credit: STScI

channel 3 and 4 are on the LONG detector. MIRI MRS is the only configuration of JWST which offers the medium-resolution spectroscopy at wavelengths longer than 5.2 μm. The spectral resolving power of MRS lies between 1500 to 3500 for the longest to the shortest wavelength. Furthermore, the 4 channels of MRS are divided into 12 sub-bands. In the IFU images, we have both the spectral and spatial information. MRS 4-point dither pattern is used for the extended source observations in order to resolve the PSF and sampling the spectral line resolution. Background emission starts to become strong in channel 3 and dominates in channel 4. In the case of having a very bright isolated point source, for which we can be sure that it is not contaminated by any other source, we can skip observing the background emission. This is far from the situation which we have in the GC, where background correction is always needed. Otherwise, the background is mainly important to correct for the unexpected imperfections and artefacts of the detectors as well as the cosmic showers.

4.2.2 MIR simulations for observations of Sgr A* with JWST

The GC will only be observed in MIR in August 2023 with the MIRI and NIRSpec instruments of JWST. However, already now the MIR emission towards the GC observed with JWST MIRI can be simulated by using the MIRI instrument simulator (MIRISim Klaassen et al. 2021). Work in this direction was presented in the Bachelor theses of S. Vider and J. Bardey in our working group and I briefly outline the main results here.

As input in these simulations, MIR data from VLT/VISIR presented in Sabha (2015) were used. An exemplary, simulated image based on these data is shown in Fig. 4.8, which shows an image of the overlay of the four channels of MIRI pointed at the S-cluster and the IRS13N sources. The results of S. Vider showed that the observations of the S-cluster and IRS13N cluster are possible with the MRS through all channels.

When the data from JWST will be reduced and analyzed, one can compare the observed spectra of dusty sources with the simulated ones, e.g. obtained using Monte Carlo Radiative Transfer codes, which should further constrain the fundamental parameters of these sources. The results the two Bachelor theses show that with JWST it will be possible to obtain information about the nature of the S-stars and dusty stellar objects from the observed spectra. Hence, JWST observations will shed light on young stars and their formation in the extreme environment of the Galactic Centre in particular.

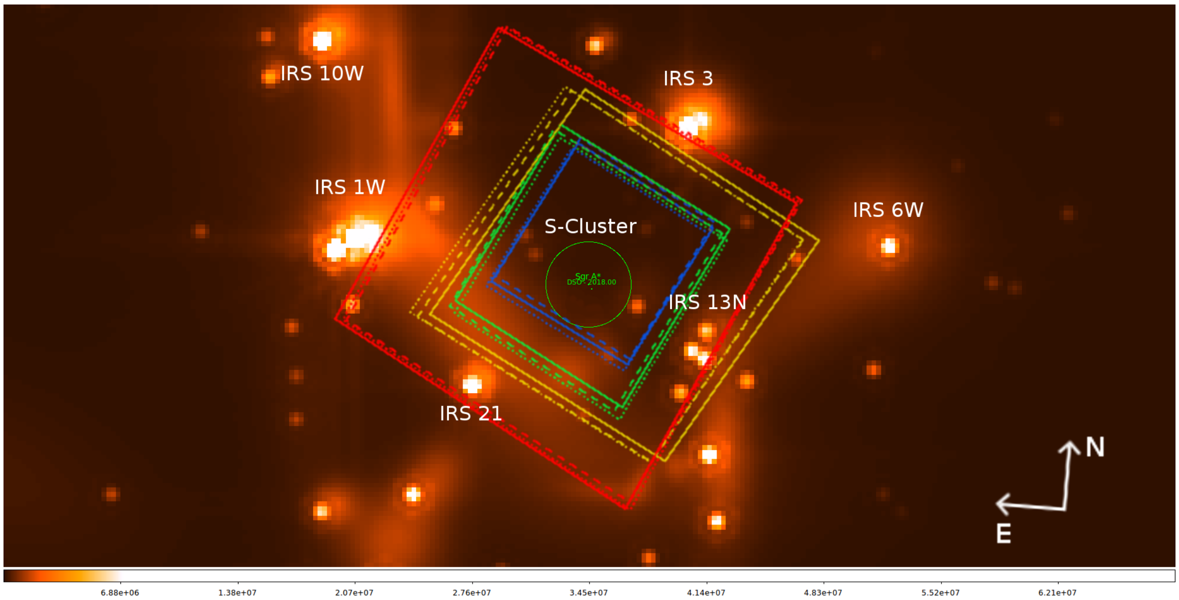

Figure 4.8: A simulated image depicting the IFU footprint on the sky pointed at the S-cluster and IRS13N sources. The green circle marks the region where the DSO/G2 orbits Sgr A*. The observations of the S-cluster and IRS13N cluster are possible with the MRS through all channels. Image credit: Bachelor thesis of S. Vider.

4.3 Data reduction

The JWST data are accessible via the Mikulski Archive for Space Telescopes portal[7]. The JWST science calibration pipeline processes the data from all JWST instruments. The pipeline is provided in Python and is accessible via Github. The data reduction process in the pipeline consists of three main stages. There are different modules on each stage of the pipeline in order to process the data from different instruments and observing modes. The three pipeline stages are as follows:

- Stage 1: The detector-level corrections and ramp fitting are applied to individual exposures. These corrections are needed for almost all imaging and spectroscopic data.
- Stage 2: Further instrument-level corrections for individual exposures are applied to the exposures. There are two pipeline modules for this stage, one for the imaging and the other for the spectroscopic data.
- Stage 3: It combines the calibrated data from multiple exposures. This stage comprises five modules for imaging, spectroscopic, coronagraphic, aperture masking interferometry, and time series observation modes.

In case there are issues with the final calibrated data, one can access the output from each stage of the pipeline or the uncalibrated data and run the data through the customized pipelines. In most cases, the science data files in MAST are sufficient to start the analysis.

[7] https://mast.stsci.edu/portal/Mashup/Clients/Mast/Portal.html

The Space Telescope Science Institute (STScI) has developed several data analysis and visualization (Jdaviz) tools to handle the JWST observations. These tools are categorized into four groups: Imviz, Specviz, Cubeviz, and Mosviz.

1. Imviz provides image visualization and is able to visualize and analyze 2D astronomical images.

2. Specviz stands for spectra visualization and is capable of visualizing and analyzing the 1D astronomical spectra.

3. Cubeviz is designed to visualize and analyze the IFUs, which can be used for the data produced by the MIRI, MRS, and NIRSpec IFUs as well as 1D spectra extraction from the cube.

4. Mosviz is a visualization and analysis tool to investigate multi-object spectroscopy (MOS), viewing 2D and 1D spectra.

I summary, I showed here some of the important aspects of the JWST mission, and introduced briefly some essential instruments of the Webb telescope. I provided an introduction to the data handling tools. In the Chapter. 7, I present some examples of the Galactic Center JWST NIRSpec data and three quasars observed with JWST MIRI. These studies give us an insight to the type of the observed data by the space telescope and the strength of the telescope in practice.

CHAPTER 5

Constraining the accretion flow density profile near Sgr A* using the L′ band emission of the S2 Star

Measuring the density of the ambient medium of black holes helps to understand the inflow-outflow mechanisms. The SMBH Sgr A* is categorised as an extremely low-luminous source (Narayan et al. 1998) which has a radiatively inefficient and diluted accretion flow (Yuan et al. 2003).

As the periapse of the star S2 happened in 2018, this closest ever observed approach at a distance of 14.5 mas to Sgr A* provided a unique opportunity to study both relativistic predictions (Zucker et al. 2006; Parsa et al. 2017; Gravity Collaboration et al. 2018; Do et al. 2019) and the ambient medium of Sgr A*.

In the following publication, I analysed the NIR L′-band data between 2004 and 2018, which offer the possibility of observing gas and dust in order to detect any bow shock effects. I applied aperture photometry on the data to obtain the light curve of the S2 star. I did not detect any significant change in the flux density of S2 between 2002 and 2018. There is only 2.5 % intrinsic flux variability measurable on the light curve of S2 star.

Furthermore, I used the light curve of the S2 star and the analytical dust extinction model to infer the density slope of the ambient medium around Sgr A* and put an upper limit on the density of the ambient medium. The upper limit of the ambient density is $\sim 1.87 \times 10^9\ \mathrm{cm}^{-3}$ at the S2 periapse and the density slope corresponds to 3.20.

These results are included in the peer-reviewed paper, which is published in A&A. For this publication, I did the majority of the data reduction and the entire data analysis which present by far the crucial and most time-demanding part of the publication. I wrote the entire paper in collaboration with M. Zajaček. Credit: Hosseini et al., A&A 644, A105 (2020).

A&A 644, A105 (2020)
https://doi.org/10.1051/0004-6361/202037724

Astronomy & Astrophysics

Constraining the accretion flow density profile near Sgr A* using the L'-band emission of the S2 star

S. Elaheh Hosseini[1,2], Michal Zajaček[3,2,1], Andreas Eckart[1,2], Nadeen B. Sabha[4,1], and Lucas Labadie[1]

[1] I. Physikalisches Institut der Universität zu Köln, Zülpicher Strasse 77, 50937 Köln, Germany
e-mail: hosseini@ph1.uni-koeln.de
[2] Max-Planck-Institut für Radioastronomie (MPIfR), Auf dem Hügel 69, 53121 Bonn, Germany
[3] Centre for Theoretical Physics, Polish Academy of Sciences, Al. Lotnikow 32/46, 02-668 Warsaw, Poland
[4] Institut für Astro- und Teilchenphysik, Universität Innsbruck, Technikerstrasse 25/8, 6929 Innsbruck, Austria

Received 13 February 2020 / Accepted 27 September 2020

ABSTRACT

Context. The density of the ambient medium around a supermassive black hole (SMBH) and the way it varies with distance plays an important role in our understanding of the inflow-outflow mechanisms in the Galactic centre (GC). This dependence is often fitted by spherical power-law profiles based on observations in the X-ray, infrared (IR), submillimetre (submm), and radio domains.

Aims. Nevertheless, the density profile is poorly constrained at the intermediate scales of 1000 Schwarzschild radii (R_s). Here we independently constrain the spherical density profile using the stellar bow shock of the star S2 which orbits the SMBH at the GC with the pericentre distance of 14.4 mas ($\sim$1500 R_s).

Methods. Assuming an elliptical orbit, we apply celestial mechanics and the theory of bow shocks that are at ram pressure equilibrium. We analyse the measured IR flux density and magnitudes of S2 in the L'-band (3.8 micron) obtained over seven epochs in the years between 2004–2018. We put an upper limit on the emission from S2's associated putative bow shock and constrain the density profile of the ambient medium.

Results. We detect no significant change in S2 flux density until the recent periapse in May 2018. The intrinsic flux variability of S2 is at the level of 2–3%. Based on the dust-extinction model, the upper limit on the number density at the S2 periapse is $\sim$1.87 $\times$ 10^9 cm^{-3}, which yields a density slope of at most 3.20. Using the synchrotron bow-shock emission, we obtain the ambient density of $\lesssim$1.01 $\times$ 10^5 cm^{-3} and a slope of $\lesssim$1.47. These values are consistent with a wide variety of media from hot accretion flows to potentially colder and denser media comparable in properties to broad-line-region clouds. However, a standard thin disc can be excluded at the distance of S2's pericentre.

Conclusions. With the current photometry sensitivity of 0.01 mag, we are not able to make stringent constraints on the density of the ambient medium in the GC using S2-star observations. We can distinguish between hot accretion flows and thin, cold discs, where the latter can be excluded at the scale of the S2 periapse. Future observations of stars in the S cluster using instruments such as Mid-IR Extremely Large Telescope Imager and Spectrograph at Extremely Large Telescope with the photometric sensitivity of as much as 10^{-3} mag will allow the GC medium to be probed at intermediate scales at densities as low as $\sim$700 cm^{-3} in case of non-thermal bow-shock emission. The new instrumentation, in combination with discoveries of stars with smaller pericentre distances, will help to independently constrain the density profile around Sagittarius A* (Sgr A*).

Key words. infrared: stars – black hole physics – Galaxy: center

1. Introduction

The Galactic centre (GC) is a unique astrophysical setting where one can study the dynamical effects in one of the densest stellar clusters (Alexander 2005; Merritt 2013; Schödel et al. 2014) and the mutual interaction of stars, gaseous-dusty structures, the magnetic field, and the supermassive black hole (SMBH; Genzel et al. 2010; Eckart et al. 2017). The dynamical centre traced by orbiting stars coincides with the non-thermal compact and variable radio source Sagittarius A* (Sgr A*) within 0.03″ (Menten et al. 1997). Because of its well-constrained mass of $M_{\rm BH}$ = (4.15 ± 0.13 ± 0.57) × 10^6 $M_\odot$ (Parsa et al. 2017) based mainly on monitoring of fast-moving S stars (see also Schödel et al. 2002; Ghez et al. 2008; Gillessen et al. 2009, 2017; Boehle et al. 2016), Sgr A* is associated with the SMBH, leaving only a little space for alternative scenarios of its compact nature (Eckart et al. 2017). Given its distance of 8.1 kpc (Eisenhauer et al. 2003; Reid et al. 2003; Gravity Collaboration 2019), it is the nearest SMBH, which allows us to perform high-precision astrometric and interferometric observations of Sgr A* and its immediate surroundings. In recent years, this provided an opportunity to confirm general relativistic predictions by measuring the gravitational redshift (Gravity Collaboration 2018a; Do et al. 2019a) as well as the Schwarzschild precession (Gravity Collaboration 2020) by monitoring the bright S2 star (also referred to as S0-2) that orbits Sgr A* with a period of 16.2 years.

Sgr A* belongs to extremely low-luminous sources, with its bolometric luminosity that is eight to nine orders of magnitude below its Eddington limit (Narayan et al. 1998; Yuan & Narayan 2014). Its broadband spectral energy distribution is best described by a class of radiatively inefficient accretion flows (RIAFs; Yuan et al. 2003). In order to better comprehend its low-luminous, diluted accretion flow, it is of prime importance to constrain its density at large, intermediate, and eventually small spatial scales. This has been done by

Open Access funding provided by Max Planck Society.

analysing the radiative properties of its surroundings. At larger scales, the analysis of the X-ray bremsstrahlung emissivity profile of 1.3 keV plasma in the central hot bubble yielded a number density of $n_{\rm B} \approx 26\,\eta_{\rm f}^{-1/2}{\rm cm}^{-3}$ (with $\eta_{\rm f}$ being the filling factor), close to the Bondi radius (Baganoff et al. 2003; Wang et al. 2013), which lies at $r_{\rm B} \approx 4''(T_{\rm a}/10^7\,{\rm K})^{-1} \approx 0.16\,{\rm pc}$ given the plasma temperature $T_{\rm a}$ (Wang et al. 2013). Density constraints at the scale of 10–100 Schwarzschild radii (hereafter denoted $r_{\rm s}$) were obtained by analysing the polarised millimetre (mm) and submillimetre (submm) emission, which implies non-thermal self-absorbed synchrotron radiation in the mm domain that becomes optically thin at submm wavelengths (Aitken et al. 2000; Agol 2000; Bower et al. 2003). Marrone et al. (2006, 2007) detected the Faraday rotation of the polarised submm emission based on which they constrain the accretion-rate of Sgr A* to $\dot{M} \sim 2\times10^{-9} - 2\times10^{-7}\,M_{\odot}\,{\rm yr}^{-1}$, which corresponds to the maximum number density of $n_{\rm a}^{\rm max} < 1.4\times10^7\,{\rm cm}^{-3}$ close to the event horizon. Generally, the hot accretion flow in the GC is described by a power-law density profile $n \propto r^{-\gamma}$, where the power-law slope is typically inferred to be $\gamma \sim 0.5{-}1.0$ (Wang et al. 2013) in agreement with the RIAF-type flows. Spherical Bondi-type flow with $\gamma \sim 3/2$ is also consistent with the X-ray surface brightness profile up to $3''$ from Sgr A* (Różańska et al. 2015). Hence, the number densities of the ambient flow and the corresponding slopes are still quite uncertain, especially at intermediate spatial scales where the fast-moving S stars are located. This uncertainty was further enhanced by the possible detection of a cooler ($\sim10^4$ K) and a denser disc with a number density of $\sim10^5{-}10^6\,{\rm cm}^{-3}$ at the radius of $\sim$0.004 pc, which is comparable to the semi-major axis of the bright S2 star (Murchikova et al. 2019). However, the detection by Murchikova et al. (2019) is questionable, especially the association of the recombination double-peak line of H30α at 1.3 mm with the gaseous material at milliparsec spatial scales; it is especially controversial given that near-infrared (NIR) line maps, for example of the recombination Brγ line that can trace ionised material of 10^4 K, do not seem to imply any existence of such a compact disc-like structure. On the other hand, there are indications of denser material traced by the Brγ line (Peißker et al. 2020a) and the blueshifted H30α line (Royster et al. 2019) at larger spatial scales closer to the Bondi radius, which the study of Murchikova et al. (2019) could be associated with. This underlines the need for better and independent constraints on the accretion-flow density at the intermediate range of radii.

The fast-moving stars of the S cluster could in principle be used to constrain the accretion flow density at intermediate scales. As fast-moving probes, these stars drive shocks into the ambient medium and provide radiative energy that can temporarily affect the radiative properties of the accretion flow as well as form localised density and extinction enhancements. Any detected flares linked to an orbiting star would thus provide a way to infer density and other properties of the intercepted ambient medium. Quataert & Loeb (2005) analysed the possibility that the stellar wind shocks in the central arcsecond could contribute to the ambient TeV and non-thermal broad-band emission. It was predicted that the interaction of the fast-moving B-type S2 star with the ambient hot accretion flow is expected to form a bow shock, which should result in a month-long thermal X-ray bremsstrahlung flare with the peak luminosity of $L_{\rm X} = 4\times10^{33}\,{\rm erg\,s^{-1}}$ (Giannios & Sironi 2013; Christie et al. 2016). The contribution to the emerging X-ray flux is also expected to come from UV and optical photons of S2 that are Compton-upscattered by electrons of the inner hot RIAF (Nayakshin 2005). According to these models, the S2 bow-shock X-ray luminosity is in principle comparable to the quiescent X-ray emission of Sgr A* and hence could be detected with the current X-ray instruments. The non-detection of any significant X-ray flare around the pericentre crossings of S2 star in 2002 and 2018 is consistent with a diluted hot RIAF flow in the central arcsecond (Yuan et al. 2003). The low X-ray flux from the bow shock is also in agreement with numerical 3D adaptive-mesh refinement simulations of the motion of S2 through the RIAF (Schartmann et al. 2018).

The detection and the monitoring of the dusty G2 source or the Dusty S-cluster Object (DSO; Gillessen et al. 2012; Eckart et al. 2013; Witzel et al. 2014; Valencia-S et al. 2015; Peißker et al. 2020b; Ciurlo et al. 2020) triggered an effort to predict and observe its potential interaction with the ambient environment. Narayan et al. (2012) predicted the radio synchrotron emission from the DSO bow shock to be comparable to the quiescent radio emission of Sgr A*. In theory, electrons in the ambient accretion flow are expected to be accelerated in the bow-shock region. The main sources of uncertainty are the bow-shock size, which depends on the stellar-wind characteristics and the ambient density, and the magnetic field strength that is enhanced in the bow shock. For the more realistic estimates of the DSO/G2 bow-shock size, assuming the low-mass star model, the radio synchrotron emission was calculated to be well below the radio emission of Sgr A*, and therefore no detectable flare was expected (Crumley & Kumar 2013; Zajaček et al. 2016). This was observationally confirmed by the non-detection of any enhanced radio or mm emission by Bower et al. (2015) and Borkar et al. (2016), who constrain the DSO/G2 cross-section to $<2\times10^{29}\,{\rm cm}^2$.

The bow-shock synchrotron emission can be generalised to the S stars, predicting their broad-band synchrotron spectrum with the peak close to 1 GHz and associated monochromatic light-curves (Ginsburg et al. 2016). Ginsburg et al. (2016) estimated that the synchrotron emission from S-star bow shocks can be comparable to the Sgr A* radio (10 GHz) and IR flux densities (10^{14} GHz) for rather extreme combinations of the wind mass-loss rate and its terminal velocity – $(\dot{m}_{\rm w}, v_{\rm w}) = (10^{-5}\,M_{\odot}\,{\rm yr}^{-1}, 10^3\,{\rm km\,s}^{-1})$ and $(\dot{m}_{\rm w}, v_{\rm w}) = (10^{-6}\,M_{\odot}\,{\rm yr}^{-1}, 4\times10^3\,{\rm km\,s}^{-1})$. These values deviate from those inferred for S2 (Martins et al. 2008; Habibi et al. 2017): $(\dot{m}_{\rm w}, v_{\rm w}) = (<3\times10^{-7}\,M_{\odot}\,{\rm yr}^{-1}, 10^3\,{\rm km\,s}^{-1})$. For these observationally inferred values, the S star non-thermal flux densities are below those of Sgr A*. Another, independent way to constrain the density of the ambient medium is the detection of deviation from the Keplerian ellipse due to hydrodynamic drag force. Gillessen et al. (2019) claimed the detection of a significant deviation for the DSO/G2 object due to the drag force, from which they inferred a density of $4\times10^3\,{\rm cm}^{-3}$ at the DSO/G2 pericentre close to 1000 $r_{\rm s}$.

Here we report NIR L'-band emission from one of the brightest members of the S cluster, star S2. Close to its first observed pericentre passage in 2002, Clénet et al. (2004) reported a brightening of S2 in L'-band, which could be associated with its interaction with the ambient medium at the scale of 1500 Schwarzschild radii[1]. Based on our reanalysis of the 2002 epoch and an additional seven epochs, including close to the subsequent pericentre passage in 2018, we can exclude any significant brightening related to the pericentre passage of S2 in L'-band. The intrinsic fractional variability of the S2 light curve is only $\sim$2.5%. Using the model of the thermal dust emission in the shocked ambient medium, we place an upper limit on

[1] The S2 pericentre distance according to Gravity Collaboration (2018a) is 1513 Schwarzschild radii.

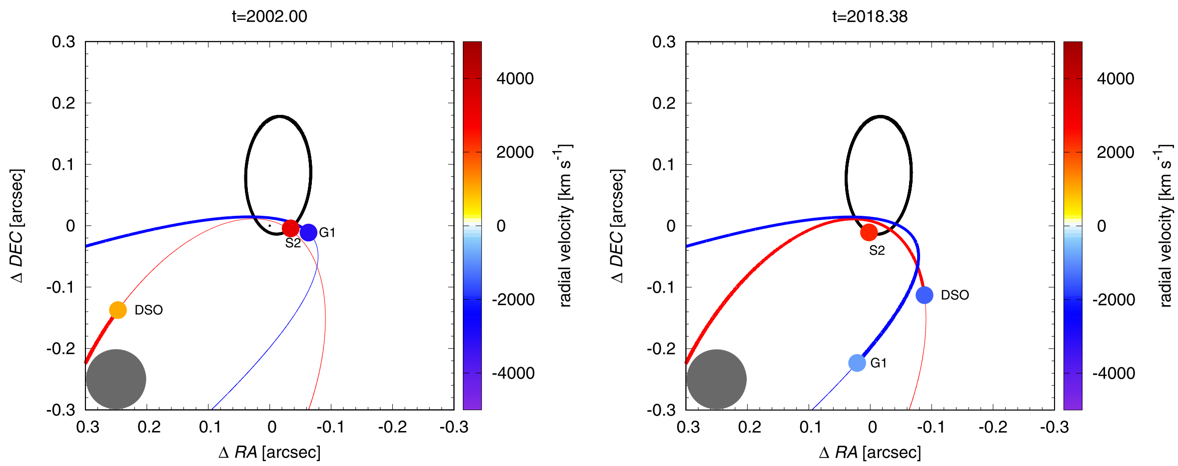

Fig. 1. S2 star and known dusty objects close to its orbit. *Left panel*: position of S2 and the dusty source G1 close to the pericentre of S2 around 2002. We also show the orbit of the DSO (Dusty S-cluster Object, also known as G2). The points of the sources represent colour-coded radial velocities according to the axis on the right. The grey circle in the bottom left corner represents the diffraction limited FWHM of 98 mas corresponding to NACO L'-band. *Right panel*: position of S2 and dusty source G1 at the pericentre passage of S2 at 2018.38. The orbital parameters were adopted from Gravity Collaboration (2018a) (S2 star), Valencia-S et al. (2015) (DSO source), and Witzel et al. (2017) (G1 source).

the ambient density of $\lesssim 10^9\,\mathrm{cm}^{-3}$, which can accommodate a wide variety of ambient media at the S2 pericentre distance of 1500 Schwarzschild radii, except for a standard thin cold disc. The bow-shock synchrotron model gives a tighter upper limit of $\sim 10^5\,\mathrm{cm}^{-3}$. An improved photometric sensitivity of the next-generation of instruments, in particular Mid-IR Extremely Large Telescope Imager and Spectrograph (METIS) at Extremely Large Telescope (ELT), will help to further constrain the density at intermediate scales.

The current paper is structured as follows. Section 2 describes the observations and data-reduction methods used for this work. We then briefly discuss the photometry and its results for S2 in Sects. 2.1 and 2.2, respectively. In Sect. 3 we constrain the slope and density of the ambient accretion flow using S2 star observations in L' band. Section 3.1 is dedicated to the exploration of the extinction caused by the ambient gas and dust inside the Bondi radius. In Sect. 3.2, the upper limit of the ambient density is inferred based on the thermal bow-shock emission. In Sect. 3.3, we then constrain the ambient density based on the non-thermal bow-shock emission. We discuss the obtained density values in the broader context of the accretion flows and the GC gaseous-dusty structures in Sect. 4. Finally, in Sect. 5 we summarise the main results.

2. Observations and data reduction

Observations of the GC in the NIR were carried out with the European Southern Observatory (ESO) Very Large Telescope (VLT) Unit 1 (UT1)-YEPUN on Paranal, Chile. The data were obtained from the IR camera Coude NIR Camera (CONICA) and the Nasmyth Adaptive Optics System (NAOS) adaptive optics (AO) module, known as NACO. The central parsec of the GC has been frequently observed with the VLT in the L'-band ($3.8\,\mu$m, $0.0271''\,\mathrm{pixel}^{-1}$).

In Table 1, we summarise the obtained data that are analysed in this study. The total time-coverage of the data set is from 2004.317 until 2018.307. The only applied criterion on the epoch selection is the imaging quality, because a large number of the available data sets in the archive were observed during poor atmospheric conditions, in particular bad and fast seeing. We used the standard data-reduction process that consists of the sky subtraction, flat-fielding, and bad pixel correction for all imaging data and combined them via a shift-add algorithm to obtain a final array size of $28'' \times 28''$ for all epochs.

The first observed periapse of S2 occurred in 2002. The spatial resolution of NACO at $3.8\,\mu$m is $0.096''$, while the distance between Sgr A* and S2 in 2002 is approximately $0.040''$. Therefore, it is impossible to obtain the emission of S2 from the images completely separated from Sgr A* emission. Furthermore, we know that Sgr A* is flaring in the observation which is done in 2002 (Genzel et al. 2003), and in 2002 and 2003 the NIR-excess extended source denoted G1 is sufficiently close to the S2-Sgr A* system that it cannot be disentangled from the Sgr A*-S2 system (Clénet et al. 2004; Witzel et al. 2017).

We show the superposition of S2 and G1 in Fig. 1, where we plot the projected orbits of S2, G1, and DSO/G2. Immediately before the pericentre passage around 2002, the mutual separation between S2 and G1 was less than 0.1 arcsec; see Fig. 1 (left panel). The G1 cloud is currently going to larger distances from Sgr A* (more than 0.2 arcsec, see Fig. 1, right panel), and therefore potential changes of the brightness of S2 after 2002 pericentre passage would be due to other effects, most likely due to bow-shock emission, which we analyse in this contribution. Hence, to prevent further uncertainties in our analysis, we excluded the first observed periapse of S2.

2.1. Photometry

Flux densities of S2 and calibrators were determined via aperture photometry using a circular aperture of 82 mas in L'-band. Dereddened fluxes were computed with the extinction of $A_L = 1.09 \pm 0.13$ (Fritz et al. 2011) and a zero magnitude value of $F_0(L) = 249$ Jy.

The magnitude calibration is done by considering S26, S30, and S35 as calibrators using their known brightness from Gillessen et al. (2009). These S-stars are chosen because they are sufficiently isolated over the epochs of our study. In Fig. 2, we show the surroundings of S2 within about $\pm 1''$ on 9 May 2013.

In general, the grainy background at the centre of our Galaxy is variable due to the proper motion of the stars (Sabha et al. 2012). Therefore, to correct for background brightness, we used

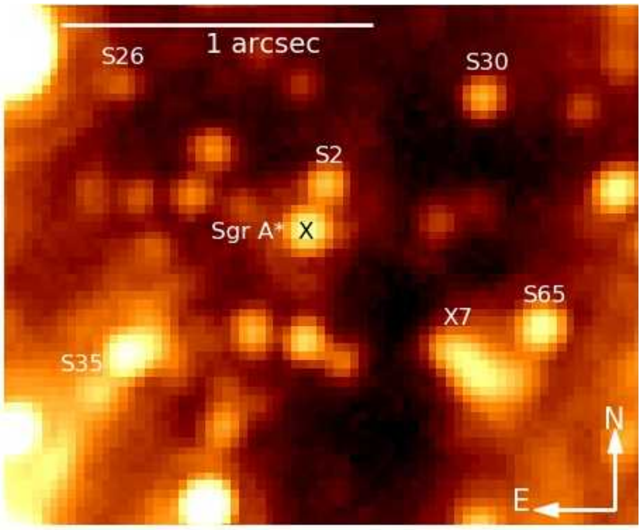

Fig. 2. NACO L'-band mosaic of the GC in 2013.356. North is up and east is to the left. The identification of three stars (S26, S30 and S35) as photometric calibrators is depicted in particular. The black cross shows the IR counterpart of Sgr A*. In order to check any variability in the flux of S2, we used S65 as a reference star.

five apertures with the same size as our photometric apertures close enough to the calibrators and S2 to get an appropriate representative of the existing background. Because of the high-velocity S-stars, the background is highly variable, and therefore background apertures are not located at the same position for all the epochs considered in this study.

2.2. Photometry results

S2 is an early B-type dwarf of spectral type B0–B2.5 V with a stellar wind that has an estimated velocity of $v_w \sim 1000\,\mathrm{km\,s^{-1}}$ and a mass-loss rate of $\dot{m}_w \lesssim 3 \times 10^{-7}\,M_\odot\,\mathrm{yr}^{-1}$ (Martins et al. 2008). We did the aperture photometry with local background subtraction for seven selected epochs from 2004 to 2018. S65 flux and magnitude were also studied in order to use this object as a test star to reveal any meaningful changes in S2 flux or magnitude.

The photometry results are presented in Table 1. As shown in Fig. 3, there is essentially no change detected in the measured flux density of S2 within the uncertainties over the seven epochs. The total coverage is 15 years, which is close to the S2 orbital period around Sgr A*, including epochs close to the pericentre passages of S2. The light curve has a mean value of the flux density of $\overline{F} = 8.88 \pm 0.33$ mJy, with a difference between maximum and minimum values of 0.90 mJy. In terms of the L'-band magnitude, the mean magnitude of S2 in the L'-band is 11.12 ± 0.04. The intrinsic variability of S2 is characterised by a normalised excess variance (Nandra et al. 1997),

$$\sigma^2_{\mathrm{rms}} = \frac{1}{N\overline{f}^2} \sum_{i=1}^{N} [(f_i - \overline{f})^2 - \sigma_i^2], \tag{1}$$

where f_i are individual flux measurements, $\overline{f} = 1/N \sum_{i=1}^{N} f_i$ is the mean flux density, and σ_i are individual measurement errors. We obtain the value of the fractional variability $F_{\mathrm{var}} = \sqrt{\sigma^2_{\mathrm{rms}}} = 2.52\%$ in terms of the flux density and $M_{\mathrm{var}} = 0.22\%$ in terms of the magnitude. For the control star S65, we obtain $F_{\mathrm{var}} = 4.53\%$, which is almost a factor of two larger than S2. These values are fully consistent with no intrinsic changes in the L'-band flux density of S2 within measurement uncertainties. For completeness, the mean, the maximum difference, and the fractional variability F_{var} are listed in Table 1 for both S2 and S65.

In order to study the S2 flux and magnitude closely during its periapse in May 2018 at around 1500 R_s distance from Sgr A*, we performed the aperture photometry on all single exposures from the observation on 2018.307, on the position of S2 and the IR counterpart of radio source Sgr A*. The physical separation of S2 and Sgr A* was only 1.38 mpc, corresponding to 34.6 mas, while the angular resolution is 99.5 mas in L'-band. The photometry results are shown in Fig. 4. As can be seen, there is no sudden increase in the received flux from the position, and therefore Sgr A* is in its quiescent state in L'-band over the observation 2018.307. In addition to the non-detection of any flare from the IR counterpart of Sgr A*, no apparent increase in the S2 flux was observed within the measurement uncertainties.

For the 2002.663 epoch, we measure 17.41 ± 1.18 mJy at the –at that time– combined position of S2, G1, and L'-band counterpart of Sgr A*. Taking into account S2's mean stellar flux density of 8.88 ± 0.33 mJy (dreddened with $A_L = 1.09$) and the G1 L'-band flux density of $\sim 2.58 \pm 1.40$ mJy close to the 2002 epoch (Witzel et al. 2017), the flux of Sgr A* ends up being around 6.03 ± 0.52 mJy. Schödel et al. (2011) obtains the mean flux of Sgr A* in the L'-band as 4.33 ± 0.18 mJy, which leads us to 1.70 mJy surplus in the measured flux density. However, due to the lack of a longer (at least days) light-curve time coverage during the S2 periapse passage of the variable source black hole counterpart SgrA* in 2002, it is not possible to determine whether this flux density excess is due to a Sgr A* flare or the S2 stellar bow-shock effect. However, since during the subsequent pericentre passage in 2018 the flux density of S2 is within the uncertainty comparable to its mean value (see Table 1), the excess can be attributed to the Sgr A* flare, unless the accretion flow density changes dramatically by several orders of magnitude from one periapse to another. The flux excess of 1.70 mJy that corresponds to the magnitude change of ~ 0.19 mag would require the pericentre number density of $\sim 4.2 \times 10^{10}\,\mathrm{cm^{-3}}$ according to the dust-extinction model we present in Sect. 3.2. Considering the synchrotron bow-shock emission (see Sect 3.3), the required density at the pericentre is smaller, $n_a \sim 2.1 \times 10^5\,\mathrm{cm^{-3}}$, but still larger by two orders of magnitude than expected for the RIAF density profile with $\gamma \approx 1$, $n_a \sim 7.2 \times 10^3\,\mathrm{cm^{-3}}$. Such a large density present only for epoch 2002 is unlikely. The excess flux of 1.70 mJy can therefore be attributed to the L'-band flare of Sgr A*. In the L'-band, Sgr A* is permanently variable (Schödel et al. 2011) with the flux densities in the range between 1 mJy and 10 mJy (Ghez et al. 2005; Eckart et al. 2008; Dodds-Eden et al. 2009).

3. Constraining the slope and density of the ambient accretion flow using S2's L'-band emission

In this section, we develop a simple method for inferring the density slope and the maximum density at the pericentre of a wind-blowing star using the observed light curve and an analytical dust extinction model. This method is suitable for stars with an unresolved bow shock. For a fully resolved bow shock at least two positions of a star along an elliptical orbit, one can infer the density slope from the bow-shock size ratio and an orbital eccentricity; see Appendix B for more details. Furthermore, we also consider the non-thermal bow-shock

Table 1. L'-band flux and magnitude of S2 and S65 for seven epochs over a 15-year interval from 2004.317 to 2018.307.

UT date	Decimal date	S2 flux (mJy)	S65 flux (mJy)	S2 mag	S65 mag	Observation ID
2004 April 25	2004.317	9.02 ± 0.30	14.56 ± 0.94	11.10 ± 0.04	10.59 ± 0.07	60.A-9026(A)
2005 May 14	2005.367	9.30 ± 0.30	15.07 ± 0.91	11.07 ± 0.04	10.55 ± 0.07	073.B-0085(D)
2006 May 29	2006.408	9.30 ± 0.30	15.07 ± 0.91	11.07 ± 0.04	10.55 ± 0.07	077.B-0552(A)
2007 April 01	2007.249	8.88 ± 0.19	14.49 ± 0.63	11.12 ± 0.02	10.59 ± 0.05	179.B-0261(A)
2008 May 26	2008.402	8.54 ± 0.15	14.19 ± 0.59	11.16 ± 0.02	10.61 ± 0.05	081.B-0648(A)
2013 May 09	2013.356	8.40 ± 0.25	14.82 ± 1.12	11.18 ± 0.03	10.57 ± 0.08	091.C-0159(A)
2018 April 22	2018.307	8.70 ± 0.10	13.62 ± 0.33	11.13 ± 0.01	10.64 ± 0.03	0101.B-0052(B)
Mean		8.88 ± 0.33	14.55 ± 0.48	11.12 ± 0.04	10.59 ± 0.03	
difference (max – min)		0.90	1.45	0.11	0.09	
$F_{\rm var} = \sqrt{\sigma^2_{\rm rms}}$ (%)		2.52	4.53	0.22	0.51	

Notes. The DIT for all cases is 0.200 s. Light-curve characteristics, namely the mean, the difference between the maximum and the minimum, and the fractional variability are also included. With the fractional variability of 2.52%, no significant difference is detected for S2 flux within the uncertainties. The reported fluxes are dereddened.

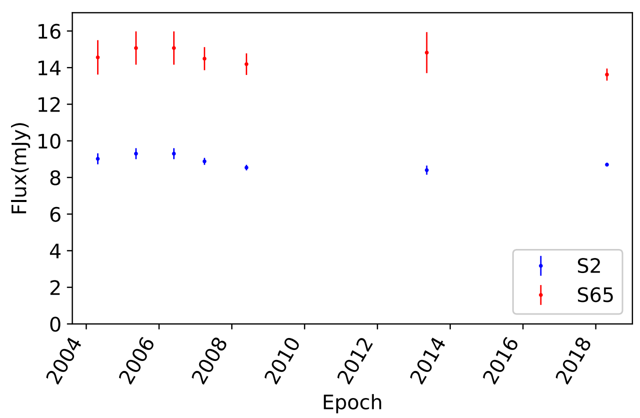

Fig. 3. Light curve of S2 and S65 in L'-band over seven observational epochs.

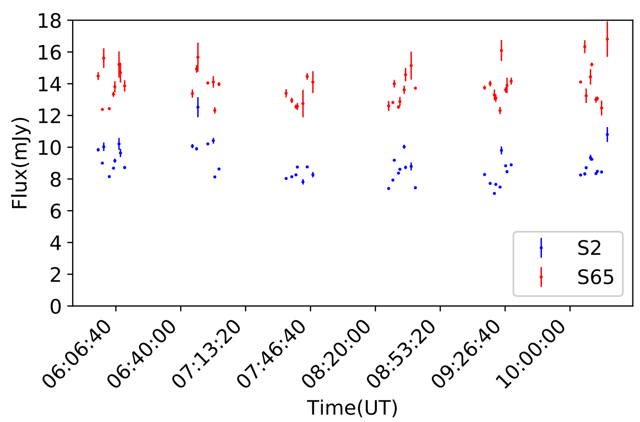

Fig. 4. Light curve at the position of S2 and the IR counterpart of Sgr A* and our reference star, S65, in 2018.307 in L'-band. The light curve shows that the IR counterpart of Sgr A* is in quiescence during our observation, and therefore the light curve belongs to S2.

emission as an independent way of constraining the ambient density. The S2 star is currently intensively monitored by the Very-Large-Telescope Interferometer GRAVITY, as well as the NIR imager NACO and SINFONI at VLT, which is capable of performing integral field spectroscopy. Using the data over the past 25 years, post-Newtonian effects were measured, including the gravitational redshift (Gravity Collaboration 2018a) and the Schwarzschild precession (Parsa et al. 2017; Gravity Collaboration 2020), which are consistent with general relativity so far. Its highly eccentric orbit ($e = 0.885$) implies that the ambient gas density is expected to change along its orbit; it is expected to be the lowest close to its apocentre and the highest close to the pericentre due to the radial power-law profile of the hot X-ray atmosphere (Wang et al. 2013). The dust component is expected to coexist to a certain extent in this hot environment, which is also manifested by the presence of L'-band dusty sources in the central ~0.04 pc, namely DSO/G2, G1, and several other dusty and bow-shock sources in the central arcsecond (Gillessen et al. 2012; Valencia-S et al. 2015; Witzel et al. 2017). In particular, for the orbital solutions and radiative properties of the dust-enshrouded objects, see Peißker et al. (2020b) and Ciurlo et al. (2020). An increase in the ambient gas-and-dust density ratio along with the change in the orbital velocity are expected to lead to a larger local extinction around S2 due to the formation of a bow shock, and hence to a change in the NIR magnitudes and corresponding colour indices. We considered here in particular the NIR L'-band emission of S2, which can trace such a change as S2 moves through the accretion flow of different gas and dust density; see Fig. 5 for an illustration. A potential formation of a stellar bow shock associated with S2 can enhance the colour change despite the insufficient capability of current NIR instruments to resolve the bow-shock structure; see Fig. 5. Both the detection as well as the non-detection of the L'-band magnitude can be used to constrain the density as well as the slope of the gas-and-dust density distribution. The density changes along the S2 orbit depends on the density slope γ. Assuming the radial gas distribution, $n_{\rm a} \approx n_0(r/r_0)^{-\gamma}$, where $\gamma > 0$, the density ratio between the pericentre and the apocentre can be estimated as,

$$\frac{n_{\rm a,P}}{n_{\rm a,A}} = \left(\frac{r_{\rm A}}{r_{\rm P}}\right)^{\gamma} = \left(\frac{1+e}{1-e}\right)^{\gamma}. \tag{2}$$

As the orbital eccentricity is well constrained for S2, $e = 0.885$, the ratio can be estimated to be $n_{\rm a,P}/n_{\rm a,A} \sim 4.05$, 16.39, and 66.36 for the plausible density slopes of 0.5, 1.0, and 1.5, where the first two values represent the radiatively inefficient accretion flow (see e.g. Xu et al. 2006; Wang et al. 2013) and the last value corresponds to the spherical steady Bondi flow (Różańska et al. 2015). As the variation in density is large (by a factor of 16.4) for a rather small variation in the density slope (by a factor of

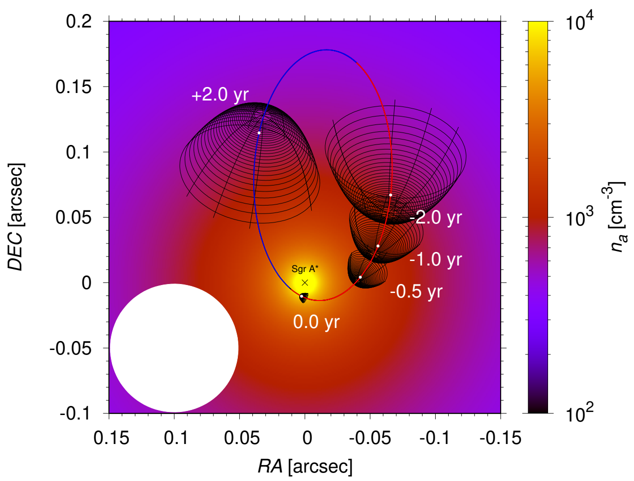

Fig. 5. Illustrative figure of the motion of S2 through the hot flow around Sgr A* of variable density. The density may change by as much as an order of magnitude from the apocentre to the pericentre, from several hundred particles per cubic centimetre to several thousand particles per cubic centimetre, respectively, depending on the power-law slope of the radial number density distribution. For the exemplary calculation, we used $n_{\mathrm{a}} = n_{\mathrm{B}}(r/r_{\mathrm{B}})^{-1}$, where $n_{\mathrm{B}} = 20.3\,\mathrm{cm}^{-3}$ is the particle density at the Bondi radius. The white circle in the bottom left corner depicts the L'-band point spread function corresponding to 8m-class telescopes, from which it is apparent that the S2 bow shock remains unresolved, especially close to the pericentre.

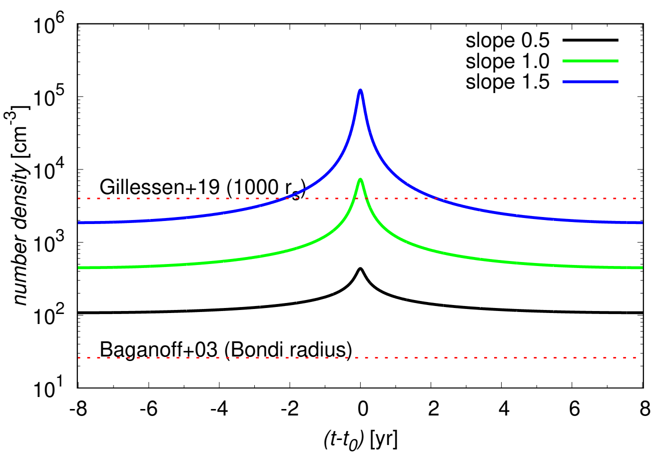

Fig. 6. Temporal evolution of the number density of the ambient medium for the three different density slopes of the radial density profile, $n_{\mathrm{a}} = n_0(r/r_0)^{-\gamma}$, where γ is equal to 0.5, 1.0, and 1.5; see the plot legend. The dashed red lines indicate the number densities that were observationally inferred by Baganoff et al. (2003) ($26\,\mathrm{cm}^{-3}$ at the Bondi radius) and Gillessen et al. (2019) ($4000\,\mathrm{cm}^{-3}$ at $\sim 1000\,r_{\mathrm{s}}$).

three), the L'-band observations of S2 can be used to constrain the density distribution of the hot accretion flow close to Sgr A* at the length scales of the order of 1500 Schwarzschild radii, where there are essentially no constraints for the ambient density (see, however, Gillessen et al. 2019).

In the further model, we approximate the orbit of S2 with an ellipse with a semimajor axis of $0.12538'' \approx 5\,\mathrm{mpc}$ and an eccentricity of 0.88473 according to recent GRAVITY measurements (Gravity Collaboration 2018a). These orbital elements imply that S2 covers a large distance range, with a pericentre distance of $r_{\mathrm{p}} = 119.2\,\mathrm{AU} = 1512\,r_{\mathrm{s}}$ and an apocentre distance of $r_{\mathrm{a}} = (1+e)/(1-e)r_{\mathrm{p}} = 16.35 r_{\mathrm{p}} = 24724\,r_{\mathrm{s}}$. The power-law density distribution is adopted according to the Chandra X-ray studies of the extended emission of Sgr A* in the X-ray domain (Baganoff et al. 2003; Wang et al. 2013). The density distribution can be scaled with respect to the Bondi capture radius, $n_{\mathrm{a}} \approx n_{\mathrm{a,B}}(r/r_{\mathrm{B}})^{-\gamma}$, where $n_{\mathrm{a,B}} \approx 26\eta_{\mathrm{f}}^{-1/2}\,\mathrm{cm}^{-3}$ and $r_{\mathrm{B}} \approx 4''(T_{\mathrm{a}}/10^7\,\mathrm{K})^{-1} = 0.16\,\mathrm{pc}$ (Baganoff et al. 2003; Wang et al. 2013). Figure 6 shows the number gas density per cubic centimetre (cm) that is expected to be intercepted by S2 star during its entire orbit (zero time stands for the orbit periapse). Different lines stand for different density slopes (0.5; 1.0; 1.5) according to the key. The bottom dashed red line depicts the inferred number density close to the Bondi radius according to X-ray observations of Baganoff et al. (2003), while the upper dashed red line stands for the number density of $n_{\mathrm{a}}^{\mathrm{DSO/G2}} \sim 4\times10^3\,\mathrm{cm}^{-3}$ inferred for the periapse of the DSO/G2 object (Gillessen et al. 2019).

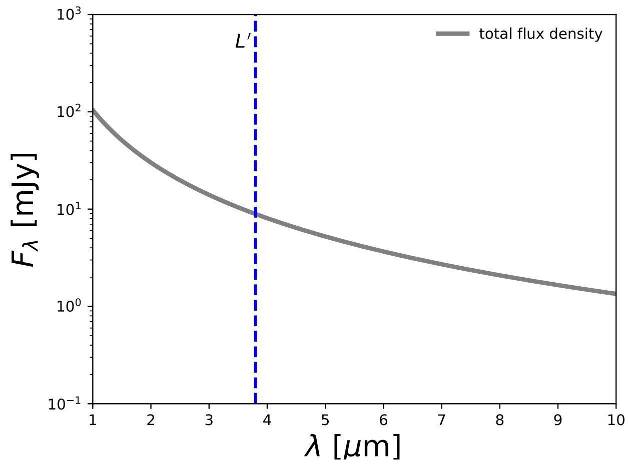

Fig. 7. Total SED of the S2 star (black solid line) around L' band.

We see that due to an eccentric orbit, S2 can in principle serve as a good probe of the ambient gaseous-dusty medium. For the S2 stellar blackbody emission, we adopt the stellar parameters that can reproduce the L' flux density of $\sim$9 mJy. For the model with $\log(L_{\mathrm{S2}}/L_{\odot}) = 4.54$, $T_{\mathrm{S2}} = 26800\,\mathrm{K}$, $R_{\mathrm{S2}} = 6\,R_{\odot}$, we obtain the L' flux density of $F_L = 8.9\,\mathrm{mJy}$; see also Fig. 7 for the spectral energy distribution (SED) of S2 around L'-band.

3.1. Extinction estimate inside the Bondi radius

We assume that the ambient gas inside the Bondi radius has a power-law profile, $n_{\mathrm{a}} \approx n_{\mathrm{a,B}}(r/r_{\mathrm{B}})^{-\gamma}$, which we scaled to the number density at the Bondi radius r_{B}. To estimate the local extinction due to the gas and dust inside the Bondi radius, we calculate the local column density of hydrogen,

$$N_{\mathrm{h}} = \int_{r_{\mathrm{S2}}}^{r_{\mathrm{B}}} n_{\mathrm{a}}(r)\mathrm{d}r = \frac{n_{\mathrm{a,B}} r_{\mathrm{B}}^{\gamma}}{1-\gamma}\left(r_{\mathrm{B}}^{1-\gamma} - r_{\mathrm{S2}}^{1-\gamma}\right), \tag{3}$$

where we integrated from a certain inner radius associated with S2, in this case its pericentre distance of $r_P = a_{\mathrm{S2}}(1-e_{\mathrm{S2}}) \approx 0.577\,\mathrm{mpc}$, up to the Bondi radius. The column density estimate for the number density of $n_{\mathrm{B}} \approx 26\,\mathrm{cm}^{-3}$ (Baganoff et al. 2003) at the Bondi radius and the maximum density power-law slope of $\gamma \approx 1.5$ for the Bondi-type flow is $N_{\mathrm{h}}(\gamma = 1.5) = 4.02\times10^{20}\,\mathrm{cm}^{-2}$, whereas for the flat slope of $\gamma = 0.5$, we get $N_{\mathrm{h}}(\gamma = 0.5) = 2.41\times10^{19}\,\mathrm{cm}^{-2}$. The visual extinction due to the ambient gas inside the Bondi radius for the steep density

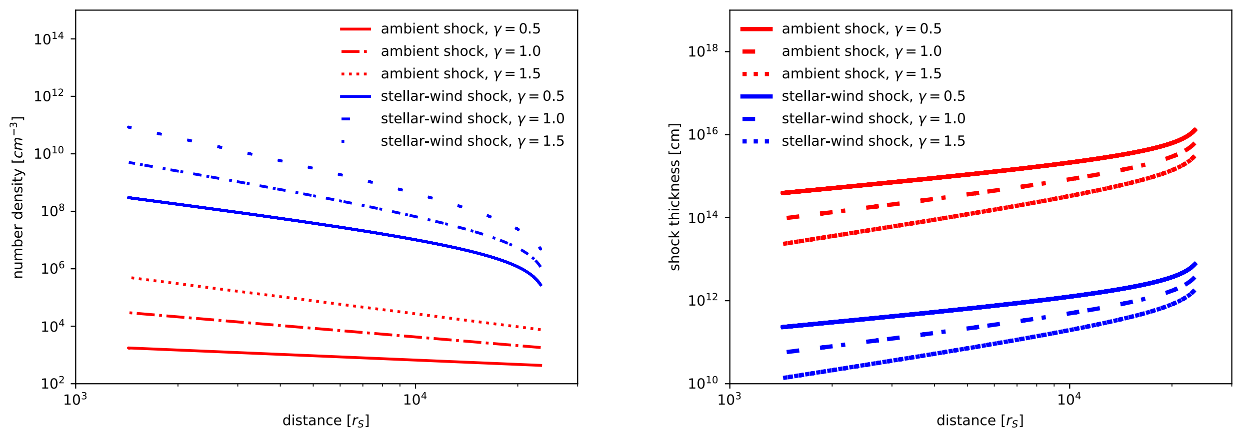

Fig. 8. Number density and thickness of the two shock layers in the two-shock approximation model as a function of the distance from Sgr A* (in Schwarzschild radii). *Left*: number density (expressed in cm^{-3}) of the shock driven into the ambient medium (red lines) and of the shocked stellar wind (blue lines) calculated for three specific values of the ambient density slope: $\gamma = 0.5$, 1.0, and 1.5. *Right*: thickness (expressed in cm) of the stellar-wind (blue lines) and ambient shock layers (red lines) calculated for the three different density slopes as in the *left panel*.

profile ($\gamma = 1.5$) is given by $A_V \approx 5.6 \times 10^{-22} N_\mathrm{h}(\mathrm{cm}^{-2}) = 0.23$ mag (see e.g. Reina & Tarenghi 1973; Gorenstein 1975; Predehl & Schmitt 1995), which corresponds to the extinction $A_K \sim 0.1\,A_V = 0.023$ mag in the NIR K-band and $A_L \approx 0.5\,A_K = 0.012$ mag in the NIR L'-band (see Schödel et al. 2010, for the extinction analysis towards the GC), in which our observations were carried out. For the flat density profile of $\gamma = 0.5$, we get $A_L \approx 0.0007$ mag. Therefore, no increase in the L'-band magnitude within uncertainties is expected from the S2 plunging in deeper towards higher ambient densities. In summary, the upper limit on the ambient extinction inside the Bondi radius is $A_L \lesssim 0.012$ mag. The only substantial increase at longer NIR wavelengths can be produced locally due to the bow-shock formation characterised by its density, radial scale, and thickness, which allows us to estimate the extinction.

3.2. Constraining the ambient density based on the thermal bow-shock emission

The S2 bow shock is modelled using a two-shock scenario (Dyson 1975), where one shock is driven into the ambient medium (ambient shock) and the other is formed from the shocked stellar wind (stellar-wind shock). These two layers are separated by a contact discontinuity at a distance approximately given by the stagnation radius; see Eq. (B.1). This treatment is based on the analytical theory of Dyson (1975), who modelled an interaction of a fast stellar wind with an expanding gas globule. In the first approximation, two layers (warm and cold) mix to form one shocked layer. In the second approximation, two layers are separated by a contact discontinuity. We apply the second approximation in a similar way to Scoville & Burkert (2013) for the GC NIR-excess source DSO/G2 interacting with the ambient diluted medium (see also their Fig. 3 for the illustration). The extinction estimate is based on the number density of gas and dust inside the shock and its characteristic length-scale, or 'thickness'. At the stagnation point, the ambient shock is characterised by the number density $n_\mathrm{ams} = 4n_\mathrm{a}$ and a thickness of $t_\mathrm{ams} = 0.65R_0$. The stellar wind shock has a characteristic number density of $n_\mathrm{sws} = n_\mathrm{w}v_\mathrm{w}^2/c_\mathrm{s}^2$, where $n_\mathrm{w} = \dot{m}_\mathrm{w}/4\pi R_0^2 v_\mathrm{w}\mu m_\mathrm{H}$ is the stellar wind number density with the mean molecular weight of $\mu = 0.5$ (ionised gas) and the hydrogen mass of m_H and the sound speed of the stellar wind gas $c_\mathrm{s} = (k_\mathrm{B}T_\mathrm{sw}/\mu m_\mathrm{H})^{1/2}$ is evaluated for the temperature of $T_\mathrm{sw} = 10^4$ K. The thickness of the stellar wind is given by $t_\mathrm{sws} = 2.3(c_\mathrm{s}/v_\mathrm{w})^2 R_0$. We show both the number density and the thickness of both shocks in Fig. 8 as a function of the distance of S2 from Sgr A* in Schwarzschild radii. We see that the ambient shock is thicker and less dense than the stellar wind shock for all ambient density profiles considered in the legend.

In our model, we further consider that the dust is more likely to exist in the ambient medium through which S2 moves along its orbit, and therefore the ambient shock is expected to be more relevant in terms of the localised extinction and its contribution in the L'-band. The B-type stars typically do not contain dust in their stellar winds, and therefore the stellar wind shock is not likely to contribute to L'-band emission. However, for completeness, we consider both shock layers in assessing the constraints on the ambient number density. This is also due to the complex dynamics of dust grains and their potential of being dragged by a denser material in the stellar-wind shock; especially smaller grains may be affected (see e.g. van Marle et al. 2011). During the motion of S2, the two shock layers are affected by hydrodynamic instabilities that lead to the mixing of both layers (Schartmann et al. 2018), which is likely to lead to the exchange of material and the actual density of the gaseous-dusty mixed layer may be closer to the denser stellar-wind shock.

We calculate the limits on the ambient number density at the S2 periapse as well as the limits for the density slope γ. The upper limit is obtained if we associate the upper limit for the extinction with the standard deviation, $A_\mathrm{shock} \lesssim 0.04$ mag. Another estimate is based on the fractional variability with $A_\mathrm{shock} \sim 0.02$ mag. The values of the density and the slope are inferred from the extinction-column density relation $A_V \approx 5.6 \times 10^{-22} N_\mathrm{h}(\mathrm{cm}^{-2})$, where $N_\mathrm{h} \sim n_\mathrm{shock} t_\mathrm{shock}$ with the shock number density n_shock and a shock thickness t_shock for each shock layer as explained above. The extinction in L'-band is approximately given by $A_L = 0.5 \times 0.1 \times A_V$ (Schödel et al. 2010). This model allows us to compute the whole light curve along the S2 trajectory. In Table 2, we list the density slope and the number density constraints for each extinction value, with the shock layer taken into account. For the ambient shock, which is more likely to lead to an increased dust emission, the upper limits on the number density are in the range $n_\mathrm{a}^\mathrm{ams} \lesssim 7.15 \times 10^8 - 1.87 \times 10^9\,\mathrm{cm}^{-3}$ with the density slope $\gamma \lesssim 3.03 - 3.20$. For the stellar-wind

Table 2. Summary of constraints for the ambient density close to the GC at the S2 periapse based on the two extinction limits, 1σ and fractional variability, and analytical bow-shock models for both the ambient shock and the stellar-wind shock thermal emission.

Thermal emission – upper limit	Power-law slope	Ambient number density (periapse)
Ambient shock ($A = 0.04$)	3.20	$1.87 \times 10^9\,\mathrm{cm}^{-3}$
Stellar-wind shock ($A = 0.04$)	1.57	$1.86 \times 10^5\,\mathrm{cm}^{-3}$
Thermal emission – upper limit	Power-law slope	Ambient number density (periapse)
Ambient shock ($A = 0.02$)	3.03	$7.15 \times 10^8\,\mathrm{cm}^{-3}$
Stellar-wind shock ($A = 0.02$)	1.41	$7.53 \times 10^4\,\mathrm{cm}^{-3}$
Non-thermal emission – upper limit	Power-law slope	Ambient number density (periapse)
Peak flux density of 0.91 mJy (maximum flux difference)	1.47	$1.01 \times 10^5\,\mathrm{cm}^{-3}$
Peak flux density of 0.22 mJy (fractional variability)	1.17	$1.88 \times 10^4\,\mathrm{cm}^{-3}$

Notes. In addition, we include the ambient density upper limit for the non-thermal synchrotron emission based on the maximum flux difference of 0.90 mJy and the fractional variability of 0.2 mJy.

shock, the number densities are smaller by four orders of magnitude and the density slope is smaller by a factor of two, $n_{\mathrm{a}}^{\mathrm{sws}} \lesssim 7.53 \times 10^4 - 1.86 \times 10^5\,\mathrm{cm}^{-3}$ and $\gamma \lesssim 1.41 - 1.57$.

Figure 9 shows a comparison of model light curves with the actual L'-band data, with the upper panels representing the larger extinction value of $A = 0.04$ based on the standard deviation of the light-curve points and the lower panels showing results with the smaller extinction of $A = 0.02$ based on the fractional variability. The peak of the observed light curve has an apparent offset from the peak of the modelled light curves (at the periapse), which is most likely a systematic effect and not an intrinsic brightening.

3.3. Constraining the ambient density based on the non-thermal bow-shock emission

The thermal bow-shock emission in L'-band is clearly affected by the presence of dust along the S2 orbit. While on one hand the dust is clearly present in dusty objects whose orbits lie in the S cluster, the hot ambient medium likely destroys the dust particles continually. In cases where the presence of dust is diminished along the S2 orbit, the thermal emission of the bow shock in the L'-band is even smaller than we predicted in Sect. 3.2.

Another way to constrain the ambient density at the S2 pericentre is to take into consideration the broadband non-thermal synchrotron emission of the bow shock, which does not depend on the presence of dust. When the bow shock develops ahead of the star, it provides a volume where electrons can be accelerated by the enhanced magnetic field. Subsequently, they cool off by emitting synchrotron emission. Ginsburg et al. (2016) used the same mechanism to claim that the non-thermal emission of stellar bow shocks in the S cluster may be comparable to the radio and NIR emission of Sgr A*, and therefore could be detected.

One can reverse the task and instead constrain the upper limit of the ambient density based on the statistical variations we detect in the L'-band light curve of S2. According to Table 1, the maximum flux difference in our light curve is 0.90 mJy, while the rms fractional variability is at the level of 0.2 mJy. Therefore, the maximum contribution of the bow-shock synchrotron emission in L'-band can only be at this flux density level, which allows us to place an upper limit on the ambient density.

For the calculation of the bow-shock synchrotron light curve and broad-band spectrum, we follow the model of Sądowski et al. (2013), originally developed for the estimate of the bow-shock emission of the DSO/G2 object; see also Zajaček et al. (2016). As in Sądowski et al. (2013) and Zajaček et al. (2016), for calculating synchrotron light curves and spectra, we use the temperature profile of the ADAF, $T_{\mathrm{a}} = 9.5 \times 10^{10}(r/r_{\mathrm{s}})^{-1}$ (Yuan et al. 2003), with the ratio between the magnetic and the gas pressure of $\chi = P_{\mathrm{mag}}/P_{\mathrm{gas}} = 0.3$, and the Mach number of the star at the pericentre distance of S2, $\mathcal{M} = 2.6$. Other relevant parameters were adopted from particle-in-cell simulations performed by Sądowski et al. (2013); specifically, the slope of the high-energy power-law electron distribution, $p = 2.4$, the minimum Lorentz factor, $\zeta = 7.5$, and the fraction of accelerated electrons to high energies, $\eta = 0.05$. Specifically for S2, we used its mass-loss rate $\dot{m}_{\mathrm{w}} \simeq 3 \times 10^{-7}\,M_{\odot}\,\mathrm{yr}^{-1}$ and the terminal wind velocity $v_{\mathrm{w}} \sim 10^3\,\mathrm{km\,s}^{-1}$ inferred from spectroscopy (Martins et al. 2008; Habibi et al. 2017).

In contrast to Sądowski et al. (2013), we perform only the plowing synchrotron model, in which the accelerated electrons are kept in the shocked region and radiate in the shocked magnetic field. The plowing model is more likely to contribute in L'-band than the local model, in which accelerated electrons leave the shock and radiate in the unshocked magnetic field. Due to the short cooling time for the NIR L'-band synchrotron emission, $t_{\mathrm{cool}} \approx 0.25(B/0.08\,\mathrm{G})^{-3/2}(\nu_{\mathrm{c}}/8 \times 10^{13}\,\mathrm{Hz})^{-1/2}$ yr, the local model would have a negligible contribution.

In Fig. 10 (left panel), we plot the L'-band synchrotron light curve for the peak flux density of 0.91 mJy, which corresponds to the maximum flux difference, and the light curve with the peak flux density of 0.22 mJy, which corresponds to the fractional variability. The non-thermal bow-shock emission is also compared with the Sgr A* mean flux density in L'-band (Schödel et al. 2011), the S2 total flux, and the actual S2 measured flux density from 2018.307, which are all larger by at least a factor of a few than the bow-shock non-thermal emission. In the right panel of Fig. 10, we plot the SED of the S2 bow-shock synchrotron emission calculated for the pericentre for both L'-band flux density values (maximum difference and fractional variability). We also compare the synchrotron bow-shock SED with the SED of Sgr A* calculated using the advection-dominated accretion flow model (ADAF; Yuan et al. 2003; Yuan & Narayan 2014). Taking into account the maximum flux difference as an upper limit for the L'-band synchrotron contribution, we get the pericentre number density of $n_{\mathrm{a}} = 1.01 \times 10^5\,\mathrm{cm}^{-3}$ (the slope of 1.47). The fractional variability flux limit yields the number density of $1.88 \times 10^4\,\mathrm{cm}^{-3}$ (the density slope of 1.17). Both limiting cases are summarised in Table 2. For both density limits, the bow-shock synchrotron flux density would be comparable to that of Sgr A* at frequencies of a few GHz, where the peak of its SED occurs.

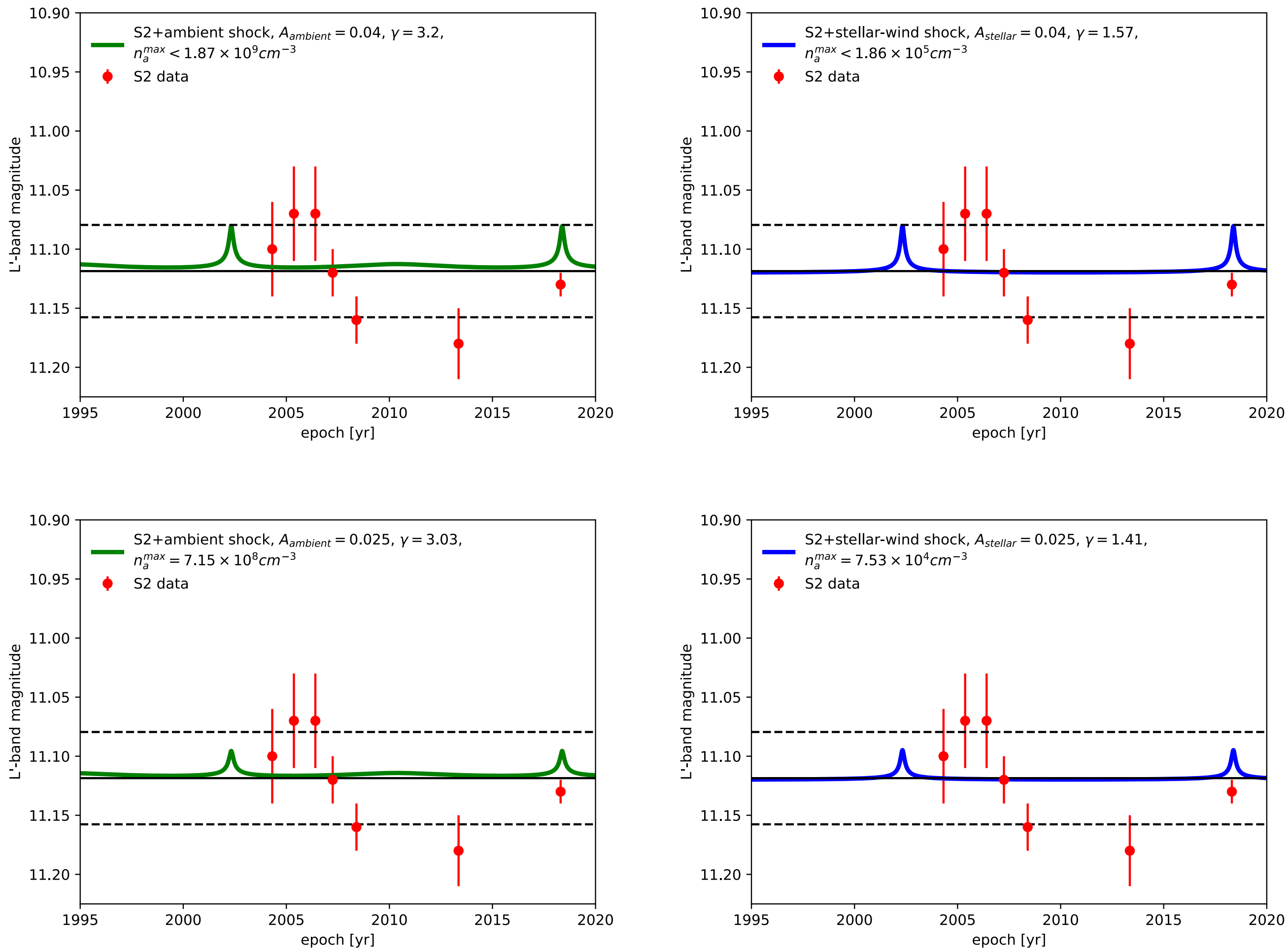

Fig. 9. Comparison of model light curves based on the mean S2 emission and the modelled thermal emission of its bow shock (solid green and blue lines) with the observed L'-band emission of S2 (red points with errorbars). *Upper panels*: modelled thermal emission of the bow shock is associated with the extinction of $A = 0.04$ mag, which was inferred from the standard deviation of observed light curve points. We model the thermal dust emission of the ambient bow shock (solid green line in *left panel*) and the thermal emission of the stellar-wind shock (solid blue line in *right panel*) separately. The horizontal solid black line represents the light curve mean value, while the dashed black lines stand for the standard deviation. *Lower panels*: as in the upper panels, but for the extinction of $A = 0.02$ mag based on the excess variance of the observed light-curve points.

To separate Sg A* and the predicted S2 bow-shock emission is challenging as it requires highly sensitive measurements at cm to decimetre (dm) wavelengths with an angular resolution of a tenth of an arcsecond or better. However, around the time of the periapse passage, long-term (weeks to a few months) light curves should reveal an overall increase of the spatially unresolved emission of both sources. Such a data set is not available at present. Very-long-baseline interferometry (VLBI) measurements at GHz frequencies (or cm wavelengths) could in principle be possible due to the high brightness temperature of the S2 bow-shock emission at its pericentre. We outline here a few basic estimates. For the assumed maximum non-thermal excess in L'-band of ~1 mJy, the calculated peak of the bow-shock synchrotron spectrum is at 4.61 GHz. The peak flux density is expected to be 0.86 Jy at the S2 pericentre, which is comparable to or even larger than the flux density of Sgr A* at cm wavelengths. The characteristic size of the bow shock given by the stagnation distance would be $R_0 \sim 5.6 \times 10^{13}$ cm at the pericentre, which gives the angular scale of ~0.5 mas, which is below the resolution capabilities of the cm VLBI, namely ~1 mas at best. The angular distance between the S2 radio source and Sgr A* at the pericentre is ~14.4 mas, which is smaller than the intrinsic size of Sgr A* at 6 cm (~20 mas), because of λ^2 scatter-broadening of the size of Sgr A* (Bower et al. 2006; Doeleman et al. 2008). The brightness temperature[2] of the S2 bow shock at its pericentre would be large, $T_B \sim 8.5 \times 10^{10}$ K, comparable to that of Sgr A*, $\gtrsim 2 \times 10^{10}$ K (Krichbaum et al. 1998; Doeleman et al. 2008). However, before and after the S2 pericentre, its brightness temperature is expected to drop rather fast, remaining above 10^6 K from the epoch 2017.08 up to 2020.54, with the peak at the pericentre in 2018.38. Taking into account the smaller contribution of S2 bow-shock non-thermal emission at L'-band at the level of ~0.2 mJy, which results from a smaller ambient density, mainly the characteristic size is affected; it increases to $R_0 = 1.29 \times 10^{14}$ cm, which corresponds to the angular scale of 1.1 mas, which is at the limit of the

[2] We estimate the brightness temperature using the standard relation derived from the Rayleigh-Jeans approximation in the radio domain, $T_B = \frac{c^2}{2k_B}\frac{F_\nu}{\Omega\nu^2}$, where the solid angle $\Omega \approx \pi R_0^2/d_{GC}^2$ with R_0 being the stagnation radius of the bow shock.

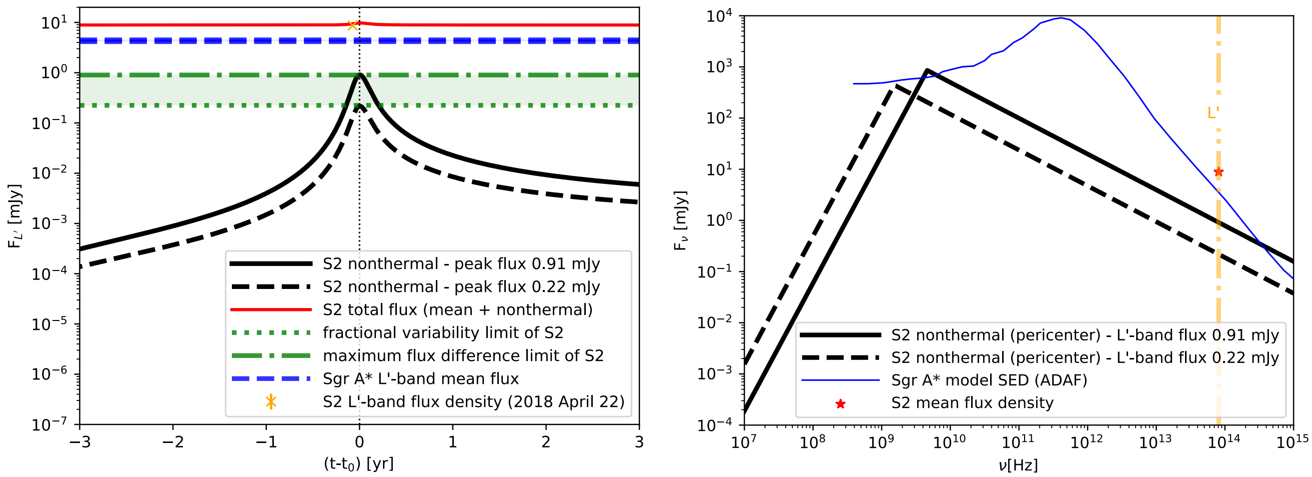

Fig. 10. Non-thermal contribution of the S2 bow shock to its L'-band emission. In the *left panel*, we plot the L'-band light curve as calculated for the S2 bow-shock synchrotron emission for the peak flux of 0.91 mJy (solid black line) and for the peak flux of 0.22 mJy (dashed black line). For comparison, we also show the fractional variability of S2 (dotted green line) and its maximum flux difference (dot-dashed line). The measured mean flux of Sgr A* in L'-band, 4.33 ± 0.18 mJy, is depicted by a dashed blue line. The sum of the mean flux density of S2 with the maximum potential contribution of the non-thermal bow-shock emission is represented by a solid red line. The measured flux density of S2 from 2018.307 is marked by an orange cross. In the *right panel*, we show the SED of S2 bow-shock synchrotron emission as calculated for the S2 pericentre for the L'-band flux of 0.91 mJy (solid line) and for the L'-band flux of 0.22 mJy (dashed line). The orange dot-dashed line marks the L'-band frequency range and the red star symbol represents the mean flux density of S2 in L'-band. The blue solid line represents the SED of Sgr A* based on the advection dominated accretion flows (ADAFs; Yuan et al. 2003; Yuan & Narayan 2014).

resolving power of the cm VLBI. However, as for a lower density the resulting spectrum of the S2 bow shock is shifted towards the lower frequency at 1.5 GHz (see Fig. 10), the bow-shock size is actually smaller than the typical VLBI beam FWHM of $\sim 3''$. With the peak flux of 435 mJy, the brightness temperature of $T_{\rm B} \sim 7 \times 10^{10}$ K is again comparable to that of Sgr A* and remains above 10^6 K in the time window between 2016.98 and 2020.90. In general, the cm VLBI observations could reveal a deviation from the Gaussian core of Sgr A* in the epochs of ~1.5 years before and after the pericentre when the brightness temperature is still above 10^6 K. At the pericentre, it is not possible to resolve the S2 bow-shock emission because of the scatter-broadening of Sgr A* and the bow-shock source. Only the flux excess could be detected; however, in that case a corresponding light curve at cm wavelengths would need to be analysed to distinguish the long-term bow-shock excess from the short-term stochastic radio flares.

Based on the upper limit inferred from the maximum synchrotron contribution to the L'-band emission of S2, accretion flows exceeding the particle density of $\sim 10^5\,{\rm cm^{-3}}$ at $\sim 1500\,r_{\rm s}$ are unlikely. On the other hand, the presence of the Bondi-type flow with $\gamma \sim 3/2$ cannot be excluded based on our L'-band light-curve analysis.

4. Discussion

Our observational analysis of the L'-band emission of the star S2 yields a light curve that is essentially flat within uncertainties and shows intrinsic flux variations due to the interaction of S2 with the ambient medium or due to intrinsic stellar variability at the level of ~2.5% only, as given by the fractional variability. Using the theory of a two-layer bow shock (Dyson 1975), we are therefore only able to place an upper limit on the ambient density at the S2 periapse as well as an upper limit on the density slope. The upper limit considering the contribution of the ambient bow shock, which is more likely to contain dust, is $n_{\rm a} \lesssim 1.87 \times 10^9\,{\rm cm^{-3}}$, and the upper limit for the slope is $\gamma \lesssim 3.20$. These values change only slightly when one considers the smaller extinction of ($A = 0.02$) as indicated by the excess variance, $n_{\rm a} \sim 7.15 \times 10^8\,{\rm cm^{-3}}$ and $\gamma = 3.03$. If the stellar-wind shock layer were found to contain dust, which would require the turbulence and the mixing of shocked layers, then the density and the slope constraints would decrease to $n_{\rm a} = 7.53{\times}10^4 - 1.86{\times}10^5\,{\rm cm^{-3}}$ and $\gamma = 1.41-1.57$. The non-thermal synchrotron emission of the bow-shock appears to put tighter constraints on the S2 pericentre density: $n_{\rm a} \lesssim 1.01 \times 10^5\,{\rm cm^{-3}}$ for the maximum flux difference and $n_{\rm a} \lesssim 1.88 \times 10^4\,{\rm cm^{-3}}$ for the fractional variability. For the slope, we obtain $\gamma \lesssim 1.47$ for the maximum flux difference and $\gamma \lesssim 1.17$ for the fractional variability.

Therefore, the L'-band data is consistent with the S2 star interacting with a hot, diluted ambient flow with a power-law density slope of $\gamma \sim 0.5$ (generally the advection-dominated flow (ADAF); Wang et al. 2013) and with a spherical Bondi-type solution with a density slope of $\gamma \sim 1.5$ (also consistent with the convection-dominated flow (CDAF); Różańska et al. 2015). Moreover, we cannot exclude the possibility that S2 interacts with an even denser and colder type of medium, such as the proposed cool disc with densities in the interval of $n_{\rm CD} \sim 10^5-10^6\,{\rm cm^{-3}}$ (Murchikova et al. 2019). Indeed, the uppermost limit for the density $n_{\rm a} < 1.87 \times 10^9\,{\rm cm^{-3}}$ is well in the range for the number density of broad-line region (BLR) clouds $n_{\rm BLR} \sim 10^8-10^{11}\,{\rm cm^{-3}}$ (Gaskell 2009). Although we do not expect the presence of BLR clouds in such a low-luminosity nucleus as Sgr A* (see, however, Bianchi et al., 2019 for the discovery of the compact BLR in the low-luminosity Seyfert galaxy NGC3147 with $L/L_{\rm Edd} \sim 10^{-4}$), we cannot exclude the presence of denser gaseous-dusty structures, with which stars can occasionally interact, such as dust-enshrouded objects monitored in the S-cluster (Peißker et al. 2020b; Ciurlo et al. 2020). This is also supported by the multiphase medium of Sgr A* on the scale of one parsec (Moser et al. 2017), which could also be present on smaller scales due to for example thermal instability (Różańska et al. 2017). In particular, Peißker et al. (2020a) report a detection of the proper motion of a Brγ filament, whose estimated distance is close to the Bondi radius at ~0.2 pc. At comparable scales, Royster et al. (2019) used the H30α line to trace a blueshifted, ionised gas with a velocity of between −480 and −300 km s^{-1}, which appears to be outflowing. Hence, the environment close to the Bondi radius is complex in terms of both kinematics and density.

Based on the flat L'-band light curve and the upper limits on the density, we can exclude the presence of a cold, thin accretion disc (Shakura & Sunyaev 1973), whose number densities close to the periapse of S2 at ~1500 r_s can be estimated using the relation for the number density as given by the standard accretion disc theory; see also Frank et al. (2002). Using the mean atomic weight of $\mu = 0.615$ for the fully ionised gas, we obtain

$$n_{\rm thin} = 2.7\times10^{12}\left(\frac{\alpha}{0.1}\right)^{-7/10}\left(\frac{\dot{m}}{10^{-8}\,M_\odot\,{\rm yr}^{-1}}\right)^{11/20} \times\left(\frac{M_\bullet}{4\times10^6\,M_\odot}\right)^{5/8}\left(\frac{R}{1500\,r_{\rm s}}\right)^{-15/8} f^{11/5}\,{\rm cm}^{-3}, \quad (4)$$

where the factor f stands for $f = [1-(r_s/R)^{1/2}]^{1/4}$. We calculate a number density range of $n_{\rm disc} = 7.6\times10^{11}$–$9.6\times10^{12}$ cm^{-3} for the accretion rate in the range $\dot{m} = 10^{-9}$–$10^{-7}\,M_\odot$ yr^{-1} and a viscous parameter of $\alpha = 0.1$ for the S2 pericentre distance. In Fig. 11, we plot the thin disc density profiles up to 100 r$_s$, since the density profile below this radius is relatively uncertain and the accretion flow likely breaks up due to the accumulation of poloidal magnetic flux, which results in a magnetically arrested disc (MAD; Narayan et al. 2003). This transition occurs where the magnetic energy density and the gravitational potential energy are at balance, $B^2/8\pi = GM_\bullet\rho_{\rm flow}/R_{\rm m}$, from which we can easily derive the magnetospheric radius,

$$R_{\rm m} \sim \frac{8\pi GM_\bullet\rho_{\rm flow}}{B^2} \quad (5)$$

$$= 90.5\left(\frac{M_\bullet}{4\times10^6\,M_\odot}\right)\left(\frac{n_{\rm flow}}{10^6\,{\rm cm}^{-3}}\right)\left(\frac{B_{\rm pol}}{10\,{\rm G}}\right)^{-2} r_{\rm s}, \quad (6)$$

where the poloidal magnetic field is scaled to 10 G and the number density of the flow to 10^6 cm^{-3} according to the synchrotron models of the Sgr A* flares (Yusef-Zadeh et al. 2006; Eckart et al. 2012). The putative MAD part of the flow is highlighted by the blue vertical line in Fig. 11.

The thin disc is expected to contain dust from the sublimation radius towards larger distances. If we associate the effective thin disc temperature, $T_{\rm eff} = [3GM_\bullet\dot{m}/(8\pi r^3\sigma_{\rm B})]^{1/4}$, with the dust sublimation temperature of $T_{\rm sub} = 1000$ K, we get a relation for the dust sublimation radius (see also Czerny & Hryniewicz 2011)

$$r_{\rm sub} = 163\left(\frac{M_\bullet}{4\times10^6\,M_\odot}\right)^{1/3}\left(\frac{\dot{m}}{10^{-7}\,M_\odot{\rm yr}^{-1}}\right)^{1/3}\left(\frac{T_{\rm sub}}{1000\,{\rm K}}\right)^{-4/3} r_{\rm s}. \quad (7)$$

We obtain the range of $r_{\rm sub} = 35$–$163\,r_s$ for the accretion rate range of $\dot{m} = 10^{-9}$–$10^{-7}\,M_\odot$ yr^{-1}. Hence, the dusty bow-shock layer should be formed when the S2 plunges through the disc midplane close to its periapse at ~1500 r_s. The formation of the shock in the disc material would lead to the extinction increase in L'-band magnitude by 0.65 mag for the density of 4.9×10^{11} cm^{-3} and by as much as 2.30 mag for the density of 6.13×10^{12} cm^{-3}. We can therefore exclude the possibility that the S2 star crosses a thin, dense, and cold disc.

Although the comparison with the thin disc density in Fig. 11 may seem purely academic for the Sgr A* environment, it is still instructive to compare our upper limits with the thin-disc density for two reasons. Firstly, although the presence of a thin disc was implicitly excluded already based on X-ray and mm observations (Yuan et al. 2003; Baganoff et al. 2003; Dexter et al. 2010), the upper density limit inferred from the stellar bow shock is independent of these previous measurements. Secondly, the transition between the hot advection-dominated accretion flows (ADAFs) and thin discs at such low accretion-rate values, such as those for Sgr A*, is still not well understood. For α discs, the viscously stable branch at low $\dot{m}$ exists in the stability curve of surface density–accretion rate or Σ-$\dot{m}$ plot and these discs would be both geometrically and optically thin; see e.g. Frank et al. (2002). Furthermore, they would primarily cool via the free-free emission instead of black-body radiation (Tylenda 1981) and one of the main reasons why such a disc is likely not present for Sgr A* is the short time for plasma to cool down via bremsstrahlung due to the low-angular momentum of the flow. On the other hand, they are low accretion-rate systems where the thin disc was detected, such as for example the maser source NGC4258 (Gammie et al. 1999) and NGC3147 (Bianchi et al. 2019). Most likely, the boundary conditions of the flow, that is, either feeding by stellar winds or the inflow of gas from larger scales, determine the transition between the ADAF and the thin disc at low $\dot{m}$ and vice versa. In addition, hybrid models of discs have been suggested, with an outer thin disc part and an inner hot ADAF part, with the transition at 10–100 gravitational radii (Gammie et al. 1999).

In order to better constrain the density and lower the upper density limit and the slope, the photometry precision needs to improve, with values below 0.01 mag. Also, a more precise theory for the bow shock formation and its corresponding NIR emission needs to be taken into account. However, the current methodology that we provide here can be directly transferred to the more precise photometry.

In terms of future instruments, the METIS at ELT will be particularly well suited for high-precision photometry in near- and mid-IR domains. All observing modes of METIS will initially work with a single conjugate adaptive optics (SCAO) system at or close to the diffraction limit of the 39m ELT. At a wavelength of 3.5 μm, the ELT will allow operation at an angular resolution of 23 milliarcseconds. Here, METIS will have a point source sensitivity (10-σ in 1 hour) of 21.2 mag (or about 1 μJy) (Brandl et al. 2018a,b). In the N band at a wavelength around 10 μm, the point-source sensitivity can be expected to be about 1.6 orders of magnitude lower. The field of view of about $10''\times10''$ in imaging and $1.0''\times0.5''$ in IFU (integral field unit) spectroscopy mode at L- and M-bands is ideally suited for the densely populated GC region. However, the limiting sensitivity for flux density measurements in this field will be determined by confusion due to source crowding. Hence, the effective sensitivity available to determine flux densities and to establish light curves can safely be assumed to be an order of magnitude lower than the nominal point-source sensitivity, but will still be about an order of magnitude better than the currently reached sensitivity. For specific estimates of the potentially probed density range, we consider the limiting flux density value for the bow-shock emission in the L'-band to be 0.01 mJy, which corresponds to an ~10^{-3} mag difference in the S2 star L'-band magnitude. Taking into account the model of thermal ambient-shock emission, which is the least sensitive in terms of the

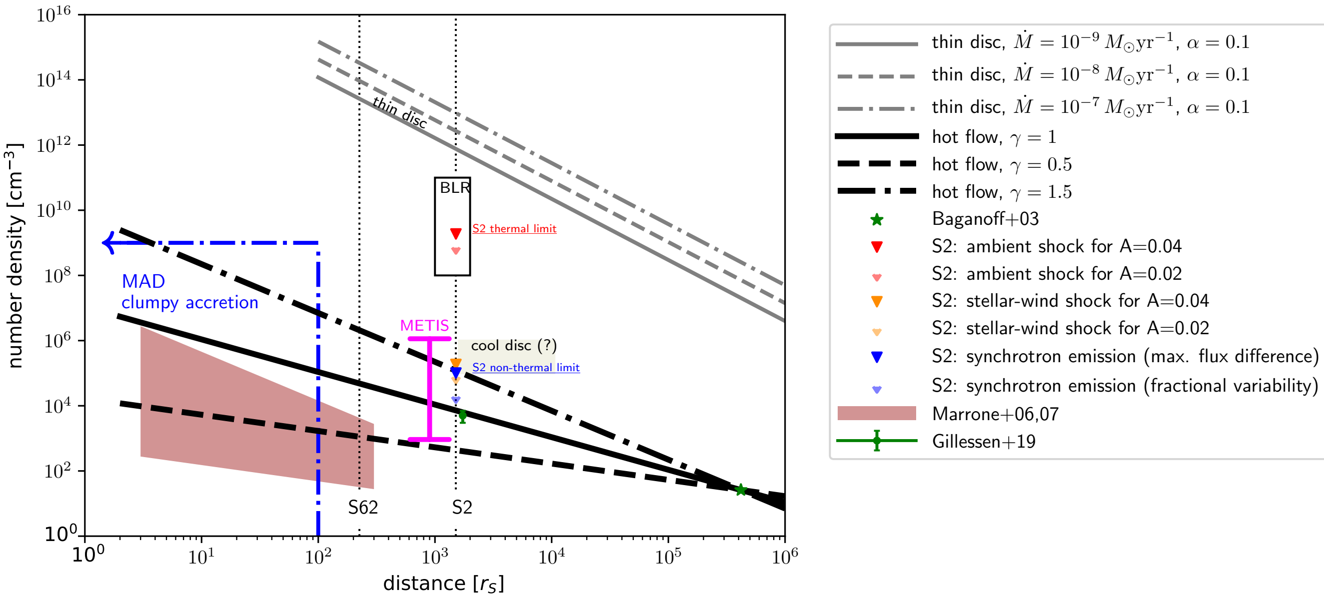

Fig. 11. Comparison of the upper density limits that are marked as downward arrows inferred from the L'-band light curve of the S2 star based on modelling ambient and stellar-wind shocks for the dust-extinction values of 0.04 and 0.02 mag with different density profiles and structures according to the plot legend and the description. Alongside the density limit based on the thermal bow-shock emission, we also depict the limit based on the non-thermal bow-shock emission (bluish downward arrows). For comparison, we show the density limit of 26 cm^{-3} inferred by Baganoff et al. (2003) based on the analysis of the X-ray thermal bremsstrahlung profile. Then we show the density constraint of $(5 \pm 3) \times 10^3$ cm^{-3} inferred from the potential hydrodynamic drag acting on the DSO/G2 object (Gillessen et al. 2019). The general density power-law profiles are depicted by black lines: the solid line stands for the slope of 1.0, the dashed line represents the flat profile of $\gamma = 0.5$, and the dot-dashed line depicts the steeper Bondi-like spherical flow with $\gamma = 1.5$. The shaded rectangle shows the distance and the density limits ($n \sim 10^5$–10^6 cm^{-3}) of the putative cool disc whose discovery is claimed by Murchikova et al. (2019). The black-framed rectangle depicts the typical densities of the broad-line region (BLR) clouds in the range of $n \sim 10^8$–10^{11} cm^{-3}. The gray lines depict the number density values expected for a thin disc (Shakura & Sunyaev 1973) for the accretion rate of $\dot{M} = 10^{-9}$–$10^{-7}\,M_\odot\,\mathrm{yr}^{-1}$ and the viscosity parameter of $\alpha = 0.1$. The brown-shaded area to the lower left shows the set of density profiles determined using the rotation measure of the submillimeter polarisation measurements (Marrone et al. 2006, 2007) for the inner radii of $r_{\mathrm{in}} = 300\,r_{\mathrm{s}}$ and $r_{\mathrm{in}} = 3\,r_{\mathrm{s}}$, density slopes of $\gamma = 0.5 - 1.5$, and the accretion rates in the range 2×10^{-9}–$2 \times 10^{-7}\,M_\odot\,\mathrm{yr}^{-1}$. The blue dot-dashed vertical at $100\,r_{\mathrm{s}}$ and the blue dot-dashed arrow to the left denote the region of a potential magnetically arrested flow (MAD), where the accretion flow changes from continuous to clumpy due to the accumulated poloidal magnetic flux (see e.g. Narayan et al. 2003; Tursunov et al. 2020). The dotted vertical lines mark the periapsis of the S62 star at $\sim 225\,r_{\mathrm{s}}$ and the periapsis of the S2 star at $\sim 1512\,r_{\mathrm{s}}$. Next to the S2 pericentre vertical line, we highlight the range of densities potentially being explored using L'-band METIS at ELT imaging mode.

density, we obtain a value of $\sim 1.5 \times 10^6$ cm^{-3}. This provides an improvement by three orders of magnitude in comparison to the current upper limit. The more sensitive non-thermal bow-shock emission model implies a lower ambient-density limit of only ~ 700 cm^{-3}, which is two orders of magnitude lower than current limits in Table 2. The density range probed by METIS is also shown specifically in the summary plot in Fig. 11. In particular, using the lower limit of 700 cm^{-3} inferred from the non-thermal model, METIS should be able to directly detect a non-thermal emission increase in case the hot-flow slope is larger than $\gamma = 0.5$ between the Bondi radius and the S2 pericentre distance. Further details will have to be determined through observations on the target.

The next-best target to observe both the potential thermal and non-thermal bow-shock emission at the periapse would be S62 in early 2023 which appears to be a suitable time to observe the closest S-star to the SMBH by the JWST. This will be an opportunity to shed further light on the density of the accretion flow around Sgr A* along the S62 orbital plane (Peißker et al. 2020c), in particular at its pericentre distance of $r_{\mathrm{P}}^{S62} \approx 225\,r_{\mathrm{s}} \sim 18$ AU, where the conditions of the accretion flow were only constrained via the rotation measure (Marrone et al. 2006, 2007); see Fig. 11. The detection of the bow-shock emission of S62 would provide an independent means of assessing the ambient number density on the scale of $\sim 100\,r_{\mathrm{s}}$. Furthermore, the S stars S2 and S62 as well as the dusty source DSO/G2 orbit Sgr A* at different inclinations. Therefore, detecting the bow-shock emission for each of them would enable us to constrain the density profile of the accretion flow around Sgr A* not only as a function of distance, but for a broader range of inclinations.

NIR bow-shock emission from the S stars, which is expected to be most prominent at the pericentre, could be detected via peculiar, longer K_{s} or L'-band flares. Moreover, the total bow-shock flare duration would be of the order of a few months up to one year and the peak flux is coincident with the pericentre of the star, see our model predictions in Fig. 9 for the thermal dust emission and in Fig. 10 for the non-thermal synchrotron emission associated with the bow shock. The start of the flux increase would be half a year before the pericentre. In terms of the shocked stellar wind, Giannios & Sironi (2013) and Christie et al. (2016) calculated the timescale of approximately one month for the X-ray bremsstrahlung flare produced by S2 bow-shock with the luminosity of 4×10^{33} erg s^{-1}. However, Schartmann et al. (2018) argued that for the expected accretion-flow density, the X-ray emission from the bow shock is beyond the detection limit. Ginsburg et al. (2016) calculated the non-thermal synchrotron emission, which for the typical parameters assumed for S2, the mass-loss rate of $\dot{m}_{\mathrm{w}} \sim 10^{-7}\,M_\odot\,\mathrm{yr}^{-1}$

and the terminal wind velocity of $v_w \sim 10^3\,\mathrm{km\,s^{-1}}$, is below the quiescent emission of Sgr A*. Therefore, the stochastic IR flares of Sgr A* (Witzel et al. 2012, 2018), including the very bright ones (Do et al. 2019b), are not associated with the stellar bow shocks in the S cluster as they evolve on a timescale of several hours only, which can be interpreted as an orbital timescale of plasmoids close to the innermost stable circular orbit (Gravity Collaboration 2018b). In other words, some short-term NIR flares could be associated with short-period stars orbiting Sgr A* on the scale of the innermost stable circular orbit (Leibowitz 2020), which could be disentangled from the stochastic background via their periodic or quasi-periodic signal. However, the bright IR flare analysed by Do et al. (2019b) could be associated with a change of accretion state due to the recent pericentre passage of S2 in 2018 or even the pericentre passage of DSO/G2 in 2014. The time delay between the pericentre and the average flare statistics may be interpreted via the viscous timescale of the hot accretion flow, which can be of the order of one to ten years (Czerny et al. 2013).

5. Conclusions

For the brightest star in the S cluster, S2, we obtained a light curve in the NIR L'-band, which is flat within the measurement uncertainties with the fractional flux variability of only 2.52% in terms of the L'-band flux density. When we associate the flux density standard deviation of 0.04 mag with the local dust extinction due to the bow shock, we can place an upper limit of $n_a < 1.87 \times 10^9\,\mathrm{cm^{-3}}$ on the ambient number density at $\sim$1500 r_s for the warm bow shock driven into the ambient medium, which is expected to contain dust. For the colder and the denser stellar-wind shock, the number density limit is $n_a < 1.86 \times 10^5\,\mathrm{cm^{-3}}$, which is nevertheless less firm because of the limited presence of dust in stellar winds of B-type stars. Considering the non-thermal bow-shock emission, which does not rely on the existence of dust, we can place an upper density limit of $1.01 \times 10^5\,\mathrm{cm^{-3}}$.

These limits cannot yet constrain the type of the hot accretion flow and therefore both the radiatively inefficient accretion flow with the density profile of $\gamma = 0.5$ and the spherical Bondi-type flow with $\gamma = 1.5$ can accommodate these number densities. However, we can firmly exclude the standard, thin accretion disc extending all the way to 1 500 r_s, the density of which would be at least two orders of magnitude greater and the star-disc interactions would produce a shock with a local extinction of 0.65−2.30 mag in L' band, which is much larger than the inferred 1σ excess of 0.04 mag of the L'-band light curve, and a difference of 0.11 mag between the maximum and the minimum magnitude.

In terms of future prospects, a major challenge is to detect and directly resolve bow shocks associated with the S-stars in NIR bands because of the high confusion and stellar density close to Sgr A*. It may become possible when high-resolution mid-IR imaging becomes available with the next generation of instruments, namely METIS at the ELT, because bow shocks are generally more prominent because of the dust emission in mid-IR bands. High-precision photometry associated with METIS with the flux sensitivity of the $\sim$0.01 mJy in L'-band is expected to improve the density constraints by two to three orders of magnitude in comparison with our current upper limits. For the non-thermal bow-shock emission, the direct detection of the flux excess is plausible in cases where the hot-flow density slope is larger than $\gamma \sim 0.5$ between the Bondi radius and the S2 pericentre distance.

Acknowledgements. The authors would like to thank the referee for his/her constructive suggestions and Persis Misquitta for the diligent proofreading of this paper. S. Elaheh Hosseini is a member of the International Max Planck Research School for Astronomy and Astrophysics at the Universities of Bonn and Cologne. We thank the Collaborative Research Centre 956, sub-project A02, funded by the Deutsche Forschungsgemeinschaft (DFG) – project ID 184018867. Michal Zajacek acknowledges the financial support from the National Science Centre, Poland, grant No. 2017/26/A/ST9/00756 (Maestro 9).

References

Agol, E. 2000, ApJ, 538, L121
Aitken, D. K., Greaves, J., Chrysostomou, A., et al. 2000, ApJ, 534, L173
Alexander, T. 2005, Phys. Rep., 419, 65
Baganoff, F. K., Maeda, Y., Morris, M., et al. 2003, ApJ, 591, 891
Bianchi, S., Antonucci, R., Capetti, A., et al. 2019, MNRAS, 488, L1
Boehle, A., Ghez, A. M., Schödel, R., et al. 2016, ApJ, 830, 17
Borkar, A., Eckart, A., Straubmeier, C., et al. 2016, MNRAS, 458, 2336
Bower, G. C., Wright, M. C. H., Falcke, H., & Backer, D. C. 2003, ApJ, 588, 331
Bower, G. C., Goss, W. M., Falcke, H., Backer, D. C., & Lithwick, Y. 2006, ApJ, 648, L127
Bower, G. C., Markoff, S., Dexter, J., et al. 2015, ApJ, 802, 69
Brandl, B. R., Absil, O., Agócs, T., et al. 2018a, in Proc. SPIE, SPIE Conf. Ser., 10702, 107021U
Brandl, B. R., Quanz, S., Snellen, I., et al. 2018b, in The Cosmic Wheel and the Legacy of the AKARI Archive: From Galaxies and Stars to Planets and Life, eds. T. Ootsubo, I. Yamamura, K. Murata, T. Onaka, et al., 41
Broderick, A. E., Fish, V. L., Doeleman, S. S., & Loeb, A. 2011, ApJ, 735, 110
Christie, I. M., Petropoulou, M., Mimica, P., & Giannios, D. 2016, MNRAS, 459, 2420
Ciurlo, A., Campbell, R. D., Morris, M. R., et al. 2020, Nature, 577, 337
Clénet, Y., Rouan, D., Gendron, E., et al. 2004, A&A, 417, L15
Crumley, P., & Kumar, P. 2013, MNRAS, 436, 1955
Czerny, B., & Hryniewicz, K. 2011, A&A, 525, L8
Czerny, B., Kunneriath, D., Karas, V., & Das, T. K. 2013, A&A, 555, A97
Dexter, J., Agol, E., Fragile, P. C., & McKinney, J. C. 2010, ApJ, 717, 1092
Do, T., Witzel, G., Gautam, A. K., et al. 2019a, ApJ, 882, L27
Do, T., Hees, A., Ghez, A., et al. 2019b, Science, 365, 664
Dodds-Eden, K., Porquet, D., Trap, G., et al. 2009, ApJ, 698, 676
Doeleman, S. S., Weintroub, J., Rogers, A. E. E., et al. 2008, Nature, 455, 78
Dyson, J. E. 1975, Ap&SS, 35, 299
Eckart, A., Schödel, R., García-Marín, M., et al. 2008, A&A, 492, 337
Eckart, A., García-Marín, M., Vogel, S. N., et al. 2012, A&A, 537, A52
Eckart, A., Mužić, K., Yazici, S., et al. 2013, A&A, 551, A18
Eckart, A., Hüttemann, A., Kiefer, C., et al. 2017, Found. Phys., 47, 553
Eisenhauer, F., Schödel, R., Genzel, R., et al. 2003, ApJ, 597, L121
Frank, J., King, A., & Raine, D. J. 2002, Accretion Power in Astrophysics: Third Edition (Cambridge, UK: Cambridge University Press)
Fritz, T. K., Gillessen, S., Dodds-Eden, K., et al. 2011, ApJ, 737, 73
Gammie, C. F., Narayan, R., & Blandford, R. 1999, ApJ, 516, 177
Gaskell, C. M. 2009, New Astron. Rev., 53, 140
Genzel, R., Schödel, R., Ott, T., et al. 2003, Nature, 425, 934
Genzel, R., Eisenhauer, F., & Gillessen, S. 2010, Rev. Mod. Phys., 82, 3121
Ghez, A. M., Hornstein, S. D., Lu, J. R., et al. 2005, ApJ, 635, 1087
Ghez, A. M., Salim, S., Weinberg, N. N., et al. 2008, ApJ, 689, 1044
Giannios, D., & Sironi, L. 2013, MNRAS, 433, L25
Gillessen, S., Eisenhauer, F., Trippe, S., et al. 2009, ApJ, 692, 1075
Gillessen, S., Genzel, R., Fritz, T. K., et al. 2012, Nature, 481, 51
Gillessen, S., Plewa, P. M., Eisenhauer, F., et al. 2017, ApJ, 837, 30
Gillessen, S., Plewa, P. M., Widmann, F., et al. 2019, ApJ, 871, 126
Ginsburg, I., Wang, X., Loeb, A., & Cohen, O. 2016, MNRAS, 455, L21
Gorenstein, P. 1975, ApJ, 198, 95
Gravity Collaboration (Abuter, R., et al.) 2018a, A&A, 615, L15
Gravity Collaboration (Abuter, R., et al.) 2018b, A&A, 618, L10
Gravity Collaboration (Abuter, R., et al.) 2019, A&A, 625, L10
Gravity Collaboration (Abuter, R., et al.) 2020, A&A, 636, L5
Habibi, M., Gillessen, S., Martins, F., et al. 2017, ApJ, 847, 120
Krichbaum, T. P., Graham, D. A., Witzel, A., et al. 1998, A&A, 335, L106
Leibowitz, E. 2020, ApJ, 896, 74
Marrone, D. P., Moran, J. M., Zhao, J.-H., & Rao, R. 2006, ApJ, 640, 308
Marrone, D. P., Moran, J. M., Zhao, J.-H., & Rao, R. 2007, ApJ, 654, L57
Martins, F., Gillessen, S., Eisenhauer, F., et al. 2008, ApJ, 672, L119
Menten, K. M., Reid, M. J., Eckart, A., & Genzel, R. 1997, ApJ, 475, L111
Merritt, D. 2013, Dynamics and Evolution of Galactic Nuclei (Princeton: Princeton University Press)
Moser, L., Sánchez-Monge, Á., Eckart, A., et al. 2017, A&A, 603, A68

Murchikova, E. M., Phinney, E. S., Pancoast, A., & Blandford, R. D. 2019, Nature, 570, 83
Nandra, K., George, I. M., Mushotzky, R. F., Turner, T. J., & Yaqoob, T. 1997, ApJ, 476, 70
Narayan, R., Mahadevan, R., Grindlay, J. E., Popham, R. G., & Gammie, C. 1998, ApJ, 492, 554
Narayan, R., Igumenshchev, I. V., & Abramowicz, M. A. 2003, PASJ, 55, L69
Narayan, R., Özel, F., & Sironi, L. 2012, ApJ, 757, L20
Nayakshin, S. 2005, A&A, 429, L33
Parsa, M., Eckart, A., Shahzamanian, B., et al. 2017, ApJ, 845, 22
Peißker, F., Eckart, A., Sabha, N. B., Zajaček, M., & Bhat, H. 2020a, ApJ, 897, 28
Peißker, F., Hosseini, S. E., Zajacek, M., et al. 2020b, A&A, 634, A35
Peißker, F., Eckart, A., & Parsa, M. 2020c, ApJ, 889, 61
Predehl, P., & Schmitt, J. H. M. M. 1995, A&A, 500, 459
Psaltis, D. 2012, ApJ, 759, 130
Quataert, E., & Loeb, A. 2005, ApJ, 635, L45
Reid, M. J., Menten, K. M., Genzel, R., et al. 2003, ApJ, 587, 208
Reina, C., & Tarenghi, M. 1973, A&A, 26, 257
Royster, M. J., Yusef-Zadeh, F., Wardle, M., et al. 2019, ApJ, 872, 2
Różańska, A., Mróz, P., Mościbrodzka, M., Sobolewska, M., & Adhikari, T. P. 2015, A&A, 581, A64
Różańska, A., Kunneriath, D., Czerny, B., Adhikari, T. P., & Karas, V. 2017, MNRAS, 464, 2090
Sabha, N., Eckart, A., Merritt, D., et al. 2012, A&A, 545, A70
Sądowski, A., Sironi, L., Abarca, D., et al. 2013, MNRAS, 432, 478
Schartmann, M., Burkert, A., & Ballone, A. 2018, A&A, 616, L8
Schödel, R., Ott, T., Genzel, R., et al. 2002, Nature, 419, 694
Schödel, R., Najarro, F., Muzic, K., & Eckart, A. 2010, A&A, 511, A18
Schödel, R., Morris, M. R., Muzic, K., et al. 2011, A&A, 532, A83
Schödel, R., Feldmeier, A., Neumayer, N., Meyer, L., & Yelda, S. 2014, Class. Quant. Grav., 31, 244007
Scoville, N., & Burkert, A. 2013, ApJ, 768, 108
Shakura, N. I., & Sunyaev, R. A. 1973, A&A, 500, 33
Tursunov, A., Zajaček, M., Eckart, A., et al. 2020, ApJ, 897, 99
Tylenda, R. 1981, Acta Astron., 31, 127
Valencia-S, M., Eckart, A., Zajaček, M., et al. 2015, ApJ, 800, 125
van Marle, A. J., Meliani, Z., Keppens, R., & Decin, L. 2011, ApJ, 734, L26
Wang, Q. D., Nowak, M. A., Markoff, S. B., et al. 2013, Science, 341, 981
Wilkin, F. P. 1996, ApJ, 459, L31
Wilkin, F. P., Canto, J., & Raga, A. C. 1997, in Herbig-Haro Flows and the Birth of Stars, eds. B. Reipurth, & C. Bertout, IAU Symp., 182, 343
Witzel, G., Eckart, A., Bremer, M., et al. 2012, ApJS, 203, 18
Witzel, G., Ghez, A. M., Morris, M. R., et al. 2014, ApJ, 796, L8
Witzel, G., Sitarski, B. N., Ghez, A. M., et al. 2017, ApJ, 847, 80
Witzel, G., Martinez, G., Hora, J., et al. 2018, ApJ, 863, 15
Xu, Y.-D., Narayan, R., Quataert, E., Yuan, F., & Baganoff, F. K. 2006, ApJ, 640, 319
Yuan, F., & Narayan, R. 2014, ARA&A, 52, 529
Yuan, F., Quataert, E., & Narayan, R. 2003, ApJ, 598, 301
Yusef-Zadeh, F., Roberts, D., Wardle, M., Heinke, C. O., & Bower, G. C. 2006, ApJ, 650, 189
Zajaček, M., Eckart, A., Karas, V., et al. 2016, MNRAS, 455, 1257
Zhang, Q., & Zheng, X. 1997, ApJ, 474, 719

Appendix A: Flux table

Table A.1. Dereddened fluxes of S2 and S65 in L'-band in 2018.307.

UT time	S2 (mJy)	S65 (mJy)
05:57:34.4735	9.84 ± 0.11	14.48 ± 0.25
05:59:43.8697	9.00 ± 0.02	12.38 ± 0.06
06:00:25.8029	10.03 ± 0.27	15.61 ± 0.62
06:02:34.9990	1.63 ± 0.05	2.94 ± 0.23
06:03:17.5402	8.15 ± 0.01	12.43 ± 0.05
06:05:26.7352	8.68 ± 0.04	13.34 ± 0.17
06:06:08.8654	9.15 ± 0.13	13.81 ± 0.35
06:08:16.4643	10.21 ± 0.38	15.21 ± 0.83
06:09:01.9952	9.64 ± 0.26	14.70 ± 0.63
06:11:10.5931	8.72 ± 0.10	13.86 ± 0.36
06:45:59.1812	10.07 ± 0.13	13.38 ± 0.26
06:48:07.7927	9.90 ± 0.10	14.93 ± 0.24
06:48:49.5321	12.52 ± 0.63	15.67 ± 0.92
06:53:54.6491	10.21 ± 0.04	14.05 ± 0.08
06:56:44.5710	10.41 ± 0.18	14.11 ± 0.36
06:57:29.3005	8.13 ± 0.03	12.32 ± 0.20
06:59:38.1146	8.63 ± 0.03	13.97 ± 0.13
07:34:08.2162	8.03 ± 0.05	13.4 ± 0.26
07:37:02.3746	8.14 ± 0.03	12.95 ± 0.17
07:39:11.7988	8.26 ± 0.02	12.55 ± 0.14
07:39:54.9392	8.75 ± 0.06	12.57 ± 0.22
07:42:48.1058	7.82 ± 0.17	12.75 ± 0.87
07:44:58.3101	8.76 ± 0.06	14.46 ± 0.21
07:47:53.4375	8.27 ± 0.17	14.10 ± 0.69
08:26:49.3672	7.40 ± 0.03	12.60 ± 0.32
08:28:59.1627	7.93 ± 0.03	12.82 ± 0.02
08:29:42.3116	9.18 ± 0.06	14.00 ± 0.24
08:31:51.9218	8.37 ± 0.02	12.53 ± 0.11
08:32:36.0531	8.61 ± 0.08	12.88 ± 0.29
08:34:47.4474	10.03 ± 0.13	13.62 ± 0.26
08:35:30.1790	8.73 ± 0.11	14.57 ± 0.42
08:38:23.3029	8.79 ± 0.25	15.14 ± 0.88
08:40:33.6955	7.45 ± 0.03	13.72 ± 0.03
09:16:05.5965	8.28 ± 0.03	13.75 ± 0.13
09:18:58.3609	7.72 ± 0.02	14.01 ± 0.18
09:21:09.3821	7.09 ± 0.03	13.30 ± 0.34
09:21:52.5156	7.66 ± 0.02	13.09 ± 0.24
09:24:03.3459	7.49 ± 0.02	12.31 ± 0.23
09:24:46.0790	9.80 ± 0.25	16.09 ± 0.66
09:26:55.2871	8.83 ± 0.05	13.62 ± 0.17
09:27:38.2308	8.46 ± 0.10	13.89 ± 0.49
09:29:47.4548	8.89 ± 0.07	14.16 ± 0.22
10:05:26.0274	8.25 ± 0.02	14.11 ± 0.08
10:07:35.2335	8.32 ± 0.10	16.33 ± 0.41
10:08:18.1657	8.71 ± 0.10	13.24 ± 0.46
10:10:30.5604	9.35 ± 0.18	14.43 ± 0.49
10:11:11.8925	9.24 ± 0.03	15.21 ± 0.12
10:13:20.2894	8.34 ± 0.03	12.99 ± 0.19
10:14:03.2225	8.48 ± 0.02	13.07 ± 0.12
10:16:13.2227	8.44 ± 0.09	12.47 ± 0.47
10:19:10.3576	10.80 ± 0.47	16.81 ± 1.12

As described in Sect. 2.2, we performed photometry for the single exposures of the observation 0101.B-0052(B) in 2018.307. As shown in Fig. 4 there is no significant change in flux at the position of S2 and the IR counterpart of Sgr A*, suggesting that Sgr A* is in its quiescent period in L'-band during the observation epoch of 2018.307.

Appendix B: The S2 star bow-shock evolution along the orbit: formula for the density slope

The size of a bow shock formed due to the supersonic motion of the star close the supermassive black hole is scaled by the stand-off distance R_0, which depends on two stellar parameters, the mass-loss rate $\dot{m}_w$ and the terminal wind velocity v_w, as well as on the density of the ambient medium ρ_a and the relative velocity of the star with respect to the surrounding medium v_{rel}. In the most general form, it can be expressed in the following way (Wilkin 1996; Zhang & Zheng 1997; Christie et al. 2016),

$$R_0 = \left(\frac{\dot{m}_w v_w}{\Omega(1+\alpha)\rho_a v_{rel}^2}\right)^{1/2} \simeq C_\star v_{rel}^{-1} \rho_a^{-1/2}, \tag{B.1}$$

where Ω stands for the solid angle into which the stellar wind is blown (in case it is fully isotropic $\Omega = 4\pi$). The coefficient α is the ratio of thermal and the ram pressure of the ambient medium, $\alpha = P_{th}/P_{ram}$. The supersonic motion takes place when the Mach number is larger than one, $M = v_{rel}/c_s = 1/\sqrt{\kappa\alpha} > 1$, where c_s is the sound speed and κ is an adiabatic index. The last equality in Eq. (B.1) is valid for the supersonic limit when $\alpha \to 0$, that is, when the thermal pressure is low. The term $C_\star = (\dot{m}_w v_w/\Omega)^{1/2}$ then represents a stellar parameter that we assume to be constant during one orbital period, which for S-stars with a semi-major axis a is typically (in years),

$$\tau_{orb} = 11.85 \left(\frac{a}{0.1''}\right)^{3/2} \left(\frac{M_\bullet}{4\times10^6\,M_\odot}\right)^{-1/2} \text{yr}. \tag{B.2}$$

The stellar parameter $C_\star$ may be evaluated for the mass-loss rate $\dot{m}_w$ and the terminal wind velocity v_w as inferred for S2 based on spectroscopic information (Martins et al. 2008),

$$C_\star = 7.1\times10^{12}\left(\frac{\dot{m}_w}{10^{-7}\,M_\odot\,\text{yr}^{-1}}\right)^{1/2}\left(\frac{v_w}{10^3\,\text{km}\,\text{s}^{-1}}\right)^{1/2} \text{g}^{1/2}\,\text{cm}^{1/2}\,\text{s}^{-1}. \tag{B.3}$$

Now we consider the relation between the scale lengths of the bow shock R_0 at two different positions. We assume that the number density profile near the GC as a function of distance r from the black hole has a power-law form:

$$n_a = n_0 \left(\frac{r}{r_0}\right)^{-\gamma}, \tag{B.4}$$

where the power-law index γ is positive, $\gamma \geq 0$. It follows directly from Eq. (B.1) that the ratio of the standoff radii between two positions of the bow shock along the orbit is as follows,

$$\frac{R_{01}}{R_{02}} = \frac{v_{rel2}}{v_{rel1}}\left(\frac{\rho_{a2}}{\rho_{a1}}\right)^{1/2} = \frac{v_{rel2}}{v_{rel1}}\left(\frac{n_{a2}}{n_{a1}}\right)^{1/2} = \frac{v_{rel2}}{v_{rel1}}\left(\frac{r_1}{r_2}\right)^{\gamma/2}, \tag{B.5}$$

where the subscripts 1 and 2 stand for two positions along the elliptical orbit characterised by velocities v_{rel1} and v_{rel2} and distances from the focus (SMBH) r_1 and r_2 ($r_1 > r_2$), respectively. The last equality in Eq. (B.5) is derived using a general expression for the power-law density profile, Eq. (B.4). Unless otherwise indicated in the text, we consider the ambient medium to be stationary with respect to the star, and therefore the relative velocity is approximately given by the orbital velocity of the star around the GC, $v_{\rm rel} \simeq v_\star$. By taking this into consideration, we obtain a slightly modified relation for the ratio,

$$\frac{R_{01}}{R_{02}} = \frac{v_{\star 2}}{v_{\star 1}}\left(\frac{n_{a2}}{n_{a1}}\right)^{1/2} = \left(\frac{r_1}{r_2}\right)^{(\gamma+1)/2}\left(\frac{2a-r_2}{2a-r_1}\right)^{1/2}. \tag{B.6}$$

The last equality is obtained using the expression for the orbital velocity of a star on an elliptic orbit, or the opposite equation, $v_\star = \sqrt{\mu(2/r - 1/a)}$, where $\mu = GM_\bullet$. In cases where the orbital elements for a given S star are constrained, one can invert Eq. (B.6) to get the power-law index γ as function of the bow-shock standoff ratio at two positions $R_{01}(r_1)/R_{02}(r_2)$, orbital distances r_1 and r_2, and the semi-major axis a,

$$\gamma_{12} = \frac{2\log\left[R_{01}(r_1)/R_{02}(r_2)\right] + \log\left[(2a-r_1)/(2a-r_2)\right]}{\log(r_1/r_2)} - 1. \tag{B.7}$$

The number of parameters in relation B.7 may be reduced when evaluated at special points on the orbit, especially the pericentre (true anomaly $\nu = 0°$), the apocentre ($\nu = 180°$), and the semi-latus rectum ($\nu = 90°$). From classical celestial mechanics, we easily obtain the ratios for corresponding distances and velocities at the apocentre and the pericentre for a general elliptical orbit with an eccentricity e. The ratio of the distances from the supermassive black hole is $(r_{\rm P}/r_{\rm A}) = (1-e)/(1+e)$[3] and the ratio of velocities is $(v_{\rm orbP}/v_{\rm orbA}) = (1+e)/(1-e)$. Thus, the ratio between the apocentre and the pericentre bow-shock size is simply a function of two parameters: the orbital eccentricity e and the power-law index for the ambient density distribution γ,

$$\frac{R_{0A}}{R_{0P}} = \left(\frac{1+e}{1-e}\right)^{1+\gamma/2}. \tag{B.8}$$

In the same way as in Eq. (B.7), one can express the power-law index in the following way,

$$\gamma_{AP} = 2\left[\log(R_{0A}/R_{0P})/\log\left[(1+e)/(1-e)\right] - 1\right]. \tag{B.9}$$

A similar simple expression is obtained when evaluating the ratio between the points at the latus-rectum intersection with the ellipse and the pericentre. We denote the standoff distance at that point $R_{0,90}$ (the true anomaly is 90 degrees). The following relation then holds:

$$\frac{R_{0,90}}{R_{0P}} = \frac{(1+e)^{(\gamma+2)/2}}{(1+e^2)^{1/2}}, \tag{B.10}$$

from which the density power-law index trivially follows (or from Eq. (B.7)),

$$\gamma_{LP} = \frac{2\log\left[R_{0,90}/R_{0P}\right] + \log(1+e^2)}{\log(1+e)} - 2. \tag{B.11}$$

As the star passes through the medium with a variable density $n_{\rm a}$, the bow-shock emission is also expected to change. An upper limit for the thermal bow-shock emission is given by the rate of thermalised kinetic terms of the stellar and ambient winds, $L_{\rm th} = 1/2\dot{m}_{\rm w}(v_{\rm rel}^2 + v_{\rm w}^2) \simeq 1/2\dot{m}_{\rm w}(v_\star^2 + v_{\rm w}^2)$ (Wilkin et al. 1997). The ratio of thermal bow-shock luminosities between two points is then given by,

$$L_{\rm th1}/L_{\rm th2} = (\beta_1^2 + 1)/(\beta_2^2 + 1), \tag{B.12}$$

[3] We use the indices P, A, and 90° to denote the quantities evaluated at the pericentre, apocentre, and the semi-latus rectum, respectively.

Table B.1. Power-law index γ and the corresponding ratio between the apocentre and the pericentre bow-shock sizes and the thermal emission luminosities calculated for different eccentricities.

e	γ	$(R_{0A}/R_{0P})_0$ (Eq. (B.8))	$L_{\rm thA}/L_{\rm thP}$ (S2)
0	≥ 0	1	1
0.5	0.0	3.0	0.19
0.5	0.5	3.9	0.19
0.5	1.0	5.2	0.19
0.5	2.0	9.0	0.19
0.9	0.0	19.0	1.8×10^{-2}
0.9	0.5	39.7	1.8×10^{-2}
0.9	1.0	82.8	1.8×10^{-2}
0.9	2.0	361.0	1.8×10^{-2}

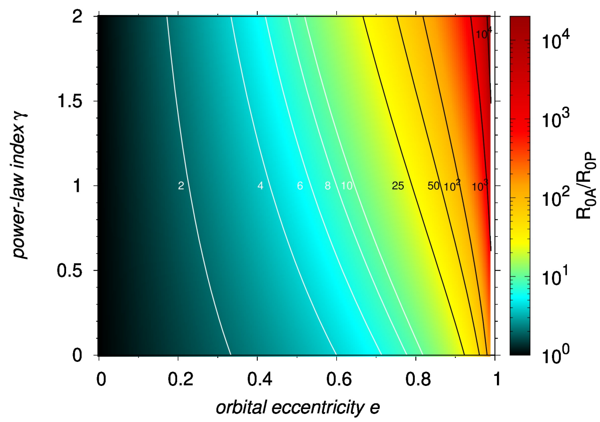

Fig. B.1. Colour-coded ratio R_{0A}/R_{0P} of stellar bow-shock sizes between the apocentre and the pericentre of the corresponding orbit in the $e-\gamma$ plane (see also Eq. (B.8)). The white and black lines correspond to the contours of the constant ratio with numbers indicating the value of R_{0A}/R_{0P} for a given contour.

where $\beta = v_\star/v_{\rm w}$. Table B.1 summarises different exemplary values of the index γ and the corresponding values of the ratio of bow-shock sizes between the apocentre and the pericentre – Eq. (B.8) – as well as the ratio of luminosities of thermal emission, Eq. (B.12), for different eccentricities. As a standard prototype of S stars, we take S2 with inferred $a \simeq 0.123''$, $e \simeq 0.88$, and $v_{\rm w} = 1000\,{\rm km\,s^{-1}}$ (Martins et al. 2008; Habibi et al. 2017; Gravity Collaboration 2018a).

In Fig. B.1, we plot the colour-coded ratio R_{0A}/R_{0P} in the e-γ plane (eccentricity–power-law index). We see that in general the ratio R_{0A}/R_{0P} has a broad range between 1 and 10^4 for plausible values of the density power-law slope, $\gamma \in (0, 2)$, and the orbital eccentricity, $e \in (0, 0.99)$. For the mean eccentricity of $e = 2/3$ in the thermal (isotropic) distribution of eccentricities, $n(e){\rm d}e = 2e{\rm d}e$, and the flat density profile of $\gamma = 0.5 - 1.0$ (Wang et al. 2013), the ratio R_{0A}/R_{0P} is between 7.5 and 11.2 according to Eq. (B.8). *Effect of thermal pressure.* In the analysis above, we considered the thermal pressure of the ambient medium to be negligible with respect to the ram pressure, that is, $\alpha = P_{\rm th}/P_{\rm ram} \rightarrow 0$. Yet, at different distances from the SMBH, the factor $\alpha(r) = P_{\rm th}/P_{\rm ram} = c_{\rm s}(r)^2/v_\star(r)^2$ may in principle change and become non-negligible. The ratio of standoff radii between the apocentre and the pericentre of the orbit then becomes

$$\frac{R_{0A}}{R_{0P}} = \left(\frac{R_{0A}}{R_{0P}}\right)_0 \left(\frac{1+\alpha_{\rm P}}{1+\alpha_{\rm A}}\right)^{1/2}, \tag{B.13}$$

where $(R_{0A}/R_{0P})_0$ is the ratio with a neglected thermal pressure, Eq. (B.8). The thermal term at the pericentre may be evaluated as follows,

$$\alpha_{\rm P} = c_{\rm s}(r_{\rm P})^2/v_\star(r_{\rm P})^2 = \frac{\kappa k_{\rm B} T_{\rm P}}{\overline{\mu} m_{\rm p}} \frac{a}{\mu} \frac{1-e}{1+e}\,, \tag{B.14}$$

where $T_{\rm P}$ is the gas temperature at the pericentre, $\overline{\mu}$ is the mean molecular weight, and $m_{\rm p}$ is a proton mass. The ratio of the thermal terms at the apocentre and the pericentre is then

$$\frac{\alpha_{\rm A}}{\alpha_{\rm P}} = \frac{T_{\rm A}}{T_{\rm P}}\left(\frac{1+e}{1-e}\right)^2 = \left(\frac{r_{\rm P}}{r_{\rm A}}\right)^\delta \left(\frac{1+e}{1-e}\right)^2 = \left(\frac{1+e}{1-e}\right)^{2-\delta}, \tag{B.15}$$

where $\delta \geq 0$ is a power-law index of the spherical temperature profile of the ambient medium, $T_{\rm a}(r) = T_0(r_0/r)^\delta$, where $T_0 = T_{\rm a}(r_0)$. The extra term in Eq. (B.13) would vanish if $\alpha_P = \alpha_A$, which would occur if $e = 0$. Using Eq. (B.15) we may rewrite Eq. (B.13) in the following form,

$$\frac{R_{0A}}{R_{0P}} = \left(\frac{R_{0A}}{R_{0P}}\right)_0 \underbrace{\left[\frac{1+\alpha_{\rm P}(T_{\rm P},a,e)}{1+\alpha_{\rm P}(T_{\rm P},a,e)\left(\frac{1+e}{1-e}\right)^{2-\delta}}\right]^{1/2}}_{F_{AP}(T_{\rm P},a,e,\delta)}. \tag{B.16}$$

For the estimation of the factor F_{AP} in brackets, which arises because of thermal pressure, we consider the orbital elements of S2 and the following temperature profile of the ambient medium (Psaltis 2012; Broderick et al. 2011),

$$T_{\rm P} = T_0\left(\frac{GM_\bullet}{rc^2}\right)^\delta, \tag{B.17}$$

where $\delta = 0.84$ and $T_0 = 9.5\times10^{10}$ K. After calculation, the correction term is $\simeq 0.8$ for S2 star, and so every ratio in Table B.1 should be slightly adjusted, $R_{0A}/R_{0P} \simeq 0.8(R_{0A}/R_{0P})_0$, if the temperature profile, Eq. (B.17), holds. Including the thermal pressure term, the formula for the density power-law index γ based on the ratio of the apocentre and the pericentre standoff radii changes accordingly,

$$\gamma'_{AP} = 2[(\log(R_{0A}/R_{0P}) - \log F_{AP})/\log[(1+e)/(1-e)] - 1]. \tag{B.18}$$

Similarly, using the semi-latus rectum–pericentre ratio $R_{0,90}/R_{0P}$, one can derive the slope γ'_{LP} modified by the thermal therm F_{LP} in the following way,

$$\gamma'_{LP} = \frac{2[\log(R_{0,90}/R_{0P}) - \log F_{LP}] + \log(1+e^2)}{\log(1+e)} - 2, \tag{B.19}$$

where the thermal term is expressed by

$$F_{LP}(T_{\rm p},a,e) = \left[\frac{1+\alpha_{\rm P}(T_{\rm P},a,e)}{1+\alpha_{\rm P}(T_{\rm P},a,e)\frac{(1+e)^{2-\delta}}{(1-e)^2}}\right]^{1/2}. \tag{B.20}$$

CHAPTER 6

Discovery of a dense association of stars in the vicinity of the supermassive black hole Sgr A*

The young stellar population around Sgr A* has been puzzling for scientists over the last decades and has been introduced as "Paradox of Youth" (Ghez et al. 2003). Up to now we know of three stellar populations around Sgr A*, the IRS16 complex, the S-star cluster and IRS13.

In this paper we discover another dense association of stars located at a distance of $\sim 6''$ corresponding to $\sim$0.25 pc north-east of Sgr A*. I investigated this sample of in total 42 stars within a radius of $1.35''$ around the bow shock source IRS 1W. I analyse the proper motions of these source in K_s band and determine their brightness in H and L' bands. I identified a sub-sample of stars which have similar proper motion directions towards the north-west. The dispersion velocity of this subsample motivates me to consider them as an association of stars. I name them N-sources due to their northward flying direction. This association of stars can be a bound system due to a putative intermediate mass black hole (IMBH) with a mass of about $10^3 M\odot$. However, I discuss another plausible scenario that this is a projection of a disk-like distribution of young He-stars and/or dust-enshrouded stars. However, in the Chanda image from 0.5 to 8 keV, there is no significant X-ray emission at the position of N-sources, which weakens the IMBH scenario. In contrast, the location of IRS13E and N-sources on the west and east side of Sgr A*, respectively, strengthens the disk-like distribution scenario.

The results of this publication are submitted to ApJ and I am currently incorporating the reviewers comments. I did the entire data reduction and analysis and wrote the entire publication by myself. The remaining authors contributed with comments during the writing process. Credit: Hosseini et al., submitted to ApJ.

Draft version February 6, 2023
Typeset using LaTeX **twocolumn** style in AASTeX631

Discovery of a dense association of stars in the vicinity of the supermassive black hole Sgr A*

S. Elaheh Hosseini [1,2] Andreas Eckart [1,2] Michal Zajaček [3,1] Silke Britzen [2] Harshitha K. Bhat [1,2,1] and Vladimír Karas [4]

[1] I.Physikalisches Institut der Universität zu Köln, Zülpicher Str. 77, D-50937 Köln, Germany
[2] Max-Planck-Institut für Radioastronomie (MPIfR), Auf dem Hügel 69, D-53121 Bonn, Germany
[3] Department of Theoretical Physics and Astrophysics, Faculty of Science, Masaryk University, Kotlářská 2, 611 37 Brno, Czech Republic
[4] Astronomical Institute of the Czech Academy of Sciences, Boční II 1401, CZ-141 00 Prague, Czech Republic

ABSTRACT

We focus on a sample of 42 sources adjacent to the bow shock source IRS 1W (N-sources), located at the distance of 6.05″ north-east of the supermassive black hole (SMBH) Sagittarius A* (Sgr A*), within the radius of 1.35″. We present the first proper motion measurements of N-sources and suggest that a larger subset of N-sources (28 sources) exhibit a north-westward flying angle. These sources can be bound by an intermediate mass black hole (IMBH), or the concentration that we observe is due to a disk-like distribution projection along the line of sight. We detect the N-sources in H, K_s, L' bands. The north-westward flying sources could be a bound collection of stars. We discuss a tentative existence of an IMBH or an inclined disk distribution to explain a significant overdensity of stars. The first scenario of having an IMBH implies the lower limit of $\sim 10^3\ M\odot$ for the putative IMBH. The second scenario suggests that the appearance of the N-sources might be influenced by the projection of a disk-like distribution of younger He-stars and/or dust-enshrouded stars. Our measurements for the first time reveal that the dense association of stars containing IRS 1W is a co-moving group of massive, young stars. This stellar association might be the remnant core of a massive stellar cluster bound by an IMBH that is currently being tidally stripped as it inspirals towards Sgr A*. The cluster exhibits features similar to the IRS 13N cluster.

Keywords: black hole physics – IRS 1W – Galactic Centre – Sgr A* – Intermediate mass black hole – IRS 13 – N-sources

1. INTRODUCTION

The extended radio source Sgr A consists of three components: Sgr A East, which is a non-thermal supernova remnant, Sgr A West which is a thermal region associated with the ionized mini-spiral structure, and the compact variable radio source Sgr A * associated with the supermassive black hole (SMBH) of $\sim 4 \times 10^6\ M_\odot$ (Balick & Brown 1974; Goss & McGee 1996; Eckart & Genzel 1996; Ghez et al. 1998; Eckart et al. 2017; GRAVITY Collaboration et al. 2019; Event Horizon Telescope Collaboration et al. 2022, and references therein) at the center of the Milky Way. The thermal Sgr A West region or the mini-spiral (Ekers et al. 1983; Lo & Claussen 1983) is detected as a distinct filamentary structure in near- and mid-infrared bands (Clénet et al. 2004; Viehmann et al. 2006; Mužić et al. 2007; Bhat et al. 2022) as well as in the mm- and radio domain (Zhao et al. 2009, 2010; Moser et al. 2017). It is composed of three clumpy streamers orbiting around Sgr A* that consist of dust and ionized and atomic gas with the dust temperature of ~ 100 K and the gas temperature of $\sim 10^4$ K (Yusef-Zadeh et al. 1998; Kunneriath et al. 2012).

A surprisingly large number of massive young stars with the age of a few million years resides in the Milky Way's innermost half parsec (pc). They form at least one disk-like structure of clockwise orbiting stars (CW) (Genzel et al. 2003; Levin & Beloborodov 2003). Paumard et al. (2006) also propose the existence of a second disk of counter-clockwise orbiting stars (CCW), which, however, appears to be less populous. The existence of disk-like structures suggests the association of star-formation in the Galactic Center with the accretion disks that formed during the previous enhanced accretion activity of Sgr A*.

The mechanism which leads to the presence of young stars with the age of $\lesssim$ 5Myr is still not completely understood because there are several factors in the Galactic Center environment that should be inhibiting the star-formation process, such as intense UV radiation and stellar winds, large turbulence, enhanced magnetic field, and the tidal forces from the SMBH (Morris 1993). This problem is known as the "Paradox of youth" (Ghez et al. 2003), though with the advance of star-formation and dynamical models in galactic nuclei, it has been possible to explain the occurrence of young stars in the Galactic Center, see e.g. Mapelli & Gualandris (2016) for a review.

Three plausible scenarios are generally discussed:

1. *in-situ* star-formation approach, in which stars form in the gravitationally unstable accretion disk or within an infalling molecular cloud that gets shocked due to collisions with the surrounding gas or is tidally compressed (Morris 1993; Levin & Beloborodov 2003; Nayakshin et al. 2006; Hobbs & Nayakshin 2009; Lu et al. 2009; Bartko et al. 2009; Paumard et al. 2006; Jalali et al. 2014; Bartko et al. 2010);

2. *in-spiral* star formation approach which claims that the star cluster first starts forming outside the central parsec, e.g. within the circum-nuclear disk or even further away in the central molecular zone. The presence of an IMBH can shorten the dynamical friction timescale, which needs to be at most a few million years long in order for stars to be still young when they settle around the SMBH (Gerhard 2001; McMillan & Portegies Zwart 2003; Hansen & Milosavljević 2003; Portegies Zwart et al. 2006; Berukoff & Hansen 2006; Rizzuto et al. 2020; Peißker et al. 2021);

3. *rejuvenation* scenario, which proposes that late-type stars have undergone collisions with other stars, a dense accretion disc, or a jet, which caused their colder outer layers to be stripped off and made them appear hotter and younger than they actually would be (Morris 1992, 1993; Genzel et al. 2003; Zajaček et al. 2020a,b). In addition, late-type stars aligned with an accretion disk accrete material from it, which also leads to their rejuvenation by gaining fresh hydrogen (Cantiello et al. 2021).

Apart from the cluster of young stars centered around Sgr A* within ~ 0.5 pc, there is a distinct concentration of infrared sources IRS 13 located at the projected distance of $\sim 3-4''$ ($\sim 0.12-0.16$ pc) south-west of Sgr A *. IRS 13 has been studied as a suitable candidate for the first two aforementioned scenarios for the origin of young stars in the central parsec. IRS 13 consists of two components – the northern part IRS 13N and the eastern part IRS 13E. IRS 13N hosts young, infrared-excess sources (Maillard et al. 2004; Eckart et al. 2004; Paumard et al. 2006; Mužić et al. 2008; Eckart et al. 2013). IRS 13E mainly contains massive Wolf- Rayet (WR) stars and the violet supergiant E1(OBI) (Maillard et al. 2004; Moultaka et al. 2005; Paumard et al. 2006), whereas the rest of the stars are fainter ones, identified as late-type stars and are most likely the background stars (Fritz et al. 2010).

The velocity dispersion of the IRS 13E sources motivated the speculation about the existence of an intermediate-mass black hole (IMBH) to bind the cluster. The required mass of the assumed IMBH was inferred to be about $\sim 10^4 M_\odot$ (Maillard et al. 2004; Schödel et al. 2005). The existence of the prominent X-ray source in the IRS 13E cluster reinforced the discussion about the IMBH. On the other hand, Zhu et al. (2020) argue that a colliding wind scenario between E2 and E4 can explain the X-ray spectrum as well as the morphology of IRS 13E and suggests that there is no significant evidence that IRS 13E hosts an IMBH more massive than $\sim 10^3 M_\odot$. In general, the occurrence of IMBHs in nuclear star clusters is expected based on dynamical arguments. Rose et al. (2021) propose that dynamical mechanisms operating in galactic nuclei, specifically black hole-star collisions, mass segregation, and relaxation, are particularly effective in the formation of IMBHs of $\lesssim 10^4 M_\odot$. Their findings imply that at least one IMBH is likely to exist in the central parsec of the Galaxy. Another channel for the occurrence of IMBHs in galactic nuclei is their infall within massive stellar clusters (Spitzer 1969; Portegies Zwart & McMillan 2002; Rasio et al. 2004; Fragione 2022), which directly relates dense stellar associations such as IRS13 with an IMBH. Rose et al. (2021) suggest that the collisions between black holes and stars can contribute to the diffuse X-ray emission in the Galactic Center region. Hence, also a growing black hole inside IRS13E that collides with the surrounding stars could contribute to the X-ray emission of the cluster.

Another apparent concentration of stars in the inner parsec of the Galactic Center is associated with the source IRS 1W that is located within the northern arm of the mini-spiral. The mini-spiral contains mostly hot, ionized gas traced by bright Brγ emission. Vollmer & Duschl (2000) interpret the kinematics of the ionized gas in the northern arm to be Keplerian. IRS 1W has been studied previously as a bow shock source interacting with the material of the northern arm. Its broad-band infrared continuum emission is consistent with the temperature of ~ 300 K (Tanner et al. 2002; Tanner et al. 2003; Tanner et al. 2005) suggesting the presence of warm dust in its bow shock.

Ott et al. (1999) used the speckle camera SHARP on the New Technology Telescope (NTT) and showed that IRS 1W is an extended source which could be a young star. Previously it was suggested that it could have formed in the northern arm of the mini-spiral or from the accreted gas and dust in the infalling material out of the northern arm. However, due to the current low inferred mass of the minispiral gas of $\sim 100 M_\odot$ it is unlikely that it formed within the northerm arm. Tanner et al. (2005) observed IRS 1W alongside IRS 10W and IRS 21 by W.M. Keck 10 meter and Gemini 8 meter telescopes and identified them as bow-shock sources with central sources as Wolf-Rayet stars. The stellar-wind properties and kinematics of IRS 1W are similar to the properties of the clockwise orbiting He emission-line stars. Viehmann et al. (2006) showed that IRS 1W is very red and has a featureless spectral energy distribution (SED). Sanchez-Bermudez et al. (2014) analyzed the bow-shock orientation alongside the proper motion and confirmed that IRS 1W is a Wolf-Rayet star with a bow shock created by the interaction between the mass-losing star and the surrounding interstellar gas.

The apparent stellar overabundance in the vicinity of IRS 1W could hypothetically be a stellar cluster similar to IRS 13 that is getting tidally disrupted upon the approach towards the SMBH. We investigate this possibility in more detail in this paper. We focus on the area around IRS 1W that contains 42 sources including IRS 1W. The geometrical center of these sources is situated at $\sim 6.02'' \pm 0.8$ *RA*., $0.28'' \pm 0.79$ *Dec*. with respect to Sgr A* in 2005.366 epoch within the circular region with a radius of $1.35''$.

The paper is structured as follows. In Section 2, we describe analyzed datasets in the near-infrared (NIR) domain. The identification of stars associated with IRS 1W that constitute an apparent overabundance in comparison with other fields around Sgr A* is analyzed in Section 3. The NIR photometry colour-colour diagram of the sources is presented in Section 4. Proper motions of the sources are analyzed in Section 5, where the significant stellar concentration with the common proper motion in the north-western direction is identified. We discuss potential clustering scenarios (IMBH-bound cluster or a projected disk-like distribution) in Section 6. Finally, we summarize the main results in Section 7.

2. OBSERVATIONS AND DATA REDUCTION

The Galactic Center observations presented in this paper are obtained in the infrared and X-ray domains. The infrared observations were carried out using the Nasmyth Adaptive Optics System/Coude NIR Camera (NAOS/CONICA) at the European Southern Observatory (ESO) Very Large Telescope (VLT). The M-type supergiant IRS 7 located at $\sim 5.5''$ north of Sgr A* (Becklin & Neugebauer 1975; Lebofsky et al. 1982; Yusef-Zadeh & Morris 1991) serves as a natural guide star for the adaptive optics system. The X-ray data was obtained using the Chandra X-ray observatory. The K_s-band data ($2.2\,\mu m$) were taken at Unit 4 (UT4)-YEPUN from 2002 to 2013 and from 2014 at UT1-Antu on Paranal, Chile. The K_s-band images taken with the S13 camera have a pixel scale of 13 mas/pixel and there is one data set among our studied data sets in K_s-band data taken by the S27 camera which has a pixel scale of 27 mas/pixel. We use 16 epochs from 2003.451 to 2018.311 (28 observations) to derive the proper motions of a group of stars located at the east side of the bow-shock object IRS 1W in a circular region with the radius of about $1.35''$. The X-ray data span the energy range from 0.5 to 8 keV and from 4 to 8 keV in 2005.

In this work, for the photometric purposes, we use the H-($1.6\,\mu$m), K_s-($2.2\,\mu$m) and L'-(3.8μm) band data obtained with the NACO@VLT with a pixel scale of 13, 13, and 27 mas/*pixel*, respectively, and the X-ray data with the pixel scale of 492 mas/pixel. In Table 1, we summarize all data sets which are a part of our analysis.

Date	Camera	Filter	Observation ID
2003.451	S13	K_s	713-0078(A)
2003.453	S13	K_s	713-0078(A)
2003.456	S13	K_s	713-0078(A)
2003.464	S13	K_s	271.B-5019(A)
2003.763	S13	K_s	072.B-0285(A)
2004.518	S13	K_s	073.B-0775(A)
2004.663	S13	K_s	073.B-0775(A)
2004.671	S13	K_s	073.B-0775(B)
2004.728	S13	K_s	073.B-0085(C)
2005.270	S13	K_s	073.B-0085(I)
2005.366	S13	K_s	073.B-0085(D)
2005.371	S13	K_s	073.B-0085(D)
2005.374	S13	K_s	073.B-0085(D)
2005.467	S27	K_s	073.B-0085(F)
2005.569	S13	K_s	075.B-0093(C)
2005.574	S13	K_s	075.B-0093(C)
2005.577	S13	K_s	075.B-0093(C)
2005.585	S13	K_s	075.B-0093(C)
2006.585	S13	K_s	077.B-0014(D)
2007.253	S13	K_s	179.B-0261(C)
2007.256	S13	H	179.B-0261(A)
2009.503	S13	K_s	183.B-0100(D)
2009.508	S13	K_s	183.B-0100(D)
2010.240	S13	K_s	183.B-0100(L)
2013.667	S13	K_s	091.B-0183(B)
2017.456	S13	K_s	598.B-0043(L)
2018.306	S13	K_s	598.B-0043(O)
2018.311	S13	K_s	0101.B-0052(B)
2008.400	L27	L'	081.B-0648(A)

Table 1. Summary of NIR observations in H, K_s, L' bands including the date, camera, filter, and observation ID. K_s-band data is used for proper-motion measurements. Photometric measurements are performed in all bands. The pixel scale of NACO S13 camera is 13 mas/pixel and that of S27 is 27 mas/pixel.

The standard data reduction process is applied to all of our infrared data sets that consists of the sky subtraction, flat-fielding, bad and dead pixel correction and finally combining the images for each epoch via a shift-and-add algorithm to

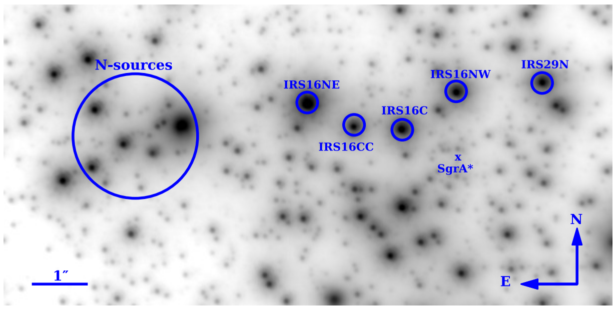

Figure 1. The image obtained in K_s-band from 2005.366 epoch. Symbol "x" denotes the position of Sgr A*. The encircled N-sources at the projected distance of ~ 6.05″ with respect to Sgr A* stands for the region of our study.

obtain the final array. The X-ray data reduction follows the procedure as explained in Mossoux & Eckart (2017).

3. SOURCE IDENTIFICATION

We study sources within a circular region located at ~ 6.05″ north-east of Sgr A* with a radius of ~ 1.35″ (shown in Fig. 1). In this section, we show that the circular region is not chosen arbitrarily but it rather encompasses the stellar overabundance in the region. By increasing the aperture size, the density of sources drops significantly. In addition, there is a visible gap between the N-sources' region and the IRS16 sources' region.

The brightest star in this region is the aforementioned bow-shock source IRS 1W. We identify 42 sources including IRS 1W in the previously described region. We name the sources starting with the letter N from N1 for IRS 1W to N42. In Fig. 2, we show the identified sources in K_s-band. We call these sources the N-sources for simplicity. The N-sources are not only identified in the K_s-band but also in the H- and the L'-bands.

We determined the positions of the N-sources using the `StarFinder` software (Diolaiti et al. 2000) in the K_s-band high-pass filtered images from 2003.451 to 2018.311 over 16 epochs.

When we investigate the number of the N-sources with respect to the radial distance from the geometrical center of the N-sources (Fig. 3), we find a gradual decrease in the number of the sources with the increasing radial distance. This is an expected trend for at least partially relaxed star cluster with a cusp-like power-law density distribution.

To test the cluster hypothesis for the N-sources, it is crucial to compare its number density with random areas distributed isotropically at a comparable distance from Sgr A*. A stable cluster or a stellar association in the Galactic Center must necessarily be characterized by an overdensity with respect to other comparable regions. To this goal, we select random eleven circular regions with two conditions. First, the center of each region should have the same distance from Sgr A* as

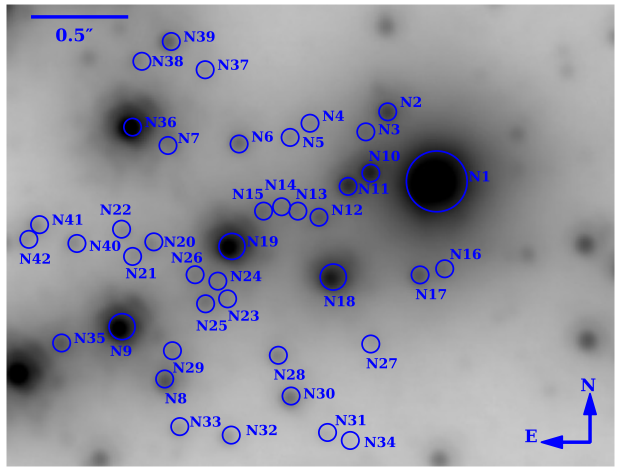

Figure 2. The K_s-band image from 2005.366 epoch. The sources are labeled from N1/IRS 1W to N42. The figure is a zoom-in of the encircled N-sources' region in Fig. 1, which is located at ~ 6.05″ north-east of Sgr A*.

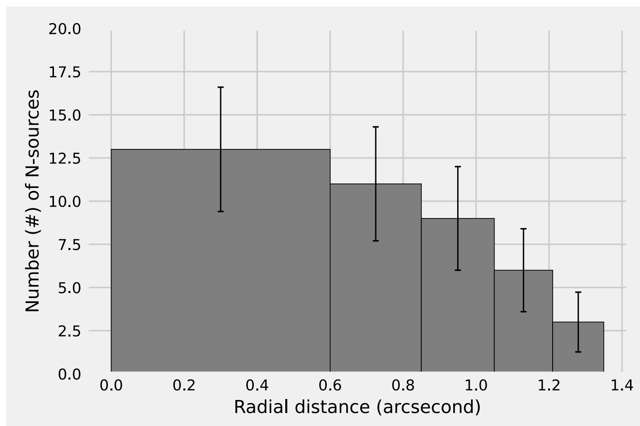

Figure 3. Distribution of N-sources as a function of the projected distance with respect to the geometrical center of the association. The y-axis denotes the number of sources and the x-axis shows the radial distance (in arcseconds) from the geometrical center of N-sources. The length of the bins in the histogram is defined by concentric apertures centered at the geometrical center of N-sources. In addition, each annulus has an equal area to the central disk, with the radius of 0.6″ for the central disk, and the radial extent of 0.6″ to 0.8″ for the first annulus, 0.8″ to 1.0″ for the second annulus, 1.0″ to 1.2″ for the third annulus, and 1.2″ to 1.3″ for the fourth annulus.

the distance of the N-sources' region. Second, each of these circular regions should have the same radius as the chosen aperture representing the N-source region. These comparison regions are labeled from "Region 1" to "Region 11" as shown in the Appendix, Fig. 12. The number of detected stars in K_s-band in each region is listed in Table 2. The mean

Aperture ID	number of sources
N-sources	42
Region 1	15
Region 2	13
Region 3	13
Region 4	16
Region 5	16
Region 6	17
Region 7	14
Region 8	14
Region 9	12
Region 10	15
Region 11	16

Table 2. Number of sources in eleven randomly chosen regions with a comparable distance from Sgr A* and a radius to the N-source association region. Each region is located at a distance of about 6.05″ from Sgr A* and its radius is ∼ 1.35″. The mean number of sources in these 11 regions is 14.6 ± 1.5

number of sources in our eleven random samples is 14.6±1.5. The number of sources in our 11 regions shows that the N-source region is characterized by a significant stellar over-density, which leads us to speculate that the N-sources or their subgroup form a bound stellar association.

4. COLOUR-COLOUR DIAGRAM

The flux densities of N-sources in H, K_s and L'-bands are obtained using aperture photometry with an aperture radius of 4, 4 and 3 pixels in H, K_s and L'-bands, respectively. Our reference stars for photometry are IRS 10W, IRS21 and IRS16NW and their magnitudes are taken from Blum et al. (1996). In order to optimize the background subtraction for each source and reference stars, we use two apertures around the source with the same size as photometry apertures. The flux densities for Vega in H, K_s- and L'-bands are 1050, 667 and 248 Jy, respectively. All N-sources are detected in H, K_s and L'-bands. The results are presented in the colour-colour diagram, see Fig. 4. An interpretation of the colour-colour diagram shown in Fig. 4 is possible in the framework of the corresponding diagrams shown in Fig. 16 of Eckart et al. (2013). Within the uncertainties, the sources that are located to the right of the single-component black-body line are objects reddened by the extinction towards the Galactic Center region. Objects that are located above the black-body line experience additional local extinction due to dust locally present in or in front of the IRS 1W region.

5. PROPER MOTION

For the first time, we derive and present proper motions of N-sources. The prevailing angle of the proper motion is northward, which suggests that N-sources could be a co-moving group of stars.

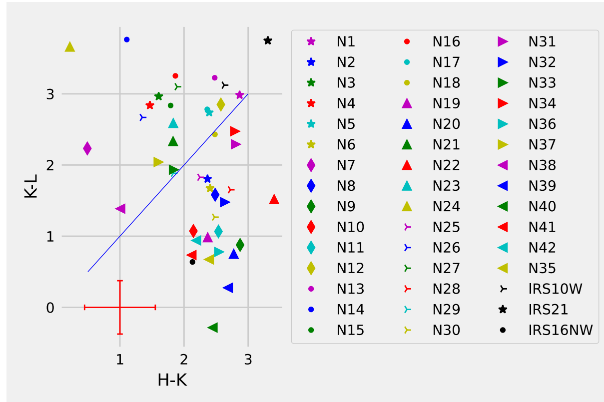

Figure 4. HKL two-colour diagram. The solid blue line denotes the colors of a one-component black body at different temperatures. The red cross represents the uncertainty of the values.

In order to study the proper motions of candidate stars, we identified the N-sources in K_s-band images from 2003 to 2018. With the aid of the S2 star position in each epoch, the position of each source was transformed into the common coordinate system with the central position of Sgr A*. As an example, we show the best-fitting proper motions based on the derived positions as a function of time in right-ascension (R.A.) and declination (Dec.) directions in Fig. 13 for the star N2.

We adopt the distance of 8 kpc to Sgr A* (Shapley 1928; Reid 1993; Eisenhauer et al. 2003; Gravity Collaboration et al. 2019) to transform the proper motions to velocities. The inferred velocities are listed in Table 3 alongside the R.A. and Dec. coordinates with respect to Sgr A* for all the sources. IRS 1W, IRS 16C, IRS 16CC, IRS 16NE, and IRS 16NW are adopted as reference stars (Table 4), which show an agreement in terms of the inferred velocities with the presented values in Paumard et al. (2006) within uncertainties.

In Fig. 5, we show the proper motions of the N-sources superposed on a K_s-band (2.2 μm) image. In general, these sources move towards either north-east or north-west. In Fig. 6, we plot the distribution of the N-sources with respect to their flying angle, which indicates two distinct populations of stars. The North-West (NW) flying sources are depicted in blue, whereas the North-East flying ones in red. The Gaussian-like distribution of the number of the North-West flying sources with respect to the flying angle supports the clustering model of these sources. On the other hand, North-East (NE) flying sources exhibit a flat distribution of the number of sources with respect to the flying angle. In summary, 28 sources out of the total 42 identified N-sources move NW-ward (N1, 2, 3, 4, 5, 6, 7, 9, 10, 11, 12, 15, 18, 19, 22, 23, 24, 25, 26, 27, 30, 31, 35, 36, 37, 39, 40, 42), while

Name	$\Delta\alpha$ $(arcsec)$	$\Delta\delta$ $(arcsec)$	$V_{\rm R.A.}$ *(km/s)*	$V_{\rm Dec.}$ *(km/s)*	*V (km/s)*	Angle *(degree)*
N1	5.15 ± 0.01	0.58 ± 0.01	-89.11 ± 16.31	349.24 ± 43.99	360.43 ± 42.81	-14.31 ± 8.56
N2	5.39 ± 0.01	0.95 ± 0.01	-72.43 ± 10.62	336.35 ± 36.78	344.06 ± 36.03	-12.15 ± 6.09
N3	5.51 ± 0.01	0.84 ± 0.01	-48.16 ± 28.06	111.11 ± 31.85	121.10 ± 31.28	-23.43 ± 35.88
N4	5.80 ± 0.01	0.89 ± 0.01	-86.84 ± 15.93	304.88 ± 27.68	317.01 ± 26.98	-15.90 ± 8.30
N5	5.91 ± 0.01	0.82 ± 0.01	-115.28 ± 13.65	271.89 ± 32.23	295.32 ± 30.15	-22.98 ± 9.80
N6	6.18 ± 0.01	0.79 ± 0.01	-180.12 ± 15.55	479.31 ± 29.96	512.04 ± 28.57	-20.60 ± 5.62
N7	6.53 ± 0.01	0.77 ± 0.01	-63.33 ± 34.51	99.35 ± 45.50	117.82 ± 42.62	-32.52 ± 49.92
N8	6.57 ± 0.01	-0.49 ± 0.01	97.83 ± 12.51	299.19 ± 43.23	314.78 ± 41.27	18.11 ± -0.57
N9	6.82 ± 0.01	-0.20 ± 0.01	-89.11 ± 16.31	349.62 ± 43.99	360.80 ± 42.82	-14.3 ± 8.55
N10	5.48 ± 0.01	0.63 ± 0.01	-121.34 ± 9.86	521.78 ± 25.41	535.70 ± 24.85	-13.09 ± 3.29
N11	5.59 ± 0.01	0.56 ± 0.01	-96.70 ± 12.51	185.05 ± 25.79	208.79 ± 23.58	-27.59 ± 12.67
N12	5.75 ± 0.01	0.39 ± 0.01	-269.23 ± 14.79	203.25 ± 28.06	337.34 ± 20.62	-52.95 ± 10.6
N13	5.89 ± 0.01	0.43 ± 0.01	61.43 ± 15.55	401.95 ± 27.68	406.62 ± 27.46	8.69 ± 3.17
N14	5.96 ± 0.01	0.44 ± 0.01	129.31 ± 17.82	497.89 ± 27.68	514.41 ± 27.16	14.56 ± 2.30
N15	6.07 ± 0.01	0.41 ± 0.01	-48.16 ± 15.93	200.22 ± 32.23	205.93 ± 31.56	-13.52 ± 12.99
N16	5.10 ± 0.01	0.12 ± 0.01	106.56 ± 21.24	236.24 ± 31.47	259.16 ± 29.99	24.28 ± 2.90
N17	5.22 ± 0.01	0.08 ± 0.01	186.19 ± 16.31	324.60 ± 22.37	374.21 ± 21.03	29.84 ± 0.93
N18	5.69 ± 0.01	0.06 ± 0.01	-32.61 ± 17.44	580.93 ± 37.92	581.84 ± 37.87	-3.21 ± 3.87
N19	6.24 ± 0.01	0.23 ± 0.01	-98.97 ± 9.48	308.67 ± 42.85	324.15 ± 40.91	-17.78 ± 7.91
N20	6.66 ± 0.01	0.24 ± 0.01	195.67 ± 14.79	304.12 ± 32.23	361.63 ± 28.26	32.76 ± 1.60
N21	6.73 ± 0.01	0.18 ± 0.01	243.07 ± 16.68	295.78 ± 40.95	382.84 ± 33.36	39.41 ± 3.97
N22	6.80 ± 0.01	0.31 ± 0.01	-59.53 ± 10.24	286.68 ± 47.02	292.80 ± 46.08	-11.73 ± 7.83
N23	6.25 ± 0.01	-0.06 ± 0.01	-91.39 ± 20.86	306.77 ± 38.68	320.09 ± 37.55	-16.59 ± 11.18
N24	6.31 ± 0.01	0.04 ± 0.01	-73.56 ± 28.44	447.08 ± 36.40	453.09 ± 36.21	-9.34 ± 8.62
N25	6.36 ± 0.01	-0.06 ± 0.01	-38.68 ± 16.31	273.40 ± 31.85	276.12 ± 31.62	-8.05 ± 8.64
N26	6.43 ± 0.01	0.07 ± 0.01	-131.96 ± 30.34	428.50 ± 47.02	448.36 ± 45.82	-17.12 ± 10.99
N27	5.47 ± 0.01	-0.26 ± 0.01	-81.15 ± 17.06	211.21 ± 28.44	226.26 ± 27.24	-21.02 ± 13.28
N28	5.98 ± 0.01	-0.35 ± 0.01	53.09 ± 14.41	503.96 ± 29.58	506.75 ± 29.46	6.01 ± 2.55
N29	6.54 ± 0.01	-0.33 ± 0.01	74.70 ± 16.68	150.54 ± 37.54	168.05 ± 34.44	26.39 ± 1.27
N30	5.91 ± 0.01	-0.58 ± 0.01	-95.94 ± 15.93	190.74 ± 28.44	213.51 ± 26.40	-26.70 ± 14.53
N31	5.72 ± 0.01	-0.77 ± 0.01	-42.47 ± 19.34	301.46 ± 30.72	304.44 ± 30.54	-8.02 ± 8.88
N32	6.24 ± 0.01	-0.78 ± 0.01	50.43 ± 19.34	284.78 ± 30.72	289.21 ± 30.44	10.04 ± 5.49
N33	6.51 ± 0.01	-0.74 ± 0.01	117.17 ± 28.06	720.86 ± 37.54	730.32 ± 37.33	9.23 ± 3.41
N34	5.61 ± 0.01	-0.80 ± 0.01	156.61 ± 19.34	396.64 ± 40.57	426.44 ± 38.40	21.55 ± 0.84
N35	7.14 ± 0.01	-0.29 ± 0.01	-77.36 ± 22.75	289.33 ± 50.81	299.49 ± 49.44	-14.97 ± 13.65
N36	6.77 ± 0.01	0.87 ± 0.01	-21.24 ± 18.96	353.41 ± 45.5	354.05 ± 45.43	-3.44 ± 7.11
N37	6.37 ± 0.01	1.17 ± 0.01	-257.10 ± 34.13	197.18 ± 56.12	324.01 ± 43.59	-52.51 ± 22.80
N38	6.73 ± 0.01	1.22 ± 0.01	144.10 ± 22.75	319.29 ± 72.05	350.30 ± 66.34	24.29 ± 3.05
N39	6.56 ± 0.01	1.33 ± 0.01	-28.06 ± 18.58	519.88 ± 58.78	520.64 ± 58.70	-3.09 ± 4.84
N40	7.06 ± 0.01	0.25 ± 0.01	-38.68 ± 10.62	487.65 ± 37.92	489.18 ± 37.81	-4.54 ± 3.20
N41	7.27 ± 0.01	0.33 ± 0.01	122.10 ± 17.06	155.09 ± 35.27	197.39 ± 29.65	38.21 ± 5.07
N42	7.32 ± 0.01	0.27 ± 0.01	-200.60 ± 51.57	477.79 ± 118.31	518.19 ± 110.9	-22.78 ± 21.01

Table 3. Velocities of N-sources over the 16 years of monitoring. N1 represents the IRS 1W bow-shock source. The positions of N-sources are given with respect to the position of Sgr A* in 2005 epoch.

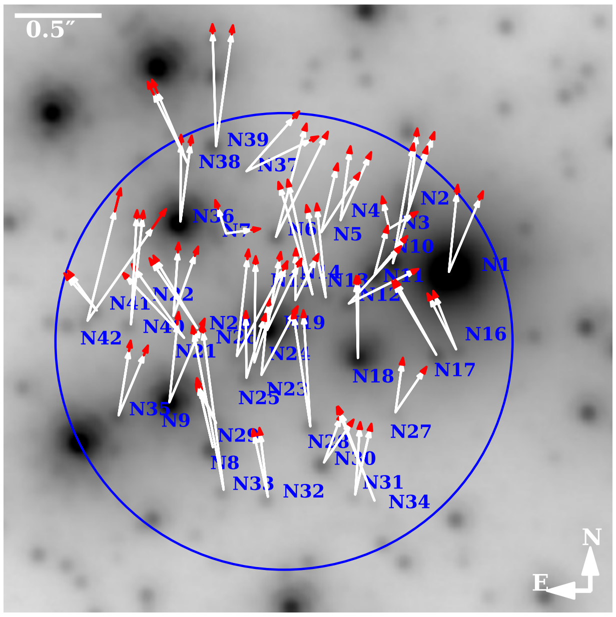

Figure 5. The K_s-band image from 2005.366 epoch with superimposed proper motions for each N source. Four arrows are shown for each source. The white arrows demonstrate the velocity vectors of each source including the uncertainty of the velocity angle, whereas the red arrows indicate the uncertainty in the velocity magnitude. The size of the arrows is proportional to the velocity magnitude. The proper motion vectors are based on Table 3 and the arrows are one order of magnitude smaller than proper motions. In total, 42 sources move North-ward (N-sources).

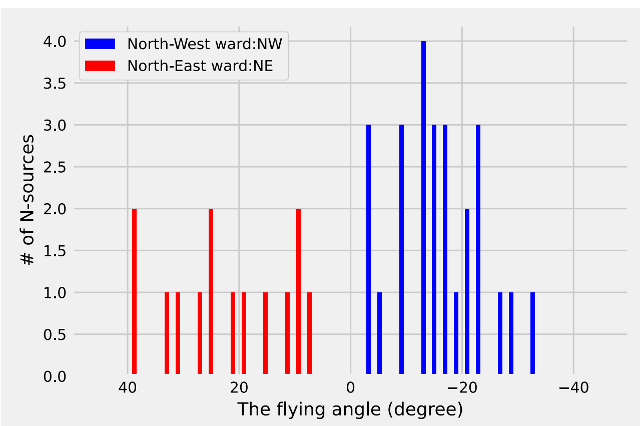

Figure 6. Distribution of flying angles of N-sources. The zero angle stands for a Northward flying angle. The negative angles indicate the North-West-ward (NW) flying angles up to −35 degrees, whereas the positive angles represent the North-East-ward (NE) flying angles up to about 40 degrees. There is an indication that the NW-ward sources are members of a denser association of stars, while the rest of the sources might be the foreground/background sources of the nuclear star cluster.

Name	$V_{\mathrm{R.A.}}$ *(km/s)*	$V_{\mathrm{Dec.}}$ *(km/s)*
IRS 1W	-89.11 ± 16.31	349.24 ± 43.99
IRS16C	-348.48± 5.31	288.19 ± 8.34
IRS16CC	-95.56 ± 5.31	266.96 ± 14.03
IRS16NE	84.18 ± 10.62	-283.64 ± 21.61
IRS16NW	195.29 ± 6.83	19.30 ± 4.17

Table 4. R.A. and Dec. velocities of the reference stars which are within uncertainties in agreement with Paumard et al. (2006).

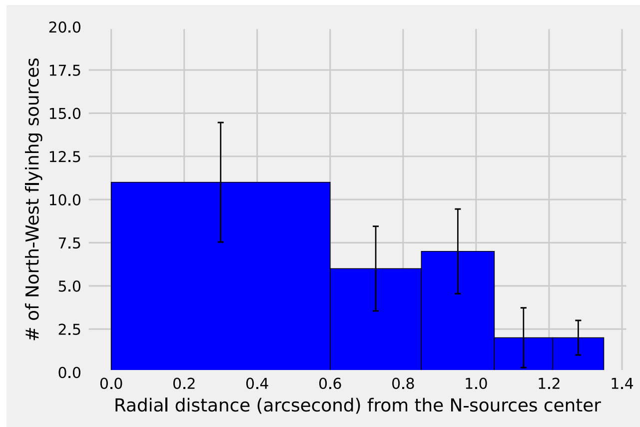

Figure 7. The spatial distribution of the NW-ward flying sources. The zero point of the x-axis is at the geometrical center of the N-sources. The spatial distribution is Gaussian-like.

the rest (14 sources) move NE-ward (N8, 13, 14, 16, 17, 20, 21, 28, 29, 32, 33, 34, 38, 41). The number of NE flying sources is consistent with the mean number in random test regions, see Table 2, which suggests that they mostly belong to the background/foreground nuclear star cluster population. On the other hand, 28 NW-ward flying sources constitute a significant overabundance that we investigate in more detail in the following Section.

6. CLUSTERING SCENARIOS

In the previous section, with the support of Fig. 6, we showed that the N-sources can be divided into two kinematically distinct categories: more abundant NW-ward flying sources and the NE-ward flying sources consisting most likely of foreground/background sources. In Figs. 7 and Fig. 8, we show the number of sources as a function of radial distance for NW-ward and NE-ward flying sources, respectively. In these two figures, we kept the geometrical center of the N-sources as the center of each population. In Fig. 7, we demonstrate that the spatial distribution of the NW-ward flying sources is Gaussian-like, while the spatial distribution of NE-ward flying sources is flat within uncertainties (see Fig. 8). Thus, based on the flying-angle distribution as well

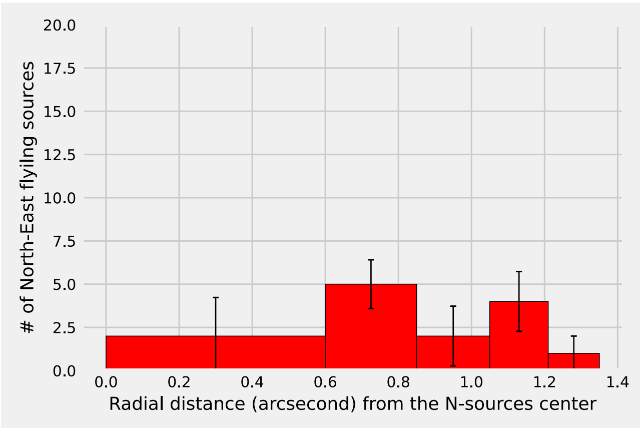

Figure 8. The spatial distribution of the NE-ward flying sources. The zero point of the x-axis is at the geometrical center of the N-sources. The spatial distribution is flat within the uncertainties.

as on the spatial distribution of the NW-ward sources, we can speculate that these sources exhibit the characteristics of a stellar cluster or an association. Therefore, we discuss two plausible scenarios which can result in a bound system or an apparent overdensity. As the first scenario, we propose the existence of an intermediate-mass black hole (IMBH), which keeps the stars bound in the vicinity of the SMBH. In the second scenario, we explain the apparent overdensity on the sky as a result of an inclined disk-like distribution of stars.

6.1. *Putative IMBH*

In the first scenario, we obtain the mass estimate of a putative IMBH for the association of NW-ward flying sources. Our co-moving group of stars has a random velocity dispersion distribution. Therefore, the center of mass of the NW-ward flying association could be associated with a massive object that would prevent this group from tidal disruption. We assume that the hypothetical IMBH is located at the geometrical center of our group of stars. In order to estimate the characteristic size of the cluster, we obtain the geometrical center of the NW-ward sources and consider the standard deviation of the source distribution as the characteristic radius of the cluster, which leads to the estimate of $R_c = 0.57'' \pm 0.10''$[1] Hence, the cluster has 10^{+3}_{-2} members within the core region [2]. We determine the required binding mass by applying the virial theorem, $M_{\rm IMBH} \sim \sigma_\star^2 R_c/G$, where $R_c = 22^{+3}_{-4}$ mpc, G is the gravitational constant, and $\sigma_\star$ is the stellar velocity dispersion. We consider two perpendicular directions for the estimate of $\sigma_\star$ – along the right ascension and the declination. For $\sigma_{\rm RA} = 66^{+4}_{-4}\,{\rm km\,s^{-1}}$, we obtain $M_{\rm IMBH} = 2.5^{+17.5}_{-2.1} \times 10^4 M_\odot$ and for $\sigma_{\rm Dec} = 114^{+16}_{-13}\,{\rm km\,s^{-1}}$, $M_{\rm IMBH} = 7.6^{+1.1}_{-7.5} \times 10^4 M_\odot$. Thus, using the virial theorem, we obtain the first estimate of the required IMBH mass of the order of $\sim 10^3 - 10^5\,M_\odot$ to bind the NW-ward flying sources gravitationally. The second estimate comes from the tidal stability criterion of the putative NW-ward cluster. This can be formulated using the condition that the effective cluster radius is smaller or comparable to its tidal (Hill) radius as it orbits Sgr A* SMBH, hence

$$R_c \lesssim d_{\rm NW} \left(\frac{m_{\rm NW}}{3M_\bullet}\right)^{1/3}, \tag{1}$$

where $d_{\rm NW} \gtrsim 6.05'' \sim 0.242\,{\rm pc}$ is the distance of the NW-ward flying association from Sgr A*, where the lower limit is given by the projected distance. For the SMBH mass, we take $M_\bullet \sim 4 \times 10^6\,M_\odot$ and the cluster radius is estimated from the dispersion of the Gaussian fit to the number density distribution, $R_c = 22^{+3}_{-4}$ mpc as before. From the tidal stability condition given by Eq. (1), the total mass of the NW-ward cluster then is $m_{\rm NW} \gtrsim 3M_\bullet(R_c/d_{\rm NW})^3$, which gives $m_{\rm NW} \gtrsim (1.03^{+0.67}_{-0.47}) \times 10^4\,M_\odot$, where we determined the upper and the lower uncertainty from the range of the effective cluster radius. Considering the total radius of the N-source region, $R_N \sim 1.35'' \sim 54\,{\rm mpc}$, we obtain $m_{\rm NW} \gtrsim 1.33 \times 10^5\,M_\odot$. Since the stars contribute $\lesssim 10^3\,M_\odot$ to the cluster mass, which follows from the total number of detected stars of the order of 10, the required mass for the tidal stability of the cluster is significantly larger and could be complemented by a single or more IMBHs of the mass $m_{\rm IMBH} \sim m_{\rm NW} \sim 10^3 - 10^5\,M_\odot$, considering the total range of the N-source region size. The mass range $\sim 10^3 - 10^5\,M_\odot$ of the hypothetical IMBH associated with the NW-ward flying association, which was inferred using both the virial theorem and the tidal stability criterion, is consistent with the expected IMBH mass of $\sim 10^2 - 10^5\,M_\odot$ in various stellar environments (Greene et al. 2020).

Using the 1999–2012 X-ray Chandra data available from the Chandra Search and Retrieval interface, we limit our study to the observations when Sgr A* was observed with an off-axis angle lower than 2 arcmin. This results in 84 obser-

[1] In order to fit a Gaussian model on the plot 14 we indicate each bin by means of three data points, at the start, center and the end of it. Each data point indicates the value and the associated uncertainty of the corresponding bin. Fitting a Gaussian model on the aforesaid plot produces the σ and its uncertainty, which represent the size of the cluster and its uncertainty.

[2] Eight sources located in the area with radius of 18 mpc : N6, 12, 15, 19, 23, 24, 25, 26.
Ten sources located in the area with the radius of 22 mpc : N5, 6, 7, 12, 15, 19, 23, 24, 25, 26.
13 sources located in the area with the radius of 25 mpc : N5, 6, 7, 11, 12, 15, 18, 19, 22, 23, 24, 25, 26.

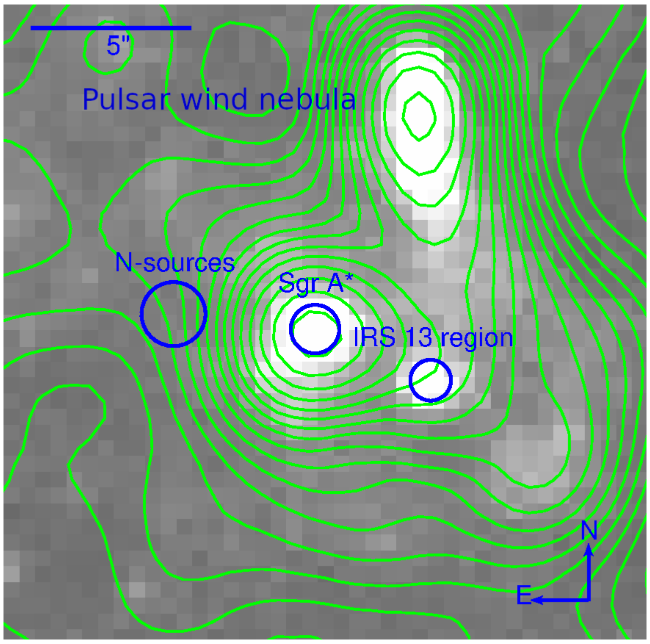

Figure 9. The Chandra X-ray image from 0.5 to 8 keV. The north is up and the east to the left. Distinct X-ray bright sources are labelled, namely Sgr A*, IRS 13, and the pulsar wind nebula. There is no significant X-ray source at the position of the N-source association. The angular scale is indicated in the upper left corner.

vations with the ACIS-I or ACIS-S/HETG cameras (Garmire et al. 2003) and a total exposure time of 4.6 Ms (see details in Mossoux & Eckart (2017)). The pixel scale of the Chandra X-ray data is 492 mas/pixel. In Fig. 9 and Fig. 15 (Appendix), we plot contours at 100, 80, 60, 40 % of the peak counts detected at the position of Sgr A*. In the central few arcseconds, Chandra observations have revealed both the extended X-ray emission as well as the emission from compact sources that can be associated with stars (e.g. X-ray binaries). These data confirm a thermal X-ray spectrum of IRS13E. Fitting the spectrum with an optically thin plasma model, one finds a temperature of 2.0 keV and an unabsorbed 2–10 keV luminosity of about $\sim 2.0 \times 10^{33}\,\mathrm{erg\,s^{-1}}$ for the IRS13 region (Zhu et al. 2020; Wang et al. 2006).

No X-ray source could be identified at the position of N-sources. We find that in a 1.5″ diameter aperture the X-ray luminosity at the position of N-sources is about three times fainter than that of IRS 13 in the 0.5 to 8 *keV* image and about 10 times fainter in the 4 to 8 *keV* image. Hence, the X-ray luminosity that can be associated with the N-source region is below $L_X \lesssim 0.2\times 10^{33}\,\mathrm{erg\,s^{-1}}$. In comparison to IRS 13E, this may indicate either a lack of hot optically-thin plasma or an increased extinction from the foreground material, possibly associated with the circumnuclear disk (CND, see Mossoux & Eckart, 2017). In fact, Moser et al. (2017) report high-velocity SiO gas south-west of IRS 1W, see their Fig. 11.

The lack of X-ray emission does not support the presence of a hypothetical IMBH accreting in a radiatively efficient way, see e.g. Schödel et al. (2005). In other words, the Eddington ratio[3] of the system $\lambda_{\rm Edd} = \kappa_{\rm bol} L_X / L_{\rm Edd} \lesssim 1.6 \times 10^{-7}$ (estimated for $m_{\rm IMBH}$ scaled to $10^4\,M_\odot$ and the bolometric correction $\kappa_{\rm bol} \lesssim 1000$) would imply a radiatively inefficient mode of accretion in the form of e.g. Advection Dominated Accretion Flow (ADAF), which is expected for IMBHs across various galactic environments (see e.g. Seepaul et al. 2022; Pacucci & Loeb 2022). Under the approximation of the spherical, Bondi-like accretion of the surrounding hot plasma onto the IMBH, we can estimate the Bondi rate as

$$\dot{M}_{\rm B} = \frac{4\pi G^2 m_{\rm IMBH}^2 \mu n_{\rm a} m_{\rm H}}{c_{\rm s}^3}\,, \tag{2}$$

where $n_{\rm a}$ is the ambient medium number density, $c_{\rm s}$ is the sound speed in the ambient plasma, $m_{\rm H}$ is the hydrogen atom mass, and μ is the mean molecular weight ($\mu \sim 0.5$ for fully ionized plasma). Here we consider the ambient plasma properties similar to those inferred for the Bondi radius, i.e. $n_{\rm a} \sim 26\,\mathrm{cm^{-3}}$ and $kT_{\rm a} \sim 1.3\,\mathrm{keV}$ (Baganoff et al. 2003). For $m_{\rm IMBH} = 10^4\,M_\odot$, we obtain $\dot{M}_{\rm B} \sim 6.1 \times 10^{-11}\,M_\odot \mathrm{yr^{-1}}$ according to Eq. (2), which implies the radiative efficiency of $\eta_{\rm R} \lesssim 6 \times 10^{-5} - 0.06$ to yield the bolometric luminosity of the IMBH of $L_{\rm bol} \lesssim \kappa_{\rm bol} L_X$, where the bolometric correction $\kappa_{\rm bol} \lesssim 1000$. Such radiative efficiencies are expected for the Eddington ratios $\lambda_{\rm Edd} \lesssim 10^{-6}$, see e.g. Yuan & Narayan (2014), depending on the electron heating parameter. Hence, Bondi-like hot flow feeding the putative IMBH can explain its low X-ray emission and thus the difficulty to detect it directly within the nuclear star cluster, not only in the IRS 1W NW-ward flying region, but also in IRS 13E. The sound speed of the virialized plasma can be estimated using the stellar velocity dispersion, i.e. $c_{\rm s} = \sqrt{2}(\sigma_{\rm RA}^2 + \sigma_{\rm Dec}^2)^{1/2} \sim 186\,\mathrm{km\,s^{-1}}$, which implies the temperature of $T_{\rm a} \sim 2.1 \times 10^6\,\mathrm{K}$. Taking the accretion luminosity of $L_{\rm bol} \lesssim \kappa_{\rm bol} L_X$ where $\kappa_{\rm bol} \lesssim 1000$, Eq. (2) implies the asymptotic number density of $n_{\rm a} \sim 8\,\mathrm{cm^{-3}}$ for $\eta_{\rm R} = 0.01$. The sound speed of the virialized gas yields the Bondi-radius estimate of,

$$\begin{aligned} R_{\rm B} &= \frac{2 G m_{\rm IMBH}}{c_{\rm s}^2} \\ &= 2.5 \left(\frac{m_{\rm IMBH}}{10^4\,M_\odot}\right)\left(\frac{T_{\rm a}}{2.1\times 10^6\,\mathrm{K}}\right)^{-1} \mathrm{mpc} \sim 0.06''\,, \end{aligned} \tag{3}$$

[3] The Eddington luminosity is estimated using the standard upper limit for the steady spherical accretion, $L_{\rm Edd} = 4\pi G m_{\rm IMBH} m_{\rm p} c/\sigma_{\rm T}$.

which is about ten times smaller than the cluster core radius, and hence the expected number of massive stars that can feed the IMBH via stellar winds is of the order of unity.

In case there is no IMBH at the center of the NW-ward flying association, it will be tidally disrupted on the orbital timescale,

$$P_{\rm orb} \gtrsim 2\pi \frac{d_{\rm NW}^{3/2}}{\sqrt{GM_\bullet}}$$
$$\sim 5577 \left(\frac{d_{\rm NW}}{0.242\,{\rm pc}}\right)^{3/2} \left(\frac{M_\bullet}{4\times10^6\,M_\odot}\right)^{-1/2} {\rm yr}\,, \quad (4)$$

which is such a short timescale in comparison with the stellar lifetime that it is unlikely that we observe the NW-ward group just at the beginning of tidal dissociation. Therefore, it is more likely that either the group is bound by a quiescent IMBH or the overdensity is due to the projection effect, in particular the inclined disk-like distribution of stars that we discuss in the following subsection.

Eventually, the lifetime of the IMBH-bound stellar association similar to the NW-ward flying group is given by the dynamical friction timescale, during which the IMBH inspirals towards Sgr A*,

$$\tau_{\rm df} = \frac{3}{8}\sqrt{\frac{2}{\pi}} \frac{\sigma_\star^3}{G^2 \rho_\star m_{\rm IMBH} \ln\Lambda}$$
$$\sim 3\times10^5 \left(\frac{\sigma_\star}{88\,{\rm km\,s^{-1}}}\right)^3 \left(\frac{\rho_\star}{2.4\times10^5\,M_\odot\,{\rm pc^{-3}}}\right)^{-1}$$
$$\times \left(\frac{m_{\rm IMBH}}{10^4\,M_\odot}\right)^{-1} \left(\frac{\ln\Lambda}{15}\right)^{-1} {\rm yr}\,, \quad (5)$$

where $\sigma_\star$ is the stellar velocity dispersion that we scale to $\sigma_\star \sim 88\,{\rm km\,s^{-1}}$ according to $M_\bullet$-$\sigma_\star$ relation (Gültekin et al. 2009); the stellar mass density $\rho_\star$ is estimated using the condition that there is the stellar mass of $M_\star(r < r_{\rm h}) \sim 2\,M_\bullet$ inside the Sgr A* sphere of influence, which is $r_{\rm h} \sim 2\,{\rm pc}$ (Merritt 2013); the IMBH mass is scaled to $m_{\rm IMBH} \sim 10^4\,M_\odot$ following the previous estimates, and the Coulomb logarithm is estimated as $\ln\Lambda \sim \ln(M_\bullet/M_\odot) \sim 15$. Hence, the stellar association would be disrupted on the timescale of the order of $\tau_{\rm df}$ as the IMBH inspirals via dynamical scattering through the nuclear star cluster. The tidal stripping of the stellar cluster during the IMBH inspiral towards the SMBH may be one of the mechanisms how early-type stars of spectral type O and B are deposited close to the SMBH on the scale of ~ 0.01 pc.

6.2. *Disk-like distribution projection*

Paumard et al. (2006) and Lu et al. (2009) categorized IRS 1W as a member of the clockwise disk and IRS13E members were introduced as members of the counter-clockwise disk. However, later Yelda et al. (2014) did not find evidence for the existence of the counter-clockwise disk and Sanchez-Bermudez et al. (2014) also did not categorize IRS 1W as a member of the clockwise disk based on the bow-shock orientation and the proper motion. The fact that the N-sources and the IRS13 region are located on opposite sides to each other at similar distances from Sgr A* (6″ and 4″, respectively), suggests that their appearance may in fact be the result of the projection of a disk-like distribution, such as the clockwise disk of young He-stars and/or dust-enshrouded stars.

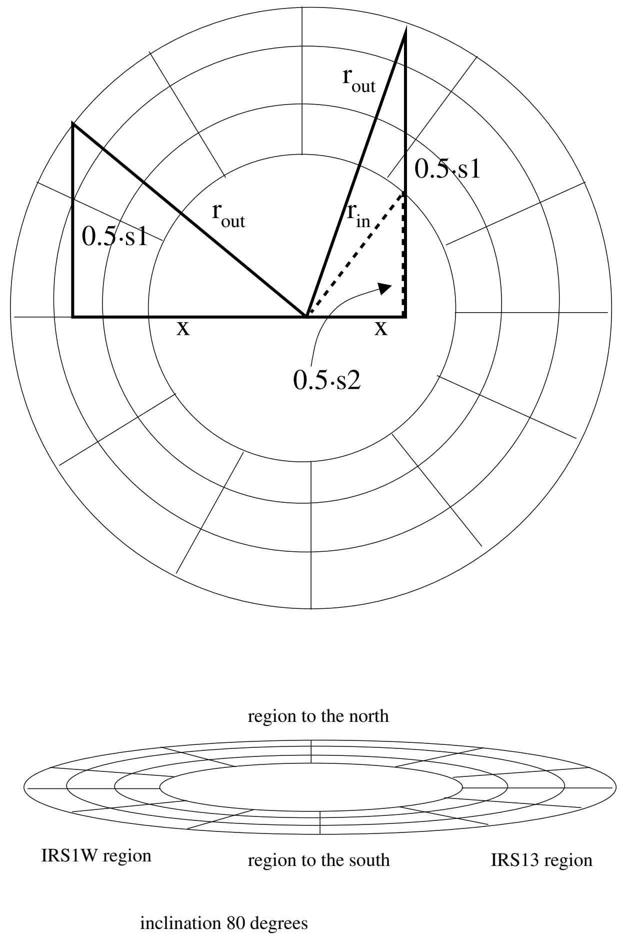

Figure 10. Top: Face on view of the East West (EW) stellar disk system with outer and inner radii given in the text. For the case of $s1$ we indicated the corresponding quantities. Bottom: The disk system is inclined by 80 degrees. The clustering at the eastern and western tips of the disk become evident.

We show that the corresponding projected stellar surface density on the sky may be about a factor of two higher than the density of the northern and southern projected disk sections. We can estimate this effect in the following way. We assume that the disk-forming fraction of stars is arranged in a disk with an inclination of $i = 10$ degrees (Levin & Beloborodov 2003; Lu et al. 2008), with an outer radius of

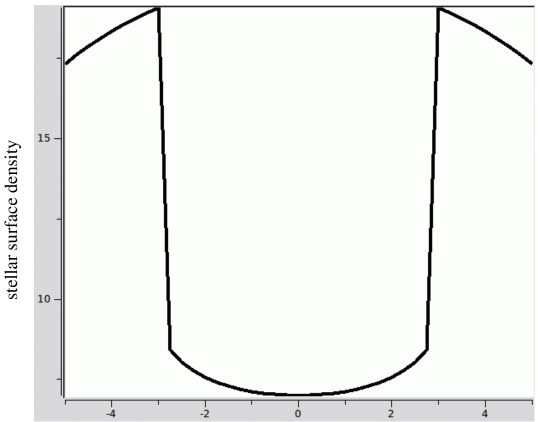

Figure 11. Stellar sky surface density in arbitrary units as a function of radius in the east west direction in arcseconds. Here also, the clustering at the eastern and western tips of the disk become evident. The source density is almost a factor of 2 higher than in the northern and southern part of the disk.

$r_{out} = 5''$, and an inner radius of $r_{in} = 1.5''$ (shown in Fig. 10). We can then calculate cross-sections through that disk system as:

$$s_I = 2\sqrt{|r_{out}^2 - x^2|} \quad (6)$$

(see the left side of the upper panel in Fig. 10.)

$$s_2 = s_1 - 2\sqrt{|r_{in}^2 - x^2|} \quad (7)$$

(see the right side of the upper panel in Fig. 10.)

The projected surface density ρ is proportional to $s_1/cos(i)$ for the regions beyond the inner radius r_{in} and is proportional to $\frac{1}{2}s_2/cos(i)$ for the regions within the inner radius r_{in} to the north and the south of Sgr A*. The fact that both N-sources and IRS13 lie on the opposite sides of Sgr A* at a rather similar distance may support this model. Hence, the overdensity of these compact stellar systems could be explained by the projection effect in which the excess in velocity dispersion is given to a large part by the disk dynamics, see Fig.11 .

7. CONCLUSIONS

For the first time, we show that N-sources are north-ward moving sources located in the Galactic Center in the vicinity of the bow-shock source IRS 1W. Moreover, we demonstrate that these sources possess a Gaussian-like number density distribution with respect to the geometrical center. The overdensity is apparent in comparison with the number of sources in random test regions at a comparable distance from Sgr A*. These circular regions have the same size as the size of the N-source region. The mean number of the detected sources in our eleven test regions is 14.6 ± 1.5, while the number of N-sources is 42, which indicates that the N-source group is potentially a stellar association in the vicinity of Sgr A*.

Further investigation of the proper motions of N-sources reveals that N-sources can be divided into two categories. One category encompasses the NW-ward flying sources which show a spatial Gaussian number density distribution, while the NE-ward flying sources have a rather spatially flat distribution. Therefore, the NW-ward flying sources could potentially be bound or have a common origin, while NE-ward flying sources most likely consist of background/foreground stars of the nuclear star cluster.

The high concentration of the N-sources, mainly the NW-ward flying group, can be interpreted in terms of the stellar cluster that is kept stable by the central IMBH or it could be the result of a disk-like stellar distribution that is projected at a high angle.

First scenario is supported by a likely occurrence of IMBHs in the Galactic center. One formation channel is a series of collisions of stellar-mass black holes with main-sequence stars, which was analyzed by Rose et al. (2021). This formation mechanism appears quite efficient and it can produce IMBHs of mass $\lesssim 10^4\,M_\odot$, which is within the uncertainties the IMBH mass constrained for IRS 1W association, specifically using either the velocity dispersion of NW-ward flying sources or the tidal stability criterion. Another mechanism is the cluster infall scenario (see e.g. Fragione 2022, and references therein), which assumes that massive clusters, such as young star-forming clusters or globular cluster, host IMBHs with a certain occupation fraction. In this regard, the NW-ward flying group could be a remnant, tidally stable core of such an infalling massive cluster. However, our present data from the Chandra X-ray telescope do not provide evidence for an X-ray bright IMBH, which may be caused by either a high level of extinction in the area or a dearth of hot, optically-thin plasma. Future spectroscopic data collected by the James Webb Space Telescope will be crucial for a better understanding of the stellar composition of the N sources and this may also help clarify their potential origin in a common cluster whose core can only be kept stable by the IMBH at a given distance from Sgr A*.

The second scenario is supported by a curious distribution of cluster-like stellar associations in the vicinity of Sgr A*. Specifically, the IRS13 and the N-source areas are positioned at $\sim 4''$ south-west and $\sim 6''$ north-east of Sgr A*, respectively, nearly along the same line, which raises the possibility that the observed overdensities may actually be formed due to the projection when the two regions are situated on the same stellar disk with the characteristics similar to that of the clockwise stellar disk.

In the current investigation, we do not find preference for any of the two models. It is therefore necessary to conduct detailed spectroscopic measurements to rule out one of the models. More information about the orbital properties of these sources, in particular specroscopically determined line-of-sight velocities, will be crucial for the further study of this and similar regions.

ACKNOWLEDGMENTS

This work was supported in part by SFB 956—Conditions and Impact of Star Formation. S. Elaheh Hosseini is a member of the International Max Planck Research School for Astronomy and Astrophysics at the Universities of Bonn and Cologne. We thank the Collaborative Research Centre 956, sub-project A02, funded by the Deutsche Forschungsgemeinschaft (DFG) – project ID 184018867. M.Z. acknowledges the financial support by the GAČR EXPRO grant No. 21-13491X "Exploring the Hot Universe and Understanding Cosmic Feedback" as well as the support of the Czech-Polish GAČR-LA collaboration grant No. GF22-04053L. V.K. acknowledges Czech Science Foundation grant No. 21-06825X.

REFERENCES

Baganoff, F. K., Maeda, Y., Morris, M., et al. 2003, ApJ, 591, 891, doi: 10.1086/375145

Balick, B., & Brown, R. L. 1974, ApJ, 194, 265, doi: 10.1086/153242

Bartko, H., Martins, F., Fritz, T. K., et al. 2009, ApJ, 697, 1741, doi: 10.1088/0004-637X/697/2/1741

Bartko, H., Martins, F., Trippe, S., et al. 2010, ApJ, 708, 834, doi: 10.1088/0004-637X/708/1/834

Becklin, E. E., & Neugebauer, G. 1975, ApJL, 200, L71, doi: 10.1086/181899

Berukoff, S. J., & Hansen, B. M. S. 2006, ApJ, 650, 901, doi: 10.1086/507414

Bhat, H. K., Sabha, N. B., Zajaček, M., et al. 2022, ApJ, 929, 178, doi: 10.3847/1538-4357/ac6106

Blum, R. D., Sellgren, K., & Depoy, D. L. 1996, ApJ, 470, 864, doi: 10.1086/177917

Cantiello, M., Jermyn, A. S., & Lin, D. N. C. 2021, ApJ, 910, 94, doi: 10.3847/1538-4357/abdf4f

Clénet, Y., Rouan, D., Gendron, E., et al. 2004, A&A, 417, L15, doi: 10.1051/0004-6361:20040031

Diolaiti, E., Bendinelli, O., Bonaccini, D., et al. 2000, in Astronomical Society of the Pacific Conference Series, Vol. 216, Astronomical Data Analysis Software and Systems IX, ed. N. Manset, C. Veillet, & D. Crabtree, 623. https://arxiv.org/abs/astro-ph/9911354

Eckart, A., & Genzel, R. 1996, Nature, 383, 415, doi: 10.1038/383415a0

Eckart, A., Moultaka, J., Viehmann, T., Straubmeier, C., & Mouawad, N. 2004, ApJ, 602, 760, doi: 10.1086/381178

Eckart, A., Mužić, K., Yazici, S., et al. 2013, A&A, 551, A18, doi: 10.1051/0004-6361/201219994

Eckart, A., Hüttemann, A., Kiefer, C., et al. 2017, Foundations of Physics, 47, 553, ArXiv: 1703.09118 , doi: 10.1007/s10701-017-0079-2

Eisenhauer, F., Schödel, R., Genzel, R., et al. 2003, ApJL, 597, L121, doi: 10.1086/380188

Ekers, R. D., van Gorkom, J. H., Schwarz, U. J., & Goss, W. M. 1983, A&A, 122, 143

Event Horizon Telescope Collaboration, Akiyama, K., Alberdi, A., et al. 2022, ApJL, 930, L12, doi: 10.3847/2041-8213/ac6674

Fragione, G. 2022, arXiv e-prints, arXiv:2202.05618. https://arxiv.org/abs/2202.05618

Fritz, T. K., Gillessen, S., Dodds-Eden, K., et al. 2010, ApJ, 721, 395, doi: 10.1088/0004-637X/721/1/395

Garmire, G. P., Bautz, M. W., Ford, P. G., Nousek, J. A., & Ricker, George R., J. 2003, in Society of Photo-Optical Instrumentation Engineers (SPIE) Conference Series, Vol. 4851, X-Ray and Gamma-Ray Telescopes and Instruments for Astronomy., ed. J. E. Truemper & H. D. Tananbaum, 28–44, doi: 10.1117/12.461599

Genzel, R., Schödel, R., Ott, T., et al. 2003, ApJ, 594, 812, doi: 10.1086/377127

Gerhard, O. 2001, ApJL, 546, L39, doi: 10.1086/318054

Ghez, A. M., Klein, B. L., Morris, M., & Becklin, E. E. 1998, ApJ, 509, 678, doi: 10.1086/306528

Ghez, A. M., Duchêne, G., Matthews, K., et al. 2003, ApJL, 586, L127, doi: 10.1086/374804

Goss, W. M., & McGee, R. X. 1996, 102, 369

GRAVITY Collaboration, Abuter, R., Accardo, M., et al. 2019, The Messenger, 178, 26, doi: 10.18727/0722-6691/5168

Gravity Collaboration, Abuter, R., Amorim, A., et al. 2019, A&A, 625, L10, doi: 10.1051/0004-6361/201935656

Greene, J. E., Strader, J., & Ho, L. C. 2020, ARA&A, 58, 257, doi: 10.1146/annurev-astro-032620-021835

Gültekin, K., Richstone, D. O., Gebhardt, K., et al. 2009, ApJ, 698, 198, doi: 10.1088/0004-637X/698/1/198

Hansen, B. M. S., & Milosavljević, M. 2003, ApJL, 593, L77, doi: 10.1086/378182

Hobbs, A., & Nayakshin, S. 2009, MNRAS, 394, 191, doi: 10.1111/j.1365-2966.2008.14359.x

Jalali, B., Pelupessy, F. I., Eckart, A., et al. 2014, Monthly Notices of the Royal Astronomical Society, 444, 1205, doi: 10.1093/mnras/stu1483

Kunneriath, D., Eckart, A., Vogel, S. N., et al. 2012, A&A, 538, A127, doi: 10.1051/0004-6361/201117676

Lebofsky, M. J., Rieke, G. H., & Tokunaga, A. T. 1982, ApJ, 263, 736, doi: 10.1086/160545

Levin, Y., & Beloborodov, A. M. 2003, ApJL, 590, L33, doi: 10.1086/376675

Levin, Y., & Beloborodov, A. M. 2003, The Astrophysical Journal, 590, L33–L36, doi: 10.1086/376675

Lo, K. Y., & Claussen, M. J. 1983, Nature, 306, 647, doi: 10.1038/306647a0

Lu, J. R., Ghez, A. M., Hornstein, S. D., et al. 2008, The Astrophysical Journal, 690, 1463–1487, doi: 10.1088/0004-637x/690/2/1463

Lu, J. R., Ghez, A. M., Hornstein, S. D., et al. 2009, ApJ, 690, 1463, doi: 10.1088/0004-637X/690/2/1463

Maillard, J. P., Paumard, T., Stolovy, S. R., & Rigaut, F. 2004, Astronomy and Astrophysics, 423, 155, doi: 10.1051/0004-6361:20034147

Mapelli, M., & Gualandris, A. 2016, in Lecture Notes in Physics, Berlin Springer Verlag, ed. F. Haardt, V. Gorini, U. Moschella, A. Treves, & M. Colpi, Vol. 905, 205, doi: 10.1007/978-3-319-19416-5_6

McMillan, S. L. W., & Portegies Zwart, S. F. 2003, ApJ, 596, 314, doi: 10.1086/377577

Merritt, D. 2013, Dynamics and Evolution of Galactic Nuclei (Princeton: Princeton University Press)

Morris, M. 1992, in American Institute of Physics Conference Series, Vol. 278, American Institute of Physics Conference Series, 21–36, doi: 10.1063/1.44027

Morris, M. 1993, ApJ, 408, 496, doi: 10.1086/172607

Moser, L., Sánchez-Monge, Á., Eckart, A., et al. 2017, A&A, 603, A68, doi: 10.1051/0004-6361/201628385

Mossoux, E., & Eckart, A. 2017, Monthly Notices of the Royal Astronomical Society, 474, 3787, doi: 10.1093/mnras/stx3026

Moultaka, J., Eckart, A., Schödel, R., Viehmann, T., & Najarro, F. 2005, A&A, 443, 163, doi: 10.1051/0004-6361:20052819

Mužić, K., Eckart, A., Schödel, R., Meyer, L., & Zensus, A. 2007, A&A, 469, 993, doi: 10.1051/0004-6361:20066265

Mužić, K., Schödel, R., Eckart, A., Meyer, L., & Zensus, A. 2008, Astronomy and Astrophysics, 482, 173, doi: 10.1051/0004-6361:20078352

Nayakshin, S., Dehnen, W., Cuadra, J., & Genzel, R. 2006, MNRAS, 366, 1410, doi: 10.1111/j.1365-2966.2005.09906.x

Ott, T., Eckart, A., & Genzel, R. 1999, in Astronomical Society of the Pacific Conference Series, Vol. 186, The Central Parsecs of the Galaxy, ed. H. Falcke, A. Cotera, W. J. Duschl, F. Melia, & M. J. Rieke, 310

Pacucci, F., & Loeb, A. 2022, arXiv e-prints, arXiv:2211.00019. https://arxiv.org/abs/2211.00019

Paumard, T., Genzel, R., Martins, F., et al. 2006, ApJ, 643, 1011, doi: 10.1086/503273

Peißker, F., Zajaček, M., Eckart, A., et al. 2021, ApJ, 923, 69, doi: 10.3847/1538-4357/ac23df

Portegies Zwart, S. F., Baumgardt, H., McMillan, S. L. W., et al. 2006, ApJ, 641, 319, doi: 10.1086/500361

Portegies Zwart, S. F., & McMillan, S. L. W. 2002, ApJ, 576, 899, doi: 10.1086/341798

Rasio, F. A., Freitag, M., & Gürkan, M. A. 2004, in Coevolution of Black Holes and Galaxies, ed. L. C. Ho, 138. https://arxiv.org/abs/astro-ph/0304038

Reid, M. J. 1993, ARA&A, 31, 345, doi: 10.1146/annurev.aa.31.090193.002021

Rizzuto, F. P., Naab, T., Spurzem, R., et al. 2020, arXiv, 5273, 5257, doi: 10.1093/mnras/staa3634

Rose, S. C., Naoz, S., Sari, R., & Linial, I. 2021. https://arxiv.org/abs/2201.00022

Sanchez-Bermudez, J., Schödel, R., Alberdi, A., et al. 2014, A&A, 567, A21, doi: 10.1051/0004-6361/201423657

Schödel, R., Eckart, A., Iserlohe, C., Genzel, R., & Ott, T. 2005, The Astrophysical Journal, 625, L111, doi: 10.1086/431307

Seepaul, B. S., Pacucci, F., & Narayan, R. 2022, MNRAS, 515, 2110, doi: 10.1093/mnras/stac1928

Shapley, H. 1928, Nature, 122, 482, doi: 10.1038/122482a0

Spitzer, Lyman, J. 1969, ApJL, 158, L139, doi: 10.1086/180451

Tanner, A., Ghez, A. M., Morris, M., et al. 2002, The Astrophysical Journal, 575, 860, doi: 10.1086/341470

Tanner, A., Ghez, A. M., Morris, M. R., & Christou, J. C. 2005, The Astrophysical Journal, 624, 742, doi: 10.1086/429214

Tanner, A., Ghez, A. M., Morris, M. R., & Christou, J. C. 2005, ApJ, 624, 742, doi: 10.1086/429214

Tanner, A. M., Ghez, A. M., Morris, M., & Becklin, E. E. 2003, Astronomische Nachrichten Supplement, 324, 597, doi: 10.1002/asna.200385093

Viehmann, T., Eckart, A., Schödel, R., Pott, J. U., & Moultaka, J. 2006, ApJ, 642, 861, doi: 10.1086/501345

Vollmer, B., & Duschl, W. J. 2000, NewA, 4, 581, doi: 10.1016/S1384-1076(99)00043-3

Wang, Q. D., Lu, F. J., & Gotthelf, E. V. 2006, Monthly Notices of the Royal Astronomical Society, 367, 937, doi: 10.1111/j.1365-2966.2006.09998.x

Yelda, S., Ghez, A. M., Lu, J. R., et al. 2014, The Astrophysical Journal, 783, 131, doi: 10.1088/0004-637x/783/2/131

Yuan, F., & Narayan, R. 2014, ARA&A, 52, 529, doi: 10.1146/annurev-astro-082812-141003

Yusef-Zadeh, F., & Morris, M. 1991, ApJL, 371, L59, doi: 10.1086/186002

Yusef-Zadeh, F., Roberts, D. A., & Biretta, J. 1998, ApJL, 499, L159, doi: 10.1086/311364

Zajaček, M., Araudo, A., Karas, V., Czerny, B., & Eckart, A. 2020a, ApJ, 903, 140, doi: 10.3847/1538-4357/abbd94

Zajaček, M., Araudo, A., Karas, V., et al. 2020b, arXiv e-prints, arXiv:2011.12868. https://arxiv.org/abs/2011.12868

Zhao, J.-H., Blundell, R., Moran, J. M., et al. 2010, ApJ, 723, 1097, doi: 10.1088/0004-637X/723/2/1097

Zhao, J.-H., Morris, M. R., Goss, W. M., & An, T. 2009, ApJ, 699, 186, doi: 10.1088/0004-637X/699/1/186

Zhu, Z., Li, Z., Ciurlo, A., et al. 2020, The Astrophysical Journal, 897, 135, doi: 10.3847/1538-4357/ab980d

APPENDIX

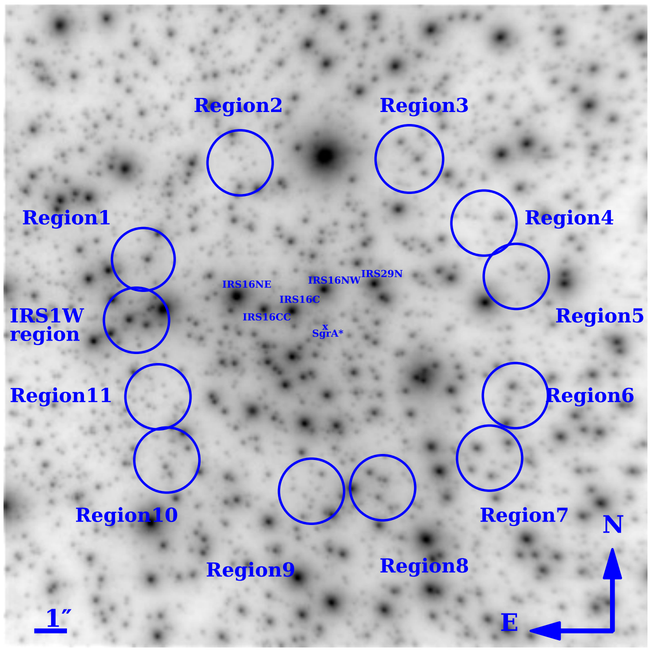

Figure 12. The K_s-band is from 2005.366 observation. The K_s-band image denotes eleven regions in addition to the assumed region of IRS 1W region. The eleven regions are chosen completely randomly in order to identify the number of sources in each region. The only criterion to choose the regions is the distance from Sgr A*. All regions are located in the distance of almost 6″ from Sgr A*. The radius of all circular regions are about 1.3″.

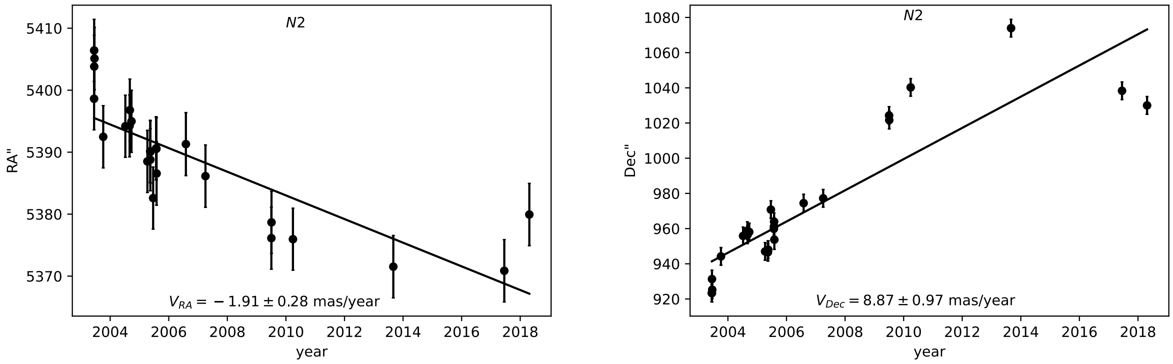

Figure 13. The plots show the derived positions of N2 star as a function of time, along with the best-fitting proper motions. The left panel is along RA and the right panel is along Dec. The slope of each best-fitting line is given in Table 3 in km/s.

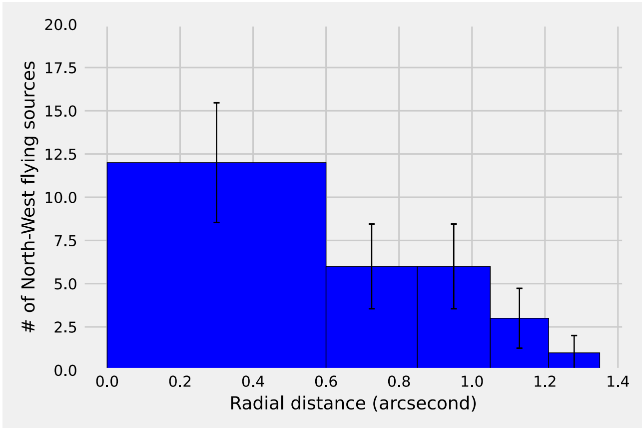

Figure 14. The spatial distribution of the NW-ward flying sources. The zero point of the x-axis is at the geometrical center of the NW ward flying sources. The spatial distribution is Gaussian-like.

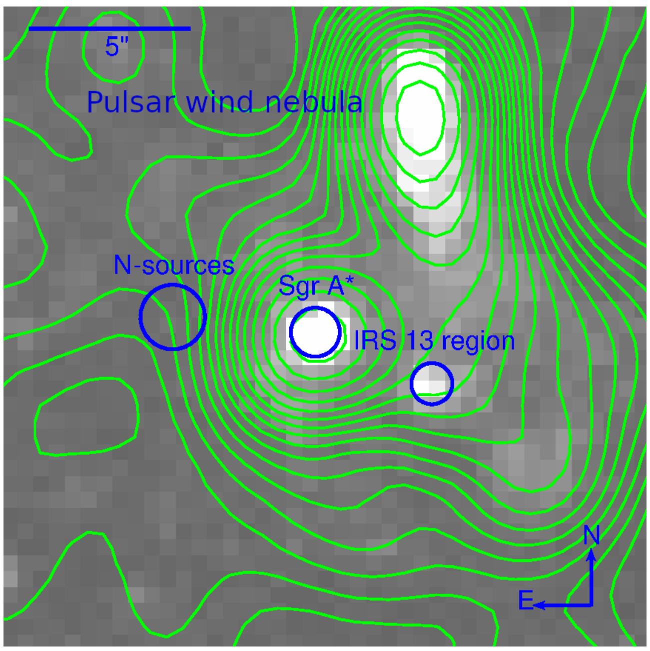

Figure 15. The Chandra X-ray image from 4 to 8 keV. The north is up and the east is to the left. Distinct X-ray bright sources are labelled, namely Sgr A*, IRS 13, and the pulsar wind nebula. There is no significant X-ray source at the position of the N-source association. The angular scale is indicated in the upper left corner.

CHAPTER 7

Sgr A* and its ambient medium in near- and mid-infrared in the era of JWST

In this chapter, I study the flare activities and brightness of the SMBH, Sgr A*, in infrared and mid-infrared regimes by means of VLT/ESO observations. First, I investigate two nights of simultaneous observations in K_s and L' band. Then, I study the brightness of Sgr A* in mid infrared, to strengthen the upper limit on the flux density of the SMBH in this regime. By having one JWST NIRSpec observations of the Galactic Center (GC) at hand, I will demonstrate the importance of upcoming JWST observations for the GC. Moreover, in order to achieve a better understanding of the upcoming JWST MIRI observations, I will dig in to the MIRI observations of three quasars. Finally, I summarize the results of the chapter with a few concluding remarks.

7.1 Observations of Sgr A* in NIR with VLT

In order to have a deeper understanding of SMBHs and their activities, it is of great importance to observe Sgr A* in different wavelengths and monitor its activities. The SMBH Sgr A* has been extensively observed in the NIR domain (Witzel et al. 2021b). Moreover, investigating its activities during the periapse of close stars to the black hole's event horizon improves our understanding of black holes.

7.1.1 The simultaneous observation of Sgr A* in K_s and L'-band during the periapse

In the infrared domain we conducted observations of Sgr A* in two bands of K_s and L' simultaneously. These observations took place in 2018 at the time of the periapse passage of the S2 star around Sgr A*. The following section is dedicated to detailed information of the infrared observations taking place in 2018 by VLT and determining the flare activity of Sgr A* in K_s and L'-band. These results are obtained within the Event Horizon Telescope

Collaboration and will be used in the subsequent publications of observing campaign of Sgr A* in the X-ray, infrared and radio regime by EHT.

7.1.2 Observations and data reduction

Observations of the GC in near-infrared (NIR) were carried out with the Unit Telescope 4 (YEPUN) of the ESO VLT in Paranal, Chile. The data were obtained from the IR camera CONICA and the NAOS adaptive optics (AO) module in K_s-band (2.2 μm) and L'-band (3.8 μm) on the nights of 22nd and 24th of April 2018. We applied the standard data reduction process consisting of sky subtraction, flat-fielding, and bad pixel correction for all imaging data.

The K_s-band data contain 120 exposures per night. The GC in K_s-band is observed throughout the course of 6 time slots with an integration time of 10.00 seconds per image, 20 exposures per time slot. The GC is observed in L'-band in between the intervals of K_s-band observations. The L'-band observations have been done within 6 time slots in the first observation night and within 5 time slots in the second observation night. Each time slot contains 10 exposures with an integration time of 0.200 seconds. Some of the exposures are excluded due to the poor image quality because of the noise in the detector. A list of the observations analyzed in the current study may be found in Table 7.1.

In the L'-band, the S-stars S26, S30, and S35 are utilized as calibrators, while in the K_s-band S6, S30, and S85 are used. The calibrator flux densities are taken from Gillessen et al. (2009b). Flux densities of Sgr A* and calibrators are measured by aperture photometry using circular apertures with a radius of 66 mas in K_s-band and 82 mas in L'-band. The flux measurements were corrected for extinction, using A_{K_s}=2.42± 0.10 and $A_{L'}$=1.09± 0.13 derived by Fritz et al. (2011).

7.1.3 Photometry

We used S65 as a reference star in both K_s and L'-band images to detect any increase in the brightness of Sgr A*. The subtracted background flux density is derived from 5 circular apertures located in "clear" regions within the central $2''$ which is an approximately constant value.

During the time of the observations, S2 and Sgr A* could not be spatially resolved. The physical separation of S2 and Sgr A* was only 1.38 mpc at the observation time which corresponds to 34.6 mas, while the spatial resolution is 46 mas in K_s-band and 99.5 mas in L'-band. S2 reached its periapse position approximately one month later, on May 19, 2018. The S2 nominal magnitude is taken from Habibi et al. (2017).

7.1.4 Results: The first observation night, 22.04.2018

Fig. 7.1 and 7.2 show the light curve of Sgr A* and the reference star, S65, on the 22nd of April 2018, in K_s and L'-band, respectively. In Fig. 7.1, there are six time intervals starting from 5:27:27.77 UT (see Table 7.1) in K_s-band. Fig. 7.2 shows the corresponding six time intervals starting from 5:57:34.47 UT (see Table 7.1) in L'-band. These L'-band observations are taken in between the K_s-band observations. As can be seen, the flux density of Sgr A* shows no increase in Fig. 7.1 and Fig. 7.2 in neither the K_s- nor the L'-band. The flux

Date	Start (UT time)	Filter	Number of frames	Number of used frames	Integration time (sec)
2018-04-22	05:27:27.77	K_s	20	20	10.00
2018-04-22	06:20:49.80	K_s	20	20	10.00
2018-04-22	07:07:13.12	K_s	20	20	10.00
2018-04-22	07:56:51.88	K_s	20	20	10.00
2018-04-22	08:48:39.73	K_s	20	20	10.00
2018-04-22	09:39:33.65	K_s	20	20	10.00
2018-04-22	05:57:34.47	L'	10	9	0.200
2018-04-22	06:45:59.18	L'	10	9	0.200
2018-04-22	07:34:08.22	L'	10	10	0.200
2018-04-22	08:26:49.37	L'	10	10	0.200
2018-04-22	09:16:05.60	L'	10	9	0.200
2018-04-22	10:05:26.03	L'	10	9	0.200
2018-04-24	05:11:24.21	K_s	20	20	10.00
2018-04-24	06:22:19.05	K_s	20	20	10.00
2018-04-24	07:32:39.96	K_s	20	20	10.00
2018-04-24	08:29:59.37	K_s	20	20	10.00
2018-04-24	09:19:21.77	K_s	20	20	10.00
2018-04-24	10:09:50.40	K_s	20	20	10.00
2018-04-24	05:59:54.27	L'	10	9	0.200
2018-04-24	07:09:50.72	L'	10	8	0.200
2018-04-24	08:02:24.79	L'	10	0	0.200
2018-04-24	08:56:01.82	L'	10	10	0.200
2018-04-24	09:47:20.54	L'	10	10	0.200

Table 7.1: The list of the observations, along with their timings. The L'-band observations were conducted in between the K_s-band observations. Due to the poor image quality in L'-band within six observation intervals, in five cases one frame and in one case two frames are left out.

density of Sgr A* and S65 on the 22nd of April 2018 in K_s and L'-band are listed in Table 9.1 and 9.2, respectively.

7.1.5 Results: The second observation night, 24.04.2018

The second night of the observation, 24th of April 2018, starts with observations in the K_s-band at 5:11:24.21 UT. The first time slot in K_s-band in Fig. 7.3 shows on average an almost six times higher flux density of Sgr A* in comparison with the flux densities in the following time slots of the observation. Furthermore, in Fig. 7.3, we see that the flux density of the reference star, S65, remains unchanged.

Interestingly, the first L'-band observational interval after the detected flare in the K_s-band reveals no flare increase in the flux density of Sgr A* (see Fig. 7.4). As the last frame with a detectable flare in K_s-band is observed at 5:25:14.4236 UT and as the first observation in L'-band after the flare detection in K_s-band is conducted at 5:59:54.27, this leaves about 34 minutes between the K_s-band and L'-band observation. Moreover, from Fig. 7.3 we can see that the peak of the flare happens in the first part of the observation

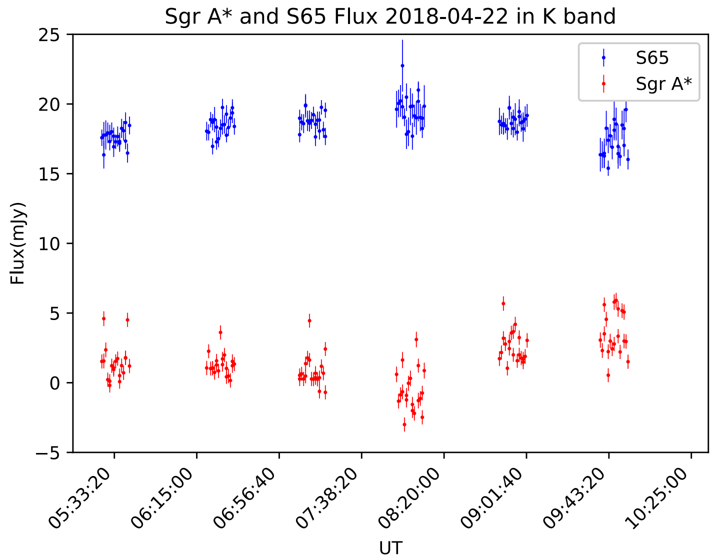

Figure 7.1: The light curve plot shows the flux density of Sgr A* and S65 in K_s-band on the 22nd of April 2018. The observations happen in six time intervals and the empty spaces in between the K_s-band observations are the time slots in which the L'-band observations are carried out. There is no flare detected in K_s-band over this course of observations.

and that the flux density is descending towards the end of the first time interval in K_s-band. Taken together, this might indicate that, within the 34 minutes between the two band observations, the flare has already descended and when the L'-band observation started, Sgr A* is in its quiescent phase again. The detailed flux density of Sgr A* and S65 in K_s and L'-band on the 24th of April 2018 are listed in Table 9.3 and 9.4. Finally, Fig. 7.5 shows two K_s-band exposures of the central 2 arcseconds. The right image is one of the exposures within the time interval, in which we have detected the flare in Sgr A* (Fig. 7.3), whereas the left image is an exposure from the quiescent phase of Sgr A*. Comparing the two images in Fig. 7.5 also clearly shows the increase in the brightness of Sgr A*.

7.1.6 Conclusion

In conclusion, we showed the simultaneous observations in K_s and L' band over two nights within the Event Horizon collaboration. We have shown a clear flare activity in the K_s band during the second night, whereas in the L' band we do at no point detect any flare activity. The origins of these flares are believed to lie in the accretion flow onto Sgr A*. Most models include some form of synchrotron emission to explain the occurring flares from the radio to the NIR regime. However, the correlation pattern between the wavelengths is not yet completely understood. Possible interpretations for the non-detection in the L'-band are that either the flare activity has decreased during the time of the filter switch or that for this specific flare there is no correlation between these two bands as e.g. already seen at other (Genzel et al. 2010; Witzel et al. 2018, 2021a). I note, however, that during the same time where the flare is recognizable in K_s band, there was a flare activity detected in X-ray observations (Event Horizon collaboration, D. Haggerd, private communication).

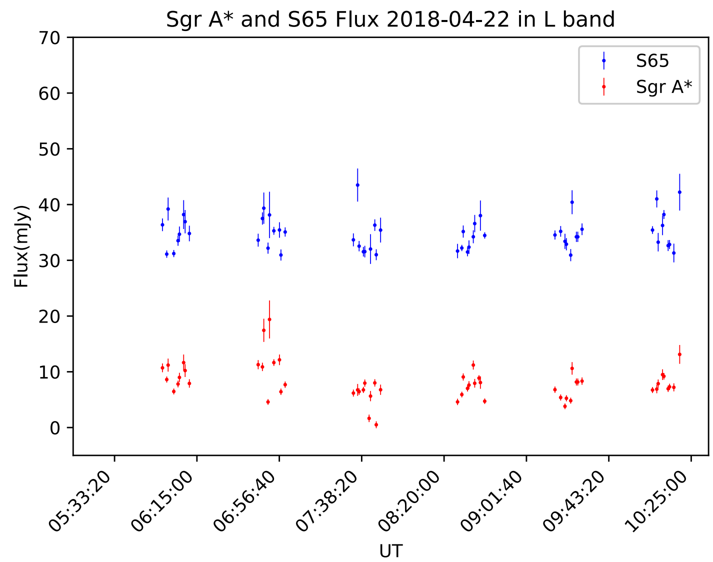

Figure 7.2: The six intervals of L′-band observations obtained on the 22nd of April 2018. The plot shows the flux density of Sgr A* and S65 within these six intervals which are in between the K_s-band time intervals in Fig 7.1. As for the K_s-band, the flux density of Sgr A* in L′-band shows there is no flare activity detected on the 22nd of April 2018.

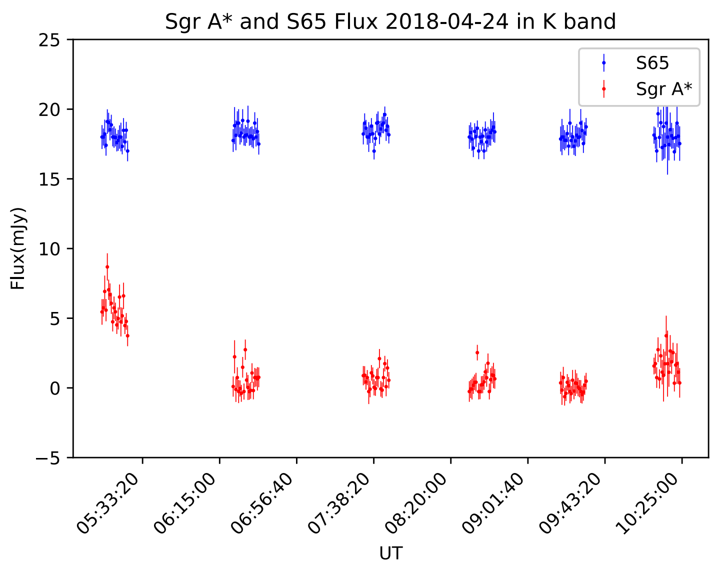

Figure 7.3: This plot depicts the flux density of Sgr A* and S65 in K_s-band on the 24th of April 2018. The observations are carried out in six time intervals. In the first time interval, which starts from 5:11:24.21 UT, there is an increase in the flux density of Sgr A* of almost of factor of 6 detectable.

Overall, however, the reason for the discrepancy in the K_s and L′ remains debated and more simultaneous observations are required.

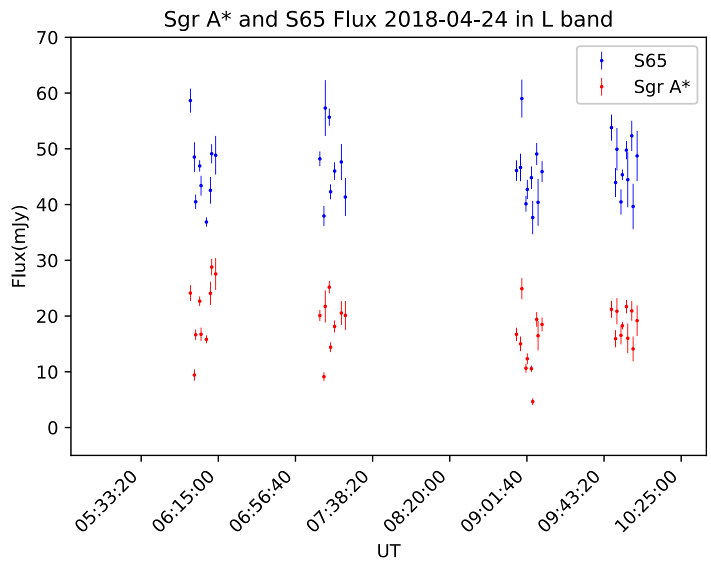

Figure 7.4: The plot shows the four L′-band observational intervals on the 24th of April 2018. The first observation block in L′-band starts at 5:59:54.27 UT, 34 minutes after the corresponding K_s-band observation. In contrast to that observations, there is no increase in the flux density of Sgr A* in L′-band.

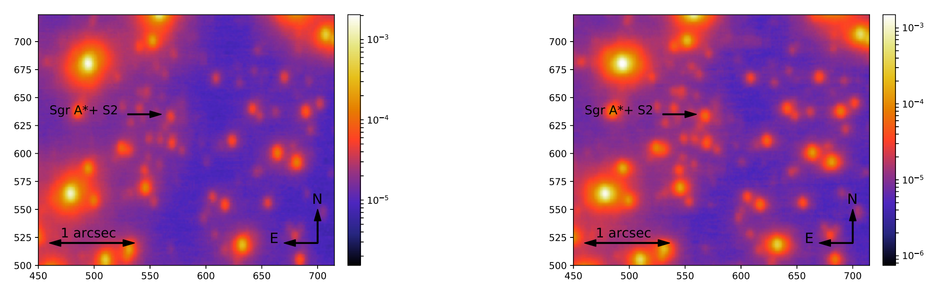

Figure 7.5: K_s-band images of the central 2 arcseconds, which are taken on the 24th of April 2018 by NAOS/CONICA. Up is north and east is left in both images, the color scale is logarithmic. The arrow in each image denotes the position of Sgr A* and S2 which are not spatially resolved at this time. Comparing the brightness at the position of the infrared counterpart of Sgr A* and S2 in the right and the left image shows a clear flaring activity of Sgr A* on the right image, whereas in the left image Sgr A* is in its quiescent phase.

7.2 Observations of Sgr A* in MIR with VLT

To date, Sgr A* has not been yet been detected at a wavelength of 8 μm. This non-detection is due to its location on a dust ridge and the high background emission emitted by the associated mini-spiral. For this reason, in the following we will present some observations of Sgr A* with VLT in order to give some constrains on future JWST observations. If observed with JWST, the successful detection of Sgr A* in MIR would support the thin synchrotron emission model.

7.2.1 Previous MIR observations of Sgr A* with VLT

Schoedel et al. (2006) observe an extended ridge of emission at the immediate vicinity of Sgr A*. They did simultaneous observations at 2.2 μm and 8.6μm on 4./5. and 5./6. of June 2006. The authors suggest that Sgr A* on the aforesaid dates was in its quasi-quiescent state because of a lack of any bright flare in 2.2 μm. They could put an upper limit on the flux density of Sgr A* at 8.6 μm of 22 ± 14 mJy and 60 ± 30 mJy for the two days, respectively. In a follow-up observation, Schödel et al. (2011) report no detection for the counterpart of Sgr A* in 8.6 μm in May 2007 with the VISIR BURST mode observations. They subtracted 5, 10 and 15 mJy at the position of Sgr A* from the maps and they obtain an upper limit of 10 mJy for the flux density of Sgr A* as the observed value (84 mJy de-reddening value). The authors conclude that the flux density of Sgr A* should be below 10 mJy and state that with the current instruments Sgr A* is not detectable in MIR even during its flaring activities. Haubois et al. (2012) provide the simultaneous observation of Sgr A* in mid-infrared, near-infrared, and sub-millimeter. For the mid-infrared observations, they used the MIR instrument in the BURST imaging mode in July 2007 for five nights. They observed a correlation between the NIR emission and sub-mm emission, but no source was detected in the MIR. They put a lowest upper limit for a flare at 8.59 μm of 22.4 mJy with an extinction of $A = 1.6 \pm 0.5$.

7.2.2 Result: Current observation of Sgr A* with VLT

For the current study I used the data observed by the VLT Imager and Spectrometer for the mid-infraRed (VISIR) in BURST mode in May, June and August 2018 in N-band (PAH1 filter at 8.59 μm) with a resolution of 45 mas/pixel. These data and reduction process are presented in detail in our common publication of Bhat et al. (2022). I applied aperture photometry to the data by using IRS5NE, IRS10W, IRS7 and IRS1W as calibrators, using an extinction of 2.04 for the PAH1 filter as given by Fritz et al. (2011).

I used three apertures for background calculations. To determine the position of Sgr A* in the N-band image, I took the position from K-band data (Parsa et al. 2017) and converted it to the corresponding coordinates in the N-band image. With this, I was able to determine the de-reddened flux density at the calculated position of the assumed counterpart of Sgr A* in N-band to 10 ± 0.3 mJy. This result is in very good agreement with the result of 10 mJy obtained by Schödel et al. (2011), thus presenting an independent support of their photometry results. The result is also in agreement with the theoretically expected spectral energy density of the mean emission from Sgr A* given by the aforementioned authors.

All in all, this result strengthens our afore-made statement that the detection of Sgr A* in MIR is highly challenging, also due to its projected position on-top of a dust ridge. Hence, further and higher sensitivity observations, e.g. with JWST, will be required to put a more restrictive upper bound on the flux density of Sgr A* in MIR.

7.3 First observations of the Galactic Center with JWST NIRSpec

As the main GC observations are scheduled for August 2023, at the moment there are no data available for the close vicinity of the SMBH SgrA*. However, there exist some NIRSpec

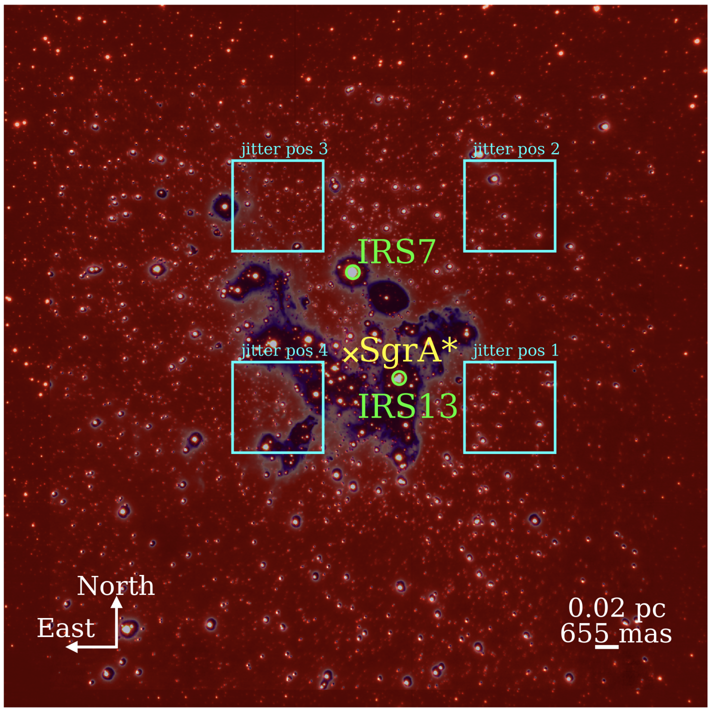

Figure 7.6: Combination of K and L band data towards the GC. The four cyan color squares show the jittering positions. The jitter position 4 has some overlaps with the dust emission from the mini-spiral. The spectra from these four jitter positions are used to produce the single spectrum (see Fig. 7.7)

IFU spectroscopy observations around the central black hole which cover some parts of the mini-spiral. The regular spectroscopy heavily limits us in structure finding. However, the integral field spectroscopy (IFU) empowers us to study the details of the structures. These data are observed within the first General Observers (GO) program of the Webb telescope observation programs. The program number is 1939 and the Principal Investigator (PI) of the program is J. Ryan Lu. The program is supposed to observe the entire central 0.36 pc in the GC. However, only some parts of these observations are available at the time of writing this thesis.

Fig. 7.6 shows the observed region. The observation is centered on Sgr A* with a fixed jitter pattern. The data is obtained by the higher-resolution G235H grating in the F170LP filter. The spectrum taken ranges from 1.6 to 3.3 μm and covers 4 disconnected 3×3 arcseconds wide field of views and no overlaps. The data from these four regions were combined into one single spectrum shown in Fig. 7.7. Unlike the ground-based spectroscopic observations, which need to get corrected for the telluric absorption and emission lines, in the space-based observations the cosmic showers/rays are challenging. Hence, a modified Whitaker-Hayes algorithm is used to correct the data. I emphasis that, although the spectrum is averaged over a wide region in the plane of sky, it already gives a very good impression of the capabilities of NIRSpec regarding GC observations, which I will discuss in the following.

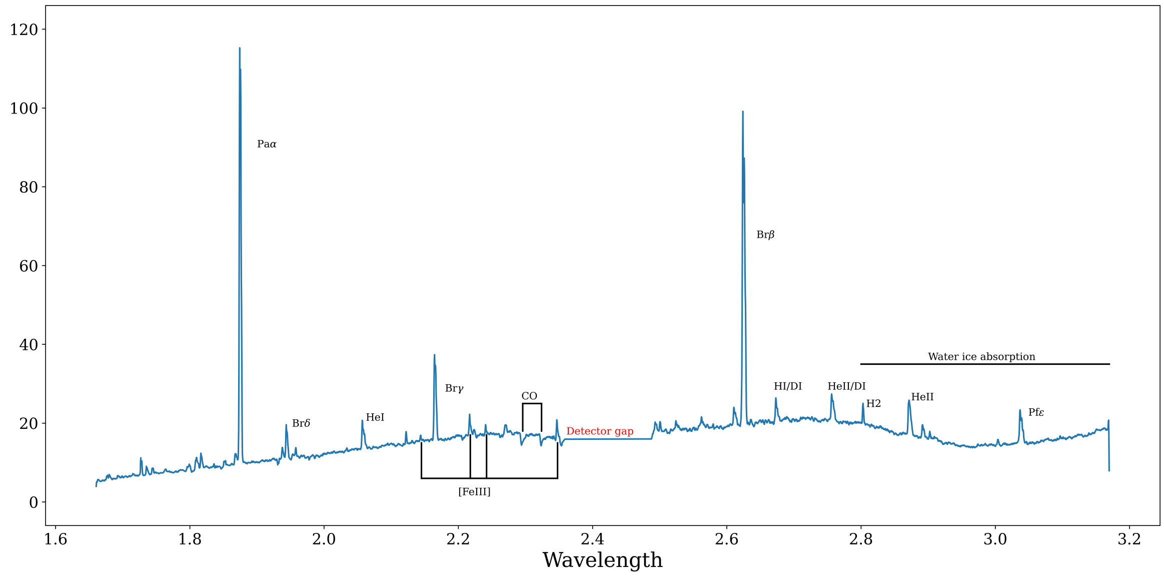

Figure 7.7: First spectrum of the GC obtained with JWST NIRSpec in units of MJy/sr. The spectrum shows several bright emission lines indicated in the figure which are in good agreement with the ground-based telescope observations from GC observed with Sinfoni (Eisenhauer et al. 2005). Image credit: F. Peißker.

7.3.1 Results

As stated before, Fig. 7.7 shows the first spectrum of the GC obtained by JWST NIRSpec. The lines close to HI and HeII around 2.7 μm can be associated with Deuterium. The observed [FeIII] lines around 2.2 – 2.3 μm might originate from the mini-spiral (jitter position 4 in Fig. 7.6). A prominent water ice absorptions are detectable. Importantly, the confusion-free Paschen α line enables new possibilities regarding the so-called dusty sources (see Ciurlo et al. 2020; Peißker et al. 2020c). However, the spectrum is dominated by emission from the interstellar medium as indicated by the height of the HeI/Brγ emission peak ratio: bright He stars in the GC would dominate the spectrum with a resulting HeI/Brγ ratio >>1; however, we find a HeI/Brγ ratio < 1.

In summary, the preliminary results presented here already indicate the great potential of JWST to put further constrains on the properties of the ambient medium of Sgr A* concerning its elemental composition. Moreover, the spectra of the GC can be used to identify the age and radial velocity of the stars, and their metallicities.

7.4 JWST MIRI observations of quasars

During the writing stage of this thesis, the MIRI data for the GC were not yet observed. Moreover, no observations of galactic centers of nearby galaxies were available yet. However, in the context of this thesis, I am interested in presenting the capability of MIRI to observe the GC. Therefore, I chose to study the spectra of three quasars which were observed within the already observed Early Released Science (ERS) programs of JWST.

Within the ERS observations, quasars appear to be the most appealing option to demonstrate the capabilities of MIRI observations. The data presented in this section are from

MIRI observations of three quasars, namely F2M1106, XID2028 and SDSSJ1652 at redshifts of 0.4, 1.5 and 2.9, respectively. The observations are conducted based on the ERS of JWST with the proposal number 1335. Certainly, the main drawback of these observations are the large redshifts of these quasars, being not lower than $z = 0.4$. In addition, due to the large distance, the quasars are only poorly resolved and almost point-source like. Despite that, we expect from this study to gain insight into the analysis and usage of MIRI data, which is great benefit for future JWST MIRI observations of the GC, for which we have guaranteed observation time within the proposal number 1226. In section 7.4.1, I first briefly introduce the basic properties of aforementioned quasars, before I discuss the JWST results (section 7.4.2).

7.4.1 Overview of the quasars

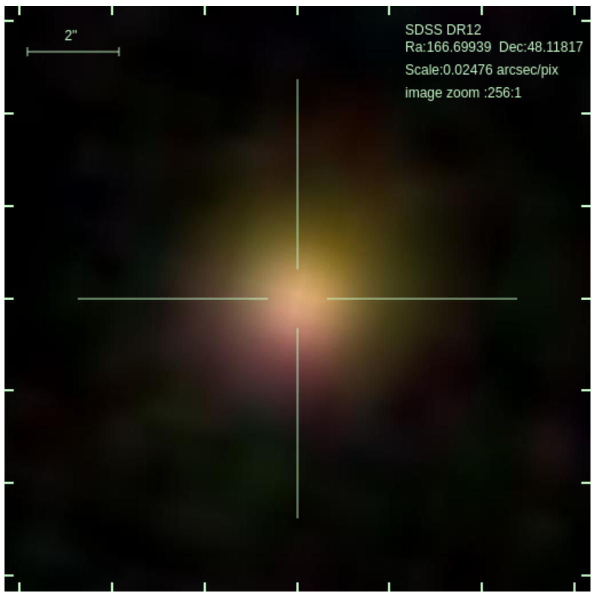

Figure 7.8: SDSS image of the quasar F2M1106. Image credits: The Sloan Digital Sky Survey (SDSS).

Quasi-stellar radio sources (quasars) are associated with extremely bright active galactic nuclei. Furthermore, quasars emit across the entire electromagnetic spectrum. Their spectra reveal absorption lines in addition to emission lines. However, usually the redshift of the absorption lines, caused by the intergalactic medium lying in front of it, are smaller than the redshifts of the emission lines. This gives us the opportunity to study the intergalactic medium in the early universe. Furthermore, for quasars within a redshift from 0 to 1, the FeII, OIII, H alpha lines are expected to be detected. From quasars within a redshift of 1 to 2, emission lines such as CIV, CIII, MgII, FeII are expected to be observed.

The first quasar in my study, which is the closest among three quasars that I study, is called F2M1106[1]. It is a red quasar and the only one among the sample which is visible in optical (see Fig. 7.8). It is located at (11^{h} 06^{min} 48.3200°, +48^{h} 07^{min} 12.30°) with a redshift of $z = 0.43499 \pm 0.00008$ corresponding to a velocity of $130407.339160 \pm 22.784230$ km s^{-1}. It

[1]This quasar is observed in surveys such as WISEA, 2MASSJ, SDSS and GALEXASC and is also called SDSS DR12 or J110648.32+480712.3.

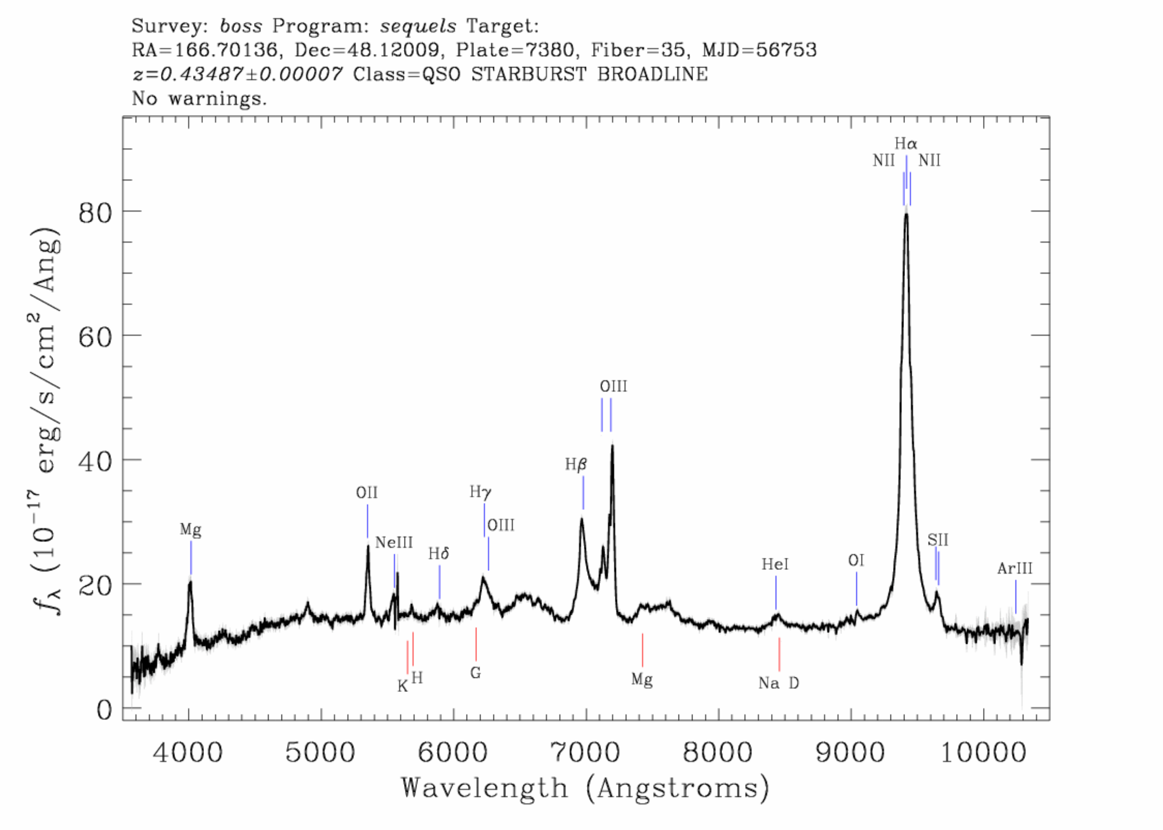

Figure 7.9: Spectrum of the quasar F2M1106 observed with SDSS showing various emission lines of different elements. Image credit: SDSS

is observed in UV, visible, NIR, far-infrared and radio regimes. The apparent magnitude of F2M1106 in UV is 20.3089 ± 0.156104 (Véron-Cetty & Véron 2006), in visible 17.697 ± 0.011, and in NIR 10.325 ± 0.006 (Cutri et al. 2013a). The flux in the radio regime is 74.55879 ± 14.93394 mJy (Shimwell et al. 2017). The SDSS spectrum observed towards F2M11106 is shown in Fig. 7.9. The spectrum of the source indicates the existence of emission lines such as Mg, OI, OII, OIII NeIII, SII, ArIII, NII, NIII, Hα, Hβ, Hγ, Hδ, and HeI.

XID2028 is an obscured quasar located at (10^{h} 02^{min} 11.2700°, $+01^{h}$ 37^{min} 6.60°) at redshift $z = 1.59200 \pm 0.00000$ (Trump et al. 2007; Brusa et al. 2010). It has been observed in the X-ray (Wang et al. 2016), visible (Gabor et al. 2009), NIR, FIR (Kartaltepe et al. 2010) and the radio regime (Schinnerer et al. 2007). Furthermore, XID2028 is observed in several surveys such as WISEA and several series of COSMOS. Unfortunately, there exists no spectrum of this source in SDSS.

The last quasar in my study, SDSSJ1652, is an obscured, extremely red quasar with outflows at the epoch of peak galaxy formation located at (16^{h} 52^{min} 2.6448°, $+17^{h}$ 28^{min} 52.39°) at a redshift of $z = 2.94229 \pm 0.00014$ with a corresponding velocity of $882076.474825 \pm 40.471987$ km s^{-1}. It is observed in the visible and NIR regime (Cutri et al. 2013b). In Fig. 7.10 we show the spectrum of SDSSJ1652 provided by SDSS. The spectrum shows emission lines such as Lyα, SIV+OIV, CIV, HeII, CIII and CII, which are among the most common absorption lines detected in quasar spectra. In section 7.4.2, I present the spectra of three aforementioned quasars, obtained by JWST MIRI, some size analysis of the quasars based on the MRS images.

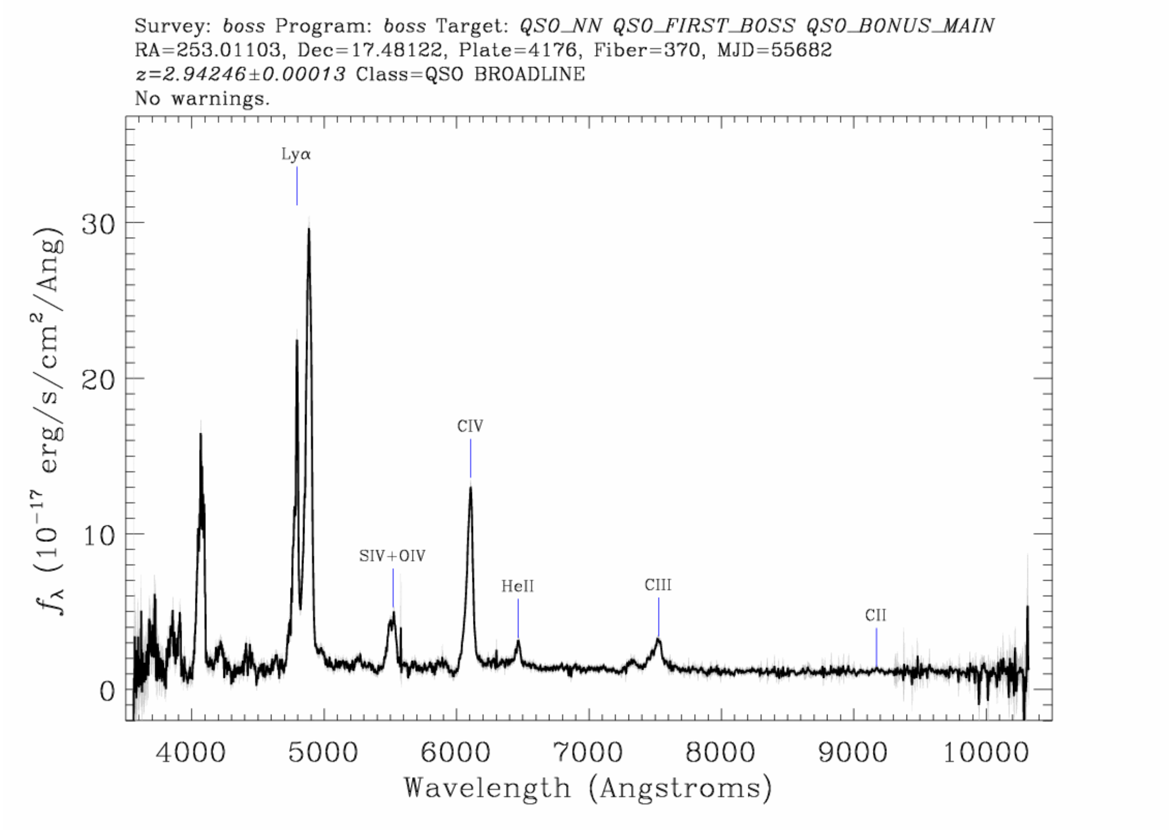

Figure 7.10: Spectrum of SDSSJ1652 taken with SDSS. Image credit: SDSS

7.4.2 Results

7.4.2.1 Size of the quasar

First, I investigate the apparent sizes of the three quasars in the obtained images. For this purpose, I take the stage-3 reduced data from the MAST portal (see Chapter 4). In Table 7.2 I lists the size, namely the Full-Width-Half-Maximum (FWHM), of the three quasars, which I determined via a Gaussian fit to the observed data. I list the mean of their measured FWHM in orthogonal directions. While XID2028 appears to be as compact as SDSSJ1652, the F2M1106 values are all somewhat larger than the value around 2.3 pixels which is obtained for SDSSJ1652 in channel 2 and 4. The latter quasar has the larges redshift and we therefore assume that here the infrared emission region can be taken as a point source for the JWST mirror.

Hence, I can estimate the infrared emission regions of the closest quasars by quadratically subtracting the SDSSJ1652 FWHM values from those of F2M1106. Using pixels scales of 0.196, 0.245, and 0.273 arcsec/pixel for channels 2 to 4, respectively, I can also calculate the source sizes in arcseconds. The results for F2M116 are given in Table 7.3.

For a Hubble constant of 70 km/s/Mpc and a cosmological deceleration factor q=0.05, we therefore find that the 7 μm to 27 μm MIR emission in F2M1106 is extended on a size scale of 1 to 1.5 kpc. This is exactly the size of many starburst rings found in nearby AGN hosts like e.g. IZw1, NGC1097, NGC6574 and others (see e.g. Purcell et al. 1993). Therefore, we argue that the nuclear emission of F21106 observed with JWST is not only provided by a compact AGN, but also by an extended star formation component.

name	redshift	chan.1	chan.2	chan.3	chan.4
F2M1106	0.434	2.43±0.02	2.48±0.02	2.92±0.02	2.41±0.03
XID2028	1.592	-	-	2.76±0.02	2.52±0.13
SDSSJ1652	2.942	-	2.33±0.04	2.72±0.02	2.27±0.03

Table 7.2: Apparent size of quasars measured in pixels for individual channels. Here the channels correspond to the following wavelength intervals: Channel 1: 4.9 - 7.65 μm, Channel 2: 7.51- 11.7 μm, Channel 3: 11.55 - 17.98 μm, Channel 4: 17.7- 27.9 μm.

name	redshift	unit	chan.2	chan.3	chan.4
F2M1106	0.434	pixels	0.85±0.02	1.06±0.02	0.81±0.03
F2M1106	0.434	arcsec	0.17±0.01	0.26±0.01	0.22±0.01

Table 7.3: Deconvolved (by quadratical subtraction) apparent quasar sizes for F2M1106 in pixels and arcseconds for individual channels.

Finally, I note that for all three quasars the FWHM of channel 3 are consistently larger than those of the other channels. One possible option would be related to the data reduction process of the stage-3 JWST pipeline. The actual origin of this discrepancy, however, is currently unclear and needs further investigation.

7.4.2.2 Spectroscopic results

Next, I investigate the spectral properties of the three quasars. I show the resulting spectra in the Figs. 7.11, 7.12 and 7.13. For all three spectra we see clear emission lines. In the MIRI observations of F2M1106 (Fig. 7.11), the CrII, FeI, FeII, KIV, KVI and CoIII emission lines are detected. For the quasar XID2028, the MgVIII, CaIV, SiIX, ArVI and FeII emission lines are detected in the MIRI spectrum (see Fig. 7.12). For SDSSJ1652, the CoII, SiIX, CaVII and MgIV emission lines among others are the detected lines in the MIRI spectrum (see Fig. 7.13). All the identified lines are well above the noise level of the observations.

However, I see that the fringing patterns affect the spectra. Particularly in channel 4, the identification of emission lines is not possible due to the strong fringing, an elevated background emission level, and the overall lack of strong emission lines. Moreover, we see that for all channels, the fringing patterns increase towards longer wavelengths. Therefore, it would be more beneficial to download the stage-2 data from MAST portal and run it through the JWST pipeline and apply the de-fringing algorithm on them. Another way to improve the quality of the spectra would be to run the data through the Q3dfit pipeline (Wylezalek et al. 2022). There de-fringing algorithms, will be very beneficial in case of nearby galaxies and Galactic Center. In summary, although these are still rather preliminary results, it shows the great potential of JWST to observe spectra with great detail within a short observation times.

7.5 Concluding remarks

In this chapter I have presented various NIR and MIR observations of the GC and quasars as their luminous extragalactic counterparts, which I have investigated during the course of my PhD. I have demonstrated the possibility of detecting flares towards Sgr A*, also showing that, possibly due to their short duration, it can be difficult to observe them simultaneously in different bands. I also confirmed the previously proposed challenge to observe Sgr A* in MIR due to its projected position on a dust ridge. Finally, I discussed novel spectra taken with JWST towards the GC and three quasars in order to demonstrate the great capability of JWST to obtain detailed, high-resolution, low-noise spectra with short observation times. My results demonstrate that with the expected, upcoming observations of JWST towards the GC, we will be able to characterize the structure, dynamics and metallicity of the ambient medium around Sgr A* and of the nuclear star cluster around it.

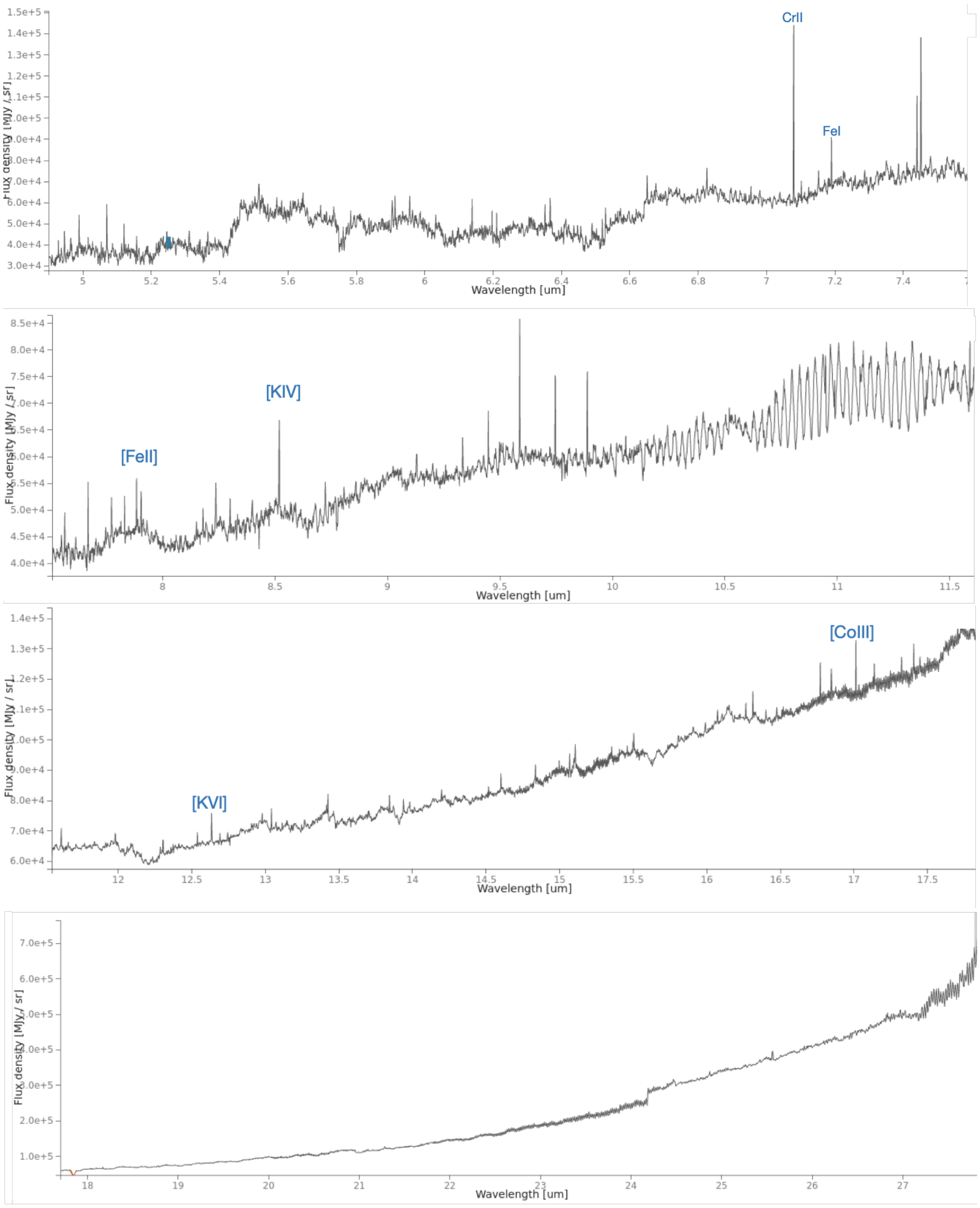

Figure 7.11: The spectra of F2M1106 from the channel 1 – 4 (from top to bottom) of the MIRI observations. Several emission lines can be detected in the spectra. In addition, for each channel we can recognize the effect of fringing towards longer wavelengths, leading to an increase in the noise. In channel 4, the spectrum is very noisy due strong fringing and a high background emission, making the identification of emission lines challenging. In addition, a lack of strong emission lines complicates line identification.

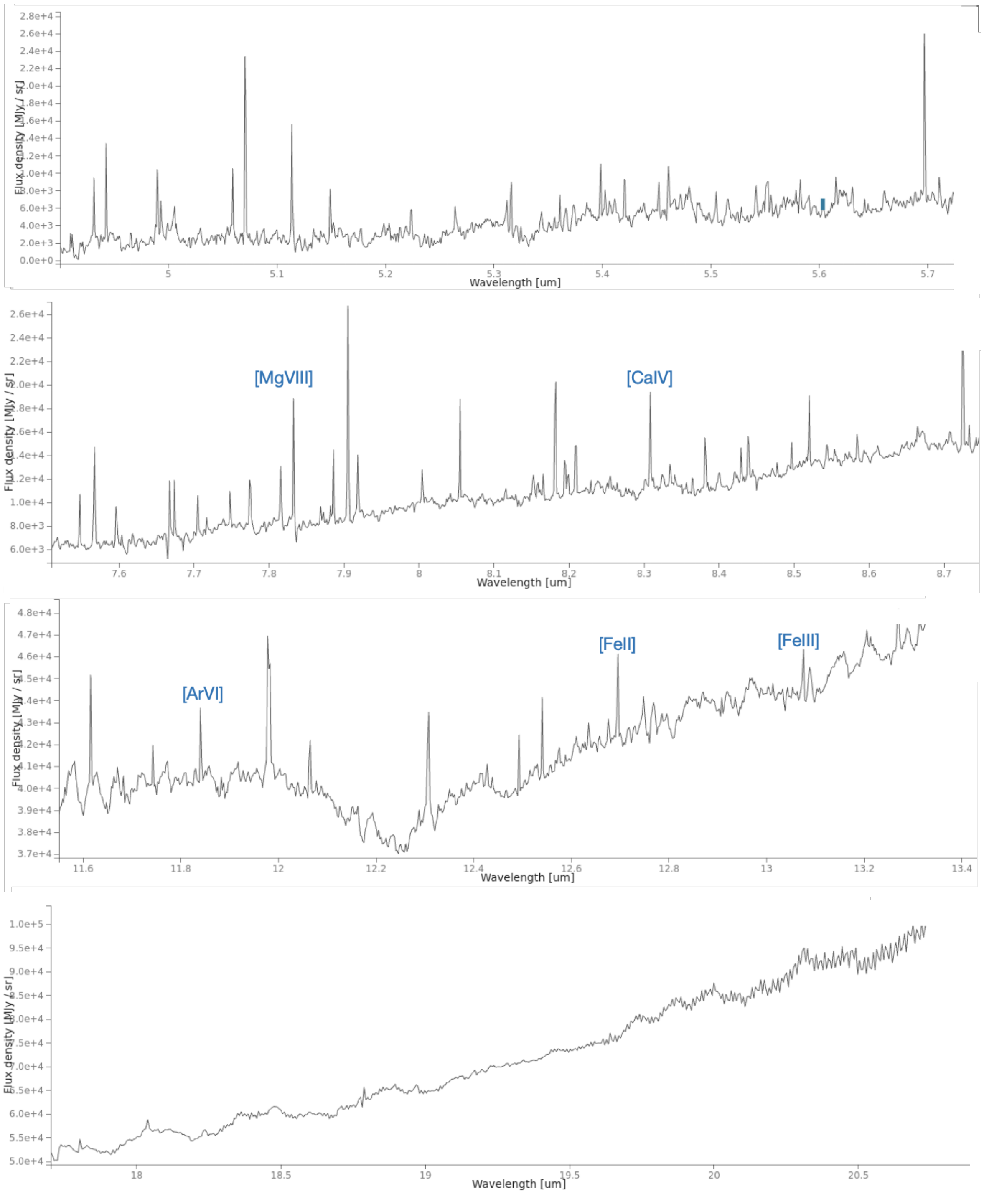

Figure 7.12: Same as in Fig. 7.11, but for the quasar XID2028.

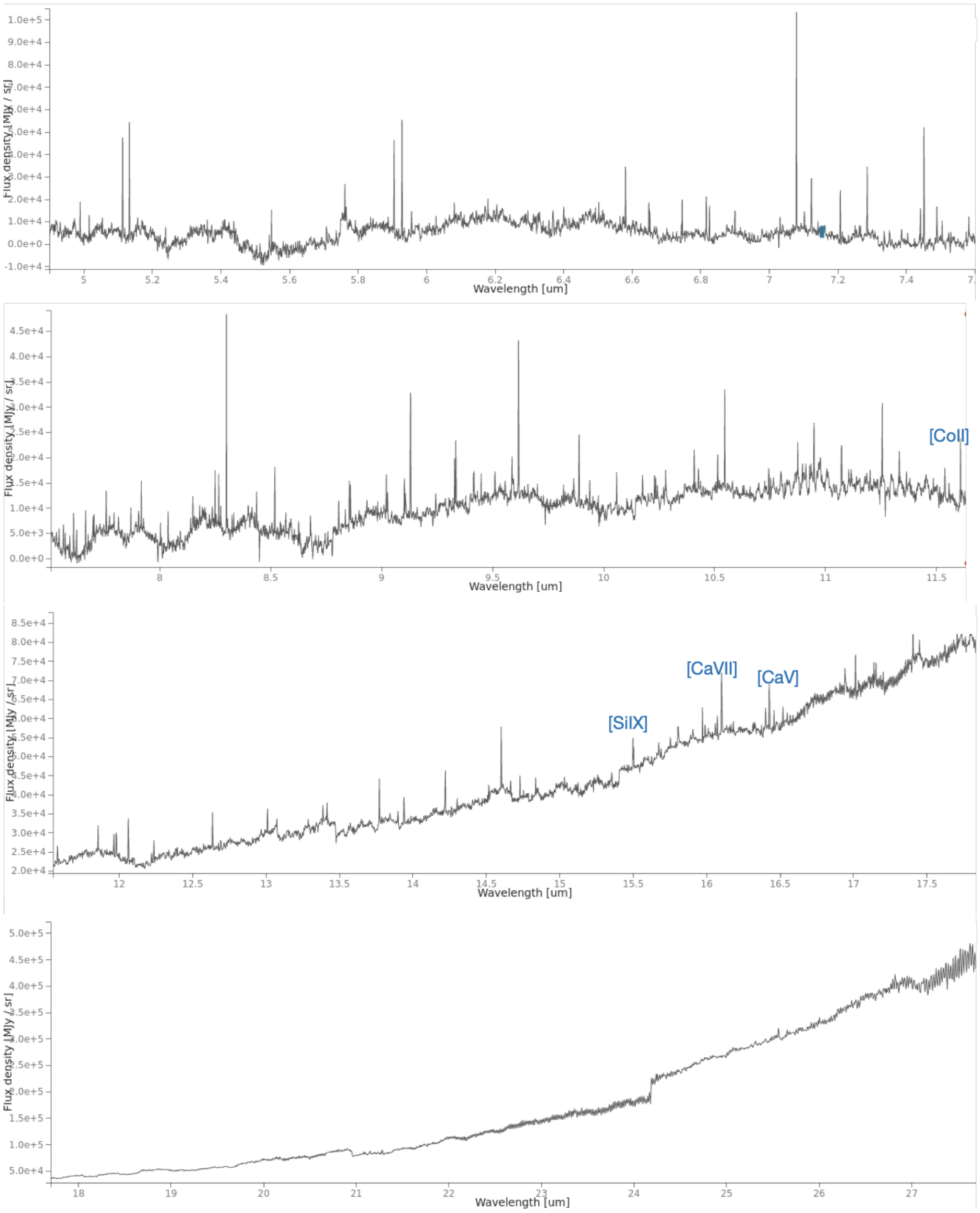

Figure 7.13: Same as in Fig. 7.11, but for the quasar SDSSJ1652.

CHAPTER 8

Summary and Outlook

8.1 Summary

In this thesis, I conducted research in the near- and mid-infrared domain in the Galactic Center (GC) at the close vicinity of the supermassive black hole (SMBH), Sgr A* and its infrared counterpart. The investigation presented in this thesis is relevant for the preparation of scientific observing programs conducted by the James Webb Space Telescope (JWST) and the MIRI spectrometer system on-board.

I began this thesis by introducing the physics of our own Milky Way, the environment of the GC focusing on its ambient medium, its associated stellar cluster as well as the SMBH, Sgr A* itself (Chapter 2). Next, I gave a brief overview of the basics of ground-based infrared astronomy (Chapter 3) and space-based observations with the focus on JWST (Chapter 4).

The first scientific paper related to my thesis (Chapter 5) is about my investigation of the ambient medium of the SMBH, Sgr A*, in mid-infrared. I constrained the accretion flow density profile near Sgr A* using the L'-band emission of the S2 star by deriving an upper density limit of 10^5 cm^{-3} at 1500 Schwarzschild radii. This research demonstrates how repeated observations of stars transiting the very center of the Milky Way in the immediate vicinity of the SMBH, Sgr A*, can be used to characterise the interstellar medium in this particular region. In this vicinity the ISM is dominated by the accretion flow onto Sgr A* and its winds. The expected bow shocks of fast-moving stars through that medium cause an enhancement of the flux density predominantly in the MIR wavelength domain. Due to the high flux density sensitivity of MIRI combined with the pointing stability of JWST, this will allow us to compare measurements of stars in this region. Hence, the GC community will be able to measure or put limits on the density of the interstellar medium in this region. The first paper in this thesis has laid the ground work for this methodology.

The second paper presented in this thesis (Chapter 6) is on the discovery of a dense association of stars in the vicinity of the SMBH, Sgr A*. The research highlights the apparent dense stellar association in the vicinity of IRS1W (N-sources) which lies opposite of IRS13E and eastward of Sgr A*. This association can be interpreted as a bound system due to a putative intermediate-mass black hole (IMBH) with a mass of about 10^{3-4} $M_\odot$ or a projection of a disk-like distribution of young He-stars and/or dust-enshrouded stars. This investigation has thus laid the groundwork for more sensitive observations with MIRI on-board JWST. Such observations including the spectroscopic information will provide the entire 3-dimensional velocity field to better probe the dynamical response of the stellar cluster to a putative IMBH.

The third part of this thesis (Chapter 7) presents first near- and mid-infrared GC observations obtained by VLT, observations with NIRSpec on-board of JWST showing the spectrum towards the GC, as well as extra-galactic observations taken by JWST-MIRI towards three quasars. The latter two show the great potential of the JWST MIRI and NIRSpec instruments to obtain high-resolution, low-noise spectra towards the GC. Unfortunately, at the time at which this thesis was submitted, no MIRI data on the GC had been taken. However, my preparatory work has allowed for the successful adoption of the GC as a MIRI team guaranteed time target, which will be observed in late 2023.

8.1.1 Relevance for future JWST observations

Overall, in this thesis I concentrated on the scientific applications and results obtained in the framework of MIRI projects which are focused on GC research. The technical aspects, I was involved in, comprehend the inclusion of tests of different operating modes of the simulation program MIRISim in its latest version, specifically for the GC, for observation planning and for verification of the detectability of different objects with MIRI and NIRSpec. It also included the designing of a sample application for the international astronomical community, in collaboration with the MIRI test team, for observation planning with MIRISim and data reduction with the data analysis pipeline. Finally, my work included the testing of the MIRISim application for the upcoming GC observations within the Guaranteed Time Observations for the Nearby Galaxy Collaboration. This also included the verification of the image quality on initial MIRI observational data of the GC and quasars which is shown in the final chapter of the thesis. Additional, more technical parts of the DLR-supported project were carried out in a participation in the MIRI Science Team, Calibration Team and Operations Group in the context of MIRI post-delivery support.

8.2 Outlook

By the aid of deep and high-resolution IFU data provided by the MIRI and NIRSpec instruments of JWST, we expect our understanding of the GC concerning the SMBH Sgr A*, star formation and the possible presence of IMBHs to be revolutionised within a few years time. The upcoming observations with JWST enable us to get access to the so-far neglected MIR wavelength regime in the GC. For example, the MIRI observations of the GC will be used to investigate the close approach of stars to the SMBH. Furthermore, MIRI observations from the adjacent region of IRS 1W can provide the radial velocities of the N-sources. This would allow us to fit their orbits, which would present a major step forward to confine the mass of the postulated IMBH.

In addition, MIRI observations on dusty sources, which might be associated with young stellar objects (Eckart et al. 2004, 2013; Moultaka et al. 2005; Mužić et al. 2010; Peißker et al. 2019, 2020c, 2021a; Ciurlo et al. 2020), can directly contribute to solving the "Paradox of Youth" with all its implications to star formation in crowded stellar fields. This can serve as a blueprint to extragalactic sources opening the door to explain so far speculative star formation processes in other galaxy centers. Furthermore, the dust filaments (Mužić et al. 2007; Bhat et al. 2022), bow-shock sources, dusty sources and YSOs in IRS13 , X3, X7 and X8 are important candidates to investigate with the MIRI instrument.

Next to the JWST, the Extremely Large Telescope (ELT), which is currently under construction, will outperform all the optical telescopes existing up to this date with a diameter of 39 m and a collecting area of about 1,000 m^2. The Multi-Adaptive Optics Imaging Camera for Deep Observations (MICADO) on the ELT with a field of view of about $19'' \times 19''$ and a relative astrometric resolution of about 1 mas will reveal unprecedented details about the GC. We expect many more resolved sources to be observed, which opens an opportunity to deepen our understanding of accretion flow mechanisms of black holes and star formation in the vicinity of black holes.

Furthermore, the Mid-infrared ELT Imager and Spectrograph (METIS) can be used to investigate the proper motion and the origin of the filaments in the GC, which will allow to put constrains on the wind and outflow motions around the SMBH, Sgr A*. In addition, as during the last years stars belonging to the S-star cluster, which are closer to Sgr A* than the S2 star, were observed (Peißker et al. 2020b,a; GRAVITY Collaboration et al. 2021), the method developed in Chapter 5 of this thesis would be a great opportunity to constrain the ambient medium density of Sgr A* with ELT at even smaller distance to it.

CHAPTER 9

Appendix

In Table 9.1 to 9.4 I list the observational data in K_s and L$'$-band from 22.04.2018 and 24.04.2018.

Date	UT time	Filter	Sgr A* (mJy)	S65 (mJy)
2018-04-22	05:27:27.7743	K_s	1.53 ± 0.51	17.58 ± 0.59
2018-04-22	05:28:10.6704	K_s	1.56 ± 0.53	17.76 ± 0.95
2018-04-22	05:28:54.1529	K_s	4.60 ± 0.53	16.35 ± 0.98
2018-04-22	05:29:36.3104	K_s	2.36 ± 0.53	17.78 ± 1.05
2018-04-22	05:30:20.7227	K_s	0.22 ± 0.51	17.93 ± 0.74
2018-04-22	05:31:03.7129	K_s	-0.19 ± 0.51	17.31 ± 0.64
2018-04-22	05:31:46.8436	K_s	0.11 ± 0.51	17.89 ± 0.62
2018-04-22	05:32:30.6488	K_s	1.22 ± 0.51	18.01 ± 0.67
2018-04-22	05:33:13.5090	K_s	0.95 ± 0.51	16.93 ± 0.73
2018-04-22	05:33:55.7793	K_s	1.06 ± 0.51	17.69 ± 0.62
2018-04-22	05:34:38.6875	K_s	1.54 ± 0.50	17.29 ± 0.52
2018-04-22	05:35:22.5070	K_s	1.73 ± 0.51	17.67 ± 0.72
2018-04-22	05:36:08.4177	K_s	0.51 ± 0.51	17.31 ± 0.63
2018-04-22	05:36:52.2950	K_s	0.08 ± 0.51	17.18 ± 0.62
2018-04-22	05:37:34.6384	K_s	1.23 ± 0.51	18.25 ± 0.69
2018-04-22	05:38:19.0569	K_s	0.71 ± 0.51	18.08 ± 0.70
2018-04-22	05:39:04.1524	K_s	1.80 ± 0.51	18.67 ± 0.73
2018-04-22	05:39:46.3737	K_s	1.77 ± 0.50	17.34 ± 0.58
2018-04-22	05:40:29.5719	K_s	4.51 ± 0.51	16.48 ± 0.69
2018-04-22	05:41:12.6704	K_s	1.20 ± 0.51	18.46 ± 0.64
2018-04-22	06:20:49.8042	K_s	1.06 ± 0.51	18.05 ± 0.67
2018-04-22	06:21:34.4458	K_s	2.26 ± 0.50	17.97 ± 0.58
2018-04-22	06:22:17.5522	K_s	1.02 ± 0.50	18.88 ± 0.55
2018-04-22	06:23:00.9025	K_s	1.03 ± 0.50	16.96 ± 0.58
2018-04-22	06:23:44.0070	K_s	1.06 ± 0.50	18.69 ± 0.59

2018-04-22	06:24:26.6891	K_s	0.74 ± 0.52	18.88 ± 0.91
2018-04-22	06:25:09.6864	K_s	1.57 ± 0.50	17.28 ± 0.56
2018-04-22	06:25:51.3438	K_s	1.28 ± 0.50	18.34 ± 0.58
2018-04-22	06:26:34.4630	K_s	0.85 ± 0.51	17.51 ± 0.61
2018-04-22	06:27:16.6304	K_s	3.61 ± 0.51	18.25 ± 0.64
2018-04-22	06:27:59.7117	K_s	1.30 ± 0.51	19.75 ± 0.62
2018-04-22	06:28:42.9800	K_s	1.71 ± 0.51	18.50 ± 0.69
2018-04-22	06:29:26.6951	K_s	1.99 ± 0.51	18.53 ± 0.66
2018-04-22	06:30:11.2257	K_s	1.03 ± 0.51	19.27 ± 0.65
2018-04-22	06:30:54.5711	K_s	0.42 ± 0.50	17.76 ± 0.51
2018-04-22	06:31:37.3946	K_s	0.48 ± 0.51	18.31 ± 0.61
2018-04-22	06:32:19.7216	K_s	0.16 ± 0.51	18.99 ± 0.64
2018-04-22	06:33:02.6469	K_s	1.53 ± 0.51	19.73 ± 0.61
2018-04-22	06:33:45.7505	K_s	1.22 ± 0.51	19.36 ± 0.73
2018-04-22	06:34:28.9178	K_s	1.34 ± 0.50	18.39 ± 0.59
2018-04-22	07:07:13.1175	K_s	0.53 ± 0.50	17.80 ± 0.55
2018-04-22	07:07:55.7177	K_s	0.27 ± 0.51	18.98 ± 0.61
2018-04-22	07:08:38.0800	K_s	0.64 ± 0.50	18.70 ± 0.59
2018-04-22	07:09:21.7354	K_s	0.27 ± 0.51	18.59 ± 0.68
2018-04-22	07:10:04.6969	K_s	1.37 ± 0.51	19.92 ± 0.69
2018-04-22	07:10:47.7391	K_s	0.48 ± 0.52	19.87 ± 0.84
2018-04-22	07:11:30.9094	K_s	1.78 ± 0.51	18.79 ± 0.73
2018-04-22	07:12:14.7568	K_s	1.63 ± 0.51	18.78 ± 0.76
2018-04-22	07:12:57.0831	K_s	4.45 ± 0.50	18.62 ± 0.56
2018-04-22	07:13:39.5556	K_s	0.27 ± 0.51	18.82 ± 0.61
2018-04-22	07:14:22.6287	K_s	0.25 ± 0.50	19.23 ± 0.58
2018-04-22	07:15:05.6510	K_s	0.68 ± 0.51	18.55 ± 0.66
2018-04-22	07:15:48.9194	K_s	0.36 ± 0.51	17.64 ± 0.66
2018-04-22	07:16:33.5469	K_s	0.25 ± 0.51	18.83 ± 0.63
2018-04-22	07:17:15.9911	K_s	0.36 ± 0.51	18.85 ± 0.61
2018-04-22	07:17:58.9685	K_s	-0.62 ± 0.51	18.06 ± 0.61
2018-04-22	07:18:43.0579	K_s	1.18 ± 0.50	19.76 ± 0.52
2018-04-22	07:19:25.9884	K_s	0.68 ± 0.50	18.15 ± 0.58
2018-04-22	07:20:09.6918	K_s	-0.69 ± 0.51	17.67 ± 0.62
2018-04-22	07:20:52.1539	K_s	2.42 ± 0.50	19.55 ± 0.55
2018-04-22	07:56:51.8827	K_s	0.60 ± 0.56	19.62 ± 1.32
2018-04-22	07:57:37.2482	K_s	-1.30 ± 0.53	20.04 ± 0.99
2018-04-22	07:58:21.9270	K_s	-0.80 ± 0.54	20.22 ± 1.14
2018-04-22	07:59:05.0092	K_s	1.63 ± 0.58	22.75 ± 1.86
2018-04-22	07:59:47.5694	K_s	-0.60 ± 0.53	19.80 ± 0.89
2018-04-22	08:00:30.7068	K_s	-3.00 ± 0.51	19.05 ± 0.64
2018-04-22	08:01:14.5833	K_s	-0.90 ± 0.53	20.49 ± 0.99
2018-04-22	08:01:58.6577	K_s	-1.20 ± 0.54	17.83 ± 1.06
2018-04-22	08:02:41.6840	K_s	-0.00 ± 0.54	18.01 ± 1.03
2018-04-22	08:03:24.9321	K_s	0.31 ± 0.56	19.81 ± 1.33
2018-04-22	08:04:08.2329	K_s	-2,00 ± 0.53	19.85 ± 0.91
2018-04-22	08:04:51.6171	K_s	-1.50 ± 0.54	17.69 ± 0.97

2018-04-22	08:05:36.3789	K_s	-2.20 ± 0.52	19.15 ± 0.80
2018-04-22	08:06:20.2230	K_s	3.10 ± 0.56	19.01 ± 1.22
2018-04-22	08:07:04.0785	K_s	-1.20 ± 0.56	20.19 ± 1.43
2018-04-22	08:07:46.6000	K_s	1.23 ± 0.50	21.00 ± 0.54
2018-04-22	08:08:29.1232	K_s	-1.10 ± 0.53	19.03 ± 0.98
2018-04-22	08:09:11.5243	K_s	-2.40 ± 0.51	18.24 ± 0.68
2018-04-22	08:09:56.1679	K_s	-0.70 ± 0.52	18.98 ± 0.84
2018-04-22	08:10:38.6621	K_s	0.87 ± 0.57	19.84 ± 1.51
2018-04-22	08:48:39.7330	K_s	1.73 ± 0.53	18.75 ± 0.98
2018-04-22	08:49:23.6496	K_s	2.17 ± 0.51	18.51 ± 0.66
2018-04-22	08:50:06.8276	K_s	5.68 ± 0.52	18.60 ± 0.77
2018-04-22	08:50:50.1713	K_s	3.19 ± 0.51	18.46 ± 0.66
2018-04-22	08:51:32.5810	K_s	2.78 ± 0.50	18.44 ± 0.54
2018-04-22	08:52:17.5683	K_s	1.04 ± 0.52	18.21 ± 0.78
2018-04-22	08:53:01.0096	K_s	2.45 ± 0.50	19.70 ± 0.54
2018-04-22	08:53:44.1769	K_s	2.96 ± 0.52	19.74 ± 0.85
2018-04-22	08:54:26.7681	K_s	3.57 ± 0.52	18.60 ± 0.83
2018-04-22	08:55:10.1348	K_s	2.00 ± 0.50	19.05 ± 0.55
2018-04-22	08:55:52.7008	K_s	3.66 ± 0.51	18.24 ± 0.64
2018-04-22	08:56:35.8401	K_s	4.19 ± 0.54	18.91 ± 1.15
2018-04-22	08:57:19.5458	K_s	1.58 ± 0.51	17.98 ± 0.60
2018-04-22	08:58:02.6832	K_s	3.24 ± 0.52	19.45 ± 0.89
2018-04-22	08:58:45.2092	K_s	2.00 ± 0.51	19.10 ± 0.70
2018-04-22	08:59:27.7714	K_s	1.77 ± 0.51	18.66 ± 0.66
2018-04-22	09:00:10.6917	K_s	1.70 ± 0.52	18.22 ± 0.93
2018-04-22	09:00:53.7882	K_s	1.48 ± 0.51	18.75 ± 0.65
2018-04-22	09:01:37.0024	K_s	1.89 ± 0.52	18.92 ± 0.92
2018-04-22	09:02:19.4307	K_s	3.04 ± 0.52	19.18 ± 0.82
2018-04-22	09:39:33.6517	K_s	3.06 ± 0.55	16.36 ± 1.21
2018-04-22	09:40:17.6693	K_s	2.31 ± 0.53	16.36 ± 0.96
2018-04-22	09:41:00.7034	K_s	3.51 ± 0.54	16.46 ± 1.06
2018-04-22	09:41:43.7550	K_s	5.60 ± 0.52	16.27 ± 0.83
2018-04-22	09:42:27.1911	K_s	4.55 ± 0.54	18.26 ± 1.25
2018-04-22	09:43:09.6284	K_s	0.54 ± 0.50	15.39 ± 0.55
2018-04-22	09:43:52.1497	K_s	2.23 ± 0.53	17.40 ± 0.93
2018-04-22	09:44:36.1653	K_s	2.99 ± 0.52	17.72 ± 0.84
2018-04-22	09:45:19.9906	K_s	2.43 ± 0.52	16.90 ± 0.87
2018-04-22	09:46:03.7332	K_s	2.78 ± 0.51	18.12 ± 0.60
2018-04-22	09:46:46.7635	K_s	5.79 ± 0.56	18.90 ± 1.51
2018-04-22	09:47:30.1210	K_s	5.91 ± 0.54	18.56 ± 1.18
2018-04-22	09:48:12.5621	K_s	3.34 ± 0.51	16.44 ± 0.71
2018-04-22	09:48:54.8193	K_s	5.30 ± 0.57	16.95 ± 1.59
2018-04-22	09:49:37.9706	K_s	2.21 ± 0.51	16.24 ± 0.68
2018-04-22	09:50:22.1471	K_s	5.17 ± 0.53	18.49 ± 1.03
2018-04-22	09:51:04.5892	K_s	2.99 ± 0.52	17.03 ± 0.79
2018-04-22	09:51:47.7788	K_s	5.07 ± 0.55	18.24 ± 1.42
2018-04-22	09:52:32.1343	K_s	2.96 ± 0.52	19.60 ± 0.91

2018-04-22	09:53:14.5633	K_s	1.51 ± 0.51	16.02 ± 0.72

Table 9.1: K_s-band observations in 22.04.2018

Date	UT time	Filter	Sgr A* (mJy)	S65 (mJy)
2018-04-22	05:57:34.4735	L′	10.71 ± 0.79	36.37 ± 1.14
2018-04-22	05:59:43.8697	L′	8.61 ± 0.55	31.11 ± 0.66
2018-04-22	06:00:25.8029	L′	11.20 ± 1.17	39.20 ± 2.06
2018-04-22	06:03:17.5402	L′	6.47 ± 0.53	31.21 ± 0.64
2018-04-22	06:05:26.7352	L′	7.81 ± 0.60	33.52 ± 0.92
2018-04-22	06:06:08.8654	L′	8.99 ± 0.83	34.68 ± 1.38
2018-04-22	06:08:16.4643	L′	11.65 ± 1.45	38.20 ± 2.59
2018-04-22	06:09:01.9952	L′	10.22 ± 1.15	36.93 ± 2.09
2018-04-22	06:11:10.5931	L′	7.91 ± 0.76	34.81 ± 1.40
2018-04-22	06:45:59.1812	L′	11.28 ± 0.82	33.61 ± 1.16
2018-04-22	06:48:07.7927	L′	10.88 ± 0.75	37.50 ± 1.10
2018-04-22	06:48:49.5321	L′	17.44 ± 2.08	39.35 ± 2.81
2018-04-22	06:50:57.7229	L′	4.59 ± 0.51	32.18 ± 1.00
2018-04-22	06:51:42.6497	L′	19.39 ± 3.41	38.14 ± 4.16
2018-04-22	06:53:54.6491	L′	11.65 ± 0.60	35.29 ± 0.71
2018-04-22	06:56:44.5710	L′	12.15 ± 0.95	35.44 ± 1.39
2018-04-22	06:57:29.3005	L′	6.42 ± 0.57	30.95 ± 1.00
2018-04-22	06:59:38.1146	L′	7.69 ± 0.57	35.08 ± 0.83
2018-04-22	07:34:08.2162	L′	6.18 ± 0.63	33.67 ± 1.16
2018-04-22	07:36:17.2320	L′	6.75 ± 1.07	43.50 ± 2.97
2018-04-22	07:37:02.3746	L′	6.45 ± 0.58	32.54 ± 0.93
2018-04-22	07:39:11.7988	L′	6.75 ± 0.55	31.54 ± 0.86
2018-04-22	07:39:54.9392	L′	7.97 ± 0.65	31.56 ± 1.04
2018-04-22	07:42:48.1058	L′	5.64 ± 0.92	32.02 ± 2.67
2018-04-22	07:44:58.3101	L′	8.01 ± 0.66	36.31 ± 1.04
2018-04-22	07:45:42.2473	L′	0.50 ± 0.62	31.00 ± 0.98
2018-04-22	07:47:53.4375	L′	6.78 ± 0.92	35.42 ± 2.23
2018-04-22	08:26:49.3672	L′	4.60 ± 0.57	31.66 ± 1.29
2018-04-22	08:28:59.1627	L′	5.92 ± 0.51	32.21 ± 0.56
2018-04-22	08:29:42.3116	L′	9.07 ± 0.64	35.16 ± 1.09
2018-04-22	08:31:51.9218	L′	7.02 ± 0.56	31.49 ± 0.77
2018-04-22	08:32:36.0531	L′	7.62 ± 0.70	32.36 ± 1.22
2018-04-22	08:34:47.4474	L′	11.21 ± 0.81	34.22 ± 1.16
2018-04-22	08:35:30.1790	L′	7.94 ± 0.78	36.59 ± 1.55
2018-04-22	08:38:23.3029	L′	8.07 ± 1.12	38.02 ± 2.71
2018-04-22	08:40:33.6955	L′	4.72 ± 0.50	34.46 ± 0.57
2018-04-22	09:16:05.5965	L′	6.79 ± 0.57	34.54 ± 0.82
2018-04-22	09:18:58.3609	L′	5.39 ± 0.55	35.19 ± 0.96
2018-04-22	09:21:09.3821	L′	3.81 ± 0.51	33.40 ± 1.36
2018-04-22	09:21:52.5156	L′	5.25 ± 0.55	32.89 ± 1.10

2018-04-22	09:24:03.3459	L′	4.82 ± 0.54	30.93 ± 1.09
2018-04-22	09:24:46.0790	L′	10.61 ± 1.13	40.42 ± 2.15
2018-04-22	09:26:55.2871	L′	8.17 ± 0.63	34.21 ± 0.92
2018-04-22	09:27:38.2308	L′	8.17 ± 0.63	34.21 ± 0.92
2018-04-22	09:29:47.4548	L′	8.33 ± 0.66	35.57 ± 1.05
2018-04-22	10:05:26.0274	L′	6.73 ± 0.54	35.43 ± 0.69
2018-04-22	10:07:35.2335	L′	6.89 ± 0.74	41.01 ± 1.53
2018-04-22	10:08:18.1657	L′	7.87 ± 0.75	33.25 ± 1.66
2018-04-22	10:10:30.5604	L′	9.49 ± 0.96	36.25 ± 1.74
2018-04-22	10:11:11.8925	L′	9.20 ± 0.59	38.21 ± 0.80
2018-04-22	10:13:20.2894	L′	6.96 ± 0.58	32.64 ± 0.98
2018-04-22	10:14:03.2225	L′	7.30 ± 0.56	32.83 ± 0.81
2018-04-22	10:16:13.2227	L′	7.21 ± 0.72	31.31 ± 1.68
2018-04-22	10:19:10.3576	L′	13.12 ± 1.69	42.22 ± 3.30

Table 9.2: L′-band observations in 22.04.2018

Date	UT time	Filter	Sgr A* (mJy)	S65 (mJy)
2018-04-24	05:11:24.2143	K_s	5.45 ± 0.92	18.00 ± 0.86
2018-04-24	05:12:07.4617	K_s	5.74 ± 0.63	18.00 ± 0.61
2018-04-24	05:12:51.4141	K_s	6.92 ± 1.14	18.22 ± 1.03
2018-04-24	05:13:34.4076	K_s	5.58 ± 0.80	17.41 ± 0.75
2018-04-24	05:14:16.4347	K_s	8.68 ± 0.98	19.11 ± 0.88
2018-04-24	05:14:59.4362	K_s	7.04 ± 0.73	19.04 ± 0.70
2018-04-24	05:15:42.3767	K_s	6.69 ± 0.81	18.52 ± 0.76
2018-04-24	05:16:25.4289	K_s	6.07 ± 0.76	18.87 ± 0.73
2018-04-24	05:17:10.4166	K_s	4.74 ± 0.69	18.00 ± 0.67
2018-04-24	05:17:53.4773	K_s	5.74 ± 0.82	18.00 ± 0.77
2018-04-24	05:18:38.4007	K_s	5.46 ± 0.66	17.97 ± 0.64
2018-04-24	05:19:23.4496	K_s	4.52 ± 0.65	17.60 ± 0.63
2018-04-24	05:20:08.3730	K_s	4.98 ± 0.79	17.76 ± 0.75
2018-04-24	05:20:51.4927	K_s	6.52 ± 0.90	18.00 ± 0.84
2018-04-24	05:21:36.4231	K_s	4.74 ± 1.05	18.00 ± 1.03
2018-04-24	05:22:19.4107	K_s	5.17 ± 0.58	17.33 ± 0.57
2018-04-24	05:23:02.4523	K_s	6.60 ± 0.95	18.48 ± 0.88
2018-04-24	05:23:46.4223	K_s	4.47 ± 0.61	17.65 ± 0.61
2018-04-24	05:24:30.4201	K_s	4.77 ± 0.60	18.49 ± 0.60
2018-04-24	05:25:14.4236	K_s	3.74 ± 0.75	17.00 ± 0.74
2018-04-24	06:22:19.0477	K_s	0.10 ± 0.73	17.75 ± 0.82
2018-04-24	06:23:04.4614	K_s	2.23 ± 1.19	18.82 ± 1.33
2018-04-24	06:23:47.4347	K_s	-0.11 ± 0.90	18.12 ± 1.07
2018-04-24	06:24:32.4544	K_s	0.74 ± 0.74	19.00 ± 0.85
2018-04-24	06:25:15.4460	K_s	-0.26 ± 0.83	19.00 ± 1.00
2018-04-24	06:26:00.4454	K_s	-0.04 ± 0.58	18.08 ± 0.62
2018-04-24	06:26:43.4643	K_s	-0.39 ± 0.61	18.28 ± 0.66

2018-04-24	06:27:26.4344	K_s	1.48 ± 0.74	19.19 ± 0.81
2018-04-24	06:28:09.3997	K_s	-0.26 ± 0.58	18.00 ± 0.61
2018-04-24	06:28:52.4974	K_s	2.74 ± 0.73	18.11 ± 0.75
2018-04-24	06:29:35.4887	K_s	0.56 ± 0.55	18.15 ± 0.57
2018-04-24	06:30:18.4779	K_s	0.03 ± 0.90	19.14 ± 1.11
2018-04-24	06:31:03.3998	K_s	-0.26 ± 0.59	18.00 ± 0.62
2018-04-24	06:31:46.4129	K_s	-0.18 ± 0.60	18.07 ± 0.65
2018-04-24	06:32:29.4544	K_s	1.07 ± 0.70	18.02 ± 0.75
2018-04-24	06:33:13.4578	K_s	-0.19 ± 0.63	17.88 ± 0.69
2018-04-24	06:33:58.4136	K_s	0.74 ± 0.69	19.00 ± 0.78
2018-04-24	06:34:41.4413	K_s	0.74 ± 0.64	18.00 ± 0.68
2018-04-24	06:35:24.4683	K_s	0.65 ± 0.84	18.39 ± 0.97
2018-04-24	06:36:08.4681	K_s	0.76 ± 0.71	17.50 ± 0.76
2018-04-24	07:32:39.9564	K_s	0.88 ± 0.69	18.22 ± 0.75
2018-04-24	07:33:23.4358	K_s	0.91 ± 0.65	19.00 ± 0.70
2018-04-24	07:34:06.4710	K_s	0.43 ± 0.56	18.64 ± 0.59
2018-04-24	07:34:49.4705	K_s	0.74 ± 0.54	18.00 ± 0.55
2018-04-24	07:35:36.4586	K_s	-0.26 ± 0.90	18.00 ± 1.07
2018-04-24	07:36:19.4210	K_s	-0.09 ± 0.58	18.17 ± 0.61
2018-04-24	07:37:02.4593	K_s	1.08 ± 0.56	18.79 ± 0.57
2018-04-24	07:37:46.4648	K_s	0.86 ± 0.61	18.23 ± 0.65
2018-04-24	07:38:29.4723	K_s	0.04 ± 0.58	16.99 ± 0.60
2018-04-24	07:39:12.4779	K_s	-0.04 ± 0.53	17.90 ± 0.54
2018-04-24	07:39:55.4589	K_s	0.74 ± 0.62	19.00 ± 0.67
2018-04-24	07:40:38.4443	K_s	0.74 ± 0.71	19.05 ± 0.79
2018-04-24	07:41:23.5143	K_s	2.10 ± 0.69	18.21 ± 0.72
2018-04-24	07:42:07.4778	K_s	-0.07 ± 0.56	18.58 ± 0.59
2018-04-24	07:42:51.4470	K_s	-0.16 ± 0.56	18.87 ± 0.59
2018-04-24	07:43:34.5057	K_s	0.74 ± 0.67	19.00 ± 0.73
2018-04-24	07:44:17.4342	K_s	1.74 ± 0.56	19.61 ± 0.58
2018-04-24	07:45:00.5033	K_s	0.09 ± 0.69	18.49 ± 0.77
2018-04-24	07:45:43.4337	K_s	1.43 ± 0.62	18.78 ± 0.66
2018-04-24	07:46:27.4991	K_s	0.55 ± 0.59	18.16 ± 0.62
2018-04-24	08:29:59.3657	K_s	-0.26 ± 0.74	18.00 ± 0.85
2018-04-24	08:30:42.5113	K_s	-0.08 ± 0.65	18.32 ± 0.73
2018-04-24	08:31:25.5113	K_s	-0.08 ± 0.75	17.86 ± 0.85
2018-04-24	08:32:08.4728	K_s	0.19 ± 0.62	17.21 ± 0.65
2018-04-24	08:32:51.5191	K_s	0.40 ± 0.56	18.41 ± 0.58
2018-04-24	08:33:35.5337	K_s	0.41 ± 0.67	18.02 ± 0.73
2018-04-24	08:34:18.5490	K_s	2.53 ± 0.56	18.63 ± 0.56
2018-04-24	08:35:02.5184	K_s	-0.26 ± 0.57	17.00 ± 0.59
2018-04-24	08:35:46.4971	K_s	-0.26 ± 0.55	18.00 ± 0.57
2018-04-24	08:36:29.4429	K_s	0.22 ± 0.62	17.66 ± 0.66
2018-04-24	08:37:12.4789	K_s	0.24 ± 0.62	18.06 ± 0.67
2018-04-24	08:37:55.4433	K_s	0.43 ± 0.57	17.00 ± 0.59
2018-04-24	08:38:38.5527	K_s	1.15 ± 0.58	18.51 ± 0.61
2018-04-24	08:39:21.4670	K_s	0.73 ± 0.65	17.64 ± 0.69

2018-04-24	08:40:04.4663	K_s	1.77 ± 0.70	18.00 ± 0.73
2018-04-24	08:40:47.4989	K_s	-0.26 ± 0.57	18.00 ± 0.60
2018-04-24	08:41:31.5503	K_s	0.59 ± 0.83	18.33 ± 0.95
2018-04-24	08:42:16.4359	K_s	0.93 ± 0.62	18.49 ± 0.66
2018-04-24	08:43:01.5658	K_s	0.89 ± 0.91	18.71 ± 1.06
2018-04-24	08:43:44.5240	K_s	0.65 ± 0.71	18.37 ± 0.78
2018-04-24	09:19:21.7716	K_s	0.36 ± 0.80	17.86 ± 0.90
2018-04-24	09:20:04.4819	K_s	-0.16 ± 1.06	18.00 ± 1.30
2018-04-24	09:20:47.4723	K_s	0.74 ± 0.77	18.00 ± 0.86
2018-04-24	09:21:30.5556	K_s	-0.63 ± 0.64	17.77 ± 0.72
2018-04-24	09:22:13.5341	K_s	-0.39 ± 0.55	17.76 ± 0.57
2018-04-24	09:22:56.5168	K_s	0.40 ± 0.59	18.25 ± 0.62
2018-04-24	09:23:39.5539	K_s	0.16 ± 0.62	17.35 ± 0.66
2018-04-24	09:24:22.4762	K_s	-0.26 ± 0.85	19.00 ± 1.02
2018-04-24	09:25:05.5376	K_s	-0.41 ± 0.55	17.75 ± 0.57
2018-04-24	09:25:48.5632	K_s	0.55 ± 0.74	18.02 ± 0.82
2018-04-24	09:26:33.5437	K_s	-0.23 ± 0.59	17.34 ± 0.62
2018-04-24	09:27:18.5983	K_s	0.36 ± 0.94	17.72 ± 1.08
2018-04-24	09:28:03.5422	K_s	0.32 ± 0.73	18.13 ± 0.81
2018-04-24	09:28:46.5026	K_s	0.06 ± 0.66	17.98 ± 0.72
2018-04-24	09:29:30.5060	K_s	-0.05 ± 0.62	18.00 ± 0.68
2018-04-24	09:30:13.5613	K_s	-0.26 ± 0.82	19.00 ± 1.01
2018-04-24	09:30:56.5058	K_s	-0.48 ± 0.64	18.47 ± 0.72
2018-04-24	09:31:39.4651	K_s	-0.3 ± 0.62	17.53 ± 0.67
2018-04-24	09:32:22.5595	K_s	0.19 ± 0.69	18.29 ± 0.77
2018-04-24	09:33:07.5262	K_s	0.48 ± 0.60	18.73 ± 0.64
2018-04-24	10:09:50.3978	K_s	1.57 ± 0.60	18.14 ± 0.62
2018-04-24	10:10:33.5252	K_s	1.74 ± 0.72	17.92 ± 0.76
2018-04-24	10:11:17.5508	K_s	0.74 ± 0.74	17.00 ± 0.81
2018-04-24	10:12:01.5106	K_s	2.74 ± 0.89	19.67 ± 0.97
2018-04-24	10:12:46.5259	K_s	0.64 ± 0.69	17.97 ± 0.75
2018-04-24	10:13:30.5296	K_s	2.30 ± 0.86	19.03 ± 0.93
2018-04-24	10:14:15.4991	K_s	1.13 ± 0.88	17.25 ± 0.95
2018-04-24	10:14:59.5497	K_s	0.90 ± 1.88	18.75 ± 2.36
2018-04-24	10:15:43.5676	K_s	1.73 ± 0.88	17.39 ± 0.93
2018-04-24	10:16:26.5017	K_s	3.74 ± 1.44	19.00 ± 1.49
2018-04-24	10:17:09.5371	K_s	1.74 ± 2.37	18.00 ± 2.70
2018-04-24	10:17:53.5084	K_s	1.12 ± 1.04	17.46 ± 1.14
2018-04-24	10:18:36.5269	K_s	2.65 ± 1.14	18.53 ± 1.23
2018-04-24	10:19:21.5174	K_s	1.87 ± 0.87	18.09 ± 0.93
2018-04-24	10:20:06.5090	K_s	2.53 ± 0.71	17.91 ± 0.73
2018-04-24	10:20:50.5087	K_s	0.34 ± 0.60	16.94 ± 0.63

Table 9.3: K_s-band observations in 24.04.2018

Date	UT time	Filter	Sgr A* (mJy)	S65 (mJy)
2018-04-24	05:59:54.2699	L′	58.65 ± 1.42	58.65 ± 1.65
2018-04-24	06:02:03.6762	L′	48.52 ± 1.00	48.52 ± 2.15
2018-04-24	06:02:46.6076	L′	40.50 ± 0.96	40.50 ± 0.79
2018-04-24	06:04:56.6002	L′	46.93 ± 0.85	46.93 ± 0.52
2018-04-24	06:05:39.7347	L′	43.39 ± 1.20	43.39 ± 1.28
2018-04-24	06:08:33.6633	L′	36.87 ± 0.71	36.87 ± 0.33
2018-04-24	06:10:42.6578	L′	42.55 ± 2.08	42.55 ± 1.89
2018-04-24	06:11:25.5900	L′	49.11 ± 1.49	49.11 ± 1.22
2018-04-24	06:13:34.5851	L′	48.85 ± 2.85	48.85 ± 2.97
2018-04-24	07:09:50.7207	L′	48.20 ± 1.00	48.20 ± 0.83
2018-04-24	07:12:02.5121	L′	37.95 ± 0.79	37.95 ± 1.32
2018-04-24	07:12:45.6428	L′	57.31 ± 2.88	57.31 ± 4.51
2018-04-24	07:14:55.6339	L′	55.67 ± 1.12	55.67 ± 1.05
2018-04-24	07:15:38.5614	L′	42.29 ± 0.88	42.29 ± 0.85
2018-04-24	07:17:48.9540	L′	46.01 ± 1.09	46.01 ± 1.07
2018-04-24	07:21:26.6003	L′	47.64 ± 2.13	47.64 ± 2.72
2018-04-24	07:23:36.6025	L′	41.35 ± 2.59	41.35 ± 2.90
2018-04-24	08:56:01.8162	L′	46.10 ± 1.19	46.10 ± 1.34
2018-04-24	08:58:13.8069	L′	46.65 ± 1.31	46.65 ± 1.97
2018-04-24	08:58:56.7402	L′	59.01 ± 1.89	59.01 ± 2.90
2018-04-24	09:01:09.7399	L′	40.13 ± 0.79	40.13 ± 0.90
2018-04-24	09:01:52.6723	L′	42.72 ± 0.97	42.72 ± 1.22
2018-04-24	09:04:05.6670	L′	44.82 ± 0.57	44.82 ± 1.52
2018-04-24	09:04:48.6004	L′	37.67 ± 0.60	37.67 ± 2.50
2018-04-24	09:06:58.5937	L′	49.07 ± 1.31	49.07 ± 1.49
2018-04-24	09:07:41.7262	L′	40.40 ± 2.63	40.40 ± 3.70
2018-04-24	09:09:51.7224	L′	45.91 ± 1.25	45.91 ± 1.37
2018-04-24	09:47:20.5426	L′	53.80 ± 1.52	53.80 ± 1.84
2018-04-24	09:49:33.7633	L′	43.95 ± 1.54	43.95 ± 2.11
2018-04-24	09:50:17.7009	L′	49.92 ± 2.35	49.92 ± 3.30
2018-04-24	09:52:28.9280	L′	40.47 ± 1.62	40.47 ± 1.77
2018-04-24	09:53:13.6630	L′	45.34 ± 0.66	45.34 ± 0.46
2018-04-24	09:55:24.6675	L′	49.76 ± 1.21	49.76 ± 1.13
2018-04-24	09:56:09.0032	L′	44.46 ± 2.65	44.46 ± 4.45
2018-04-24	09:58:18.8474	L′	52.33 ± 1.76	52.33 ± 2.21
2018-04-24	09:59:01.7859	L′	39.65 ± 2.22	39.65 ± 3.58
2018-04-24	10:01:11.7881	L′	48.73 ± 2.74	48.73 ± 4.01

Table 9.4: L′-band observations in 24.04.2018

Bibliography

Arp, H. 1965, ApJ, 141, 43

Baade, W. 1946, PASP, 58, 249

Babcock, H. W. 1939, Lick Observatory Bulletin, 498, 41

Balick, B. & Brown, R. L. 1974, ApJ, 194, 265

Becklin, E. E. & Neugebauer, G. 1975, ApJ, 200, L71

Beichman, C. A., Rieke, M., Eisenstein, D., et al. 2012, in Society of Photo-Optical Instrumentation Engineers (SPIE) Conference Series, Vol. 8442, Space Telescopes and Instrumentation 2012: Optical, Infrared, and Millimeter Wave, ed. M. C. Clampin, G. G. Fazio, H. A. MacEwen, & J. Oschmann, Jacobus M., 84422N

Berukoff, S. J. & Hansen, B. M. S. 2006, ApJ, 650, 901

Bhat, H. K., Sabha, N. B., Zajaček, M., et al. 2022, ApJ, 929, 178

Blitz, L. & Spergel, D. N. 1991, ApJ, 379, 631

Blum, R. D., Ramírez, S. V., Sellgren, K., & Olsen, K. 2003, The Astrophysical Journal, 597, 323

Brown, R. L. 1982, ApJ, 262, 110

Brusa, M., Civano, F., Comastri, A., et al. 2010, ApJ, 716, 348

Carignan, C., Chemin, L., Huchtmeier, W. K., & Lockman, F. J. 2006, The Astrophysical Journal, 641, L109

Christopher, M. H., Scoville, N. Z., Stolovy, S. R., & Yun, M. S. 2005, ApJ, 622, 346

Ciurlo, A., Campbell, R. D., Morris, M. R., et al. 2020, Nature, 577, 337

Cutri, R. M., Wright, E. L., Conrow, T., et al. 2013a, Explanatory Supplement to the AllWISE Data Release Products, Explanatory Supplement to the AllWISE Data Release Products, by R. M. Cutri et al.

Cutri, R. M., Wright, E. L., Conrow, T., et al. 2013b, Explanatory Supplement to the AllWISE Data Release Products, Explanatory Supplement to the AllWISE Data Release Products, by R. M. Cutri et al.

Diolaiti, E., Bendinelli, O., Bonaccini, D., et al. 2000, A&AS, 147, 335

Do, T., Hees, A., Ghez, A., et al. 2019, Science, 365, 664

Doyon, R., Hutchings, J. B., Beaulieu, M., et al. 2012, in Society of Photo-Optical Instrumentation Engineers (SPIE) Conference Series, Vol. 8442, Space Telescopes and Instrumentation 2012: Optical, Infrared, and Millimeter Wave, ed. M. C. Clampin, G. G. Fazio, H. A. MacEwen, & J. Oschmann, Jacobus M., 84422R

Dwek, E., Arendt, R. G., Hauser, M. G., et al. 1995, ApJ, 445, 716

Eckart, A. & Genzel, R. 1996, Nature, 383, 415

Eckart, A. & Genzel, R. 1997, MNRAS, 284, 576

Eckart, A., Genzel, R., Ott, T., & Schödel, R. 2002, MNRAS, 331, 917

Eckart, A., Hüttemann, A., Kiefer, C., et al. 2017, Foundations of Physics, 47, 553, ArXiv: 1703.09118

Eckart, A., Moultaka, J., Viehmann, T., Straubmeier, C., & Mouawad, N. 2004, ApJ, 602, 760

Eckart, A., Mužić, K., Yazici, S., et al. 2013, A&A, 551, A18

Eckart, A., Ott, T., & Genzel, R. 1999, A&A, 352, L22

Eggen, O. J., Lynden-Bell, D., & Sandage, A. R. 1962, ApJ, 136, 748

Einasto, J., Saar, E., Kaasik, A., & Chernin, A. D. 1974, Nature, 252, 111

Eisenhauer, F., Genzel, R., Alexander, T., et al. 2005, The Astrophysical Journal, 628, 246

Eisenhauer, F., Schödel, R., Genzel, R., et al. 2003, ApJ, 597, L121

Ekers, R. D., Goss, W. M., Schwarz, U. J., Downes, D., & Rogstad, D. H. 1975, A&A, 43, 159

Ekers, R. D., van Gorkom, J. H., Schwarz, U. J., & Goss, W. M. 1983, A&A, 122, 143

Event Horizon Telescope Collaboration, Akiyama, K., Alberdi, A., et al. 2022, ApJ, 930, L12

Event Horizon Telescope Collaboration, Akiyama, K., Alberdi, A., et al. 2019, ApJ, 875, L1

Finkbeiner, A. 2012, Nature, 490, 24

Fischer, S., Moratschke, D., Straubmeier, C., et al. 2008, in Society of Photo-Optical Instrumentation Engineers (SPIE) Conference Series, Vol. 7010, Space Telescopes and Instrumentation 2008: Optical, Infrared, and Millimeter, ed. J. Oschmann, Jacobus M., M. W. M. de Graauw, & H. A. MacEwen, 70103K

Fischer, S., Straubmeier, C., Eckart, A., Rossi, L., & Mazy, E. 2006, in Society of Photo-Optical Instrumentation Engineers (SPIE) Conference Series, Vol. 6265, Space Telescopes and Instrumentation I: Optical, Infrared, and Millimeter, ed. J. C. Mather, H. A. MacEwen, & M. W. M. de Graauw, 62653A

Fried, D. L. 1996, in European Southern Observatory Conference and Workshop Proceedings, Vol. 54, European Southern Observatory Conference and Workshop Proceedings, 363

Fritz, T. K., Gillessen, S., Dodds-Eden, K., et al. 2011, ApJ, 737, 73

Gabor, J. M., Impey, C. D., Jahnke, K., et al. 2009, ApJ, 691, 705

Gardner, J. P., Mather, J. C., Clampin, M., et al. 2006, Space Sci. Rev., 123, 485

Genzel, R., Eisenhauer, F., & Gillessen, S. 2010, Reviews of Modern Physics, 82, 3121

Genzel, R., Schödel, R., Ott, T., et al. 2003, ApJ, 594, 812

Genzel, R., Thatte, N., Krabbe, A., Kroker, H., & Tacconi-Garman, L. E. 1996, The Astrophysical Journal, 472, 153

Genzel, R., Watson, D. M., Crawford, M. K., & Townes, C. H. 1985, ApJ, 297, 766

Gerhard, O. 2001, ApJ, 546, L39

Ghez, A. M., Duchêne, G., Matthews, K., et al. 2003, ApJ, 586, L127

Ghez, A. M., Klein, B. L., Morris, M., & Becklin, E. E. 1998, ApJ, 509, 678

Ghez, A. M., Morris, M., Becklin, E. E., Tanner, A., & Kremenek, T. 2000, Nature, 407, 349

Ghez, A. M., Salim, S., Weinberg, N. N., et al. 2008, ApJ, 689, 1044

Gillessen, S., Eisenhauer, F., Trippe, S., et al. 2009a, ApJ, 692, 1075

Gillessen, S., Eisenhauer, F., Trippe, S., et al. 2009b, ApJ, 692, 1075

Gillessen, S., Plewa, P. M., Eisenhauer, F., et al. 2017, ApJ, 837, 30

Glindemann, A., Algomedo, J., Amestica, R., et al. 2003, in Society of Photo-Optical Instrumentation Engineers (SPIE) Conference Series, Vol. 4838, Interferometry for Optical Astronomy II, ed. W. A. Traub, 89–100

Goss, W. M. & McGee, R. X. 1996a, 102, 369

Goss, W. M. & McGee, R. X. 1996b, in Astronomical Society of the Pacific Conference Series, Vol. 102, The Galactic Center, ed. R. Gredel, 369

GRAVITY Collaboration, Abuter, R., Accardo, M., et al. 2019, The Messenger, 178, 26

Gravity Collaboration, Abuter, R., Amorim, A., et al. 2018, A&A, 615, L15

Gravity Collaboration, Abuter, R., Amorim, A., et al. 2019, A&A, 625, L10

GRAVITY Collaboration, Abuter, R., Amorim, A., et al. 2021, A&A, 645, A127

Guesten, R., Genzel, R., Wright, M. C. H., et al. 1987, ApJ, 318, 124

Habibi, M., Gillessen, S., Martins, F., et al. 2017, ApJ, 847, 120

Haubois, X., Dodds-Eden, K., Weiss, A., et al. 2012, A&A, 540, A41

Helmi, A. 2008, The Astronomy and Astrophysics Review, 15, 145

Herrnstein, R. M. & Ho, P. T. P. 2002, ApJ, 579, L83

Hesser, J. E. 1992, in The Stellar Populations of Galaxies, ed. B. Barbuy & A. Renzini, Vol. 149, 1

Heywood, I., Rammala, I., Camilo, F., et al. 2022, The Astrophysical Journal, 925, 165

Hobbs, A. & Nayakshin, S. 2009, MNRAS, 394, 191

Högbom, J. A. 1974, A&AS, 15, 417

Jalali, B., Pelupessy, F. I., Eckart, A., et al. 2014, Monthly Notices of the Royal Astronomical Society, 444, 1205

Kahn, F. D. & Woltjer, L. 1959, ApJ, 130, 705

Kartaltepe, J. S., Sanders, D. B., Le Floc'h, E., et al. 2010, ApJ, 709, 572

Klaassen, P. D., Geers, V. C., Beard, S. M., et al. 2021, MNRAS, 500, 2813

Krabbe, A., Genzel, R., Eckart, A., et al. 1995, The Astrophysical Journal, 447, L95

Kunneriath, D., Eckart, A., Vogel, S. N., et al. 2012, A&A, 538, A127

Lebofsky, M. J., Rieke, G. H., & Tokunaga, A. T. 1982, ApJ, 263, 736

Levin, Y. & Beloborodov, A. M. 2003, ApJ, 590, L33

Lo, K. Y. & Claussen, M. J. 1983, Nature, 306, 647

Lord, S. D. 1992, A new software tool for computing Earth's atmospheric transmission of near- and far-infrared radiation, NASA Technical Memorandum 103957

Lucy, L. B. 1974, AJ, 79, 745

Maillard, J. P., Paumard, T., Stolovy, S. R., & Rigaut, F. 2004, Astronomy and Astrophysics, 423, 155

McConnachie, A. W., Irwin, M. J., Ferguson, A. M. N., et al. 2005, MNRAS, 356, 979

McMillan, S. L. W. & Portegies Zwart, S. F. 2003, ApJ, 596, 314

Mezger, P. G., Zylka, R., Salter, C. J., et al. 1989, A&A, 209, 337

Morris, M. 1992, in American Institute of Physics Conference Series, Vol. 278, American Institute of Physics Conference Series, 21–36

Morris, M. 1993, ApJ, 408, 496

Moultaka, J., Eckart, A., Schödel, R., Viehmann, T., & Najarro, F. 2005, A&A, 443, 163

Mužić, K., Eckart, A., Schödel, R., et al. 2010, A&A, 521, A13

Mužić, K., Eckart, A., Schödel, R., Meyer, L., & Zensus, A. 2007, A&A, 469, 993

Mužić, K., Schödel, R., Eckart, A., Meyer, L., & Zensus, A. 2008, Astronomy and Astrophysics, 482, 173

Narayan, R., Mahadevan, R., Grindlay, J. E., Popham, R. G., & Gammie, C. 1998, ApJ, 492, 554

Navarro, J. F., Frenk, C. S., & White, S. D. M. 1997, ApJ, 490, 493

Oort, J. H. 1977, ARA&A, 15, 295

Ostriker, J. P., Peebles, P. J. E., & Yahil, A. 1974, ApJ, 193, L1

Ott, T., Eckart, A., & Genzel, R. 1999, in Astronomical Society of the Pacific Conference Series, Vol. 186, The Central Parsecs of the Galaxy, ed. H. Falcke, A. Cotera, W. J. Duschl, F. Melia, & M. J. Rieke, 310

Ott, T., Eckart, A., & Genzel, R. 1999, The Astrophysical Journal, 523, 248

Parsa, M., Eckart, A., Shahzamanian, B., et al. 2017, ApJ, 845, 22

Paumard, T., Genzel, R., Martins, F., et al. 2006, ApJ, 643, 1011

Paumard, T., Genzel, R., Martins, F., et al. 2006, 643, 1011

Peißker, F., Ali, B., Zajaček, M., et al. 2021a, ApJ, 909, 62

Peißker, F., Eckart, A., & Parsa, M. 2020a, ApJ, 889, 61

Peißker, F., Eckart, A., Zajaček, M., Ali, B., & Parsa, M. 2020b, ApJ, 899, 50

Peißker, F., Hosseini, S. E., Zajaček, M., et al. 2020c, A&A, 634, A35

Peißker, F., Zajaček, M., Eckart, A., et al. 2021b, ApJ, 923, 69

Peißker, F., Zajaček, M., Eckart, A., et al. 2019, A&A, 624, A97

Pfuhl, O., Fritz, T. K., Zilka, M., et al. 2011, ApJ, 741, 108

Portegies Zwart, S. F., Baumgardt, H., McMillan, S. L. W., et al. 2006, ApJ, 641, 319

Portegies Zwart, S. F. & McMillan, S. L. W. 2002, ApJ, 576, 899

Predehl, P., Sunyaev, R. A., Becker, W., et al. 2020, Nature, 588, 227

Purcell, G. B., Buta, R., & Crocker, D. A. 1993, in American Astronomical Society Meeting Abstracts, Vol. 183, American Astronomical Society Meeting Abstracts, 77.06

Reid, M. J. 1993, ARA&A, 31, 345

Reid, M. J., Menten, K. M., Trippe, S., Ott, T., & Genzel, R. 2007, ApJ, 659, 378

Requena-Torres, M. A., Güsten, R., Weiß, A., et al. 2012, A&A, 542, L21

Richardson, W. H. 1972, Journal of the Optical Society of America (1917-1983), 62, 55

Rieke, G. H., Wright, G. S., Böker, T., et al. 2015, Publications of the Astronomical Society of the Pacific, 127, 584

Rieke, M. J., Kelly, D., & Horner, S. 2005, in Society of Photo-Optical Instrumentation Engineers (SPIE) Conference Series, Vol. 5904, Cryogenic Optical Systems and Instruments XI, ed. J. B. Heaney & L. G. Burriesci, 1–8

Rizzuto, F. P., Naab, T., Spurzem, R., et al. 2020, arXiv, 5273, 5257

Roberts, M. S. & Rots, A. H. 1973, A&A, 26, 483

Rose, S. C., Naoz, S., Sari, R., & Linial, I. 2021 [arXiv:2201.00022]

Rubin, V. C., Burstein, D., Ford, W. K., J., & Thonnard, N. 1985, ApJ, 289, 81

Sabha, N. B. I. 2015, PhD thesis, Andreas Eckart University of Cologne, Germany

Schinnerer, E., Smolčić, V., Carilli, C. L., et al. 2007, ApJS, 172, 46

Schödel, R., Eckart, A., Iserlohe, C., Genzel, R., & Ott, T. 2005, The Astrophysical Journal, 625, L111

Schödel, R., Morris, M. R., Muzic, K., et al. 2011, A&A, 532, A83

Schödel, R., Ott, T., Genzel, R., et al. 2002, Nature, 419, 694

Schoedel, R., Eckart, A., Muzic, K., et al. 2006, arXiv e-prints, astro

Shapley, H. 1928, Nature, 122, 482

Shimwell, T. W., Röttgering, H. J. A., Best, P. N., et al. 2017, A&A, 598, A104

Sohn, S. T., Anderson, J., & van der Marel, R. P. 2012, The Astrophysical Journal, 753, 7

Spitzer, Lyman, J. 1969, ApJ, 158, L139

Springel, V., White, S. D. M., Jenkins, A., et al. 2005, Nature, 435, 629

Stanek, K. Z., Mateo, M., Udalski, A., et al. 1996, in Astronomical Society of the Pacific Conference Series, Vol. 91, IAU Colloq. 157: Barred Galaxies, ed. R. Buta, D. A. Crocker, & B. G. Elmegreen, 545

Tanner, A., Figer, D. F., Najarro, F., et al. 2006, ApJ, 641, 891

Tanner, A., Ghez, A. M., Morris, M., et al. 2002, The Astrophysical Journal, 575, 860

Tanner, A., Ghez, A. M., Morris, M. R., & Christou, J. C. 2005, ApJ, 624, 742

Tanner, A., Ghez, A. M., Morris, M. R., & Christou, J. C. 2005, The Astrophysical Journal, 624, 742

Tanner, A. M., Ghez, A. M., Morris, M., & Becklin, E. E. 2003, Astronomische Nachrichten Supplement, 324, 597

Trump, J. R., Impey, C. D., McCarthy, P. J., et al. 2007, ApJS, 172, 383

Tully, R. B., Courtois, H., Hoffman, Y., & Pomarède, D. 2014, Nature, 513, 71

van der Marel, R. P., Besla, G., Cox, T. J., Sohn, S. T., & Anderson, J. 2012, The Astrophysical Journal, 753, 9

van der Marel, R. P., Fardal, M., Besla, G., et al. 2012, ApJ, 753, 8

Véron-Cetty, M. P. & Véron, P. 2006, A&A, 455, 773

Wang, S., Liu, J., Qiu, Y., et al. 2016, ApJS, 224, 40

White, S. D. M. & Rees, M. J. 1978, Monthly Notices of the Royal Astronomical Society, 183, 341

Witzel, G., Martinez, G., Hora, J., et al. 2018, ApJ, 863, 15

Witzel, G., Martinez, G., Willner, S. P., et al. 2021a, ApJ, 917, 73

Witzel, G., Martinez, G., Willner, S. P., et al. 2021b, ApJ, 917, 73

Wright, G. S., Reike, G., Barella, P., et al. 2008, in Society of Photo-Optical Instrumentation Engineers (SPIE) Conference Series, Vol. 7010, Space Telescopes and Instrumentation 2008: Optical, Infrared, and Millimeter, ed. J. Oschmann, Jacobus M., M. W. M. de Graauw, & H. A. MacEwen, 70100T

Wright, G. S., Rieke, G., Boeker, T., et al. 2010, in Society of Photo-Optical Instrumentation Engineers (SPIE) Conference Series, Vol. 7731, Space Telescopes and Instrumentation 2010: Optical, Infrared, and Millimeter Wave, ed. J. Oschmann, Jacobus M., M. C. Clampin, & H. A. MacEwen, 77310E

Wright, M. C. H., Coil, A. L., McGary, R. S., Ho, P. T. P., & Harris, A. I. 2001, ApJ, 551, 254

Wylezalek, D., Vayner, A., Rupke, D. S. N., et al. 2022, ApJ, 940, L7

Yuan, F., Quataert, E., & Narayan, R. 2003, ApJ, 598, 301

Yusef-Zadeh, F. & Morris, M. 1987, ApJ, 320, 545

Yusef-Zadeh, F. & Morris, M. 1991, ApJ, 371, L59

Yusef-Zadeh, F., Roberts, D. A., & Biretta, J. 1998, ApJ, 499, L159

Zajaček, M., Araudo, A., Karas, V., Czerny, B., & Eckart, A. 2020a, ApJ, 903, 140

Zajaček, M., Araudo, A., Karas, V., et al. 2020b, arXiv e-prints, arXiv:2011.12868

Zucker, S., Alexander, T., Gillessen, S., Eisenhauer, F., & Genzel, R. 2006, ApJ, 639, L21

Zylka, R., Mezger, P. G., Ward-Thompson, D., Duschl, W. J., & Lesch, H. 1995, A&A, 297, 83

List of Figures

List of Tables

Acknowledgements

I conclude my dissertation with my sincere gratitude to those who helped me over the past years and made my Ph.D. work a joyful experience.

First of all, I would like to thank my supervisor, Prof. Dr. Andreas Eckart. Thank you for always supporting me and giving me space and time to explore. Thank you for all our fantastic discussions over the last few years.

I also thank Prof. Dr. Anton J. Zensus and Prof. Dr. Dennis Mücher for being willing to be part of my thesis committee.

Many thanks to all the amazing people and colleagues who read my dissertation and provided me with their fruitful comments: Alex, Daniel, Mahya, Persis, and Madeleine.

A big thanks to aegroup for the nice corridor chats, wonderful lunch times, and group meetings.

To Madeleine: Thank you for bringing so much happiness and joy to my life. Thanks for all the planning and Zoom calls.

To Monica: Thank you for all the outstanding Galactic Center discussions. To Matthias: Thank you for the tremendous scientific meetings.

To Daniel: Thank you very much for listening to all my crazy plans :) and helping me to put them into action. Thanks for being by my side in the hardest times, and truly, the last steps were not possible without your mental support. I sincerely thank you.

To Mahya: My profound thanks to you. I am grateful to have you by my side. You have always been as smooth and refreshing as the spring breath for me.

To Nafise: Thanks for all the laughing times when we could not continue laughing because of the jaw pain and stomachache! :)

To "Girls from 220": Persis and Harshitha, who made the office a lovely, understanding place. I am thankful for the fantastic memories of our movie nights and all the historical, political, cultural, and linguistic discussions we had.

To Birka: Thank you for making my life much more joyful.

To the "Persian Gang": Thank you, dear Samane, Zahra, Roya, Sajjad, Dana, and the cutest Andisheh, for bringing so much happiness into my life. Spending time with you makes the time fly by.

To the kind secretaries of PH1 who always helped me with the bureaucratic matters and made the days nicer with the occasional chats. To Dr. Petra Neubauer-Guenther: Thank you for the lovely conversations and fast replies.

Last but not least, my sincerest and deepest gratitude goes to my wonderful family. Thank you, Maman and Baba, for the continued love and support and for giving me space to do what I like. And my dearest brother, Nima: you make life much more fun. Thanks for being in my life.

Finally, these years have not been easy years to be an Iranian. During the course of the years that I completed my dissertation, the PS752 flight was shot, the Internet was cut off for a month in my home country, and people were brutally murdered by the government. A girl named #MahsaAmini was innocently killed, igniting the uprising of "Woman, Life, Freedom" in Iran. I hope one day we can live in a world empty of guns and human killing machines and no one gets killed for demanding freedom.

I also thank DLR, which provided the funding for this project and made it possible for me to conduct my research on cutting-edge science questions in astrophysics and have the honor to contribute to the JWST community. This work was partially supported by the Bonn Cologne Graduate School (BCGS) for Physics and Astronomy, the DFG, via the SFB 956, and the International Max Planck Research School (IMPRS) for Astronomy and Astrophysics at the MPIfR and the Universities of Bonn and Cologne.

Selbstständigkeitserklärung

Hiermit versichere ich an Eides statt, dass ich die vorliegende Dissertation selbstständig und ohne die Benutzung anderer als der angegebenen Hilfsmittel und Literatur angefertigt habe. Alle Stellen, die wörtlich oder sinngemäß aus veröffentlichten und nicht veröffentlichten Werken dem Wortlaut oder dem Sinn nach entnommen wurden, sind als solche kenntlich gemacht. Ich versichere an Eides statt, dass diese Dissertation noch keiner anderen Fakultät oder Universität zur Prüfung vorgelegen hat; dass sie - abgesehen von unten angegebenen Teilpublikationen und eingebundenen Artikeln und Manuskripten - noch nicht veröffentlicht worden ist sowie, dass ich eine Veröffentlichung der Dissertation vor Abschluss der Promotion nicht ohne Genehmigung des Promotionsausschusses vornehmen werde. Die Bestimmungen dieser Ordnung sind mir bekannt. Darüber hinaus erkläre ich hiermit, dass ich die Ordnung zur Sicherung guter wissenschaftlicher Praxis und zum Umgang mit wissenschaftlichem Fehlverhalten der Universität zu Köln gelesen und sie bei der Durchführung der Dissertation zugrundeliegenden Arbeiten und der schriftlich verfassten Dissertation beachtet habe und verpflichte mich hiermit, die dort genannten Vorgaben bei allen wissenschaftlichen Tätigkeiten zu beachten und umzusetzen. Ich versichere, dass die eingereichte elektronische Fassung der eingereichten Druckfassung vollständig entspricht.

Köln, den 2.5.2023

E. Hosseini

(Seyedeh Elaheh Hosseini)

Teilpublikationen/eingebundene Artikel

- *Constraining the accretion flow density profile near Sgr A* using the L'-band emission of the S2 star*; **S. E. Hosseini et al. 2020** .
- *Discovery of a dense association of stars in the vicinity of the supermassive black hole Sgr A**; **S. E. Hosseini et al. 2022**, .